THE LAVES PHASE EMBRITTLEMENT OF FERRITIC STAINLESS STEEL TYPE AISI 441

MAITSE P. SELLO

UNIVERSITEIT VAN PRETORIA
UNIVERSITY OF PRETORIA
YUNIBESITHI YA PRETORIA

THE LAVES PHASE EMBRITTLEMENT OF FERRITIC STAINLESS STEEL TYPE AISI 441

BY

MAITSE P. SELLO

SUPERVISED BY
PROFESSOR WALDO E. STUMPF

Submitted in fulfilment of the requirements for the degree

Philosophiae Doctor, PhD (Metallurgy)

in the

Department of Materials Science and Metallurgical Engineering

Faculty of Engineering, Building Environment and Information Technology

University of Pretoria

REPUBLIC OF SOUTH AFRICA

2009, June 15

PREFACE

This dissertation is submitted for the degree of Doctor of Philosophy at the University of Pretoria. The research described herein was conducted under the supervision of Professor W. Stumpf in the department of Materials Science and Metallurgical Engineering, University of Pretoria.

Except where acknowledgements and references are made to previous work, this work is, to the best of my knowledge, original. This dissertation is the result of my own work and includes nothing of which is the outcome of work done in collaboration with others except where specifically indicated in the text. Neither this, nor any substantially similar dissertation has been, or is being submitted to my knowledge for any other degree, diploma, or other qualification at any other university.

____

Maitse P. Sello

ACKNOWLEDGEMENT

I would like to thank God for his guidance in my life, and also for being my strength and guidance in my life.

I would like to express my sincere thanks to my academic supervisor, Prof. Waldo E. Stumpf for his invaluable guidance, encouragement and input in this research project. I have benefited a lot from his experience and insight during this research project.

I would like to thank Mrs Sarah Havenga, Mrs Lillian Barlow and Mrs Elsie Snyman – Ferreira for their help with the administrative work.

I would like to thank Prof L. Cornish (currently at the University of Witswatersrand) and Mrs L. H. Chown for their training and guidance during thermodynamic modelling using Thermo-Calc® software at Mintek

I would like to thank Mrs A. Tuling and Mr C. van der Merwe for their help with TEM work, Dr N. van der Berg for his expertise in the electron diffraction indexing and Mr C. Coetzee for his help with the SEM.

I would also like to thank Dr S. Verryne and Prof. J de Villiers for their help in XRD analysis and also their expertise, they have always been available for help whenever needed, and for that I am very grateful.

I would like to thank everyone at the University for company and support during my time there. There are many interesting, encouraging and happy moments to remember with my friends during the course of my studies.

Finally I would like to thank my parents and siblings for supporting me in every decision that I have taken in my life, thank you for your support and patience.

THE LAVES PHASE EMBRITTLEMENT OF FERRITIC STAINLESS STEEL TYPE AISI 441

Author: **Maitse P. Sello**

Supervisor: **Professor Waldo E. Stumpf**

Department of Materials Science and Metallurgical Engineering

University of Pretoria

Philosophiae Doctor (Materials Science and Metallurgical Engineering)

Synopsis

The effect of Laves phase (Fe_2Nb) formation on the Charpy impact toughness of the ferritic stainless steel type AISI 441 was investigated. The steel exhibits good toughness after solution treatment at 850 °C, but above and below this treatment temperature the impact toughness decreases sharply. With heat treatment below 850 °C the presence of the Laves phase on grain boundaries and dislocations plays a significant role in embrittlement of the steel whereas above that temperature, an increase in the grain size from grain growth plays a major role in the impact embrittlement of this alloy. The toughness results agree with the phase equilibrium calculations made using Thermo–Calc® whereby it was observed that a decrease in the Laves phase volume fraction with increasing temperature corresponds to an increase in the impact toughness of the steel. Annealing above 900 °C where no Laves phase exists, grain growth is found which similarly has a very negative influence on the steel's impact properties. Where both a large grain size as well as Laves phase is present, it appears that the grain size may be the dominant embrittlement mechanism. Both the Laves phase and grain growth, therefore, have a significant influence on the impact properties of the steel, while the Laves phase's precipitation behaviour has also been investigated with reference to the plant's manufacturing process, particularly the cooling rate after a solution treatment.

The microstructural analysis of the grain size shows that there is a steady increase in grain size up to about 950 °C, but between 950 °C and 1000 °C there is a sudden and rapid 60 % increase in the grain size. The TEM analysis of the sample that was annealed at 900 °C shows that the Laves phase had already completely dissolved and cannot, therefore, be responsible for "unpinning of grain boundaries" at temperatures of 900 °C and higher where this "sudden" increase in grain size was found. The most plausible explanation appears to be one of Nb solute drag that loses its effectiveness within this temperature range, but this probably requires some further study to fully prove this effect.

During isothermal annealing within the temperature range of 600 to 850 °C, the time – temperature – precipitation (*TTP*) diagram for the Laves phase as determined from the transformation kinetic curves, shows two classical C noses on the transformation curves. The first one occurring at the higher temperatures of about 750 to 825 °C and the second one at much lower temperatures, estimated to possibly be in the range of about 650 to 675 °C. The transmission electron microscopy (TEM) analyses show that there are two independent nucleation mechanisms that are occurring within these two temperature ranges. At lower temperatures of about 600 °C, the pertaining nucleation mechanism is on dislocations and as the temperature is increased to above 750 °C, grain boundary nucleation becomes more dominant. Also, the morphology of the particles and the misorientation with the matrix changes with temperature. At lower temperatures the particles are more needle-like in shape, but as the temperature is increased the shape becomes more spheroidal.

The effect of the steel's composition on the Laves phase transformation kinetics shows that by lowering the Nb content in these type 441 stainless steels, had no significance effect on the kinetics on precipitation of the Laves phase. However, a Mo addition and a larger grain size of the steel, retard the formation of the Laves phase, although the optimum values of both parameters still need further quantification.

The calculation made for the transformation kinetics of the Laves phase, using the number density of nucleation sites N_o and the interfacial energy γ as the fitting parameters in this work, demonstrated a reasonable agreement with experimental results.

Keywords: Laves phase (Fe_2Nb), titanium niobium carbonitrides (Ti,Nb)(C,N), impact embrittlement, grain size, ductile-to brittle transition temperature (DBTT), Laves phase transformation kinetics, Cottrell approach to grain size, Smith model of brittle grain boundary phases, Thermo- Calc®.

TABLE OF CONTENT

TABLE OF FIGURES

NOMENCLATURE

α_3	is the three-dimensional parabolic rate constant
β^*	atomic impingement rate
δ	volume misfit of the precipitate in the matrix
δ_{disl}	effective diameter of dislocation
δ_{gb}	width of the grain boundary
γ	interfacial surface energy per unit area associated with the interface of the two phases
γ_f	effective surface energy of ferrite
γ_s	surface energy of the exposed crack surface
γ_T	true surface energy
σ_i	friction stress
σ_y	yield strength
ν	Poisson's ratio
ν^α	lattice spacing of the matrix
ν^β	lattice spacing of the precipitate phase
ν_b	mobility rate
τ	incubation time
τ_e	effective shear stress
τ_i	lattice friction shear stress
τ_N	shear stress for crack nucleation
τ_y	yield shear stress
υ^β	molar volume of the phase β,
τ_s	shear stress
Φ	extent of the reaction parameter
θ	contact angle
$\boldsymbol{a}$	mean atomic lattice distance of the matrix phase
$\boldsymbol{b}$	Burgers vector
$\bar{c}$	average concentration of the solute in the matrix alone
c_α	equilibrium solute composition within the matrix
$c_r^{\alpha\beta}$	solute concentration in the α matrix that is in equilibrium with a spherical particle of β and r is the radius of curvature
$c^{\alpha\beta}$	equilibrium solute concentration in the α matrix at which $r \to \infty$
$c^{\beta\alpha}$	corresponding concentration in the β which is in equilibrium with α;
c_i	mole fraction of species i
c_j	mole fraction of species j
d	grain size
D	diffusion coefficient of the rate controlling solute atoms in the matrix
D_{disl}	diffusion coefficient down a dislocation
D_{gb}	diffusion coefficient along the grain boundary
E	Young's elastic modulus
f_{GB}	fraction of potential grain boundary sites filled by solute
G_m	shear modulus of the matrix
G_r	growth rate
ΔG	molar free energy change of the precipitate reaction
ΔG_v	Gibbs chemical free energy released per unit volume of new phase
ΔG_ε	misfit strain energy per unit volume
ΔG^*	known as the activation energy
G°	Gibbs energy due to the mechanical mixing of the constituents of the phase
$^{id}G_{mix}$	ideal mixing contribution
$^{xs}G_{mix}$	excess Gibbs energy of mix (the non-ideal mixing contribution)
ΔG_ε	strain energy
$G_m - H_m^{SER}$	Gibbs energy relative to a standard element reference state (SER)
h	Planck constants
H_m^{SER}	enthalpy of the element in its stable state

k	Boltzman constant
k_y^s	Hall – Petch constant for shear
L_{gb}	length of grain boundary per unit volume
$L_{i,j}^k$	binary interaction parameter between species i and j
M_0	intrinsic grain boundary mobility in pure material
M_T	overall mobility due to intrinsic plus solute drag
M_B	mobility in the presence of solute drag elements
n	number of dislocations in the pileup
$\dot{N}$	nucleation rate
N'	number of dislocations that meet each particle
N^*	concentration of critical – sized nuclei
N_c	density of the grain boundary corners
N_0	initial number density of nucleation sites per unit volume
p_d	driving force for the grain boundary mobility
Δp_{ppt}	retarding force exercised by particles on the grain boundary
Q	activation energy for diffusion
r^*	critical radius
r_0	initial average particle radius
R	gas constant
S_{gb}	surface area of grain boundary per unit volume
t	time
T	absolute temperature
V'	instantaneous volume fractions of alloy precipitates
V^{eq}	equilibrium volume fractions of alloy precipitates
V^{β}	instantaneous fraction
$V^{\beta\alpha}$	maximum fraction of a given phase
$V^{i\alpha}$	maximum volume fraction of the i^{th} phase
X_s	atom fraction of solute in the bulk metal
z	coordinate normal to the interface with the value z^*

CHAPTER ONE

GENERAL INTRODUCTION

1.1 INTRODUCTION

Columbus Stainless is the primary manufacturer of flat cast and wrought stainless steel products in Southern Africa. One of the growth sectors in the use of stainless steels is in the automotive components industry and more particularly, in catalytic converters in the automotive industry. The manufacture of automobile emission control systems in South Africa is one of the fastest growing industry sectors in the world. Founded on the growth and development of catalytic converters, South Africa supplies in excess of 10% of the world's production, mainly stemming from its dominance in PGM (Platinum Group Metals) production. Catalytic converters are the largest of the auto component groupings being exported from South Africa and now amount to $500 million/year. The growth of the local catalytic converter industry has been spectacular, see Figure 1.1.

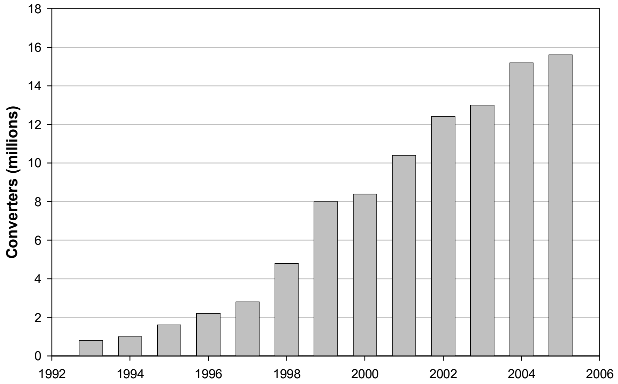

Figure 1.1. Catalytic converters growth industry in South Africa [1].

The operating temperatures for catalytic converters are in the region of 900°C but are associated with a frequent temperature variation as automobiles are used intermittently. Thus, the material for this application requires excellent thermal fatigue resistance and high temperature strength. The primary steel used in this application is type 441 stainless steel, (which is equivalent to DIN 1.4509). This steel is fully ferritic over a wide range of temperatures. Type 441 is a dual stabilised (titanium and niobium) ferritic stainless steel with 18 wt% chromium, and the typical composition of this steel is shown in the Table 1.1 below. Titanium and Niobium carbides are more stable than chromium carbides and prevent the formation of chromium carbides on grain boundaries (which results in sensitisation of the alloy in near grain boundary regions). The dual stabilisation by both Ti and Nb imparts beneficial corrosion resistance, oxidation resistance, high temperature strength and formability to the steel [2].

Table 1.1. A typical chemical composition (wt%) of type 441 ferritic stainless steels.

	C	N	Mn	Si	Cr	Ni	Ti	Nb	S	P	Remarks
Min					17.50		0.10				%Nb≥ 3xC + 0.3
Max	0.03	0.045	1.00	1.00	18.50	0.50	0.60	1.00	0.015	0.04	

Many researchers have investigated the effects of niobium stabilisation on ferritic stainless steels for their use in automotive exhaust systems [3,4,5,6], and have found that niobium additions can improve the high temperature strength of ferritic stainless steels by solid solution strengthening, which allows its operation at such high temperatures. It is, therefore, important to know how much of the niobium precipitates out as carbides or carbo-nitrides and which fraction remains in solution. Niobium stabilised ferritic stainless steels form the precipitates of Nb(C,N), M_6C (Fe_3Nb_3C) and the Laves phase type Fe_2M (Fe_2Nb).

Because C and N remain in the steels, Nb(C,N) and Ti(C,N) are easily formed in some processing stages, e.g. in hot–rolling and annealing processes. These carbo – nitrides increase the strength and decrease both the toughness and ductility. In the work by Fujita et al. [5], on 13Cr – 0.5Nb, the authors have observed that the high temperature strength of Nb added steels decreases during high temperature ageing, caused by coarse M_6C (Fe_3Nb_3C) formation in ageing.

The volume fraction of the Laves phase was observed to reach a maximum at 700°C and its dissolution occurs at temperatures over 900°C [7,8]**.** The same observation has been made by the use of thermodynamic software such as Thermo-calc® [3, 9]. The Laves phase precipitates firstly at the grain boundaries as a fine precipitate and as the steel is slowly cooled from a high temperature of about 900°C, the amount of this Laves phase increases inside the grains and they then coarsen. This intermetallic Laves phase is known to affect both the mechanical properties and corrosion resistance of ferritic stainless steel, mostly negatively. In one instance, it has been found that the fine precipitates of Laves phase at the grain boundaries improve the high temperature strength when still fine [5]. However, the rapid coarsening of the Laves phase at high temperatures reduced the high temperature strength [10]. The exact mechanism of strength reduction is still not clear and requires clarification. Sawatani et al [8], researched the effect of Laves phase on the properties of dual stabilised low carbon stainless steels as related to the manufacturing process of Ti- and Nb-stabilised low C, N-19%Cr-2%Mo stainless steel sheets, and they have found that the Laves phase has a significant influence on the mechanical properties of the steel. It was found that Laves phase on the grain boundaries shifts the brittle to ductile transition temperature to higher temperatures, and that large amounts of Laves phase degrade the room temperature ductility of cold rolled and annealed sheet and greatly enhance its strength. It was also observed that after a 20% cold rolled reduction (of a sheet that had been cold rolled and annealed after reductions between 0 and 92%) that there was a peculiarly rapid precipitation of Laves phase, which caused a severe degradation of the mechanical properties [11].

1.2 PROBLEM STATEMENT

Columbus Stainless has experienced an embrittlement problem at times during the manufacturing process of type 441 stainless steel. This problem is considered generic because it appears from the hot band material prior to annealing, whereby the materials become embrittled after hot rolling and coiling. It was assumed that the embrittlement might be attributed to the formation of an intermetallic Laves phase type. The reason for this assumption is that after the hot finishing mill (Steckel mill), the temperature of the steel strip is approximately 850°C, and the strip is then rapidly cooled (to avoid the Laves phase transformation temperature range) to approximately 650°C by means of laminar cooling with water sprays on the run-out table and is then coiled. The coil is left to cool for 3 to 5 days to approximately 50°C before further processing. For instance, one particular hot rolled coil was found to be brittle and could not be processed further. It appears furthermore that rapid cooling (by water sprays) after hot rolling alleviates the embrittlement problem, and that slow cooling of this particular hot rolled coil might have allowed the precipitation of the Laves phase below 650ºC and that this resulted in the embrittlement of the material. Also, the preliminary evaluation by Columbus Stainless of this steel indicated that this embrittlement is not related to a coarse ferritic grain size effect, as the degree of embrittlement was far higher than expected from this source.

1.3 OBJECTIVES

Laves phase precipitation is believed to be detrimental to mechanical properties, in particular leading to a low toughness in this type of steel. The following two objectives have been identified:

1. Firstly, by making use of this reject material, to determine those process variables that may affect the toughness of the material after processing, principally annealing temperatures and cooling rates from typical hot rolling temperatures; and

2. To model and experimentally determine the kinetics of precipitation of this phase, since it would then be possible to predict what volume fraction of Laves phase forms firstly, during processing and secondly, what forms possibly throughout the component's lifetime in exhaust systems.

The type 441 steel (composition shown in Table 1.1) is susceptible to Laves phase formation over a relatively wide temperature range. A number of studies of Laves phase precipitation in this steel provide suitable experimental data with which to test the precipitation model [12].

CHAPTER TWO

LITERATURE REVIEW

2.1 INTRODUCTION

Stainless steels are iron-base alloys containing a minimum of 11wt.% chromium content for adequate corrosion resistance. This chromium content is the minimum that prevents the formation of "rust" in air or in polluted atmospheres by forming a very thin surface film of chromium oxides known as the "passive film", which is self-healing in a wide variety of environments. Today, the chromium content in stainless steels approaches 30wt.% in some alloys and other elements are often added to provide specific properties or ease of fabrication. Some of these elements are nickel (Ni), nitrogen (N) and molybdenum (Mo) which are added for corrosion resistance; carbon (C), Mo, N, titanium (Ti), aluminium (Al) and copper (Cu) which are added for strength; sulphur (S) and selenium (Se) are added for machinability; and Ni is added for formability and toughness, particularly to obtain an austenitic microstructure which is far less prone to the loss of toughness from a large grain size.

2.2 CLASSIFICATION OF STAINLESS STEELS

Stainless steels are divided into three groups according to their crystal structures: austenitic (face-centred cubic, fcc), ferritic (body-centred cubic, bcc) and martensitic (body-centred tetragonal or cubic, bct). Stainless steels containing both austenite and ferrite usually in roughly equal amounts are known as "duplex stainless steels".

The general considerations for the choice of the base metal are that it should have the following properties: (a) since these alloys are used at high temperatures or under demanding conditions, they should have adequate corrosion resistance. This implies that either Cr or Al at a level of about 15% or higher, should be added to the alloy. (b) The room temperature structure should be austenitic, primarily to avoid the formation of martensite during cooling to room temperature and secondly, to prevent a ferritic structure which has a lower solubility for carbon and favours the formation of intermetallic precipitates rather than carbides. The addition of austenite formers (mainly Ni, Mn and N) is, therefore, necessary in austenitic stainless steels.

The Fe-Cr-Ni system as the base alloy is by far the most suitable as large quantities of Cr can be taken into solution and maintained in solution down to room temperature. Secondly, Ni is also a strong austenite former and Cr lowers the martensite start (M_s) temperature sufficiently to avoid the formation of martensite, see Figure 2.1.

Both nitrogen and carbon are strong austenite formers, with nitrogen being increasingly used to provide certain attractive properties such as good fracture strength and it also improves the corrosion resistance [13,14]. From Figure 2.2, it is noted that carbon is a very strong austenite former, and if the carbon content is very low, slightly more Ni may have to be added to compensate for the loss of the austenitic properties of the carbon.

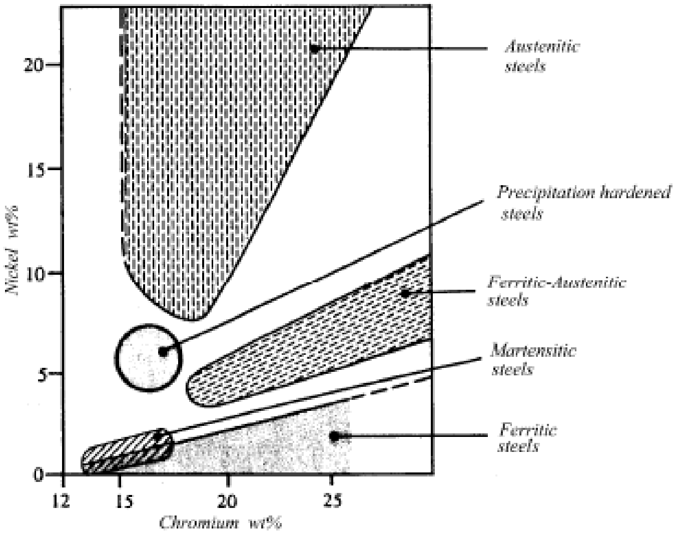

Figure 2.1. The effect of nickel and chromium content on the structure of the main stainless steels. Note in particular that Ni is a strong austenite former whereas Cr is a strong ferrite former [15].

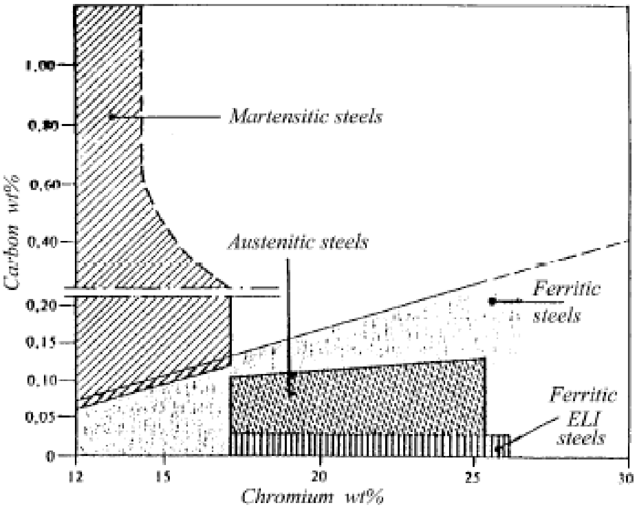

Figure 2.2. Effect of carbon and chromium contents on the structure of some of the main stainless steels. ELI is extra low interstitial steel [15].

2.2.1 FERRITIC STAINLESS STEEL

This stainless steel derives its name from the bcc crystallographic structure that is generally stable from room temperature up to the liquidus temperature. Typically, ferritic stainless steel contains approximately 11 to 30wt.% chromium and small amounts of other alloying elements. The chromium additions give the steel its corrosion resistance and it further stabilises the bcc crystal structure. Recently, a very low (C+N) content has been specified in the so-called super-ferritic stainless steels. The higher alloy compositions can also include up to 4%Ni, provided this does not alter their fully ferritic structure. Due to their adequate corrosion resistance and lower cost, ferritic stainless steels are chosen over austenitic stainless steels in less severe applications such as a replacement to mild carbon steels in automobile exhaust systems. However, poor weldability, which leads to low toughness and is also associated with grain growth in the HAZ, limits their use even with very low carbon levels.

2.2.2 AUSTENITIC STAINLESS STEEL

As with ferritic steel, the austenitic stainless steel's name originates from its fcc crystallographic structure. These steels contain 16 to 25wt% chromium and 7 to 10% nickel. Austenitic stainless steel has a high nickel content to stabilise the austenite fcc structure at room temperature. The increase in alloy content creates a higher cost of production but the fcc structure exhibits very high ductility, resulting in material with good formability and very good corrosion resistance. Another advantage of these steels is the relative ease of recrystallisation, which allows for better control of the mechanical properties.

2.2.3 MARTENSITIC STAINLESS STEEL

Martensitic stainless steels contain 12 to 17% chromium for good corrosion resistance. However, since chromium is a strong ferritic stabiliser, austenite stabilisers are added so that the necessary austenite can be formed during solution treatment for the subsequent martensite formation. Therefore, these steels have a high carbon content to stabilise the austenite at higher temperatures. The high carbon content will increase the strength through solid solution strengthening and the precipitation of a large number of (Fe, Cr) carbides. These steels use the quench and temper process to achieve a very high strength with reasonable ductility. Because of the high alloy content, these steel have a superior hardenability. The disadvantage of the high hardenability often leads to degradation of the corrosion resistance when compared with ferritic and austenitic stainless steels.

2.2.4 DUPLEX STAINLESS STEEL

These steels contain a mixture of ferrite and austenite phases at room temperature in order to combine the beneficial properties of both components. These steels typically contain 18 to 30% chromium and an intermediate amount of nickel (3-9%) that is not enough for the formation of a fully austenitic structure at room temperature. Duplex stainless steels have an intermediate level of high mechanical strength and corrosion resistance properties lying between those of austenitic and ferritic products.

2.3 COMPOSITION OF STAINLESS STEELS

The composition of stainless steel can be related to its non-equilibrium metallurgical structure by means of a Schaeffler diagram [16], which shows the microstructure obtained after a rapid cooling from 1050°C to room temperature. It is, therefore, not an equilibrium diagram and is often used in welding phase analysis. This diagram was originally established to estimate the amount of delta ferrite (that is, ferrite formed on solidification, as opposed to alpha ferrite, which is a transformation product of austenite or martensite) content of welds in austenitic stainless steels. The alloying elements commonly found in stainless steels are regarded either as austenite stabilisers or as delta ferrite stabilisers. The relative “potency” of each element is conveniently expressed in terms of an empirical equivalence to either nickel (austenite stabiliser) or chromium (ferrite stabiliser) on a weight percentage basis. The nickel and chromium equivalents, which form the two axes of the Schaeffler diagram, can be calculated as follows:

$$\%\text{Ni equivalent} = \%\text{Ni} + \%\text{Co} + 30\%\text{C} + 25\%\text{N} + 0.5\%\text{Mn} + 0.3\%\text{Cu}$$

$$\%\text{Cr equivalent} = \%\text{Cr} + 2\%\text{Si} + 1.5\%\text{Mo} + 5\%\text{V} + 5.5\%\text{Al} + 1.75\%\text{Nb} + 1.5\%\text{Ti} + 0.75\%\text{W}$$

2.3.1 STRUCTURE OF FERRITIC STAINLESS STEEL

Ferritic stainless steels at room temperature consist of alpha (α) solid solution having a body centred cubic (bcc) crystal structure. The alloy contains very little interstitial carbon and nitrogen in solution; most of the interstitial elements appear as finely distributed carbides and nitrides. A typical phase diagram of the iron-chromium system is shown in Figure 2.3.

Chromium is a ferrite stabiliser and it extends the alpha-phase field and suppresses the gamma-phase field. This results in the formation of the so-called gamma loop as seen in Figure 2.3, which, in the absence of carbon and nitrogen, extends to chromium contents of about 12 – 13wt % [17]. At the higher chromium contents, transformation to austenite is no longer possible and the metal will remain ferritic up to its melting temperature. This constitutes an entirely different class of stainless steels in which grain refinement can no longer be brought about by transformation through heat treatment.

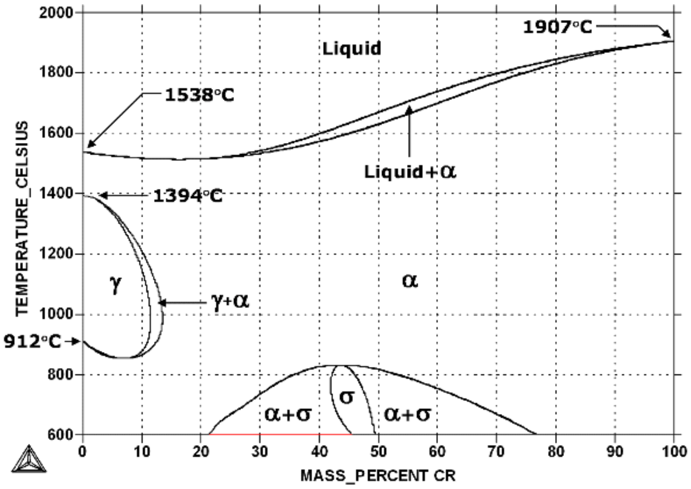

Figure 2.3. Fe-Cr equilibrium phase diagram [17].

With carbon and nitrogen present in these alloys the diagram is modified in certain respects. The effect of carbon and nitrogen is to shift the limits of the gamma loop to higher chromium contents and widens the duplex ($\alpha + \gamma$) phase area [18]. Figure 2.4 shows the changes in this part of the diagram. However, the solubility levels of the interstitials in the ferrite matrix are sufficiently low so that it is rarely possible to distinguish between solute embrittling effects and the effects of second-phase precipitates. The precipitates, in fact, become more important than the solute when the amount of interstitial elements significantly exceeds the solubility limit. The presences of carbon or nitrogen, in amounts in excess of the solubility limit, serve to increase the ductile to brittle transition temperature (DBTT). This embrittling effect is closely linked to the amount or the number and size of carbides and nitrides formed on the grain boundaries but also to the ferrite grain size. Precipitate films act as strong barriers to slip propagation across the grain boundaries and are also often inherently brittle by themselves. Grain boundary precipitates are suppressed by quenching from above the solution temperature when the interstitial content is low enough.

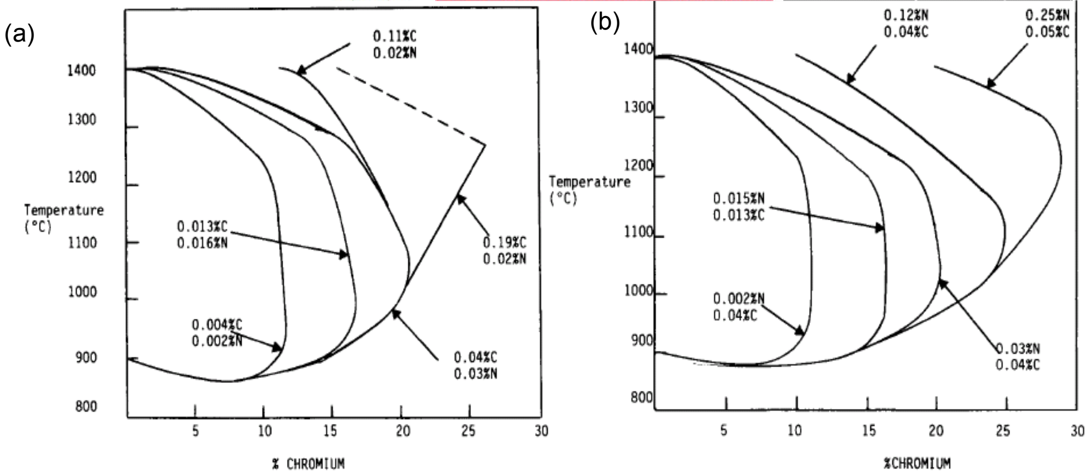

Figure 2.4. Shifting of the boundary line (α +γ)/γ in the Fe-Cr system through additions of C + N [18].

2.4 TOUGHNESS OF FERRITIC STAINLESS STEELS

Some of the metallurgical problems that are encountered in the ferritic stainless steels are too large a grain size, “475°C” embrittlement, secondary phase precipitation, high-temperature embrittlement and notch sensitivity. They all have been shown to some extent to affect the ductile–to–brittle transition temperature of the ferritic stainless steels, mostly negatively by raising it.

2.4.1 EFFECT OF GRAIN SIZE ON BRITTLE BEHAVIOUR

The effect of grain size on the impact toughness of ferritic stainless steels has been well documented over the years even though it is not always clearly understood. It has been proven previously that the DBTT tends to increase with increasing grain size, see Figure 2.5 [18,19]. The work done by Ohashi et al [20] has shown that while the transition temperature increases with increasing grain size, the upper shelf energy is largely independent of the grain size. They have also reported that in V–notched samples that the effect of grain size is very noticeable; but in brittle welded samples this grain size dependency of the upper shelf energy and the DBTT is very small but still observable. It can be concluded that the coarse grain size tends to promote crack initiation even in a blunt–notched specimen, but the grain size effect contributes mainly to the resistance of initiation of brittle fracture and only slightly to the propagation of brittle fracture [20].

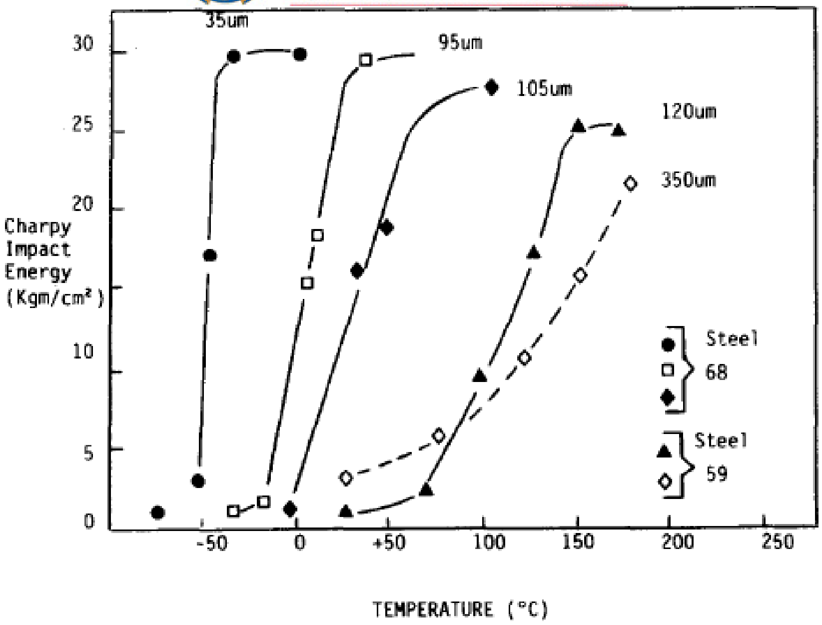

Figure 2.5. The effect of the grain size on the impact toughness for several Fe – 25Cr ferritic stainless steels. Steel 59 and 68 are the alloy numbers [18].

Figure 2.6 shows the impact transition temperature as a function of the interstitial content for two different ferritic stainless steels [21]. For a given interstitial content, both the DBTT and the upper shelf energies were not affected by the presence of 2% Mo or the change of Cr content from 18% to 25%. These findings agree with the results of Woods [22], who showed that for 18% Cr in Ti stabilised stainless steels, that 2% Mo has no effect on the impact transition temperature.

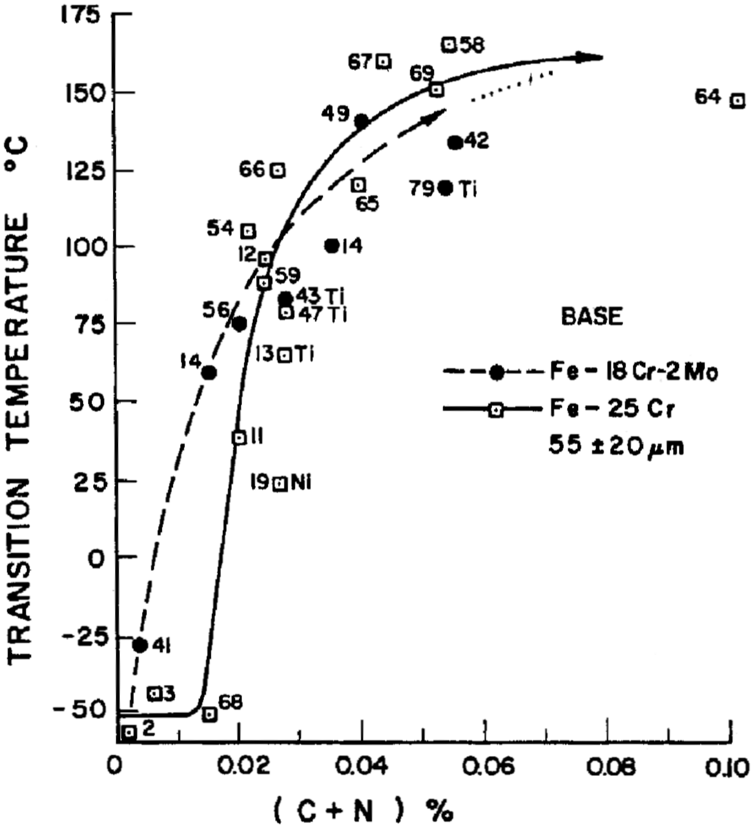

Figure 2.6. The effect of the interstitial content on the impact transition temperature for the Fe–18Cr–2Mo and Fe–25Cr steels with the grain sizes within the range 35 to 75 μm. The numbers given correspond to the alloy number [21].

For a desirable low DBTT and a high shelf energy, the combined carbon and nitrogen content should be kept below 150 ppm, below which further decreases have no further effect. Above150 ppm, however, increases in interstitial content cause a marked increase in DBTT, though once above a certain level (C + N ≈ 600 ppm) further increases are not significant. For these stainless steels a room temperature Charpy Impact Energy (CIE) value of between 14 to 70 J, and above the DBTT a value of 160J in the Upper Shelf Energy region, would be considered typical [21].

2.4.2 EMBRITTLEMENT AT 475°C

When ferritic stainless steels containing at least 12wt.% chromium are subjected to prolonged exposure to temperatures between 400 and 500°C, the notch ductility is considerably reduced while the tensile strength and hardness increase considerably. However, the increase in the tensile strength is of no practical significance since the alloy is extremely brittle [18,19]. This phenomenon is known as “475°C” embrittlement because the maximum effect occurs at about 475°C [23]. Brittle fracture is transgranular in nature and is similar in appearance to the low temperature cleavage of unembrittled steels [24]. Transgranular fracture is observed to initiate at the interaction of slip bands with grain boundaries. However, the precise mechanism of the crack nucleation by slip bands has not been resolved experimentally [24]. The recognised mechanism of "475°C" embrittlement is the precipitation through spinodal "unmixing" of Cr-rich alpha prime (α') and Fe-rich α phases, arising from the miscibility gap in the Fe-Cr equilibrium phase diagram, Figure 2.3. The kinetics of α' precipitation increase with increasing Cr content. A spinodal phase mixture exists within the miscibility gap, and the precipitation of the α' is thought to occur by a nucleation and growth mode outside the spinodal boundaries and by spinodal decomposition within [19,23].

The phenomenon of "475°C" embrittlement can be removed by heating the embrittled alloy to a temperature above 550°C for a sufficient amount of time to dissolve the α' phase followed by rapid cooling to room temperature.

2.4.3 PRECIPITATION OF THE SECONDARY PHASES IN STAINLESS STEELS

Ferritic stainless steel in the temperature range of 500 to 900 °C can also precipitate intermetallic phases such as sigma (σ), chi (χ) and Laves phases. From the Fe-Cr equilibrium phase diagram in Figure 2.3, it can be seen that sigma phase (σ) is an equilibrium phase at temperatures up to 820 °C. The sigma (σ) phase is an intermetallic compound with approximate composition of FeCr. It is hard and brittle and can result in a severe harmful influence on the toughness properties of the alloys. Although the stability range of this phase in the Fe-Cr binary system varies from 519 to 820°C, several substitutionally dissolved elements can markedly modify this temperature range. Substitutional elements such as Mo, Si and Ni shift the σ-phase boundary to a lower chromium range [18,19]. On the other hand, the precipitation of sigma phase can be strongly accelerated by the pre-existence of carbides in the alloy, particularly the $M_{23}C_6$ type [25,26,27,28]. In the lower Cr content ferritic stainless steels, sigma phase forms very slowly and is usually a service problem only after a long exposure at elevated temperatures. Cold work enhances the precipitation rate of the sigma phase considerably, and in very high chromium containing steels sigma phase has been found in an air cooled as-cast structure [18,23]. Increasing the chromium and molybdenum contents favours the formation of sigma, chi and Laves phases.

The relationship between the toughness and the Fe_2Mo Laves phase precipitates in a 9%Cr – 2%Mo ferritic martensitic steel was investigated by Hosoi et al. [29]. They observed that the DBTT increases and the upper shelf energy decreases when the Laves phase begins to precipitate during ageing.

2.4.4 NOTCH SENSITIVITY

Sensitisation in ferritic stainless steels occurs whenever the steel is heated to a sensitising temperature (usually above 900°C), such as during thermo-mechanical processing and/or welding. The precipitation of $M_{23}C_6$, an incoherent carbide with a complex cubic structure, usually occurs on the grain boundaries, which then form Cr-depleted zones along the grain boundary and places the alloy in the sensitised state, resulting in intergranular corrosion adjacent to the grain boundaries when exposed to corrosive environments. A sketch showing the carbides and the associated chromium-depleted zones along the grain boundaries is shown in Figure 2.7. Precipitation of chromium nitrides such as Cr_2N requires slow cooling through a temperature range of 500 to 700°C. Above 700°C, the diffusion of chromium is fast enough to replenish the chromium at the grain boundaries and below 500°C, the diffusion of chromium is too slow for the precipitates to form in nitrogen containing alloys. One place where this slow cooling can occur is in the heat-affected zone (HAZ) in the vicinity of a weld joint.

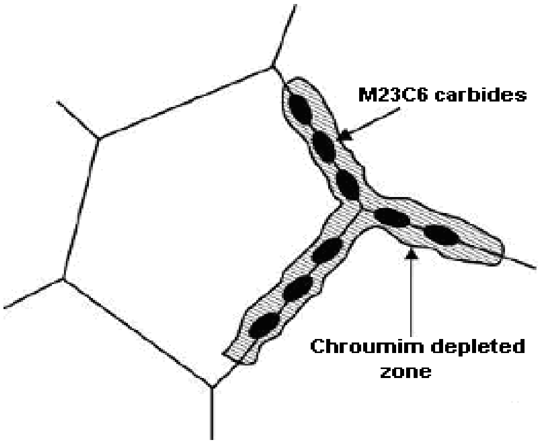

Figure 2.7. A schematic diagram of the grain boundary showing carbides in the chromium-depleted zone near the grain boundaries.

Sensitisation can be overcome by one of several methods, all of which increase production cost:

- Annealing alloys at temperatures between 950 and 1100°C in the austenite regions, allowing Cr to rediffuse back into the Cr-depleted zones.

- Retard the kinetics of sensitisation through molybdenum (Mo) additions, which lengthens the time required for sensitisation by slower diffusion of the Mo which is then thermodynamically built into the M part of $M_{23}C_6$.

- Reduce interstitial levels by better control during steelmaking processes.

- “Free” carbon and nitrogen levels can be further reduced by the addition of strong carbide and nitride forming elements such as the stabilisers Ti, Nb and Zr, thereby reducing the formation of the Cr-rich $M_{23}C_6$.

2.4.5 WELDABILITY OF FERRITIC STAINLESS STEEL

The problem faced in joining ferritic stainless steels is grain growth to coarse grain sizes in the weld zone and the heat-affected zone of fusion welds, and consequently low toughness and ductility due to the absence of any phase transformations during which grain refinement can occur. In general, austenitic stainless steels are easily weldable. When austenitic stainless steel joints are employed in cryogenic and corrosive environments, the quantity of delta-ferrite in the weld must be minimised or controlled to avoid degradation during service [30].

It has been shown that the addition of niobium and titanium to stabilise the steel does not adversely affect the weldability of the steel. The addition may in fact increase the toughness in titanium stabilised steel [31,32]. In addition dual stabilisation was found to produce tough, clean weld lines during high frequency welding when compared to only single titanium stabilised steels. An optimum balance or ratio normally exists between the titanium and niobium content (with the niobium being the greater i.e. Nb:Ti shown to be 2:1 for a 17% chromium ferritic steel) for optimum toughness and ductility of welds [33]. Finally it has been shown that dual stabilised steels can be susceptible to intergranular hot cracking in the fusion and heat-affected zones. It has been shown that niobium is in fact the most deleterious element and care should be taken to minimise this stabilising element as far as possible [23].

2.4.6 EFFECT OF NIOBIUM AND TITANIUM ADDITIONS TO FERRITIC STAINLESS STEELS

Redmond [34] has investigated the effects of residual and stabilising elements on the toughness of a series of 18%Cr-2%Mo steels which contained 0.015%C and 0.015%N. The residual elements that were varied were sulphur, manganese and silicon and they all were shown to have only a minor effect on the impact toughness. The effects of niobium and titanium dual stabilisation on the impact toughness are shown in Figure 2.8. From this figure it can be seen that as for base metal materials, increasing the titanium content resulted in a constant increase in the transition temperature. For the alloys with 0.34 and 0.44%Nb the maximum for both occurs at about 30°C for 0.2%Ti. The trend is less clear when the niobium content was varied and the titanium content was kept constant. In the welded condition, the trend still does not correlate well with the niobium content. The niobium stabilised steel had a better impact toughness than the titanium stabilised steel, with a mixed niobium-titanium stabilisation producing results between the two [34].

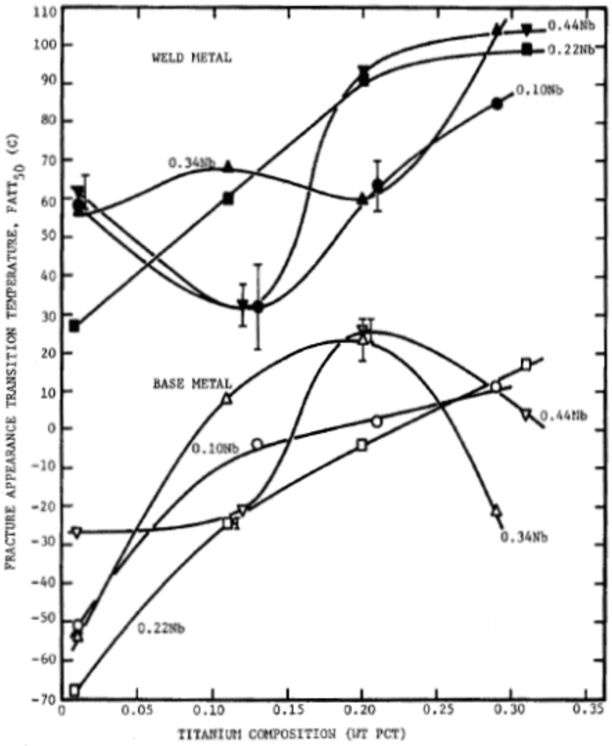

Figure 2.8. Effect of niobium and titanium additions on the impact toughness of 18%Cr-2%Mo ferritic stainless steels [34].

2.5 THEORIES OF BRITTLE FRACTURE

Brittle fracture of steel structures has been a matter of considerable concern to both engineers and metallurgists for many years, it now being generally recognised that the cleavage mode of failure occupies a central position with respect to the problem. A physical model of the process has thereby been constructed by others [35], and in so doing, previous theories were critically examined. The first of these contributions was the identification of the crack initiators from which cleavage nucleates and triggers a propagating crack in a ferritic matrix, together with the criterion for this to occur. Stroh

[36,37] proposed a wedge dislocation pile-up at a grain boundary as the initiator, Cottrell [38] a sessile wedge dislocation pile-up resulting from dislocation coalescence, and Smith [39] the combination of a wedge dislocation pile-up at a grain boundary with a contiguous brittle second-phase particle or inclusion, broken by the pile-up. All these initiators are able to nucleate a crack at a neighbouring ferrite grain if assisted by plastic flow, while the last two are also able to propagate the nucleus of the crack once formed if assisted by the stress state. An energy balance involving the effective surface energy of the metallic matrix and the initiator size (the ferritic grain, the second-phase particle, etc.) allows the tensile stress required for propagating the nucleus to be derived, thus predicting the maximum principal stress that triggers cleavage and provides a cleavage fracture criterion.

2.5.1 ZENER'S/STROH'S THEORY

Zener [ref. by Chell, 40] suggested that the local stress concentration produced at the head of a dislocation pile – up could lead to cleavage fracture when the leading dislocations were squeezed together to generate a stress concentration leading to a crack nucleus. The model shows that the crack nucleation of length $2c$ (see Figure 2.9) occurs when the shear stress τ_s created by a pile – up of n dislocations of Burger's vector b each at the grain boundary, reaches the value of:

$$\tau_s \approx \tau_i + \left(\frac{2\gamma_s}{nb}\right) \qquad \text{Equation 2.1}$$

where τ_i is the lattice friction stress in the slip plane and γ_s is the surface energy of the exposed crack surface.

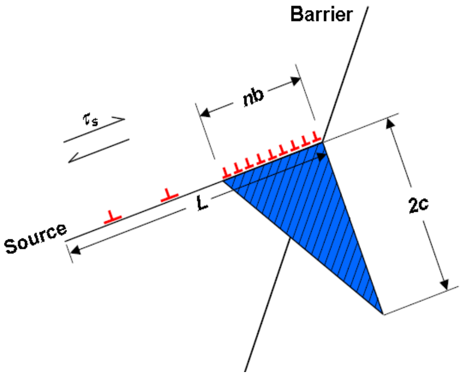

Figure 2.9. Zener's model for cleavage fracture.

Stroh [36] included the effect of the grain size d in a model, suggesting the condition for the shear stress created by a dislocation pile – up of length $d/2$ to nucleate a microcrack as follows (Figure 2.10):

$$\tau_e = \tau_y - \tau_i \geq \sqrt{\frac{E\pi\gamma}{4(1-\nu^2)d}} \qquad \text{Equation 2.2}$$

where τ_e = effective shear stress, τ_y = the yield stress, τ_i = lattice friction stress, ν is Poisson's ratio and E is Young's elastic modulus. This model indicates that the fracture of the material should depend primarily on the shear stress acting on the slip band but is also grain size dependent through a $d^{-1/2}$ relationship .

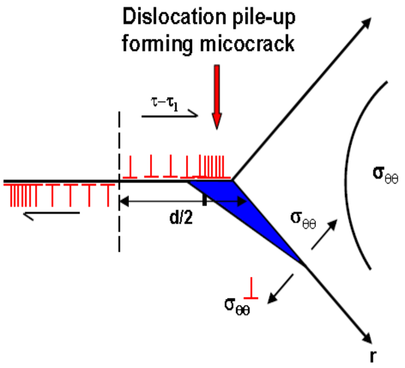

Figure 2.10. Stroh's model for cleavage fracture.

2.5.2 COTTRELL'S THEORY

Cottrell [38] proposed that a dislocation mechanism for the cleavage fracture process should be controlled by the critical crack growth stage under the applied tensile stress. This model showed that the crack's nucleation stress can be small if the microcrack is initiated by the intersection of two low energy slip dislocations to provide a preferable cleavage plane, Figure 2.11.

$$\frac{a}{2}[\bar{1}\bar{1}1] + \frac{a}{2}[111] \rightarrow a[001] \qquad \text{Equation 2.3}$$

This results in a wedge cleavage crack on the (001) plane which is the usual cleavage plane in ferritic materials. Further propagation of the crack is then controlled by the applied tensile stress. As the dislocation reaction in Equation 2.3 is accompanied by a decrease in dislocation energy, crack nucleation will be easier than if it occurs by the Zener/Stroh mechanism.

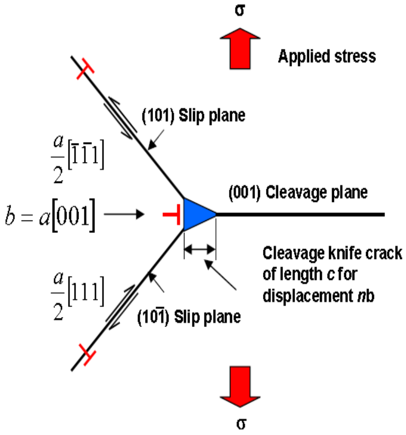

Figure 2.11. Cottrell's model for cleavage fracture.

Cleavage fracture will now be propagation controlled with the cleavage fracture stress, σ_f given by:

$$\sigma_f \geq \frac{2\gamma G_m}{k_y^s} d^{-\frac{1}{2}} \qquad \text{Equation 2.4}$$

where d is the grain size and k_y^s is the Hall – Petch constant for shear. The value of γ calculated was about 20 Jm^{-2}, i.e. about an order of magnitude greater than the surface energy of the lattice. Cottrell attributed this large value to extra work done in producing river lines or transversing grain boundaries [41]. The critical conditions for crack nucleation at the yield stress ($\sigma_f = \sigma_y$) can be expressed by the Cottrell equation [38] as:

$$\sigma_y k_y^s d^{\frac{1}{2}} = {k_y^s}^2 + \sigma_i k_y^s d^{\frac{1}{2}} \geq C_1 G_m \gamma \qquad \text{Equation 2.5}$$

where σ_y is yield stress, σ_i is friction stress, G_m is shear modulus, γ is effective surface energy of an implied crack, C_1 is constant related to the stress state (~4/3 for a notched specimen and 4 for a plain or unnotched specimen). Cottrell's model therefore emphasises the role of tensile stress and explains effects of grain size and yielding parameters on fracture. Hardening, other than by decreasing grain size, is predicted to promote brittle fracture by raising the value of tensile stress at the yield point.

Equation 2.5 expresses the conditions for plastically induced crack nucleation at a given temperature. Any factor that increases σ_i, k_y^s, or d increases the tendency for brittle fracture. In ferritic steel, a marked increase in σ_i with decreasing temperature is usually experienced. The parameter k_y^s may depend upon alloy content, test temperature or heat treatment. Generally, k_y^s will increase with the stacking fault energy, hence it will be sensitive to alloying. It is obvious from Equation 2.5 that grain size has a direct effect on the transition temperature, and thus, the expression for DBTT at which the fracture stress (σ_f) and yield strength (σ_y) are equal for only one grain size $d*$ could be derived. Thus

$$DBTT = \frac{1}{\beta}\ln\left[Bk_y d^{*\frac{1}{2}} / (C_1 G_m \gamma - k_y^{s^2})\right] \qquad \text{Equation 2.6}$$

For a given material, the relation between transition temperature and grain size may, therefore, be reduced to:

$$DBTT = D + 1/\beta \ln d^{*\frac{1}{2}} \qquad \text{Equation 2.7}$$

where D is a constant. Thus it can be predicted from Equation 2.7 that the temperature at which a DBTT behaviour occurs, decreases with smaller grain size. Plumtree and Gullberg [21] have shown that the DBTT increased linearly with grain size and that the DBTT of lower purity alloys tended to be less affected by grain size changes.

Sometimes the presence of precipitates at grain boundaries camouflages the effect of grain size on the impact toughness of the ferritic stainless steel. The heat treatment that accelerates the precipitation of the carbide and nitride, Laves or sigma phases decreases the resistance to crack initiation significantly during dynamic loading. The V–notched samples embrittled by these precipitates were found to show a toughness behaviour similar to that of the solution treated and sharply notched specimens [42]. Therefore, the precipitates assist greatly in the initiation of brittle cracks at the time of dynamic loading [20]. The DBTT increases with the volume fraction of grain boundary precipitates, thereby facilitating fracture by decreasing the surface energy for fracture (γ). Such grain boundary precipitates can act as starting or initiation points for fracture causing a marked increase in the transition temperature.

Brittle failures are typical transgranular cleavage fractures which occur in the body – centred cubic (BCC) metal at low temperatures and high strain rates. Plumtree and Gullberg [21] proposed the following model which applies only to the initiation of cleavage cracks. Crack nucleation occurs when the concentrated stresses at the tip of a blocked dislocation band equal the cohesive stress and is given by:

$$(\tau_N - \tau_i)\, nb = 2\gamma_T \qquad \text{Equation 2.8}$$

Where τ_N = shear stress for crack nucleation, τ_i = friction shear stress, n = number of dislocations in the pileup, b = burgers vector, and γ_T = true surface energy.

Equation 2.8 indicates that a crack will form when the work done by the applied shear stress $(\tau_N\, nb)$ in producing a displacement nb equals the combined work done in moving the dislocations against the friction stress $(\tau_i\, nb)$ and the work done in creating the new fracture surface $(2\gamma_T)$. In most metals where some relaxation occurs around the blocked dislocation band, the term γ is used rather than γ_T as grain boundaries, hard particles and of course, grain boundary particles act as barriers to dislocation motion, favouring crack initiation. When the second phases are inhomogeneously distributed the value of γ is reduced [43]. Subsequently the amount of work done in crack nucleation is reduced. Transgranular cleavage cracks form more easily and the toughness is reduced, compared with those alloys where γ remains high due to the second phase distribution.

2.5.3 SMITH'S THEORY

This is an alternative model that provides the starting point for growth – controlled cleavage fracture, to incorporate the effect of brittle second phase particles on grain boundaries, see Figure 2.12. Here, a brittle particle of thickness C_o at the grain boundary dividing adjacent grains, is subjected to the concentrated stress ahead of a dislocation pile – up of length D. A microcrack is initiated when a sufficiently high applied stress causes local plastic strain within the ferrite grains to nucleate a microcrack in the brittle grain boundary particle of thickness C_o. Applying Stroh's analysis, the particle will crack under the influence of the resulting dislocation pile – up if:

$$\tau_e \geq \left\{ \frac{4E\gamma_e}{\pi d\left(1-\nu^2\right)} \right\}^{\frac{1}{2}} \qquad \text{Equation 2.9}$$

where γ_e is the effective surface energy of the particle. Similarly, nucleation controlled cleavage of the ferrite will occur (at the yield point) if:

$$\tau_e \geq \left\{\frac{4E\gamma_f}{\pi d\left(1-\nu^2\right)}\right\}^{\frac{1}{2}}$$ Equation 2.10

where γ_f is the effective surface energy of ferrite. If, however, τ_e lies between these two limits and γ_f is greater than γ_e, then propagation controlled cleavage fracture is predicted with the particle's microcrack propagating into the ferrite under the combined influence of the dislocation pile – up and the applied stress. By examining the change in energy with crack length, the cleavage fracture stress, σ_f, is given by the following expression leading to an inequality expression predicting growth or propagation of the initiated crack:

$$\sigma_f^2\left(\frac{C_o}{d}\right)+\tau_e^2\left\{1+\frac{4}{\pi}\left(\frac{C_o}{d}\right)^{1/2}\frac{\tau_i}{\tau_e}\right\}^2 \geq \frac{4E\gamma_f}{\pi d\left(1-\nu^2\right)}$$ Equation 2.11

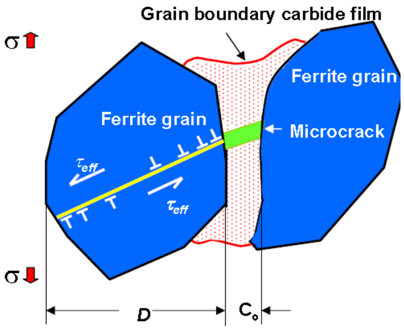

Figure 2.12. Smith's model for cleavage fracture.

In the absence of a contribution by the dislocations (the second term in Equation 2.11) the inequality expression is reduced to:

$$\sigma_f > \left[\frac{4E\gamma_f}{\pi(1-\nu^2)C_o}\right]^{\frac{1}{2}}$$ Equation 2.12

This model, therefore, emphases the importance of the precipitate's thickness C_0 and indicates clearly that the coarser particles give rise to lower fracture stresses. If, however, the effective shear stress τ_e is written as $k_y^s d^{-1/2}$, the equation predicts that σ_f is independent of grain size, other factors being equal. Indirectly, however, the grain size will determine the value of C_0 for a given volume fraction of the grain boundary phase and, therefore, does exert an indirect influence on the fracture strength. In practice, therefore, a fine grain size with a large grain boundary area per unit volume, is associated with thin precipitates, and values of σ_f are usually expected to be high with smaller grain sizes.

2.5.4 CLEAVAGE FRACTURE RESISTANCE

Analyses of the factors controlling the cleavage fracture stress have been made previously by different authors [44]. Although the fracture process in the steel does not, in general, correspond to the condition for which these expressions were derived (that is, fracture is frequently initiated at the tip of a stopped microcrack or by the joining of several microcracks by tearing), directly analogous expressions should exist for these conditions. From Equation 2.13, it should be noted that the fracture stress depends on the grain size, as well as yield strength, and that refining the grain size increases both of them.

$$\sigma_f = \left(8G_m\gamma_m / k_y\right)d^{-\frac{1}{2}} \qquad \text{(clean material)} \qquad \text{Equation 2.13}$$

$$\sigma_f = \left[\frac{2E\gamma_b}{\pi\alpha\left(1-\nu^2\right)}\right]^{\frac{1}{2}} d^{-\frac{1}{2}} \qquad \text{(less pure material)} \qquad \text{Equation 2.14}$$

where G_m and E are the shear and Young's moduli, respectively, γ_m and γ_b are the appropriate surface energy terms, ν is Poisson's ratio and α is a constant.

The most probable important environmental factor that affects the failure of the materials is the service temperature. Although many different criteria exist for the conditions of a DBTT, they all effectively point to the temperature at which $\sigma_f = \sigma_y$. It has been observed that grain refinement increases both of these stresses.

In the case of solid solution and precipitation strengthening, the ductile to brittle transition temperature is usually raised. This results from these strengthening mechanisms that do not increase the fracture stress, as grain refinement does.

2.6 THERMOMECHANICAL PROCESSING

In the previous section it was mentioned that the toughness of ferritic stainless steel depends on the grain size, and this grain size can be refined by thermomechanical processing. However, a thermomechanical process also affects the recrystallisation parameters and precipitation of carbides, nitrides, sigma and Laves phases [18,45]. The thermomechanical processes that affect the changes in microstructure of the ferritic stainless steel will be considered in this section.

2.6.1 COLD-ROLLING

Cold rolling was found to raise the DBTT, but the effect is not consistent nor is it very great [18]. Differences in cold rolling temperature and the extent of preferred grain orientation make the effects more difficult to quantify. Sawatani et al [8] have observed the effects of a reduction by cold rolling on the elongation and the amount of Laves phase precipitates present in a Ti and Nb stabilised low C, N-19%Cr-2%Mo alloy. Their results show that at a 20% cold reduction a very large amount of Laves phase is precipitated that increases the strength and decreases the elongation of the steel. Cold rolling is considered to give a high enough dislocation density to nucleate these Laves particles at dislocations and not only at grain boundaries. The optimum properties of cold rolled and annealed steel of this composition are obtained by cold reduction of more than 80%, followed by annealing at 920 °C, which will dissolve the Laves phase, followed by rapid cooling.

2.6.2 HOT-ROLLING

Ferritic stainless steel can be hot-rolled without difficulty. However, grain refinement during the hot-rolling process does not occur readily and the grain structure can be quite coarse, particularly after relatively high finishing temperatures. Hot-rolling may also accelerate the precipitation of the Laves phase. It is thus imperative not to hot work in the temperature range of the stable Laves phase precipitation in these steels. After hot rolling, the steel is usually rapidly cooled from the temperature range of 900 to 950 °C to prevent the formation of the Laves phase during cooling. Care must also be exercised when working with high interstitial content alloys, since hot-rolling at high temperatures and quenching can lead to high temperature embrittlement [46].

2.6.3 COOLING RATE

The cooling rate affects the intensity of the precipitate's formation by altering its nucleation rate. Fast cooling rates can prevent precipitation; intermediate cooling rates cause maximum age-hardening, while slow cooling rates give over-ageing which produces low strength. If the precipitation has been suppressed during cooling, it can be induced during the ageing process [47,48].

2.6.4 HEAT TREATMENT

Heat treatment is a major factor in controlling the properties of stainless steels. The ferritic steels are annealed at temperatures from 750 to 900 °C, and the upper limit should not be exceeded substantially since grain growth will induce a decrease in toughness [49]. However, by keeping (C + N) levels very low, concern about grain – size related DBTT increases can be prevented [18]. Annealing must be followed by rapid cooling to avoid prolonged exposure to the temperatures at which Laves phase will form or "475 °C" brittleness will develop.

With total (C + N) content below approximately 500 ppm, quenching generally produces optimum toughness by preventing sigma or Laves phase precipitation as well as carbide and nitride precipitation. With higher (C + N) levels, nothing is gained by quenching and if a high temperature anneal is used, rapid quenching can cause embrittlement by severe carbide and nitride precipitation. This rapid cooling embrittlement can be reduced substantially by the addition of carbide and nitride stabilisers, such as Nb and Ti.

2.7 APPLICATIONS OF STAINLESS STEELS IN AUTOMOBILE EXHAUST SYSTEM

Recently, environmental pressures have required the reduction of dangerous exhaust gas emissions from motor cars, and there has been an effort by automobile manufacturers to raise the temperature of exhaust gases from automobile engines to about 900°C in order to give a cleaner exhaust gas [50, 51]. To improve the efficiency of the automobile engines and to reduce their weight, more conventional stainless steel sheets and tubes in the application of exhaust systems are now replacing the traditional cast iron, particularly in near-engine applications. The exhaust system is divided into two main parts, the hot and the cold ends. The components of the hot end consist of the exhaust manifold, front pipe, flexible pipe and catalytic converter and the components of the cold end consist of a centre pipe main muffler and tail end pipe, see Figure 2.13. Typical operating temperatures and the current materials used for these different components are shown in Table 2.1.

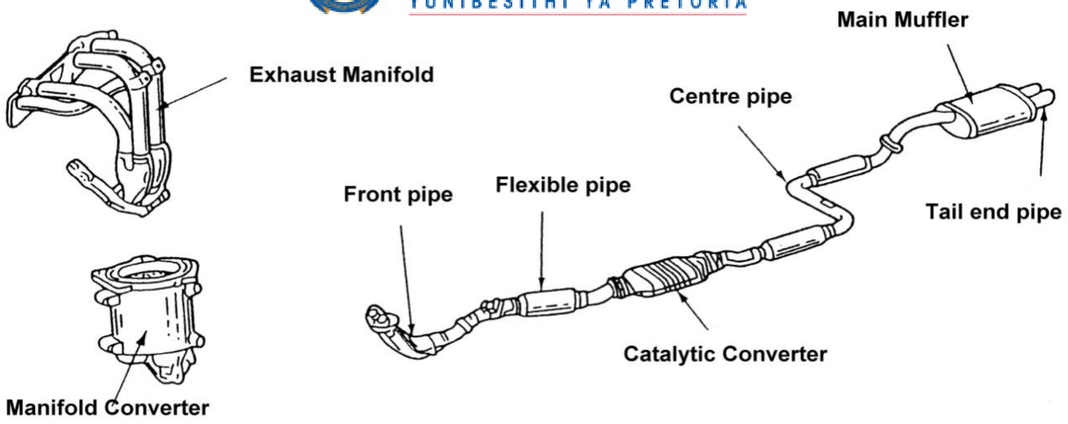

Figure 2.13. Automobile exhaust system components.

Table 2.1. Component of automobile exhaust system and their typical operating temperatures [52,53,54].

Component		Service temp (°C)	Required properties	Current materials
Exhaust manifold		950 – 750	• High temperature strength • Thermal fatigue life • Oxidation resistance • Workability	409, 441, 304, 321, 309
Front pipe		800 – 600		304, 321,309, 409
Flexible pipe				304, 321, 309 and 316Ti
Catalytic converter	Shell		• High temperature strength • High temperature salt damage resistance • Workability	441, 409, 321, 309
	Catalyst carrier[*]	1000 – 1200	• Oxidation resistance • Thermal shock resistance	
Centre pipe		600 – 400	• Salt damage resistance	304, 409, 441
Main muffler		400 - 100	• Corrosion resistance at inner surface (condensate) • Corrosion resistance at outer surface (salt damage)	409, 434, 436, 430Ti, 321, 304
Tail end pipe				304, 316

Thus, the materials for automobile exhaust systems require excellent thermal fatigue resistance and higher temperature strength. Ferritic stainless steels are the commonly used materials in exhaust systems as a compromise between inexpensive carbon steels and the higher cost of higher alloyed ferritic or austenitic steels. Ferritic stainless steels have better corrosion resistance and thus a longer life than low carbon steels and have lower cost than the more highly alloyed stainless steels. However, ferritic stainless steels have relatively low strength at elevated temperatures compared to austenitic steels. Therefore, efforts have been made to create new ferritic stainless steels with

---

[*] The catalyst carrier are usually made out of ceramic, there has been a recent development in metal carrier made out of ferritic stainless steel foils because they have good thermal shock properties and a small heat capacity [53].

excellent thermal fatigue resistance and high strengths at elevated temperatures. This has been achieved by the use of stabilising elements such as the addition of niobium and titanium, as will be discussed in the next section.

2.8 HEAT RESISTANT FERRITIC STAINLESS STEELS

Niobium-containing ferritic stainless steels are being used in automotive exhaust systems because of their excellent heat resistant properties, especially their thermal fatigue resistance which is very important for materials of exhaust systems because of the frequent heating and cooling cycles. When in solid solution, the Nb addition increases the initial high temperature strength compared with other alloying elements, see Figure 2.14 below [4]. However, Nb forms several types of precipitates during service, which can cause degradation in high temperature strength and thermal fatigue resistance [3].

In the work by Fujita et al. [5], the effect of Nb additions in 0.01C – 0.01N – 13Cr steel on the 0.2% proof strength at 900 °C is observed to be effective above 0.2 %wt Nb. On the other hand, Mo additions increase the high temperature strength approximately in proportion to the alloy addition content.

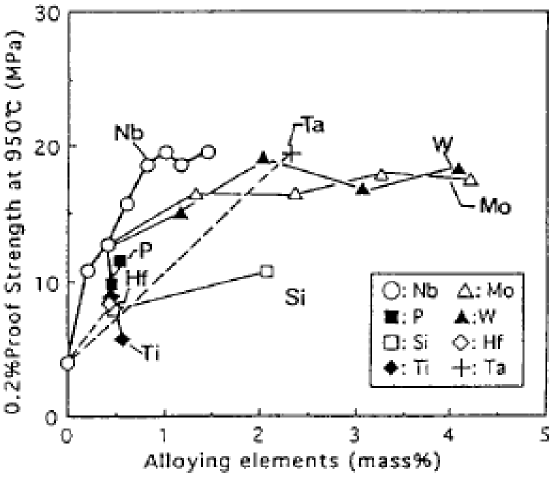

Figure 2.14. Effect of alloying element additions on the 0.2% proof strength at 900 °C of a 13%Cr ferritic steel [4].

2.9 STABILISATION

To combat the problem of sensitisation, the carbon in stainless steels is reduced through a combination of steelmaking practices and through the addition of elements with strong affinity for carbon and nitrogen. Firstly, these steels are processed by an “argon-oxygen decarburisation (AOD)” or “vacuum-oxygen decarburisation (VOD)” process to reduce the carbon content to very low levels (<0.02%C). The carbon and nitrogen in solution are further reduced through the addition of stabilising elements such as titanium (Ti) and niobium (Nb), tantalum (Ta), vanadium (V) and molybdenum (Mo). These elements form carbides, nitrides or carbo-nitrides and precipitate at higher temperatures and shorter times than chromium carbides, thus removing most of the carbon and nitrogen from solution before the chromium carbides form. Because of the high cost of Ta, it is normally not used in the stabilisation of stainless steels. Either Nb or Ti individually and/or Ti plus Nb additions have been used in stainless steels for automobile exhaust systems, and the two stabilisation methods will be compared in the next section.

2.9.1 STABILISATION WITH TITANIUM

This is the most widely used stabilising addition to stainless steels. The highly reactive element forms highly stable titanium nitride (TiN) precipitates in the presence of N and titanium carbide (TiC) in the presence of C. Whilst in the presence of both nitrogen and carbon, titanium carbonitride (Ti(C,N)) is formed owing to the mutual solubility of TiN and TiC [55]. The ratio of TiC/TiN in the Ti(C,N) is dependent upon the ratio of N/C in the alloy. In Ti stabilisation practice it is generally accepted that the level of Ti required to fully-stabilise a stainless steel is directly dependent on the C and N content, and can be calculated empirically from [55]:

$$Ti=0.2 + 4(C+N)$$

The disadvantage of Ti stabilisation is that Ti-stabilised stainless steel suffers from surface defects that require surface grinding and these result in an increase in the overall production cost. This can be overcome by combining Ti additions with other stabilising elements such as aluminium (Al), niobium (Nb) or vanadium (V).

2.9.2 STABILISATION WITH NIOBIUM

Many researchers have investigated the effects of niobium stabilisation on ferritic stainless steels for their use in automotive exhaust systems [3,4,5,6] and have found that niobium additions can improve the high temperature strength of ferritic stainless steels by solid solution strengthening, which allows its operation at such high temperatures. Generally, solute Nb readily precipitates out as a carbo-nitride when the steel is used at high temperatures of about 900°C for long times [3,4]. In addition to its stabilisation effects, small amounts of Nb in the stainless steel have been known to affect both mechanical and microstructural properties [6]. It is, therefore, important to know how much of the niobium precipitates out as carbides or as carbo-nitrides and which fraction remains in solution. Niobium stabilised ferritic stainless steels form the carbide precipitates NbC, M_6C (Fe_3Nb_3C) and the Laves phase type Fe_2M (Fe_2Nb). The main benefit of the Nb is its ability to suppress recovery, recrystallisation and grain growth in ferritic steels [4].

2.9.3 Solid Solution Hardening and Solute Drag by Niobium

Niobium addition is the most frequently used microalloying element because it has a significant effect on the microstructure and the mechanical properties of ferritic stainless steels. Depending on the state of Nb (in solid solution or in precipitates) as determined by the heat treatment, Nb has a significant effect on the recrystallisation and the grain growth. The effect of Nb on the recrystallisation and the grain growth of the austenite has been widely studied [56,57,58]. Nb addition, even in small amounts, can lead to a significant decrease in grain boundary mobility, as well as an increase in the recrystallisation temperature. Both the decrease in the grain boundary mobility and increase in the recrystallisation temperature might be caused by a solute drag effect of Nb in solid solution and the pinning effect of fine precipitates such as NbC and Fe_2Nb. Suehiro [57] has shown that Nb retards the migration of grain boundaries during recrystallisation due to the solute drag effect.

The quantitative theory of the solute drag effect on a moving grain boundary during recrystallisation was originally formulated by Lücke and Detert [59]. It was later modified by Cahn [60] and then by Lücke and Stüwe [61]. Since then, this theory has been further refined by several authors [57,58,62]. The equation proposed by Cahn on the rate of grain boundary movement as it is affected by solute drag is [63,64]:

$$\frac{p_d}{\nu_b} = \frac{1}{M_T} = \frac{1}{M_0} + \frac{\alpha X_s}{\left(1+\beta^2 \nu_b^2\right)} \qquad \text{Equation 2.15}$$

where p_d is the driving force for the grain boundary mobility and ν_b is the mobility rate, M_T is the overall mobility due to intrinsic plus solute drag, M_0 is the intrinsic grain boundary mobility in pure material, X_s the atom fraction of solute in the bulk metal, α is a term related to the binding energy of solute to the grain boundary and β is a term related to the diffusivity of the solute in the vicinity of the grain boundary.

In the work by Le Gall and Jonas [63], the authors have determined the effect of solute concentration and temperature on the grain boundary mobility against driving force using the Cahn model. Their results show that; at high concentrations and low temperatures, the mobility of the grain boundary is low and if the driving force or the temperature is increased, the increase in mobility is very significant and tends towards that of pure metals. The overall results are described by curves with approximately two slopes; M_0 representing the intrinsic mobility in the pure metal and M_B which refers to the mobility in the presence of solute drag elements.

Hillert and Sundman [65,66] developed a theory that is most general because the validity of the theory is not limited to the dilute solution case and it can be applied to both grain boundary and phase interface migrations. Suehiro et al.[58] developed the simplified model to calculate the solute drag effect on a moving phase interface, but it can also be applied to both grain boundaries and phase interfaces. They applied this model to the phase transformation in an Fe-Nb system [57]. In this model, recrystallisation is described as a phase transformation for which the driving force results from the energy stored as dislocations. It should also be mentioned that the stored energy in a plastically deformed material may give rise to the driving force for grain boundary migration in recrystallisation through the Strain Induced Boundary Migration (SIBM) mechanism.

It was shown that the Cahn equation (that is, Equation 2.15) can be simplified when the driving forces are low [63]. The overall mobility due to intrinsic plus solute drag is then given by:

$$\frac{1}{M_T} = \frac{1}{M_0} + \frac{1}{M_B}$$ Equation 2.16

where M_0 is the intrinsic mobility in a pure metal and M_B is the grain boundary mobility under solute drag conditions. The solute drag equation is then reduced to:

$$v_b = M_T p_d$$ Equation 2.17

This equation is only valid for low driving force phenomena such as grain growth, whereas with higher driving forces as with the recrystallisation, Le Gall and Jonas [63] proposed a "law of mixtures":

$$M_T = M_0(1 - f_{GB}) + M_B f_{GB}$$ Equation 2.18

where M_0 and M_B are defined as above, f_{GB} is a function of potential grain boundary sites filled by solute and is temperature dependent.

2.9.4 EFFECTS OF TEMPERATURE ON SOLUTE DRAG

The effect of temperature on solute drag during recrystallisation has been investigated in an Fe-Nb alloy [57]. These results show that Nb decreases the velocity of the recrystallising grain boundary at the composition covering the critical composition and this depends on the temperature and total driving force. This retardation was found to be caused by the solute drag effect of Nb. In work by Suehiro et al. [58], the author studied the effect of Nb on the austenite to ferrite transformation in ultra low carbon steel. Their results indicate that there is a critical temperature where the rate of transformation changes drastically. The transformation that occurs above and below the critical temperature are both partitionless massive transformations. The critical temperature was found to be composition dependent, and for the 0.25% Nb alloy it was found to be 760 °C and for 0.75%Nb alloy it was 720 °C

From Equation 2.15, however, it can be predicted that by increasing the temperature to the point where the mobility of solute atoms becomes high, solute drag becomes less effective and the overall mobility parameter approaches the intrinsic mobility factor, that is $M_T \approx M_0$. . Le Gall and Jonas [63] have observed solute drag by sulphur atoms in pure nickel, while observing that the transition from solute drag to purely intrinsic mobility of the grain boundary is not a gradual one but that it occurs at a critical temperature that provides a “break” in the mobility versus inverse temperature relation.

2.9.5 DUAL STABILISATION WITH TITANIUM AND NIOBIUM

Research conducted over the last few decades has revealed the benefits of stabilising carbon and nitrogen by using both titanium and niobium. These observations led to the development of the modern generation of ferritic stainless steels, i.e., dual-stabilised ferritic stainless steel. The dual stabilisation imparts beneficial corrosion resistance, oxidation resistance, high temperature strength and formability to the steel [2,31]. At present, it appears to be well accepted that to achieve full stabilisation of ferritic stainless steels a ratio of Nb:Ti = 2:1 is preferred [31]. The optimum limits of dual stabilisation have been established experimentally, and are given by:

$$\text{Ti} + \text{Nb} = 0.2 + (\text{C} + \text{N}) \quad \text{at min}$$

$$\text{Ti} + \text{Nb} = 0.8 \quad \text{at max}$$

To reduce grain growth during high temperature annealing extra niobium is added, leading to intermetallic precipitation. The addition of titanium and niobium is made in such a way that an extra content of niobium (ΔNb) is kept in solid solution after the carbo-nitride precipitation [67]:

$\Delta Nb = [Nb] - 7([C] + [N])$ in case of Nb stabilisation

$\Delta Nb = [Nb] - 7/2\,[C]$ in case of (Ti + Nb) stabilisation

At temperatures between 600 and 950 °C, isothermal treatment has shown that the residual niobium precipitates out to form intermetallic Fe_2Nb. Schmitt [67] has observed that depending on the temperature, a part of the precipitation occurs on the grain boundaries combined with a fine intergranular precipitation, and this strongly slows down the grain boundary mobility. The nature of the precipitates, the size and location depends also on the alloy composition. The value of the excess ΔNb content is significant, as well as the silicon and molybdenum content. Both the Si and Mo have an effect to enhance the precipitation of the Laves phase [29].

2.10 AISI TYPE 441 STAINLESS STEELS

Type 441 alloy is a low carbon, Ti and Nb stabilised, heat resisting ferritic stainless steel providing good oxidation and corrosion resistance for applications such as automotive exhaust system components. The high chromium content makes type 441 steel far more corrosion resistant than its counterpart type 409 [52]. The 441 steel is dual stabilised with niobium and titanium to provide good weld ductility and resistance to intergranular corrosion in the weld's heat affected zone. Type 441 is manufactured according to the requirements of EN 10088-2 and certified as 1.4509, see Table 2.2 for its chemical composition.

The structure of type 441 is a completely ferritic alloy, i.e. the matrix has a body centred cubic crystal structure up to its liquidus temperature. Angular carbo-nitrides of titanium and niobium that have precipitated from the melt are randomly dispersed throughout the structure. The presence of the titanium nitrides and carbides in the steel tends to lower the melting point of the steel, as shown by Gordon [55], see Figure 2.15. Excess niobium is taken into solid solution during high temperature annealing and precipitates as very fine particles of Laves phase (Fe_2Nb) upon either slow cooling or upon holding at intermediate temperatures of 600 – 950 °C [68]. Strengthening by this dispersion is responsible for improved elevated temperature strength [69].

Table 2.2. Chemical composition of type 441 stainless steel in accordance with EN 10088-2 [70].

	C	N	Mn	Si	Cr	Ni	Ti	Nb	S	P	Remarks
Min					17.50		0.10				%Nb≥ 3xC + 0.3
Max	0.03	0.045	1.00	1.00	18.50	0.50	0.60	1.00	0.015	0.04	

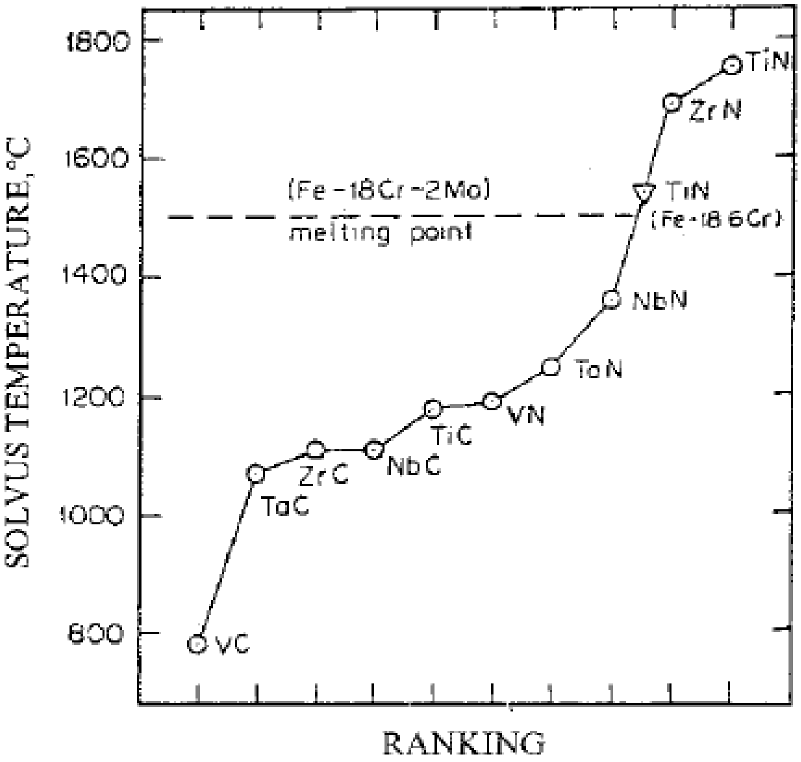

Figure 2.15. The solvus temperatures of the precipitates found in stabilised ferritic stainless steels [55].

2.11 CALPHAD METHODS

The CALPHAD (CALculations of PHAse Diagram) method primarily uses numerical techniques based on thermodynamic principles for addressing complex problems like stable and metastable phase equilibria in the multicomponent systems for equilibrium conditions. The essence of the Calphad approach is to obtain the parameters of thermodynamic models for the Gibbs energies of the constituent phases in terms of known thermodynamic and phase equilibrium data in the lower order systems, binaries and ternaries. The Gibbs energies of multicomponent alloy phases can be obtained from those of lower order systems via an extrapolation method [71]. These Gibbs energy values enable engineers and scientists to calculate reliable multicomponent phase diagrams in many instances. Experimental work is then only required for confirmatory purposes and not for the determination of the entire phase diagram. The Calphad approach in calculating phase diagrams of multicomponent alloy systems is shown schematically in Figure 2.16 [71].

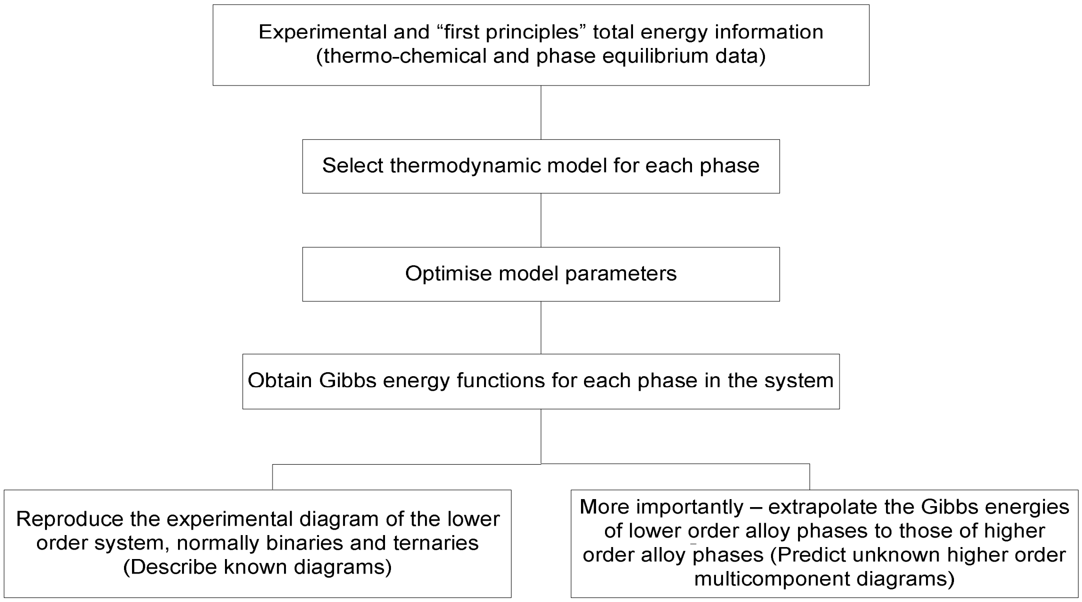

Figure 2.16. Schematic flow diagram showing the Calphad approach used to obtain a thermodynamic description of a multicomponent system.

Thermodynamic descriptions of the constituent lower order systems, normally binaries and ternaries, are obtained through experimental and “first principles” of total free energy information and phase equilibrium data [72]. However, once descriptions for the lower order systems are known, it is possible in many cases to obtain thermodynamic descriptions of the higher order systems by using an extrapolation method so that more complete phase diagrams of the system can be calculated.

The Gibbs energy of a phase is described by a model that contains a relatively small number of experimentally optimised variable coefficients. Examples of experimental information used include melting and other transformation temperatures, solubilities, as well as thermodynamic properties such as heat capacities, enthalpies of formation and chemical potentials.

For pure elements and stoichiometric compounds, the following model is commonly used:

$$G_m - H_m^{SER} = a + b \cdot T + c \cdot T \cdot ln(T) + \sum d_i \cdot T^i \qquad \text{Equation 2.19}$$

where, $G_m - H_m^{SER}$ is the Gibbs energy relative to a standard element reference state (SER), H_m^{SER} is the enthalpy of the element in its stable state at the temperature of

298.15 Kelvin and a pressure of 10^5 Pascal (1 bar), and a, b, c, and d_i are model parameters.

For multi-component solution phases, the following expression for the Gibbs energy is used:

$$G = G° + {}^{id}G_{mix} + {}^{xs}G_{mix} \qquad \text{Equation 2.20}$$

where $G°$ is the Gibbs free energy due to the mechanical mixing of the constituents of the phase, ${}^{id}G_{mix}$ is the ideal mixing contribution, and ${}^{xs}G_{mix}$ is the excess Gibbs energy of mix (the non-ideal mixing contribution).

If a phase in a multi-component solution is described with a single sub-lattice model, then the $G°$, ${}^{xs}G_{mix}$ and ${}^{xs}G_{mix}$ contributions to the Gibbs energy can be expressed as follows:

$$G° = \sum_i c_i \cdot G_j^o \qquad \text{Equation 2.21}$$

$${}^{id}G_{mix} = R \cdot T \cdot \sum_i c_i \cdot ln(c_i) \qquad \text{Equation 2.22}$$

$${}^{xs}G_{mix} = \sum_i \sum_{j>i} c_i \cdot c_j \cdot \sum_k L_{i,j}^k \cdot (c_i - c_j)^k \qquad \text{Equation 2.23}$$

where c_i and c_j are the mole fraction of species i and j respectively, and $L_{i,j}^k$ is a binary interaction parameter between species i and j. The binary interaction parameter $L_{i,j}^k$ is dependent on the value of k. When the value of k equals zero or one, the equation for ${}^{xs}G_{mix}$ becomes regular or sub-regular, respectively.

2.11.1 THERMODYNAMIC SOFTWARES

During the last few decades, the rapid development of thermodynamic and kinetic software packages, such as Thermo-Calc®, DICTRA [73,74], ChemSage, FactSage and MTDATA have made it possible to calculate complex phase equilibria in multicomponent systems. It is evident that gradually the accuracy of these calculations will become more and more dependent on the databases behind the packages. So far, a great number of binary, ternary and even quaternary systems have been assessed to obtain a sufficiently sound database for multicomponent steels [75,76,77]. However, there are still some subsystems not assessed earlier or assessed but not shown in the open literature.

2.12 INTERMETALLIC LAVES PHASE

2.12.1 CRYSTALLOGRAPHIC STRUCTURE

Many intermetallic phases belong to the group of the Laves phase with AB_2 compositions of topologically close packed (TCP) structures. Furthermore, these Laves phases are capable of dissolving considerable amounts of ternary alloying elements [78,79,80]. Laves phases are generally stabilised by the size factor principles, that is, the atomic size ratio r_A/r_B, which is ideally 1.225 with a range of 1.05 - 1.68 that is usually observed [81,82]. Three types of Laves phase (see Figure 2.17 [85]) and the Pearson symbols and their crystallographic structures are given below [83,84,85,86]:

Table 2.3. Crystallographic structure and the space groups of the three types of the Laves phase.

Typical composition	Structure	Pearson symbol	Space group	Space group number
C14, $MgZn_2$	hexagonal	*h*P12	$P6_3/mmc$	194
C15, $MgCu_2$	fcc	*c*F24	$Fd\bar{3}m$	227
C36, $MgNi_2$	hexagonal	*hP24*	$P6_3/mmc$	194

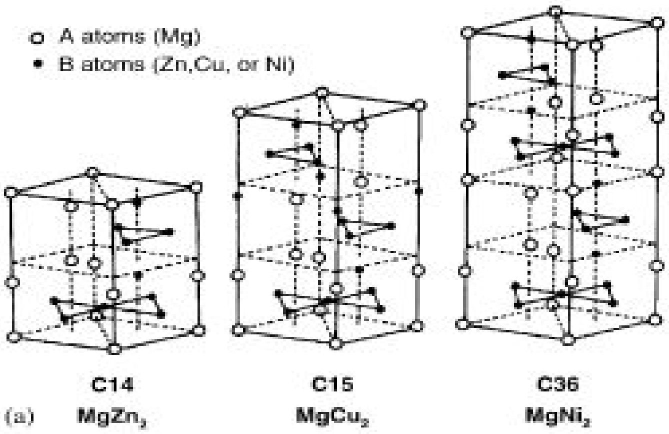

Figure 2.17. The three polytypes of the Laves phase structure in a hexagonal setting.

The Fe_2Nb Laves phase (Mg_2Zn type, C14) is a hexagonal close packed phase with the space group $P6_3/mmc$, and the lattice parameters of a=0.473 nm and c=0.772 nm with c/a = 1.633. The main factor determining its formation is the relative atomic size of the constituent atoms, with the ranges of composition quite small. This Laves phase probably does not form at its exact equilibrium composition [8,87]. In Nb and/or Ti stabilised stainless steel grades, Fe_2Nb or Fe_2Ti (more seldom) can form.

2.12.2 OCCURRENCE

The precipitation rate of the Laves phase in a Ti and Nb stabilised steel was observed to reach a maximum at 700°C and its dissolution occurs at temperatures over 900°C [88]. The same observation has been made by the use of thermodynamic software such as Thermo-Calc® [3] and its growth and coarsening rates have been simulated by Bjärbo [9] using DICTRA software. The Laves phase precipitates firstly on sub- and grain boundaries as a fine precipitate and as the steel is slowly cooled from a high temperature of about 900°C, the amount of Laves phase increases but now inside the grains and the particles then coarsen. In the work by Murata et al, [89] they have shown that the Laves phase's solvus temperature depends on the content of the alloying elements, that is, the solvus temperature increases with increasing alloying content.

The intermetallic Laves phase is known to affect the mechanical properties and corrosion resistance of ferritic stainless steel. It has been found that a fine precipitate of Laves phase at grain boundaries improves the high temperature strength when still fine [6]. However, rapid coarsening of the Laves phase at high temperatures reduced the high temperature strength [10] although the exact mechanism is still not clear and still requires clarification. In research done by Fujita et al.[5] to determine the solubility products in a niobium stabilised ferritic steel it was found that a Mo addition enhances the precipitation of the Laves phase even if the addition is as small as 0.5mass%Mo. Sawatani et al [11], studied the effect of Laves phase on the properties of dual stabilised low carbon stainless steels as related to the manufacturing process of Ti- and Nb-stabilised low (C, N)-19%Cr-2%Mo stainless steel sheets, and have found that the Laves phase has a significant influence on the mechanical properties of the steel. It was found that Laves phase on the grain boundaries shifts the brittle to ductile transition temperature to a higher temperature, and large amounts of Laves phase degrade the room temperature ductility of cold rolled and annealed sheet and greatly enhances its strength. It was also observed that after a 20% cold rolled reduction (of the sheet that was cold rolled and annealed after 0 to 92% reductions) that there was a peculiarly rapid precipitation of Laves phase, which caused a severe degradation of the mechanical properties [8]. The reason for the rapid increase in Laves phase precipitation was not clear, but it was assumed that there is possibility that an autocatalytic reaction occurs to substantially increase the precipitation rate of Laves phase. The rate of autocatalytic reaction under which the nucleation and growth of particles occur at dislocations will greatly depend on the formation rate of new dislocations from the cold work which then act as new precipitation sites.

2.12.3ORIENTATION RELATIONSHIP

Cocks and Borland [90] have investigated the orientation relationship and morphology of Fe_2Nb precipitates within the ferrite matrix in 0.6 at%Nb and 1.9 at%Nb alloys respectively, using electron diffraction techniques. They had found that there exists a single orientation relationship:

$$\{11\bar{2}0\}_{Fe_2Nb} // \{111\}_{\alpha} : \langle 0001 \rangle_{Fe_2Nb} // \langle 112 \rangle_{\alpha} \qquad \text{Equation 2.24}$$

and the morphology of these particles are disc-shaped lying on the $\{111\}_\alpha$ plane. Lath-shaped particles were found to have developed in overaged alloys and most of these particles tend to be elongated in the $\langle 112 \rangle$ matrix direction. The orientation relationship between the rod-like Laves phase particles and the matrix was found to be [11,91]:

$$\{11\bar{2}0\}_{Fe_2Nb} // \{111\}_{\alpha} : \langle 0001 \rangle_{Fe_2Nb} // \langle 110 \rangle_{\alpha} \qquad \text{Equation 2.25}$$

The analysis suggests that the habit plane, if any, must be $\{110\}_\alpha$ and the preferred growth direction must be $\langle 110 \rangle_\alpha$ [92]. The two orientation relationships are completely different from one another and the habit planes are also different. In work by Miyahara et al. [93] on Fe-10%Cr ferritic alloys, they have observed very small disk–like Laves phase (Fe_2Mo) precipitates that had formed on the $\{100\}_\alpha$ plane and which have a coherent strain field in the matrix. Therefore, it may be reasonable to consider that there can be several orientation relationships rather than only one orientation relationship. None of the above authors tried to relate the orientation relationship of the Laves phase to its precipitation morphologies.

In the work done by Murata et al. [94], the authors determined the surface interfacial energy γ_{SF} of the coherent and incoherent Laves phases in the Fe-Cr-W- C quaternary system. They observed that the coherent fine Laves phase has a lower interfacial energy than the incoherent granular Laves phase, and their estimated values were 0.1 J/m^2 and 0.468 J/m^2, respectively. Also, their results show that there is a morphological change of the Laves phase from the fine coherent precipitates to the granular ones. This morphological change occurs in a regular ageing sequence in the steel if it contains more than 4 wt.% W.

CHAPTER THREE

THEORY OF PRECIPITATION REACTIONS IN STEELS

3.1 INTRODUCTION

The formation and subsequent behaviour of individual particles in any precipitation process involve its nucleation, growth and coarsening but the overall precipitation process must account for solute concentration impingement effects. In some cases the nucleation of second phases in steel might involve the dissolution of metastable precipitates and the coarsening of stable precipitates. These stages of nucleation and growth of the precipitates will be discussed in this chapter.

3.2 CLASSICAL THEORY OF NUCLEATION

Most particle-sized second phases in steels precipitate through a nucleation and growth mechanism. During the nucleation process, the associated free energy change is dominated by the Gibbs chemical free energy, the surface free energy and the misfit free energy terms. The total free energy change can be represented by summing all of these contributions:

$$\Delta G = \frac{4}{3}\pi r^3 \Delta G_v + 4\pi r^2 \gamma + \frac{4}{3}\pi r^3 \Delta G_\varepsilon \text{, (where } \Delta G_v \leq 0\text{)} \qquad \text{Equation 3.1}$$

where ΔG_v is the Gibbs chemical free energy released per unit volume of the new phase and has a negative value, γ is the interfacial surface energy per unit area associated with the interface of the two phases and ΔG_ε is the misfit strain energy per unit volume. Plotting this equation demonstrates the dependency of the stability of the new embryo on its size, see Figure 3.1.

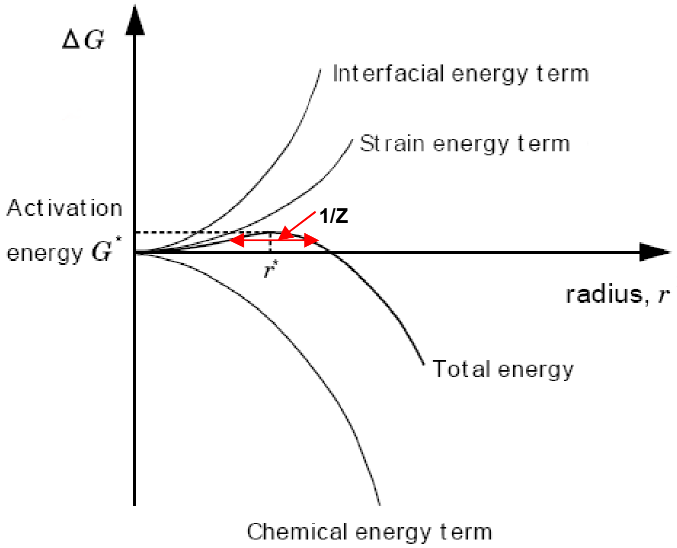

Figure 3.1 The free energy change associated with the formation of a stable nucleus with the radius r.

3.2.1 ACTIVATION ENERGY FOR NUCLEATION WITHIN THE MATRIX

From Figure 3.1, the maximum total free energy occurs at a critical radius *r** when the free energy has a value *ΔG**, known as the activation energy. An embryo with a radius larger than *r** will tend to grow spontaneously rather than dissolve since its growth leads to a decrease in free energy and then the embryo becomes a stable nucleus. At

$r = r^*$, $d\Delta G/dr$ equals zero, so that ΔG^* is given by:

$$r^* = \frac{-2\gamma^2}{(\Delta G_v + \Delta G_\varepsilon)} \qquad \text{Equation 3.2}$$

$$\Delta G^* = \frac{16\pi\gamma^3}{3(\Delta G_v + \Delta G_\varepsilon)^2} \qquad \text{Equation 3.3}$$

3.2.2 ACTIVATION ENERGY FOR NUCLEATION ON THE GRAIN BOUNDARY

In the preceding section, the formation of a nucleus has been regarded as a homogeneous process occurring with equal probability in all parts of the assembly. In practice, this is unlikely to happen unless the assembly is extremely pure, and also contains (if in the solid state) very few structural defects. More usually, the presence of impurity particles and structural defects (dislocations and sub- and grain boundaries) that enable nuclei to be formed with a much smaller free energy of activation than that of the homogeneous nuclei, occurs in most industrial alloys.

If we consider nucleation that takes place on a grain boundary, a certain surface area A of the grain boundary is removed from the system. This forms an additional driving force for nucleation and must, therefore, have a negative sign in the basic free energy equation for nucleation (see the last term in Equation 3.4 below).

$$\Delta G = K_1\left\{\Delta G_v + \Delta G_\varepsilon\right\} + K_2\gamma_{ppt}A_{ppt} + K_3\gamma_{ppt/gb}A_{ppt/gb} - \gamma_{gb}A_{gb}$$ Equation 3.4

From this equation it is clear that the system will preferentially select those higher energy grain boundary sites first where it will gain the most energy as an additional driving force.

The following relationship between the activation energy for grain boundary nucleation for the various possible grain boundary sites and the contact angle θ should, therefore, be expected, Figure 3.2. The ratio of the free energy required to form a grain boundary nucleus to that needed to form a homogeneous nucleus obviously decreases as the ratio of the grain boundary energy to the interphase boundary energy increases through the contact angle parameter cos θ.

From Figure 3.2 it may be seen that at a given contact angle θ, nucleation on grain corners requires the lowest activation energy, then grain edges and lastly grain boundaries. Grain boundaries can also lower the retarding force arising from the strain energy ΔG_ε and, thereby, create a new driving force. In cases where the surface energy and the strain energy are lowered enough through nucleation on grain boundaries, the grain boundaries may become the preferred sites fully and no nucleation within the grains will occur. This is what is typically found in Al - Mg alloys where the β-phase nucleates only on grain boundaries and embrittles the alloy [95].

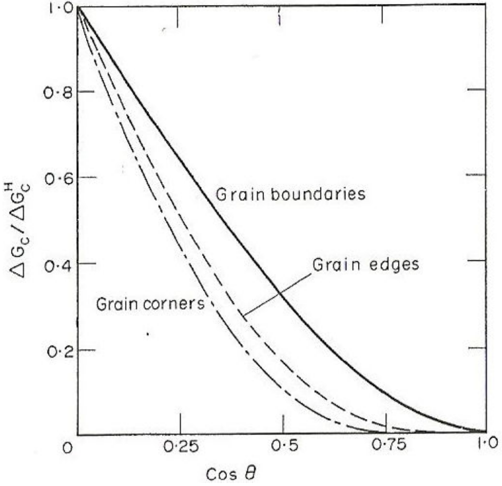

Figure 3.2. The ratio of the free energy required to form a nucleus on various types of grain boundary sites to that required to form a nucleus in the grain matrix, is plotted as a function of the contact angle parameter *cos θ*.

Precipitates on grain boundaries represent a special case because they are located on the junction of two or more different crystal orientations and may also possess different interface lattice parameters in the case of interphase boundaries. Figure 3.3 shows different possibilities of interfaces on a boundary.

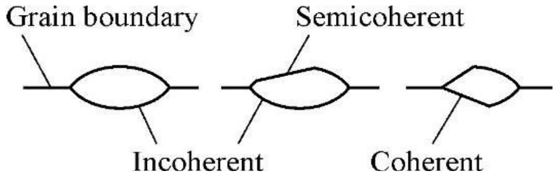

Figure 3.3. Different possibilities of the precipitate's interface on grain boundaries.

3.2.3 MISFIT STRAIN ENERGY AROUND THE PARTICLE

The structural misfit across a matrix / precipitate interface plays a prominent role in the strain energy around a coherent or semi coherent precipitate. This misfit very often leads to interfacial dislocations or ledges and steps. For incoherent particles the strain energy arises mainly out of the differences in the lattice spacing and the strain in the matrix volume because of differences in densities. Nabarro [96] derived the elastic strain energy for an ellipsoidal nucleus of β phase having semi-axes a, a and c in an isotropic α matrix as [108]:

$$\Delta G_{\varepsilon} = \frac{2}{3} G_m \delta^2 \nu^{\beta} f(c/a)$$ Equation 3.5

where G_m is the shear modulus of the matrix, δ is the volume misfit of the precipitate in the matrix and is defined as:

$$\delta = \frac{v^{\beta} - v^{\alpha}}{v^{\beta}} = \qquad \text{Equation 3.6}$$

where v^{β} and v^{α} are the lattice spacings of the precipitate phase and the matrix, respectively. Thus the elastic strain energy is proportional to the square of the volume misfit, δ^2. The function *f(c/a)* is a factor that takes into account the shape effect and is shown in Figure 3.4.

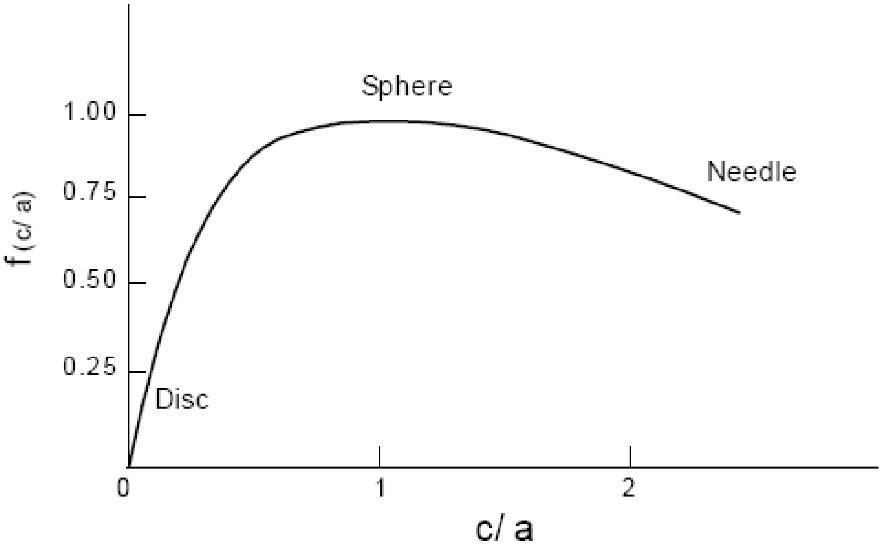

Figure 3.4. Illustration of the variation of the function f(c/a) of an incoherent nucleus with its shape.

A flat disc, therefore, provides a lower value of ΔG_{ε} but also has a higher surface area per unit volume and this results in a higher total surface energy. Therefore, a compromise has to be reached which very often leads to ellipsoidal shapes.

3.2.4 INTERFACIAL ENERGY

Boundaries between different solid phases can be classified into coherent, semi-coherent and incoherent interfaces. For nucleation in crystalline solids the interfacial energy γ can vary widely from very low values for a coherent interface to high values for an incoherent interface. The interfacial energy is a vital parameter for kinetic simulations. Even small variations of this parameter can have a massive impact on the nucleation and also strongly influences growth and coarsening of precipitates. The value of this energy is not often known, since it depends on the crystallography of the precipitate and matrix, on the chemical composition of involved phases, on their misorientation, the degree of coherency and finally, any segregation effects of other minor elements to the interface. Commonly, a mean value of the interfacial energy is used in numeric simulations, which is denoted as an “effective interfacial energy” γ. It is of great importance, therefore, to evaluate possibilities to predict these parameters from existing data (e.g. thermodynamic databases). To treat the problem of multi-component, multi-phase, multi-particle precipitation kinetics on a more physical basis it is necessary to predict the interfacial energies of the precipitates depending on the actual system state.

3.2.4.1 FULLY COHERENT PRECIPITATES

A coherent interface arises when all the lattice planes of the two phases are continuous across the interface. An interface is said to be fully coherent if each atomic plane in one crystal that intersects the interface, is matched by another plane on the opposite side of the interface.

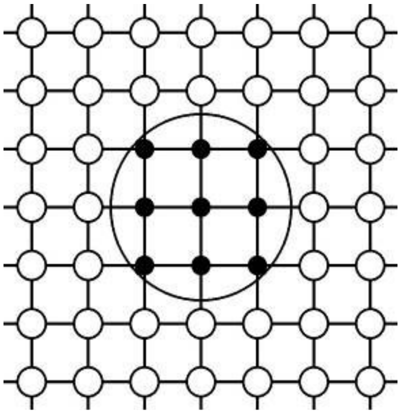

Figure 3.5. Fully coherent precipitates, with no broken inter-atom bonds and with δ=0. The interface is indicated by the circle.

The interface energy in the case of the two lattice spacings with no difference ($\delta = 0$) is only of a chemical nature through the bond-energy of atoms A and B, because there is no structural difference between their lattice spacings. Fully coherent precipitates occur whenever there is no or only insignificant lattice mismatch, at least in one direction.

Especially small precipitates often meet this condition; for example *Guinier-Preston*[1] (GP) zones in many Al-alloys. If there is no lattice mismatch at all these interfaces show identical, usually very low, interfacial energy values in every direction (see Figure 3.5). Consequently, these precipitates are usually spheres, for example in the Al-4at% Ag model alloy [97].

If the lattice parameters of the precipitate and matrix differ, considerable strain energy can be the result. Because of the different lattice structures of precipitate and matrix, the lattice will be deformed elastically, depending on the Young's modulus and also depending on the orientation of the particle in the lattice. For example, a situation where a particle has a similar lattice parameter in a horizontal direction but not in a vertical direction, is illustrated in Figure 3.6. To keep the misfit energy to a minimum these precipitates arrange themselves in the horizontal direction and develop plate or needle like shapes. Similar misfits in every direction will also lead to a spherical particle.

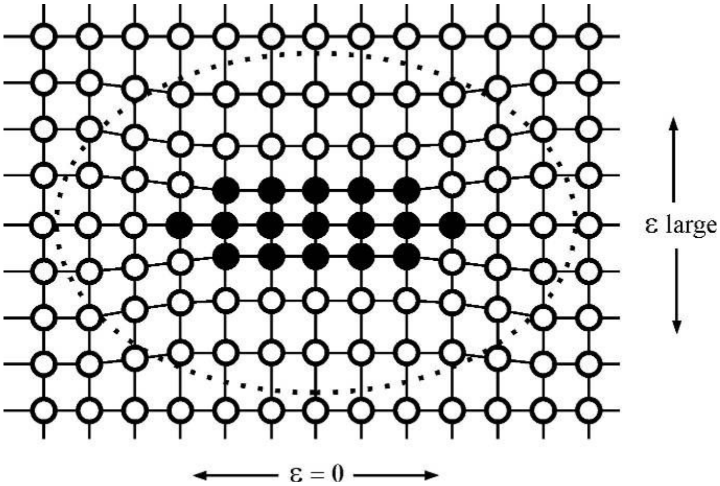

Figure 3.6. Coherent precipitate with different lattice parameters only in the vertical direction. The volume influenced by the lattice misfit, ε is marked by the dotted line.

3.2.4.2 INCOHERENT PRECIPITATES

When the interfacial plane has a very different atomic configuration in the two adjoining planes, or even if it is similar but the inter-atomic distances of the two phases differ by more than 25 %, there will not be good matching across the interface and the interface will most probably be incoherent [98]. During the evolution of a precipitate, it is very

---

[1] e.g.: Al-Cu system with monatomic, disc shaped, Cu layer in (100) plain. Fully coherent with matrix, typical diameter of 3-10nm

likely that the effective interfacial energy changes depending on the actual size and composition of the particle. A small precipitate when the ΣA/ΣV of the second phase is still large, will probably start with fully coherent interfaces and introduce only low elastic strains, despite a possible lattice misfit. During growth as the ΣA/ΣV decreases, some interfaces can transform themselves into semi coherent interfaces to reduce the elastic strain energy. This coherency loss is accompanied by the formation of vacancies and/or misfit dislocations in the interface.

3.2.4.3 SEMI-COHERENT PRECIPITATES

Semi coherent precipitates share some coherent and some incoherent interfaces with the matrix, depending on the crystal orientation. The strain associated with a coherent interface raises the total free energy of the system, and for a sufficiently large atomic misfit, it would be energetically more favourable to replace the coherent interface with a semi-coherent interface in which the misfit is periodically taken up by misfit dislocations.

Summarising these findings, the interfacial energy is dependent on crystallographic and chemical parameters and is not a single scalar value in general. For practical reasons an effective interfacial energy is often introduced in computer simulations.

3.2.5 NUCLEATION RATE

The probability of the barrier to nucleation being overcome by a potential nucleus is given by a Boltzman expression, and so the concentration of critical – sized nuclei N^*:

$$N^* = N_0 \exp\left(\frac{-\Delta G^*}{kT}\right) \qquad \text{Equation 3.7}$$

where N_0 is the initial number density of nucleation sites per unit volume, and k is the Boltzman constant. Each critical sized embryo can be made supercritical and become a nucleus by transferring an atom in contact with the embryo into it.

In the absence of the soft impingement, whereby the mean solute concentration decreases as the reaction proceeds, the nucleation rate is assumed to occur at a constant rate, and this is difficult to justify experimentally because of the different precipitation reactions that occur simultaneously [5,99,100,101,103,104]. Classical nucleation theory is used to estimate the nucleation rate for each type of precipitate. There are several formulae for the nucleation rate per unit volume that are based on the

Turnbull and Fisher nucleation model [95]. Following this model the nucleation rate can be written as:

$$\dot{N} = \left(1 - \frac{V'}{V^{eq}}\right) N_o \frac{kT}{h} \exp\left(-\frac{\Delta G^* + Q}{RT}\right) \qquad \text{Equation 3.8}$$

where Q is the activation energy for diffusion, k and h are the Boltzmann and Planck constants respectively, T is the absolute temperature, V' and V^{eq} are instantaneous and equilibrium volume fractions of alloy precipitates, respectively. The term ($1 - V'/V^{eq}$) is commonly used in the Avrami theory to account for the matrix which can no longer contribute to the transformation and that has been incorporated in the equation to account for the fact that nucleation sites are consumed as transformation proceeds [104].

If long-range diffusion occurs as in carbide precipitation, the expression exp($-Q/RT$) will be multiplied by the mole fraction $\bar{c}$ of the slowest moving solute (in this case niobium) [5,104,100]. Then the nucleation rate per unit volume in this instance is given by:

$$\dot{N} = \bar{c}\left(1 - \frac{V'}{V^{eq}}\right) N_o \frac{kT}{h} \exp\left(-\frac{\Delta G^* + Q}{RT}\right) \qquad \text{Equation 3.9}$$

The calculation of ΔG^* requires a knowledge of the chemical driving force for nucleation ΔG_V, which depends on the chemical composition of the alloy and the equilibrium concentrations (which determine the initial supersaturation) or alternatively, by the undercooling ΔT below the equilibrium transformation temperature. There are two unknowns that cannot be determined experimentally for a complete reaction kinetic calculation of precipitates to be made, that is, the interfacial energy (γ) and the initial number of nucleation site (N_0). These parameters are treated as fitting parameters and the sensitivity of the results in the context of M_6C carbide precipitation in Fe–C–Nb steel, has been made previously by Fujita et al. [103]. Their results show that the nucleation rate is affected more by the interfacial energy than by the number density.

3.2.6 THE TIME-DEPENDENT NUCLEATION RATE

The above equilibrium model did not include the likelihood of the particle's size greater than the critical embryo, r^* ever decaying. According to the *Becker-Döring* theory a decay of nuclei with $r > r^*$ is still likely. This is accounted for by the *Zeldovich* factor Z.

A nucleus is supercritical when the size is larger than the size range indicated by $1/Z$ in Figure 3.1.

According to the classical theory of nucleation, a general time-dependent equation for calculating the rate of isothermal nucleation is given by:

$$\dot{N} = Z\beta^{*} N_{o} \exp\left(-\frac{\Delta G^{*}}{kT}\right)\exp\left(\frac{\tau}{t}\right)$$ Equation 3.10

where β^* is the atomic impingement rate (which includes the temperature dependent diffusion rate), N_o the number of available nucleation sites. The simulation time is t, k is the Boltzmann constant, T is the absolute temperature, and τ is the incubation time. The gradient of the driving force ΔG within the region $1/Z$ is rather small and the cluster will move across this region predominantly by random walk with the jump frequency β^*. The expected time to cover the distance $1/Z$ is identified with the incubation time τ:

$$\tau = \frac{1}{2\beta^{*} Z^{2}}$$ Equation 3.11

$$\beta^{*} = \frac{4\pi r^{*2} D c_{\alpha}}{a^{4}}$$ Equation 3.12

where a is the mean atomic lattice distance of the matrix phase, D is the diffusion coefficient of the rate controlling solute atoms in the matrix and c_α is the equilibrium solute composition within the matrix. The atomic impingement rate β^* is the effective rate, or probability, with which the atoms change from the matrix to the nucleus surface and is, therefore, temperature dependent. Equation 3.12 holds true for spherical nuclei and a binary system.

3.2.7 CHEMICAL DRIVING FORCE

One of the critical parameters that are needed for the calculation, that is, ΔG_V the chemical free energy change per unit volume of precipitate, is given by:

$$\Delta G_{V} = \frac{\Delta G}{\upsilon^{i} V^{i\alpha}}$$ Equation 3.13

where υ is the molar volume of the i^{th} phase and ΔG is the molar free energy change of the precipitate reaction, $V^{i\alpha}$ is the maximum volume fraction of the i^{th} phase. ΔG

for the formation of some of the niobium carbides can be obtained with a CALPHAD method via explicit equations (see Section 2.11, Equations 2.16 – 2.20, which are based on minimising the Gibbs free energy relative to the standard element reference state) [102,103,104,105].

In multi-component systems of the type Fe-C-Nb-Ti, there are thermodynamic data available for the carbides and nitrides, but unfortunately not for the Laves phase (Fe_2Nb) and M_6C (Fe_3Nb_3C) type carbides. However, recently the solubility products for these phases that can be used to estimate ΔG have been determined [6,106]. Table 1 below shows the solubility products of the precipitates within the ferrite matrix.

Table 4. Solubility products of the precipitates within a ferrite matrix.

System	Product	Soluble phase
TiN	–	Ferrite
TiC	log[Ti][C] = 4.4 – 9575/T	Ferrite
NbN	log[Nb][N] = 4.96 – 12230/T	Ferrite
NbC	log[Nb][C] = 5.43 – 10960/T	Ferrite
Fe_3Nb_3C	$\log[Nb]^3[C] = 5.2178 - 11613/T$	Ferrite∗
Fe_2Nb	log[Nb] = 2.4646 – 3780.3/T	Ferrite∗

∗These solubility products were determined by Fujita and co-workers [6]

Fujita et al [6] have attempted to find thermodynamic parameters using the solubility products, and these expressions with the mole fractions (e.g. $x_{Nb}^{\alpha\beta}$) for the free energy changes of the precipitation reactions from a niobium – supersaturated ferrite matrix, are given by:

$$Fe_3Nb_3C\ (\beta);\ \Delta G^{\beta} = -222509 - RT\{6.423 + \ln(x_{Nb}^{\alpha\beta})^3(x_C^{\alpha\beta})\}$$

$$Fe_2Nb\ (\gamma);\ \Delta G^{\gamma} = -72334 - RT\{0.5469 + \ln x_{Nb}^{\alpha\gamma}\}$$

3.3 GROWTH BY SUPERSATURATION

Attempts to model particle growth by a decrease in supersaturation in a ternary or a higher system have been made by assuming a binary approach in which only solutes are considered in the growth equations; thereby violating local equilibrium at the interface. Bhadeshia stated that the procedure for modelling particle growth is falsely justified by stating that the solute considered is the one that controls growth, despite the fact that the theory of diffusion in multi-component systems has been well established [105].

3.3.1 DIFFUSION CONTROLLED GROWTH RATE

A reasonable approximation for isothermal diffusion controlled growth in a binary alloy is that the compositions of the phases in contact at the interface are locally in equilibrium. It follows that the concentrations are given by a tie–line on the equilibrium phase diagram. For a binary system, the tie–line is unique and passes through $\bar{c}$, which is the average concentration of the solute in the matrix alone. The concentration profile that develops during the precipitation of a solute–rich phase such as carbides, is shown in Figure 3.7, where $c^{\alpha\beta}$ is the concentration of the solute in the ferrite (α) matrix which is in equilibrium with the precipitate (β) and $c^{\beta\alpha}$ is the corresponding concentration in the β which is in equilibrium with α; whereas both are obtained from the phase diagram.

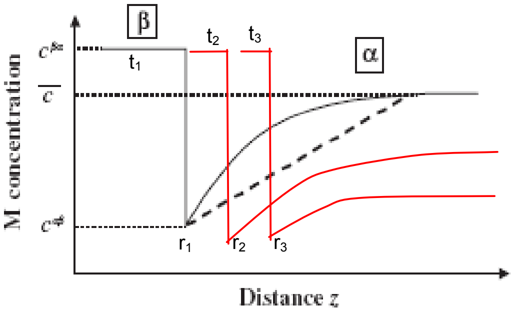

Figure 3.7. The solute concentration profile during diffusion - controlled growth of β from α. $c^{\alpha\beta}$ and $c^{\beta\alpha}$ are concentrations at the interface α/β in the matrix α and the precipitate β, respectively.

Solute is removed from the matrix as the precipitate grows but since the temperature is fixed during isothermal growth, the interface compositions must remain fixed at $c^{\alpha\beta}$ and $c^{\beta\alpha}$ if local equilibrium is to be maintained. Note that the concentration $c^{\alpha\beta}$ is affected by the Thomson-Freundlich or the Gibbs-Thomson equation and is in quasi-equilibrium with the surface energy γ and is, strictly speaking, not an equilibrium value. In order to maintain a constant concentration at the interface, the diffusion flux of the solute at the α/β interface must equal the rate at which solute is partitioned from the matrix to the precipitate so that:

$$v(c^{\beta\alpha} - c^{\alpha\beta}) = -D\frac{\partial c}{\partial z}\bigg|_{z=z^*}$$ Equation 3.14

where ν is the growth rate, z is a coordinate normal to the interface with the value z^* and D is the solute diffusivity. Note that the concentration gradient is evaluated at the position of the interface, $z = z^*$.

The prominent feature of precipitate growth is that after some incubation time and the formation of a critical nucleus (taken to have a radius, $r = 0$), the precipitate grows by depleting the matrix solute immediately ahead of the advancing interface. At any position z in the matrix phase (i.e. $z > r(t)$) the solute concentration is a monotonically decreasing function of time [107].

3.3.2 MULTICOMPONENT DIFFUSION GROWTH

In the work done by Robson and Bhadeshia [77], they treated the growth of carbides using a binary approximation, i.e. in terms of the diffusion of the substitutional element alone. This is incorrect because the mass balance equation will not be satisfied for the interstitial solute. For a ternary system like Fe–C–M, where M stands for a substitutional solute, the tie–line will not in general pass through $\bar{c}$ because it is necessary to simultaneously satisfy two conservation equations at the interface, one each for the substitutional element (M = Nb) and carbon, which diffuse at different rates:

$$v(c_M^{\beta\alpha} - c_M^{\alpha\beta}) = -D_M \left.\frac{\partial c_M}{\partial z}\right|_{z = z^*} \qquad \text{Equation 3.15}$$

$$v(c_C^{\beta\alpha} - c_C^{\alpha\beta}) = -D_C \left.\frac{\partial c_C}{\partial z}\right|_{z = z^*} \qquad \text{Equation 3.16}$$

Because $D_C >> D_M$, these equations cannot in general be simultaneously satisfied for the tie–line passing through $\bar{c}$, apparently implying that growth cannot occur with equilibrium at the interface. However, in a ternary alloy there are many tie–lines to choose from at any given temperature because of the extra degree of freedom given by the phase rule. The local equilibrium condition can be maintained by choosing a tie–line which either minimises the concentration gradient of carbon (thus, allowing substitutional solute flux to keep pace) or maximises the gradient of the substitutional solute to compensate for its slower diffusivity. The mass conservation equation can be satisfied simultaneously in two ways. The first is to choose the tie–line which greatly increases the concentration gradient of M to compensate for its lower diffusivity. This would require the carbide to have virtually the same niobium (M) concentration as the matrix with very little partitioning of Nb, but with a sharp concentration spike at the interface in order to maintain local equilibrium. This is only possible with a very large driving force and hence it is not applicable to niobium carbide precipitation in microalloyed steels [103,100]. The alternative is to select a tie–line which reduces the gradient of carbon to such an extent that the flux of carbon is reduced to a level consistent with that of niobium.

The intersection of the vertical line with the $\alpha / (\alpha + \beta)$ phase field defines the tie–line completely which fixes the interface compositions in a manner which satisfies the conservation conditions because the large diffusion coefficient of carbon is compensated for by the very small concentration gradient of carbon. All this assumes that the far field concentration $\bar{c}$ does not change during transformation, i.e. there is no 'soft–impingement' of the diffusion of different particles and very short annealing times that prevail. Note that this also maintains local equilibrium at the interface since the compositions at the interface (given by the points **c** and **d** for α and β respectively) are connected by a tie–line on the phase diagram. The locus of the matrix composition due to solute depletion during precipitation is along the direction **b** → **e** (Figure 3.8). The change in the matrix composition leads to a different choice of tie–line, the locus of $c^{\alpha\beta}$ being along **c** → **f**. This tie–line shifting continues until the reaction stops when the tie–line intersects the average composition **a** and $c^{\alpha\beta}$ = **f**.

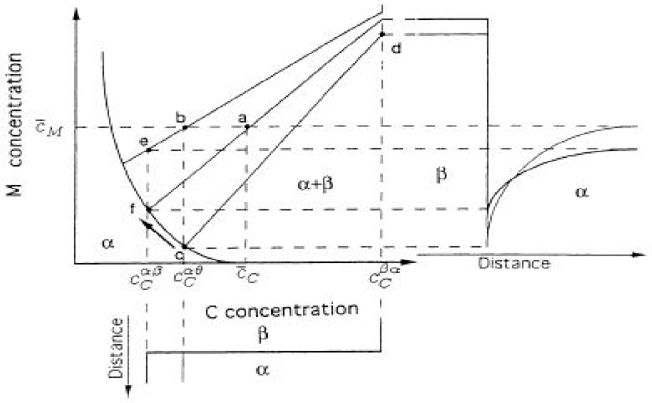

Figure 3.8. A schematic isothermal section through the Fe-C-M phase diagram, showing the ferrite matrix α and alloy carbide β fields. The alloy composition is plotted as point a [4].

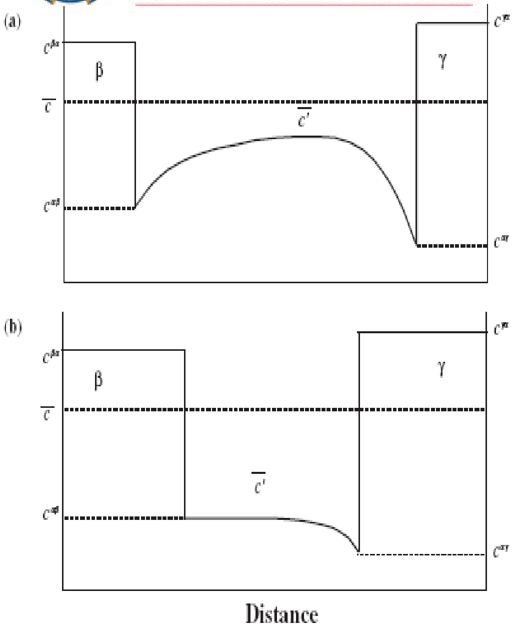

Figure 3.9. Distribution of the solute when (a) both (β) and (γ) are precipitating, and (b) where the precipitation of (β) has been completed. Note that $\bar{c}'$ is the instantaneous solute concentration in the matrix (α) [99].

The mean field approximation can be used to calculate the change in $\bar{c}$ as precipitation proceeds. The instantaneous value of the matrix composition $\bar{c}'$, is given by:

$$\bar{c}' = \bar{c} - \frac{V^{\beta}(c^{\beta\alpha} - \bar{c})}{1 - V^{\beta}} \qquad \text{Equation 3.17}$$

Once the interface compositions are defined as described previously, established theory for diffusion-controlled growth can be applied to estimate the particle radius r as a function of time:

$$r = \alpha_3 \sqrt{D_M t} \text{ with } \alpha_3 \approx \sqrt{2 \frac{\bar{c} - c^{\alpha\beta}}{c^{\beta\alpha} - \bar{c}}} \qquad \text{Equation 3.18}$$

where α_3 is the three-dimensional parabolic rate constant and this equation can only be used in the absence of the knowledge of interfacial energy or the shape of the nucleus.

The driving force for nucleation must also be affected by the soft impingement. To deal with this, the extent of the reaction parameter Φ is defined as follows:

$$\Phi = \frac{V^{\beta}}{V^{\beta\alpha}} \text{ with } V^{\beta\alpha} = \frac{\bar{c} - c^{\alpha\beta}}{c^{\beta\alpha} - c^{\alpha\beta}} \qquad \text{Equation 3.19}$$

where V^{β} is the instantaneous fraction, and $V^{\beta\alpha}$ is the maximum fraction of a given phase. The function Φ ranges from 0 to 1 and represents the fraction of excess solute remaining in the matrix relative to the equilibrium composition of the precipitate. It is assumed that the driving force (ΔG_v in Equation 3.9) for the precipitation is linearly related to Φ:

$$\Delta G_v = (1-\Phi)\Delta G_{vo} \qquad \text{Equation 3.20}$$

where ΔG_v and ΔG_{vo} are the driving forces for precipitation at an arbitrary instant and at t=0, respectively.

3.4 TRANSFORMATION KINETICS

The evolution of volume fraction of the second phase during transformation can be described using the well known *Johnson-Mehl-Avrami-Kolmogorov* (*JMAK*) equation [95], which, for spherical particles and isothermal conditions, can be expressed as

$$V_v = 1 - \exp\left(-\frac{1}{3}\pi \dot{N} G_r^3 t^4\right) \qquad \text{Equation 3.21}$$

where $\dot{N}$ is the nucleation rate, G_r is the growth rate and t is time. Equation 3.17 above is for the special case of homogeneous nucleation. However, most nucleation in steels occurs heterogeneously, for instance, with the possibility of nucleation on a grain boundary that may be higher than that on other nucleation sites. There are three types of nucleation sites on grain boundaries for the nucleation to take place: planes, edges and corners [100]. In practice, the volume fraction V_v of the second phase is determined as a function of time and this produces a very frequently found sigmoidal or S-shaped curve. A more general form of the *JMAK* equation usually used in practice, takes the form of:

$$V_v = 1 - \exp\left(-kt^n\right) \qquad \text{Equation 3.22}$$

where k is a rate constant, subsuming effects associated with nucleation and growth, and is usually empirically evaluated for each temperature, n is the time exponent, often called the Avrami exponent. For this equation to be valid, a plot of {*lnln [1/(1-V_v)]*} vs {*ln t*} should be linear with a slope n and intercept *ln k*. Table 5 shows the theoretical values of *n* and *k*.

Table 5. Values of n and k in the general form of Equation 3.19, S_{gb} is the area of grain boundary per unit volume, L_{gb} is the length of grain boundary edges per unit volume and N_c is the density of grain boundary corners. All nucleation on the grain boundaries is assumed to occur before growth [108].

Nucleation site	Time exponent, *n*	*k* – value
Homogeneous nucleation	4	$\frac{\pi}{3}\dot{N}G_r^3$
A plane on grain boundary	1	$2S_{gb}L_{gb}$
An edge on the grain boundary	2	$\pi L_{gb}G_r^2$
A corner on grain boundary	3	$\frac{4}{3}\pi N_c G_r^3$

3.5 OVERALL TRANSFORMATION KINETICS

The Johnson-Mehl-Avrami-Kolmogorov (*JMAK*) approach treats the precipitation kinetic problem as an overall kinetic theory. Robson and Bhadeshia developed a simultaneous precipitation reaction model by extending the classical *JMAK* concept of extended space to many phases [109]. Fujita and Bhadeshia improved that model to deal with carbide size and to account for the capillarity effect [100]. In their work, the *JMAK* theory has been applied to describe the kinetics of the single phase in a power plant steel, utilising MTDATA software to predict the driving forces.

3.5.1 THE ROBSON AND BHADESHIA MODEL

In a simple simultaneous reaction in which both β and θ precipitate at the same time from the parent α-phase, it is assumed that the nucleation and growth rate do not change with time and that the particles grow isotropically. If only β is formed, the untransformed α will contribute to the real volume of β. On average, a fraction

$[1 - (V_\beta + V_\theta)/V]$ of the extended volume will be in the previously untransformed material. It follows that the increase in real volume of β is given by the change in extended volume dV_β^e:

$$dV_\beta = \left(1 - \frac{V_\beta + V_\theta}{V}\right)dV_\beta^e \qquad \text{Equation 3.23}$$

and, similarly for θ

$$dV_\theta = \left(1 - \frac{V_\beta + V_\theta}{V}\right)dV_\theta^e \qquad \text{Equation 3.24}$$

In general, V_β is a complicated function of V_θ and it is not possible to analytically integrate these equations to find the relationship between the actual and extended volumes. However, in certain simple cases, it is possible to relate V_β to V_θ by multiplication with a suitable constant K:

$$V_\theta = KV_\beta \qquad \text{Equation 3.25}$$

Equations 3.20 and 3.21 can then be rewritten as:

$$dV_\beta = \left(1 - \frac{V_\beta + KV_\beta}{V}\right) dV_\beta^e \qquad \text{Equation 3.26}$$

$$dV_\beta = \left(1 - \frac{V_\theta + KV_\theta}{KV}\right) dV_\theta^e \qquad \text{Equation 3.27}$$

Accordingly, the final expressions of the volume fractions of β and θ phases are:

$$V_\beta = \left(\frac{1}{1+K}\right)\left\{1 - \exp\left[-\frac{1}{3}(1+K)\pi \dot{N}_\beta G_{r,\beta}^3 t^4\right]\right\} \qquad \text{Equation 3.28}$$

$$V_\theta = \left(\frac{K}{1+K}\right)\left\{1 - \exp\left[-\frac{1}{3}\left(\frac{1+K}{K}\right)\pi \dot{N}_\theta G_{r,\theta}^3 t^4\right]\right\} \qquad \text{Equation 3.29}$$

In practice, the multiple reactions found in most industrial steels have important complications not included in the model above. Precipitation reactions may affect each other by removing solute atoms from the matrix. Any change in the matrix composition must alter the nucleation and growth rates of the phases. Therefore, there are no simple constants linking the volume fraction of all the phases and a different approach is needed.

3.5.2 FUJITA AND BHADESHIA MODEL

The Robson and Bhadeshia model can be used to estimate the volume fraction of carbides but it would be useful also to treat particle sizes and coarsening after growth. This has been achieved by Fujita and Bhadeshia, who attempted to take better account of multicomponent diffusion and capillarity [100]. Given the small equilibrium volume fraction of carbides in most ferritic steels, they also relaxed the extended volume concept to permit particle sizes to be calculated approximately.

3.6 CAPILLARITY

The state of equilibrium between two phases changes with the curvature of the interface separating them. This is the well established Gibbs–Thompson capillary effect and is due to the curvature of the interface that then influences the change in equilibrium compositions at the particle/matrix boundary. The free energy change of the particle phase varies relatively sharply with a deviation from the stoichiometric composition so it can be assumed that the particle composition is insensitive to the curvature. However, the equilibrium composition of the matrix changes as follows [99,101,103,104,110]:

$$c_r^{\alpha\beta} = \left(1 + \frac{\gamma}{kT}\frac{\upsilon^{\beta}}{r}\frac{1-c^{\alpha\beta}}{c^{\beta\alpha}-c^{\alpha\beta}}\right)c^{\alpha\beta} \qquad \text{Equation 3.30}$$

where $c_r^{\alpha\beta}$ is the solute concentration in the α matrix that is in equilibrium with a spherical particle of β and r is the radius of curvature, which in this case also defines the instantaneous particle size. The term $c^{\alpha\beta} = c_r^{\alpha\beta}$ when $r = \infty$. The modified composition $c_r^{\alpha\beta}$ is, therefore, relatively easy to estimate for each particle. At some critical value where $r = r_c$ (where r_c is a critical radius) and $c_r^{\alpha\beta} = \bar{c}$, growth ceases and coarsening starts.

Note in particular in the case of the determination of the particle density measurements, that the number of particles per unit volume N_v first increases, as would be expected during the nucleation stage, but that soon thereafter it starts to decrease, as would be expected for the coarsening stage. This transition generally takes place after only a few minutes of annealing [111].

For a ternary alloy, capillarity is approximated by calculating the $\alpha / (\alpha + \beta)$ phase boundary on an isothermal section of the phase diagram, as a function of r, using Equation 3.30. Equation 3.30 is used to calculate $c_{r,C}^{\alpha\beta}$ and $c_{r,M}^{\alpha\beta}$ for a fixed value of interface radius of curvature r. The growth velocity can then be calculated using the curvature-modified phase boundary. Embryo particles that are smaller than the size of the critical nucleus obviously cannot grow and will dissolve again. Nucleation occurs statistically by random fluctuations in composition so that the growth part in the computational scheme must start beyond the nucleation stage. Particles nucleate at different times during the course of the reaction, giving rise to a distribution of sizes.

At any given stage of precipitation, the smaller particles will grow at a slower rate than a larger particle because the capillary effect reduces the supersaturation at the interface for small particles. Capillarity has the consequence that large particles have lower solute concentrations at the interface $c_r^{\alpha\beta}$ than small particles [112]. This drives coarsening, which becomes a natural consequence of the precipitation theory, since changes including the dissolution of particles, continue to happen as long as there are solute concentration gradients.

3.7 DISSOLUTION OF THE METASTABLE PHASE

With soft-impingement being considered, the mean solute concentration within the matrix alone decreases as the reaction proceeds. Each precipitating phase will consume or reject atomic species into the untransformed matrix, whose subsequent transformation behaviour will be altered. Consider the precipitation of β and γ from an α ferrite matrix, which initially has a uniform composition. Schematic composition profiles are shown in the earlier Figure 3.9 (a) of how the distribution of the solute might change during precipitation at the intermediate stage when both the metastable β phase and the equilibrium γ phase are precipitating in the matrix of α simultaneously. Also from Figure 3.9 (b) when the solute concentration in the matrix reaches equilibrium with β; precipitation of β has been completed and as γ precipitates further removing solute, β will start to dissolve. For the situation illustrated, the maximum fraction $V^{\beta\alpha}$, of each phase is given by a lever rule (see Equation 3.19).

3.8 PARTICLE COARSENING

3.8.1 DIFFUSION CONTROLLED COARSENING OF THE PARTICLES WITHIN MATRIX

The coarsening of particles occurs (even though the transformation is said to be completed) when there is no significant change in the precipitate volume fraction over a period of time. Note that it is traditional to separate transformation growth and coarsening but the two processes are in fact both fulfilled with capillarity effects. The coarsening rate of precipitates can be calculated using the classical theory of the Ostwald ripening equation that is due to Lifshitz and Slyozov [113] and Wagner [114] and is often called *LSW* coarsening. The *LSW* coarsening rate equation for diffusion controlled coarsening is given by:

$$r^n - r_o^n = \frac{8\gamma \upsilon^{\beta} D c^{\alpha\beta}}{9RT} t \qquad \text{Equation 3.31}$$

where r is the average particle radius, r_0 the initial average particle radius (a fictitious value as no particles exist at t = 0), γ is the interfacial energy, D is the diffusion coefficient of the rate controlling species, υ^{β} is the molar volume of the phase β, $c^{\alpha\beta}$ is the equilibrium solute concentration in the α matrix at which $r \rightarrow \infty$, R is the gas constant, T is the absolute temperature, t is the holding time at the isothermal heat treatment temperature. For intragranular particles it can be assumed that the coarsening of the particles is controlled by bulk diffusion, therefore $n = 3$.

3.8.2 DIFFUSION CONTROLLED COARSENING OF THE PARTICLES ON GRAIN BOUNDARY

The above Equation 3.31 is only valid for diffusion controlled coarsening of the particles within the matrix. But there are some scenarios whereby the particles in the grain boundaries coarsen through the diffusion of the solute atoms down the grain boundary. Here, there is a two dimensional diffusion down the grain boundary from the smaller particle to the larger particle. The theory is basically the same as for matrix diffusion and the coarsening rate equation changes to:

$$r^4 - r_o^4 = \frac{K_1 \gamma \upsilon^{\beta} D_{gb} c^{\alpha\beta} \delta_{gb}}{kT} t \qquad \text{Equation 3.32}$$

where K_1 is a constant, D_{gb} = diffusion coefficient down the grain boundary, δ_{gb} = width of the grain boundary and t = time at temperature. The above coarsening Equation 3.32 is also only fully valid if all of the precipitates were situated on grain boundaries and this, of course, is quite difficult to achieve. It may be approximated, however, by introducing a subgrain structure into the matrix in which, very often, most of the particles are “captured” by the subgrain boundaries. In the work by Kostka et al.[115] and Mukherjee et al.[116], the authors observed that the grain boundary carbides coarsen faster than the matrix carbides.

3.8.3 DIFFUSION CONTROLLED COARSENING OF THE PARTICLES ON SUBGRAIN BOUNDARIES

This mechanism may be found in cases where high temperature creep at a service temperature takes place and all of the precipitates become entangled and are, in fact, interconnected by dislocations in subgrain boundaries:

$$r^5 - r_o^5 = \frac{K_1 \gamma \upsilon^\beta D_{disl} c^{\alpha\beta} \delta_{disl} N'}{kT} t \qquad \text{Equation 3.33}$$

where K_1 = constant, δ_{disl} = effective diameter of a dislocation, N' = number of dislocations that meet each particle and D_{disl} = diffusion coefficient down a dislocation. Direct experimental evidence of this power law has not been obtained although many cases of direct and indirect evidence do exist that precipitates that are situated on subgrain boundaries, grow at a faster rate than others.

3.9 SUMMARY

Many researchers have modelled and calculated the values for the interfacial energy of the M_6C carbide and Laves phase in Fe–C–Nb systems and have estimated them to be 0.286 Jm^{-2} [103] and 0.331 Jm^{-2} [77,117,118], respectively. From these results, because of a complex unit structure of the Laves phase, its interfacial energy seems to be larger than that of M_6C carbide as would be expected. In other work also done on the Fe–C–Nb systems by Sim et al. [3], they have assumed a much higher value of 1.0 Jm^{-2} for the Fe_2Nb Laves phase because of its incoherency with the α-matrix.

Fujita et al., [99] using the *MTDATA* thermodynamic software, have modelled the precipitation kinetics in the Fe-Nb-C system for a 9Cr-0.8Nb steel at 950°C. The precipitation sequence was found to be as follows:

$$\alpha \rightarrow \alpha + Nb(C,N) + Fe_2Nb + Fe_3Nb_3C \rightarrow \alpha + NbN + Fe_3Nb_3C$$

and this shows that in this steel the equilibrium phases are NbN and Fe_3Nb_3C, and the Laves phase is a meta-stable phase. Figure 3.10 shows the comparison between the experimental and the calculated phases in obtaining the precipitation sequencing.

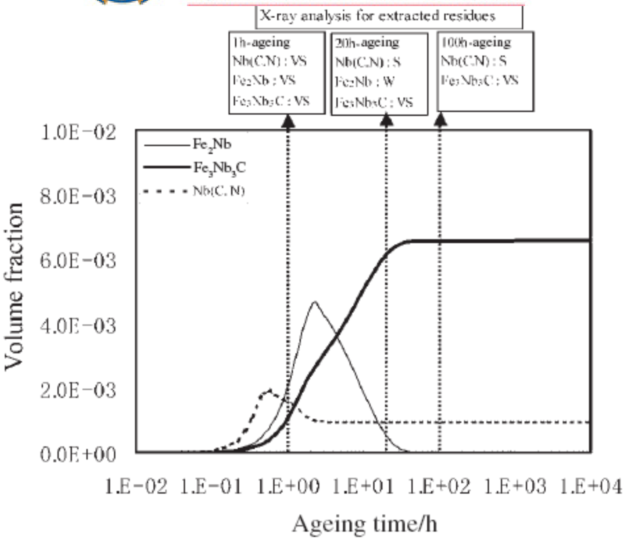

Figure 3.10. The kinetics of the precipitation sequence in 9Cr-0.8Nb ferritic stainless steel [101].

CHAPTER FOUR

EXPERIMENTAL PROCEDURES

4.1 MATERIALS

Type 441 ferritic stainless steel which is a niobium and titanium dual stabilised steel, was studied in this work. The main emphasis was on understanding the formation of the intermetallic Laves phase and its impact on the toughness of this steel. Steels A and B were supplied from Columbus Stainless in the hot rolled condition with Steel A having not received any water cooling on the hot mill's run out table due to a system failure. This coil was found to be too brittle to be processed further and was, therefore, made available for this study while specimens of Steel B were as processed normally with adequate laminar flow cooling after hot rolling.

The effect of the alloy's chemical composition was also investigated through two experimental alloys that were within the type 441 ferritic stainless steel's specification. The first experimental alloy identified as Steel C, i.e. a Nb–Ti alloy, is similar to Steel A but has a higher carbon content (almost double that of Steel A's 0.012%C) and lower Nb content of only 0.36%Nb if compared to the Steel A's Nb-content of 0.44%. The second experimental alloy identified as Steel D, is a Nb–Ti–Mo alloy very similar to Steel A but contains an additional ~0.5 wt.% Mo. The effect of even higher molybdenum (Mo) additions was studied on AISI type 444 ferritic stainless steel, that is Steel E, which is a high Mo containing steel with the nominal composition of 18Cr–2Mo; this alloy is also a dual stabilised ferritic steel with a slightly lower content of niobium and titanium. Table 4.1 shows the chemical compositions of the alloys used in the present study while Figure 4.1 shows the detailed flow chart of the research plan to study the nucleation and kinetic models for the Laves phase precipitation and its effects on the impact toughness of the AISI type 441 stainless steel.

Table 4.1. Chemical composition (in %wt) of ferritic stainless steel studied in this work.

Elements	Supplied by Columbus		Hot rolled experimental alloys		
	Steel A	Steel B	Steel C	Steel D	Steel E
	441 SS[†]	441 SS[‡]	Nb-Ti	Nb-Ti-Mo	444 SS[§]
C	0.012	0.015	0.023	0.012	0.014
Mn	0.51	0.54	0.46	0.35	0.45
Co	0.03	0.02			0.02
Cr	17.89	17.9	17.9	17.6	18.3
B	0.0004	0.0006			0.0006
V	0.12	0.14			0.12
S	0.001	0.002	0.0073	0.0018	0.003
Si	0.5		0.33	0.31	0.47
Ti	0.153	0.149	0.171	0.171	0.106
Ni	0.19	0.19	0.13	0.12	0.15
N	0.0085	0.021	0.024	0.026	0.016
Al	0.009	0.009	0.011	0.013	0.01
P	0.025	0.023	0.024	0.032	0.024
Cu	0.08	0.09	0.07	0.06	0.12
Nb	0.444	0.445	0.36	0.39	0.251
O	0.0076				
Mo		0.008	< 0.01	0.54	1.942

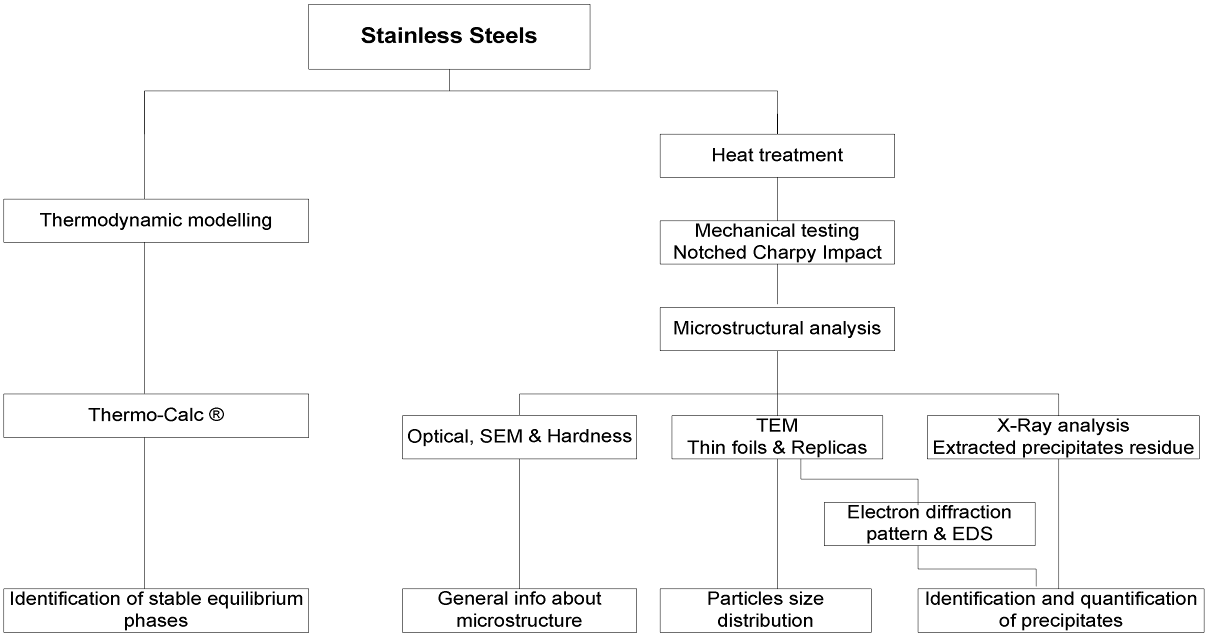

Figure 4.1. Experimental plan.

[†] Columbus Stainless MPO Number 3533603- failed during production
[‡] Columbus Stainless MPO Number 3658671 – didn't fail
[§] Columbus Stainless MPO Number 3631171

4.2 THERMODYNAMIC MODELLING

Modelling precipitation in AISI type 441 ferritic stainless steel requires knowledge of both thermodynamic and kinetic parameters for a variety of possible phases. To obtain these parameters, the computer package Thermo-Calc® version Q (TCFE3 database [119]) thermodynamic software was used to make these thermodynamic calculations. All of these experimental alloys were initially modelled to determine the precipitation temperatures of the phases present, in particular the Laves phase. This has assisted in designing a suitable heat treatment for this alloy without causing major grain growth. A detailed modelling procedure is given in Chapter 5.

4.3 HEAT TREATMENTS

The results obtained from the Thermo-Calc® modelling were used as guidance for designing an appropriate heat treatment for the alloys. The effect of the Laves phase embrittlement was studied by subjecting the specimens to different heat treatments in an inert argon atmosphere.

4.3.1 LAVES PHASE DISSOLUTION/PRECIPITATION TEMPERATURES

The first step was to determine the annealing temperatures at which the Laves phase dissolves and its impact on the mechanical properties of the steel during its re-precipitation. Most of the annealing treatments were designed around the solvus temperature of the Laves phase, which is within the range of 780 to 950 °C depending on the composition of the alloy, as reported in the literature and calculated by Thermo-Calc® predictions. Steel A was used for this part of the study and the specimens were annealed within the temperature range of 600 to 1100 °C for 30 min. followed by water quenching.

4.3.2 HEAT TREATMENT FOR THE EMBRITTLING EFFECT

Heat treatments for embrittlement of the specimens from AISI type 441: Steel A were performed on:

(1) Charpy impact specimens that had first been solution annealed at 950 °C for 1hr to dissolve the Laves phase and then quenched in water. These specimens were then reheated within the temperature range of 600 to 900°C for 30 min to re-precipitate the Laves phase and were then water quenched, see Figure 4.2. From these specimens the effect of the Laves phase re-

precipitation at different temperatures on the upper – shelf energy and DBTT in Steel A could be studied.

(2) A second set of experiments was used to determine the effect of cooling rate from typical hot rolling temperatures on the embrittlement of these materials through the application of programmed linear cooling rates on the specimens from the solution treating temperature. The programmed cooling rates were applied to specimens in a Gleeble® 1500D Thermal Simulator using subsize Charpy specimens that were annealed at 850 and 950 °C respectively for 5 minutes in an inert argon atmosphere followed directly by forced cooling with helium at different linear cooling rates ranging from 1 to 60 °C/sec, see Figure 4.3.

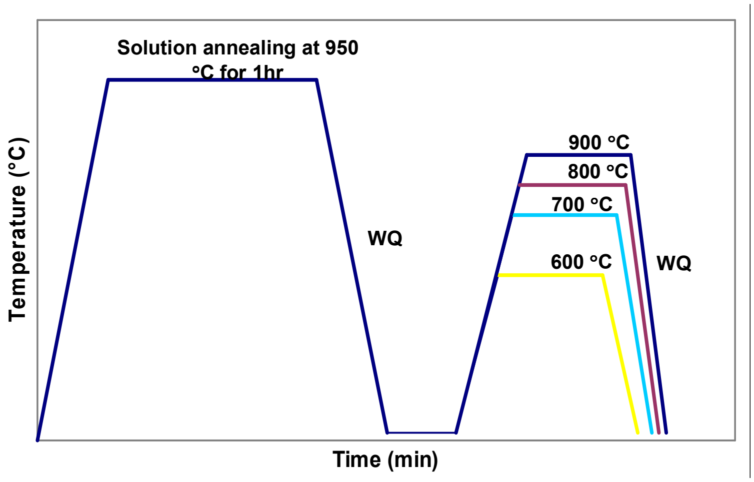

Figure 4.2. Embrittlement through reheating to determine the effect of the Laves phase re-precipitation on the DBTT and upper shelf energy of steel A.

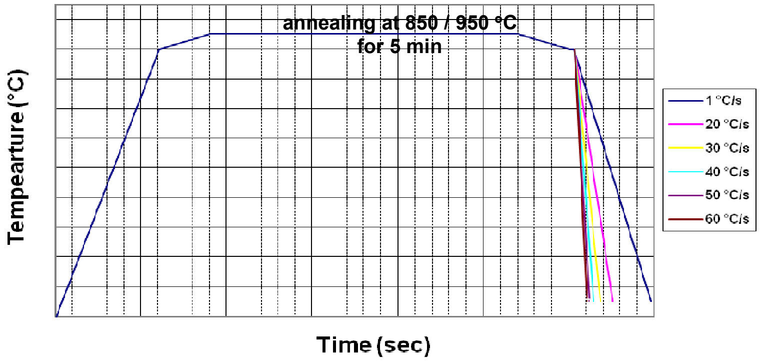

Figure 4.3. Embrittlement through cooling to determine the effect of the Laves phase re-precipitation on the Charpy impact toughness.

4.3.3 HOT-ROLLING OF EXPERIMENTAL ALLOYS

The experimental alloys C and D were prepared by Mintek in a 5 kg vacuum induction melting furnace (VIM) using scrap from Steel A as base scrap material. The as-cast alloys were homogenised in an argon atmosphere at 1200 °C and hot forged to bars of about 30 mm thick. Steel E was supplied by Columbus Stainless as a 28 mm thick hot-band material. Subsequently, these three steels, i.e. C, D and E were solution treated at 1200 °C for 1hr followed by hot rolling to a final thickness gauge of 5.5 to 6.0 mm and quenched in water. The average last pass temperature before quenching was approximately 950°C, which is above the calculated Laves phase formation temperature.

4.3.4 LAVES PHASE KINETIC STUDY

The study of the Laves phase kinetics was conducted using a small tubular furnace that provided a suitable small temperature gradient, as shown in Figure 4.4. Both the furnace and specimen temperature were monitored and controlled by the data logger model DT500 dataTaker® and PID temperature controller, respectively. A type K thermocouple was spot welded to the specimens to monitor the annealing temperature inside the furnace. Figure 4.5 shows the time- temperature profile of the specimen inside the small tubular furnace. Note that the start of the annealing time was considered from the point whereby the specimen had reached a desired temperature and had stabilised. After annealing for a required period of 1 – 1000 minutes, the specimens were subsequently quenched in water. These specimens where then subjected to the Charpy impact test and also the precipitates were extracted electrolytically from them, see Section 4.6.1.

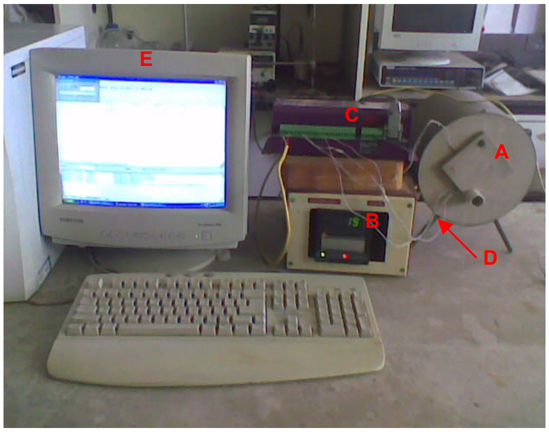

Figure 4.4. The furnace used for the precipitation kinetic study. (A) tube furnace; (B) temperature controller; (d) data logger; (D) type k thermocouple; (E) recording computer.

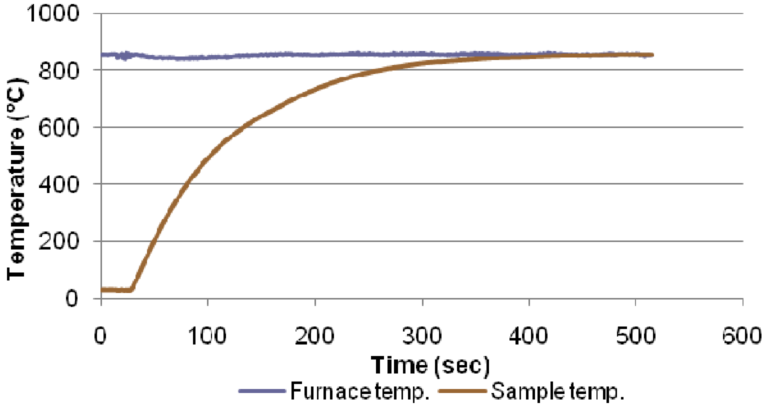

Figure 4.5. The temperature gradient of the Charpy impact specimen inside the furnace.

4.4 MECHANICAL TESTING

4.4.1 TENSILE TESTS

Tensile tests were carried out at a cross head speed of 5 mm/min at room temperature using two subsized specimens prepared according to the ASTM E8[**] standard for each measurement. The longitudinal axes of the specimens were parallel to the rolling direction of the plate throughout. The schematic drawing of the tensile specimen and its dimensions are shown in Figure 4.6 and Table 4.2, respectively.

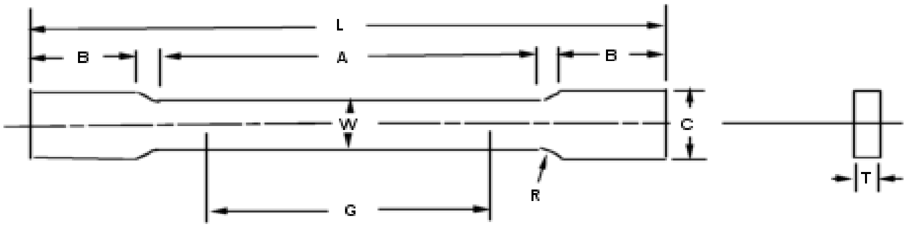

Figure 4.6. Schematic diagram of the subsize tensile test specimen.

Table 4.2. The actual dimensions for the subsize tensile test specimen.

	Parameters	Dimensions (mm)
G	Gauge length	25
W	Width	6
T	Thickness	5
R	Radius of fillet	6
L	Overall length	100
A	Length of a reduced section	32
B	Length of grip section	32
C	Width of grip section	10

[**] ASTM E8 – 08: Standard Test Methods for Tension Testing of Metallic Materials

4.4.2 NOTCHED CHARPY IMPACT TEST

Charpy impact test values were obtained as an average from three subsized specimens of 5 x 10x 55 mm^3 prepared according to the ASTM E23[††] standard. A standard 2mm V-notch was made in the specimens after the heat treatment to avoid oxidation effects from the heat treatment at the notch tip. The longitudinal axes of the specimens were parallel to the rolling direction of the plates throughout the study.

The specimens for DBTT Charpy tests were prepared by immersing them in different liquid media to obtain the desired test temperature. For the temperatures higher than 25 °C, heated water controlled by a thermal regulator was used. To achieve a 0 °C testing temperature, icy water was used and below 0 °C, a mixture of dry ice[‡‡] and ethanol or liquid nitrogen[§§] and ethanol were used, depending on the desired lower temperature one wants to reach. The mixtures were prepared inside a thermo flask and different mixing ratios of dry ice to ethanol or liquid nitrogen to ethanol were used to achieve the desired testing temperature. Once the testing temperature was reached the specimens were allowed to settle for about 5 minutes in order to normalise the temperatures before they were subjected to immediate Charpy impact testing.

4.4.3 HARDNESS TESTS

Vickers microhardness measurements were made using a load of 30 kgf to give a relatively large indentation to offset any effects due to localised variation in structure. The average of at least five readings was taken for each result.

4.5 MICROANALYSIS OF SPECIMENS

Several types of microscopy were performed to locate, identify, and quantify the microstructural components in the steels after their different treatments, ranging from optical microscopy, scanning electron microscopy to transmission electron microscopy. Analysis of small particles can often prove to be difficult but through a combination of these different techniques coupled with energy dispersive spectroscopy, one can reasonably gain insight into the precipitation behaviour.

[††] ASTM E23 – 02a: Standard Test Methods for Notched Bar Impact Testing of Metallic Materials
[‡‡] Dry ice sublimes at -78.5 °C
[§§] Liquid nitrogen boils at -196 °C

4.5.1 OPTICAL MICROSCOPY

The metallographic specimens were prepared by standard metallographic techniques on a polishing system to a 3μm finish. The specimens were then etched electrolytically in 60% nitric acid in water at a potential of 1.5 V dc for a period of 30 to 120 sec., to optimise the phase contrast and grain size effects. Microstructural analysis was carried out using Olympus PGM and Nikon Eclipse ME600 optical microscopes, both equipped with Analysis™ image software. The grain size was determined using the linear intercept method in accordance to the ASTM E 112 - 96[***] standard.

4.5.2 TRANSMISSION ELECTRON MICROSCOPY (TEM)

TEM observations were carried out using a Philips CM 200 TEM operating at an accelerating voltage of 160kV and a JOEL JEM – 2100F field emission TEM operating at an accelerating voltage of 200kV.

4.5.2.1 PREPARATION OF TEM SPECIMENS

Two types of specimens were examined using TEM: thin foils and carbon extraction replicas. From these, the types of precipitates were identified using energy dispersive X-ray analysis spectroscopy (EDS) and small angle electron diffraction patterns (SAED).

Thin foils were cut from the bulk materials as 3mm diameter discs of about 1 mm thickness using an electrospark wire cutting device. After cutting, the specimens were attached to a large steel block using hot wax. These specimens were mechanically ground from both sides with silicon carbide paper to less than 70 μm thickness before the wax was dissolved in acetone to release the thinned specimens. Electropolishing was conducted until perforation of the disc occurred using a twin jet electropolisher in a 10 % perchloric acid in 90% acetic acid solution at room temperature at a voltage of 55 dc. Finally, the specimens were cleaned using a four step ethanol cleaning process to remove all residues from the specimens.

Carbon replica specimens were firstly mounted as for metallographic examination and etched the same way. A carbon film was applied by vacuum evaporating carbon onto the etched specimen surface. The carbon film was electrolytically detached in a solution of 5 vol.% hydrochloric acid in methanol at a constant potential of 1.5 V dc after which

---

[***] ASTM E112 – 96: Standard Test Method for Determining Average Grain Size

the replicas were washed using ethanol and then floated off onto distilled water, from where the replicas could be collected on 3 mm diameter copper grids.

4.5.3 SCANNING ELECTRON MICROSCOPY (SEM)

The scanning electron microscopy (SEM) investigations were carried out on a Jeol JSM – 6300 and also on a high resolution field emission scanning microscope model Joel JSM – 6000F (SEM). The accelerating voltage was set at 15 kV and the probe current was 7 x 10^{-9} A in both electron microscopes. Both the thin foils and the metallographic specimens were used for the particle's analyses. The advantages of using TEM thin foils in a SEM is that: (1) the specimens are very clean which helps to resolve small particles; and (2) the electropolishing tends to leave fine precipitates on top of the surface, facilitating a good image and analysis of the particles.

4.6 IDENTIFICATION OF PRECIPITATES

4.6.1 XRD STUDY

XRD analysis was carried out on a PANalytical X'Pert Pro powder diffractometer with X'Celerator detector and variable divergence and receiving slits equipped with an Fe-filtered Co-K_α (λ = 1.789 Å) anode as a source of X-rays. The scanning was carried out at an angular range of 20 to 90 (°2 Theta) employing a step size of 0.017° 2 Theta. The generator setting was at 50 mA and 35 kV.

4.6.1.1 SPECIMEN PREPARATION

X-ray analysis on a larger representative volume of each steel, not only supports the TEM observations from small volumes of materials, but also provides information on the quantity of each phase with a reasonably good accuracy. Electrochemically extracted residues of second phase particles were examined by X-ray powder diffraction to identify the types and volumes of precipitates formed in these alloys. To obtain residues, the precipitates were extracted by means of potentiostatic electrolysis at a constant potential chosen between 100 and 200 mV against a silver chloride electrode in a solution of 10 vol.% acetyl acetone and 1 vol.% tetramethyl ammonium chloride in methanol (TMAC), in which only the iron matrix dissolves [8], leaving a mixture of the second phases behind as a powder residue. Also, the use of 60% nitric acid in water at a potential of 5 V dc to electrolytically extract the particles was found effective in extracting larger volumes of precipitate residue in a short space of time. The residue was vacuum suction filtered using a sub-micron glass filter paper (≤ 0.7 μm) to trap the fine particles with the filter paper pre-weighed to account for the very fine precipitates that might remain trapped in it during the filtration process. The extracted residues where rinsed with ethanol, dried and weighed to obtain the weight fraction from the previously weighed steel specimen.

4.6.1.2 ANALYSIS

Phase identification was carried out using X'Pert Highscore Plus software, using an integrated interface and fast retrieval software for the *International Centre for Diffraction Data* (ICDD) reference database, flat file format and relational databases. Any number of user reference patterns that have been modified can be added into the reference databases.

Figure 4.7 shows the calculations for user reference patterns for the phases that were expected to be present in these steels. These patterns were generated using the PowderCell 2.4 software and can be read in ICDD structure files by exporting them in a variety of forms into the X'Pert Highscore Plus software. The generation of these patterns requires the knowledge of the symmetry (translational and space group), unit cell data and atomic position parameters, see **Appendix A.**

The complexity in quantification of the carbides and nitrides expected in these steels arises from the structural phases in which these carbides and or nitrides may be formed, i.e. whether the carbides are present as NbC/ TiC and /or NbN / TiN or Nb(C,N) or Ti(C,N) or as (Ti,Nb)(C,N). All of these phases have similar peaks, but the differences arise from the peak's position of each phase, see Figure 4.7. From this figure it can be seen that there is not much of a difference in the peak's position for the carbide and nitride phases of niobium or titanium, but the combination of niobium and titanium, as in (Ti,Nb)(C,N), makes a significant difference in the positions of the peaks.

Note that, in Figure 4.7 and Figure 4.8, both figures show the simulated phase patterns and these are, therefore, not the actual results. PowderCell predictions were based on the assumption of a pure specimen that has equal amounts of phases. Therefore, the results from the precipitate residues will be slightly different from these, and they required a further refinement using Autoquan/BGMN software to obtain an accurate volume fraction for each phase.

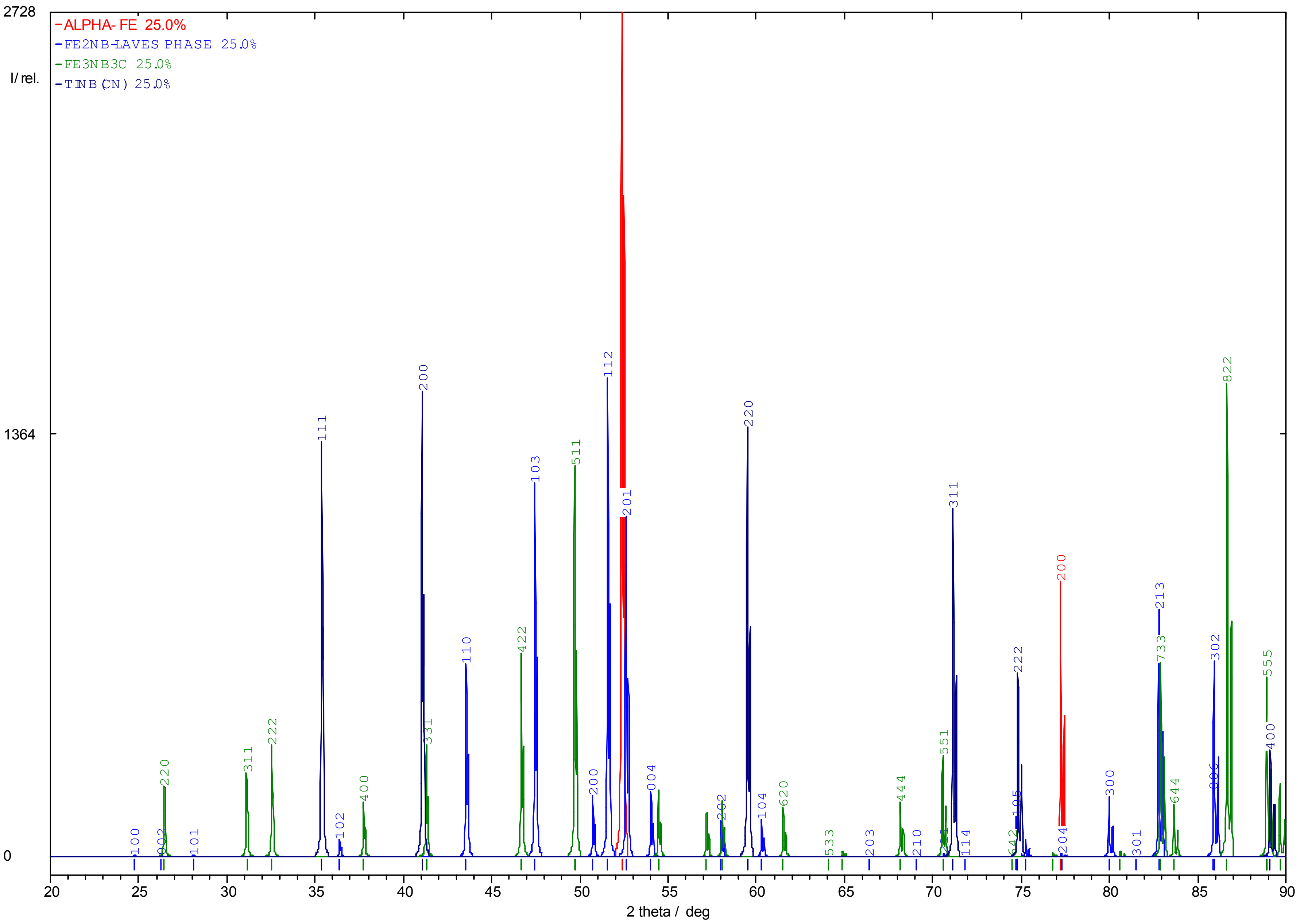

Figure 4.7. The XRD powder pattern of the phases that were expected to be present in type 441 stainless steel as generated using a PowderCell software.

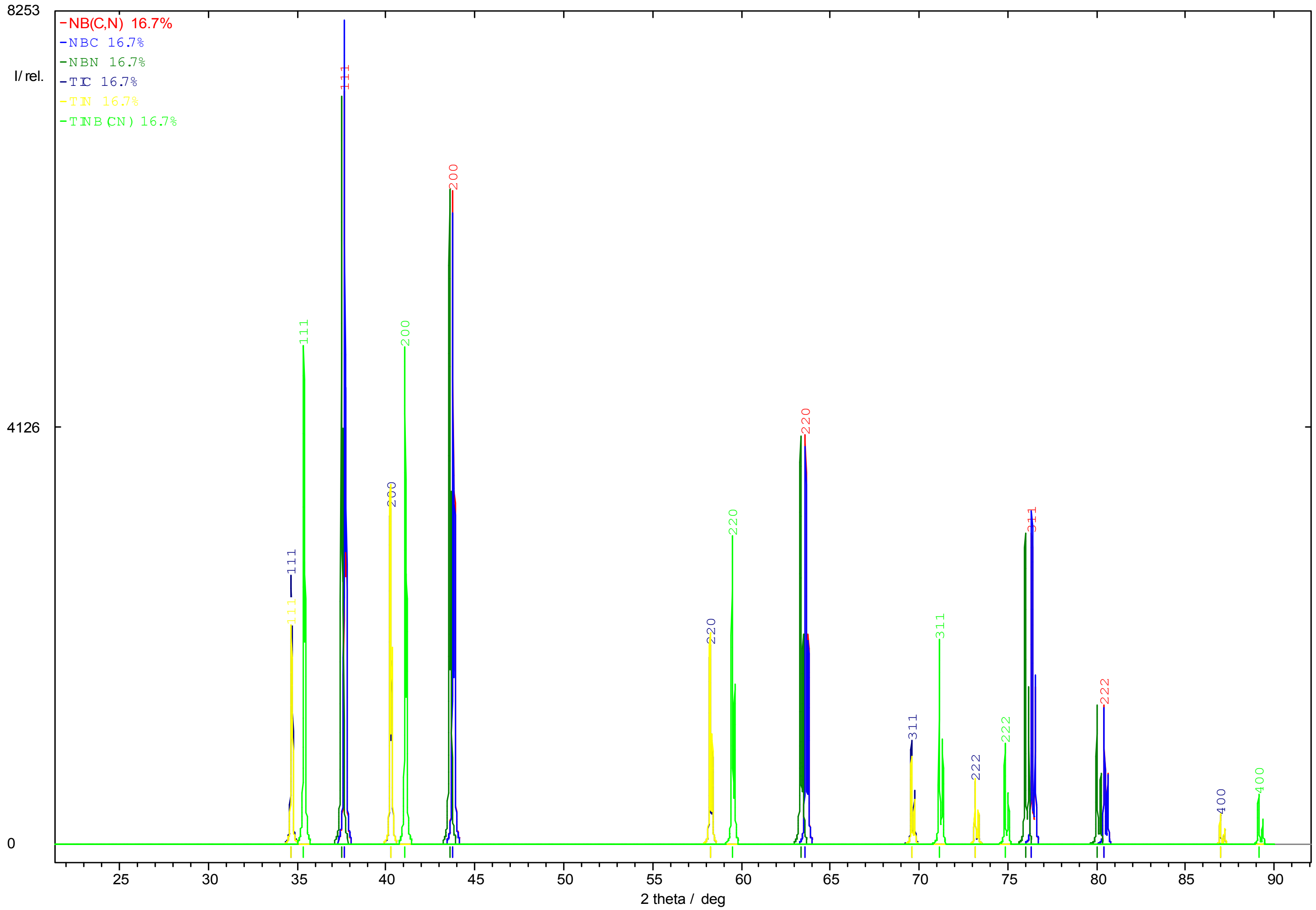

Figure 4.8. The XRD powder pattern showing the peak's positions of the carbide and nitrides of titanium and niobium. Notice the position of the (Ti,Nb)(C,N).

Quantification of the various phases' weight fractions in the powder residue was carried using Autoquan/BGMN software (GE Inspection Technologies) employing a Rietveld refinement approach [120,121]. The quantification was done using the phases' reference data from the ICDD databases or from the user reference database. A typical XRD spectrum from the analysed powder residue after quantification is shown in Figure 4.9. Notice how good is the residual differences (i.e. bottom spectrum) between the calculated and the measured spectrums.

The quantified results from the X-ray analysis are given as weight fraction, therefore for the volume fraction calculation; the densities for each phase are needed. Table 4.3 shows the densities of all phases present in these alloys [122].

Table 4.3. The density of the phase that were used in the quantifications.

Phase	Density (g/cm^3)
Fe_2Nb	8.63
Fe_3Nb_3C	8.44
α-Fe	7.87
Nb,TiC	6.39
NbC	7.80
NbN	8.40
TiC,N	7.82
TiC	4.94
TiN	4.83

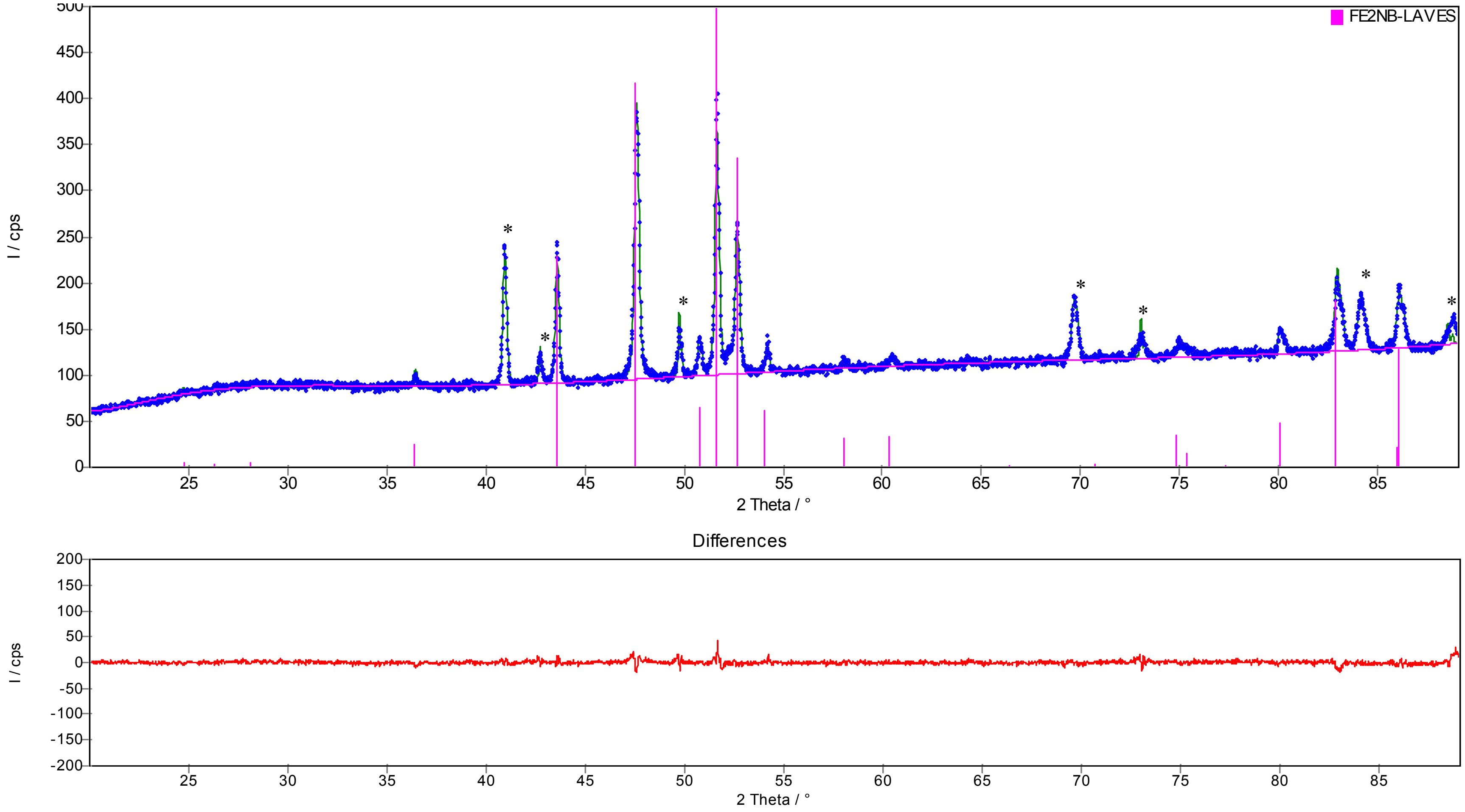

Figure 4.9. A typical XRD scan of the precipitate's residue from Steel A showing the presence of the Laves phase peaks (indicated by the lines in the top figure). The remaining peaks are the carbides and nitrides, indicated by (∗). Note the good residual difference between the calculated and the measured spectrum as is shown by the spectrum below.

4.6.2 ELECTRON DIFFRACTION PATTERNS

Selected area electron diffraction (SAED) patterns of second phases using carbon extraction replicas, is a reliable method to identify unknown precipitates because there is no interference from the matrix. The intended precipitates are chosen using a selected area aperture and a corresponding diffraction pattern is obtained. Figure 4.10 shows the schematic drawing of the geometry of diffraction.

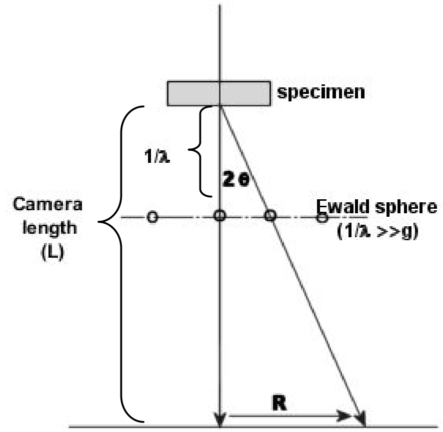

Figure 4.10. The single crystal electron diffraction pattern

R_{hkl} is the distance between the transmitted spot and the diffracted spot from the *hkl* plane. θ_B is the Bragg angle corresponding to the *hkl* plane and L is the camera length. The relationship between these parameters can be described as follows [123,124]:

$$R_{hkl}d_{hkl} = L\lambda \qquad \text{Equation 4.1}$$

where d_{hkl} is the calculated spacing of *hkl* planes and λ is wavelength given by:

$$\lambda = \frac{h}{\sqrt{2meV}}\ \text{Å} \qquad \text{Equation 4.2}$$

$$\lambda = \frac{12.236}{\sqrt{V}}\text{Å} \qquad \text{Equation 4.3}$$

Electrons accelerated by a potential difference of V volts have a kinetic energy of $\frac{1}{2}mv^2$, where:

$$\tfrac{1}{2}mv^2 = Ve \qquad \text{Equation 4.4}$$

e being the standard for an electron charge.

The wavelength λ is associated with an electron of mass m grams travelling with a velocity ν cm/sec. A relative correction is needed for the actual conditions involving the voltages used, so that the actual formula is slightly more complicated, as follows:

$$\lambda = \frac{12.236}{\sqrt{[V(1+0.9788x10^{-6}V)]}} \text{Å} \qquad \text{Equation 4.5}$$

The camera constant $(L\lambda)$ was calibrated using a gold film when the electron microscope is operating at 160 kV. From equation 4.5 above, the wavelength (λ) was calculated as 2.84 x 10^{-12} m, and the camera constant $(L\lambda)$ was determined to be 2.70 x 10^{-12} m^2 when using a camera length L of 950 mm.

4.7 THE ORIENTATION RELATIONSHIP BETWEEN THE LAVES PHASE AND THE MATRIX

The habit plane and the morphology of the Laves phase precipitates were determined from the thin foil specimens. For simplicity, because of a very small size of the precipitates to be analysed without interference from the matrix, the orientation relationship was determined firstly, by obtaining the pattern from the adjacent matrix followed by the pattern from both the matrix and the precipitates. From the two patterns, one is able to determine the pattern of the precipitate by correlating the two patterns.

CHAPTER FIVE

THERMODYNAMIC MODELLING

5.1 INTRODUCTION

Modelling precipitation in a ferritic stainless steel AISI type 441, requires knowledge of both thermodynamic and kinetic parameters for a variety of possible phases. To obtain these parameters, experimental data are required. The prerequisite thermodynamic information for modelling consists of:

1. the stable phases corresponding to the annealing temperature;
2. the phase fractions corresponding to the annealing temperature;
3. the relative phase stabilities; and
4. the equilibrium chemical compositions of possible phases.

The use of the computer package such as Thermo-Calc® version Q (TCFE3 database [125]) thermodynamic software makes these thermodynamic calculations possible.

5.2 DESCRIPTION OF THERMO-CALC® SOFTWARE

Thermo-Calc® software is a powerful and flexible software package that can perform various kinds of equilibrium thermodynamic and phase diagram calculations by minimising the total Gibbs energy of the system specified [126]. It can handle complex problems involving the interaction of many elements and phases. It is specially designed for the systems and phases that exhibit highly non-ideal behaviour [127,128].

Without an accurate and validated database, any thermodynamic software is useless and misleading. Therefore, a high quality thermodynamic database is essential for conducting reliable thermochemical calculations and simulations. The TCFE3 TCS Steels/Fe-alloys database which covers a complete and critical assessment of binary and some ternary systems as well as the iron rich corner of some higher order systems, was employed in these calculations. It was pointed out that with TCFE1 TCS Steels/Fe-alloys database (version 1.1), data for intermetallics such as σ, μ and Laves phases are less reliable and there is nothing more being said about improvements to the TCFE2 and TCFE3 databases for these phases [129]. This might be the reason why the calculations show the presence of the σ-phase in AISI type 441 stainless steel, whereas it is not expected to be formed in practice in this alloy. Also the recommended temperature range in using the database is from 700 to 2000 °C for the TCFE3. Calculations slightly outside these limits may give reasonable results but it requires experience and skill to correctly extrapolate data and interpret the calculational results. This is particularly so at temperatures of 500 °C and lower where thermodynamic equilibrium is highly unlikely in industrial processes due to slow diffusion. A lower limit of 600°C was, therefore, adopted in the thermodynamic modelling for this study. Note the use of the following phase names in the database; the number symbol # is used to denote different composition sets of the same phase, Table 5.1.

Table 5.1. The phase names as used in the TCFE3 Steels/Fe-alloys database.

Phase	database
Austenite	FCC_A1#1
Ferrite	BCC_A2
M(C,N)	FCC_A1#2

5.3 EXPERIMENTAL ALLOYS

The purpose of this research is to study the precipitation behaviour of the Laves phase in the ferritic stainless steel AISI type 441. The ternary and quaternary systems of the Fe-Nb-Ti and Fe-Nb-Ti-Mo were therefore, chosen, the latter being more of an experimental alloy. The experimental alloys' compositions were chosen within and outside the recommended Columbus Stainless composition specification for the ferritic stainless steel AISI type 441 (see Steel A & B[†††] in Table 4.1) in order to determine the effect of the Nb, Ti and Mo on the Laves phase formation and its embrittlement effect. Thermo–Calc® software was used in the design of these experimental alloys, with the main emphasis on determining the effect of composition change on the volume fraction and solvus temperature of the Laves phase. The following criteria were used in designing these alloys:

1. lowering the Nb content while keeping Ti content constant;
2. keeping both the Nb and Ti constant and adding 0.5% Mo; and
3. increasing the Nb content to 0.6 wt% and adding about 0.25%Mo.

[†††] Note that, both steels were supplied by Columbus Stainless for a research purposes. Steel A is the rejected material because it was brittle for further processing, while Steel B was acceptable.

A summary of the Thermo–Calc® predictions is given in Table 5.3, in which the results were obtained in a similar manner as those that are shown in the following sections. Note that a Mo addition increases both the volume fraction and the solvus temperature of the Laves phase precipitates, whilst reducing the Nb content lowers both the volume fraction and the solvus temperature of the Laves phase in the alloy. From this prediction it was then decided to replace 0.6Nb – 0.15Ti – 0.25Mo with a ferritic stainless steel AISI type 444, and cast the other two experimental alloys using AISI type 441 as basis from scrap metal. The chemical composition of the experimental alloys that were physically tested in this study are shown in Table 4.1.

Table 5.2. Chemical composition (in %wt) of the ferritic stainless steels studied.

Elements	Supplied by Columbus		Hot rolled experimental alloys		
	Steel A 441 SS[‡‡‡]	Steel B 441 SS[§§§]	Steel C Nb-Ti	Steel D Nb-Ti-Mo	Steel E 444 SS[****]
C	0.012	0.015	0.023	0.012	0.014
Mn	0.51	0.54	0.46	0.35	0.45
Co	0.03	0.02			0.02
Cr	17.89	17.9	17.9	17.6	18.3
B	0.0004	0.0006			0.0006
V	0.12	0.14			0.12
S	0.001	0.002	0.0073	0.0018	0.003
Si	0.5		0.33	0.31	0.47
Ti	0.153	0.149	0.171	0.171	0.106
Ni	0.19	0.19	0.13	0.12	0.15
N	0.0085	0.021	0.024	0.026	0.016
Al	0.009	0.009	0.011	0.013	0.01
P	0.025	0.023	0.024	0.032	0.024
Cu	0.08	0.09	0.07	0.06	0.12
Nb	0.444	0.445	0.36	0.39	0.251
O	0.0076				
Mo	~0	0.008	< 0.01	0.54	1.942

Table 5.3. Laves phase's compositions, volume fractions and solvus temperatures used in designing the optimum chemical composition.

Alloy	composition	% mole fraction	Solvus temperature (°C)
0.35Nb – 0.15Ti	$(FeCr)_2(Nb,Ti)$	0.62	780
0.444Nb – 0.15Ti – 0.5Mo	$(FeCr)_2(Nb,Ti,Mo)$	2.40	950
0.6 Nb – 0.15Ti – 0.25Mo	$(FeCr)_2(Nb,Ti,Mo)$	1.70	900

[‡‡‡] Columbus Stainless MPO Number 3533603- failed during production
[§§§] Columbus Stainless MPO Number 3658671 – didn't fail
[****] Columbus Stainless MPO Number 3631171

5.4 POSSIBLE STABLE PHASES AT EQUILIBRIUM

The steels in Table 4.1, apart from the primary Fe and Cr alloying elements, also contain carbon, nitrogen, titanium and niobium as common secondary alloying elements. Therefore, the precipitates of Nb(CN) and Ti(CN) and the Laves phase can, in principle, be formed.

Steels A, B and C contain mainly titanium and niobium as the secondary alloying elements; therefore, it is expected that the stable second phases will include the Laves phase Fe_2M (with M representing mainly Nb) and the carbonitrides Nb(CN)/Ti(CN). The M_6C carbide (in which, 'M' stands for metallic elements) is not expected to be formed or, alternatively, if present its quantity will be negligible. In steels C and E that contain titanium, niobium and molybdenum as the secondary alloying elements, therefore, it is expected that the stable second phases will be Laves phase, the Nb(CN)/Ti(CN) carbonitrides and possibly the M_6C carbide**.** The composition of the Laves phase will change from one alloy to another.

The phases allowed for in these calculations are listed in Table 5.4. The calculations were performed for the temperature range of 600 to 1500 °C. Also, the data for the intermetallic Laves phase are less reliable due to a scarcity of experimentally determined data. It is necessary to consider the existence of the sigma phase even though it is not expected to be formed in practice at the early stages of processing, that is, sigma phase if it happens to be formed in this alloy, is only expected to nucleate at higher service temperatures and after a long service period. The possibility of a miscibility gap for the Cr-rich phases $(\alpha+\alpha')$ was also not introduced in the calculations.

Table 5.4. Prospective phases for equilibrium calculations using Thermo-Calc® with a TCFE3 database for steels.

Steel	Alloy	Phases
A	Type 441	Liquid, ferrite, carbo-nitrides, sigma, Laves phase, M_6C
B	Type 441	Liquid, ferrite, carbo-nitrides, sigma, Laves phase, M_6C
C	Nb–Ti	Liquid, ferrite, carbo-nitrides, sigma, Laves phase, M_6C
D	Nb–Ti– Mo	Liquid, ferrite, carbo-nitrides, sigma, Laves phase, M_6C
E	Type 444	Liquid, ferrite, carbo-nitrides, sigma, Laves phase, M_6C

5.5 PHASE DIAGRAMS

The isopleth diagrams for the phases that were expected to be stable and at equilibrium over a wide range of carbon content in these types of materials, are shown in Figure 5.1. These calculations are based on the fixed chemical composition of the steels studied in this work. A line illustrates where a new phase appears or disappears, and a number representing a phase is located on the side of the line where the phase is expected to be unstable.

With type 441 stainless steel (marked with an arrow in Figure 5.1); the equilibrium phases that are formed over a wide range of temperatures are the Laves phase, titanium and niobium carbo-nitrides (FCC_A1#2) and the sigma phase. The sigma phase should not be given much consideration in this particular work since it has often been reported that this phase only precipitates after a very long period at a high service temperature [25,26,27]. Note that the carbonitrides Ti(CN)/Nb(CN) are precipitated from the melt, that is their solvus temperatures are higher than the liquidus temperature in these alloys. This result predicts that the steel is fully ferritic (BCC_A1#1) up to the liquidus temperature (line 6, Liquid). The austenitic phase will only be formed at carbon contents above 0.09 wt%C (FCC_A1 #1). Both the solvus temperature and the volume fraction of each phase in these alloys are dependent on their respective chemical compositions. Thermo-Calc® calculations show that the formation of Laves phase is more favourable at a lower carbon content, that is below 0.1 wt.%; and that above this level of carbon and based on the fixed chemical composition of these alloys, the Laves phase will not be formed. Also, note that the $M_{23}C_6$ carbide is not formed in the presence of the Laves phase, that is, in these alloys the precipitation of the $M_{23}C_6$ carbide is only limited to an alloy with a high carbon content where the Laves phase does not exist.

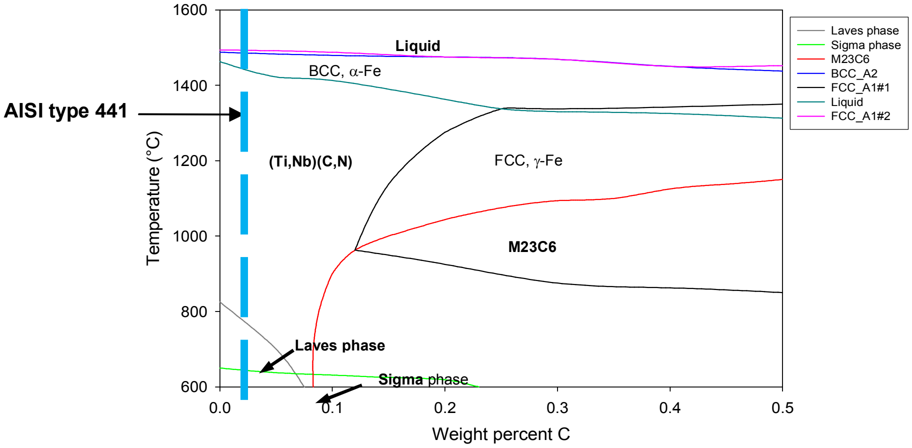

Figure 5.1. Thermo-Calc® calculation of the isopleth diagram for type 441 stainless steel with a constant amount of alloying elements and 0 to 0.5 wt.% of carbon. Below any line, these represents the stable region for the phase.

The isopleth diagram for the stable phases at equilibrium in the high Mo-containing AISI type 444 ferritic stainless steel is shown in Figure 5.2. According to Fujita et al [5], they have observed that Mo additions to these alloys do slow down the diffusivity of Nb. Therefore, the precipitation kinetics of Fe_2Nb will be expected to be slower if molybdenum is present.

There are certain aspects from these calculations that do not make sense, that is, Thermo-Calc® calculations predict the presence of austenite phase even at room temperature, but using the Fe-Cr phase diagram, and this steel is fully ferritic up to the liquidus temperature. The more useful information about phases present in this alloy can be obtained from the Thermo-Calc® “property diagram”, see Section 5.6 below.

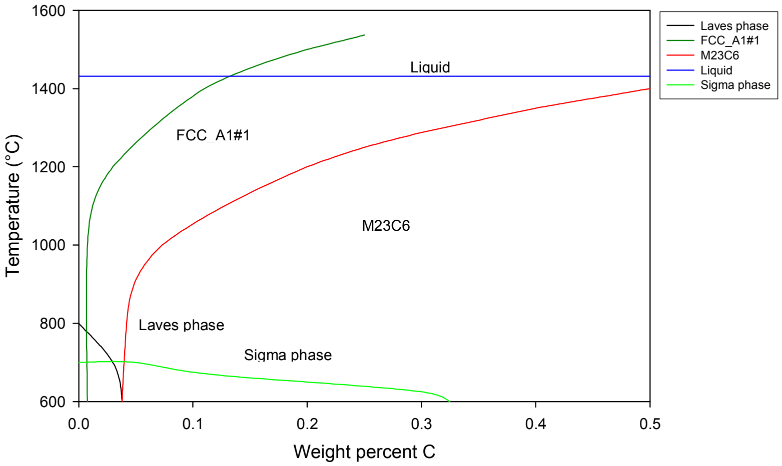

Figure 5.2. Thermo-Calc® calculation of the isopleth diagram for the high Mo-containing type 444 ferritic stainless steel E with a constant amount of alloying elements and 0 to 0.5wt.% of carbon.

5.6 PROPERTY DIAGRAMS

Some of the results obtained from these calculations are shown in Figure 5.3. in the form of a “property diagram”, which shows the dependence of the phase proportions on temperature. This diagram shows which phase has nucleated and grown at a specific temperature under equilibrium conditions. In multicomponent systems, property diagrams are often more useful than phase diagrams, as they give information within the phase region whereas phase diagrams give only the information of when the set of stable phases changes. One of the good examples of the problems of Thermo-Calc® at low temperature is that it predicts a weight faction of 25% for sigma phase, which is just impossible.

These diagrams are similar for Steels A – E, the only difference is the phase proportion as a function of temperature in these different steels. From this diagram the composition of each phase over its respective existence temperature range can be calculated.

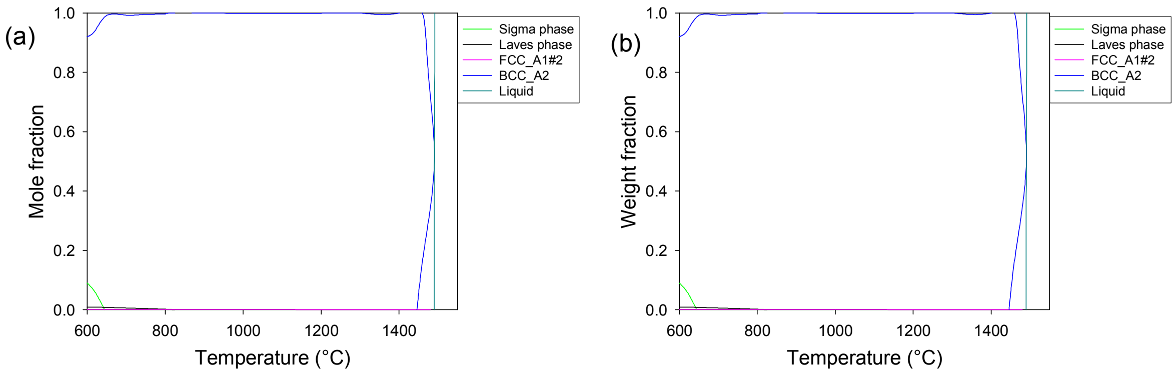

Figure 5.3. The property diagram that shows the dependence of phase proportion on temperature; (a) mole fraction of stable phase and (b) weight fraction of stable phase.

5.7 RELATIVE PHASE STABILITIES

The relative stability of a phase can be deduced by removing existing phases one by one in the equilibrium calculations. Thermo-Calc® predicts that the phase proportion of each existing secondary phase in type 441 stainless steel is independent from one to another, that is, removing one phase from the calculation won’t affect the amount of the other phase. Therefore, the removal of the sigma phase from the calculations will not affect the proportion of the carbo-nitrides or Laves phases. The temperature range of interest will be from 600°C to 950 °C, whereby it was previously determined that this is the stable region for Laves phase precipitation in these steels.

AISI Type 441: Steel A

Figure 5.4 shows the weight fraction of the equilibrium phases in steel A with composition 0.444Nb-0.153Ti. Figure 5.4 (a) shows the Laves phase weight fraction, which is estimated to be about 0.92 wt% at 600 °C and this fraction decreases with increasing temperature. The solvus temperature of Laves phase is estimated to be about 825 °C in this steel, and this is in broad agreement with results from the literature for this type of 441 stainless steel [3,9,99]. Figure 5.4 (b) is the weight fraction of the (Ti,Nb)(C,N), which is estimated to be less than 0.12 wt%. The solvus temperature of the (Ti,Nb)(NC) is predicted to be about 1480 °C. Note that the weight fraction of the (Ti,Nb)(NC) first increases with temperature up to about 825 °C before it decreases down to zero at 1480 °C. This increase below 825 °C is most likely due to the release of Nb from the dissolving Laves phase with the released Nb increasing the thermodynamic driving force for more (Ti,Nb)(C,N) to form. In this sense, there seems to be an indirect dependence between the two separate phases.

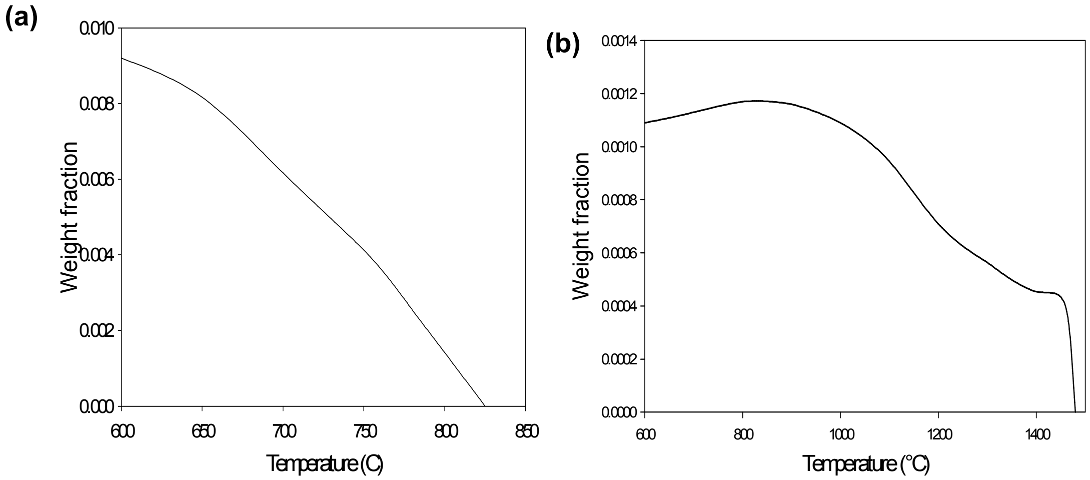

Figure 5.4. Thermo-calc® plots of weight fraction of the stable phases as a function of the temperature in the Steel A with composition 0.444Nb-0.153Ti; (a) Laves phase and (b) (Ti,Nb)(CN).

AISI type 441: Steel B

Figure 5.5 shows the weight fraction of the equilibrium phases in Steel B with composition 0.445Nb-0.149Ti. This steel is very similar to Steel A except for more than double nitrogen content, i.e. 0.021%N versus the lower 0.0085%N in Steel A. Figure 5.5 (a) shows the Laves phase's weight fraction, which is estimated to be about 0.84 wt% at lower temperatures and this decreases with increasing temperature. The solvus temperature of the Laves phase in this steel is about 800 °C, i.e. about 25°C lower than in Steel A. Figure 5.5 (b) shows the weight fraction of the (Ti,Nb)(C,N), and it is estimated to reach a maximum of 0.18 wt% at about 800 – 850 °C. This weight fraction is higher than the 0.12 wt% of steel A for this carbo-nitride, most likely due to the higher nitrogen content in steel B. The solvus temperature of the TiNb (NC) is about 1550 °C. According to Thermo-Calc®, there is not much difference in the Laves phase weight fractions between Steels A and B, but the major difference is in the weight fraction of (Ti,Nb)(C,N), which is dictated by the carbon and increased nitrogen content level.

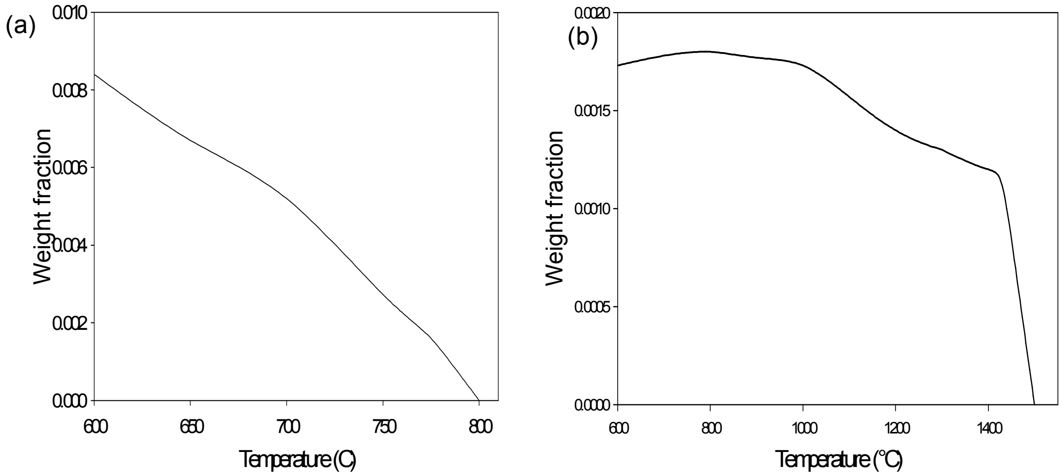

Figure 5.5. Thermo-calc® plots of weight fraction of the stable phases as a function of the temperature in the Steel B with composition 0.445Nb-0.149Ti; (a) Laves phase and (b) (Ti,Nb)(CN)).

Nb-Ti Alloy: Steel C

Figure 5.6 shows the weight fraction of the equilibrium phases in steel C with a composition of 0.36Nb-0.171Ti. Figure 5.6 (a) shows the Laves phase weight fraction, which is estimated to be about 0.57 wt% at 600 °C, and the weight proportion decreases with increasing temperature. The solvus temperature of the Laves phase is estimated to be about 760°C in this case. This predicts that the phase proportion and the solvus temperature of the Laves phase are dependent on the niobium content, that is, by lowering the niobium content to 0.36 %wt as compared to 0.444 %wtNb in Steel A, both the solvus temperature and the weight fraction will decrease, with the Laves phase's solvus temperature now as low as about 760°C.

Figure 5.6 (b) shows the weight fraction of the (Ti,Nb)(C,N), which is estimated to be about 0.24 wt% maximum at the temperatures of about 800 – 850 °C and its solvus temperature is predicted to be about 1525°C. From Table 4.1, it can be seen that this steel has a higher carbon and nitrogen content of 0.023wt% and 0.024wt% respectively than for any of the other steels studied. This means that most of the carbon and nitrogen had precipitated out as carbo-nitrides, resulting in a high content of (Ti,Nb)(C,N). Both carbon and nitrogen have a significant impact on the fraction of (Ti,Nb)(C,N), and this reduces the amount of Nb available to have contributed to the solid solution strengthening of the steel at high temperatures and also the weight fraction of Laves phase at lower temperatures. Comparing Figure 5.4(a) and Figure 5.5(a), it can be seen that by lowering the Nb content from 0.444wt% as in Steel A to 0.36wt% as in Steel C, this also lowers both the Laves phase content and its solvus temperature. This shows that the Nb content in this steel plays a more significant role in the precipitation of Laves phase than the Ti does.

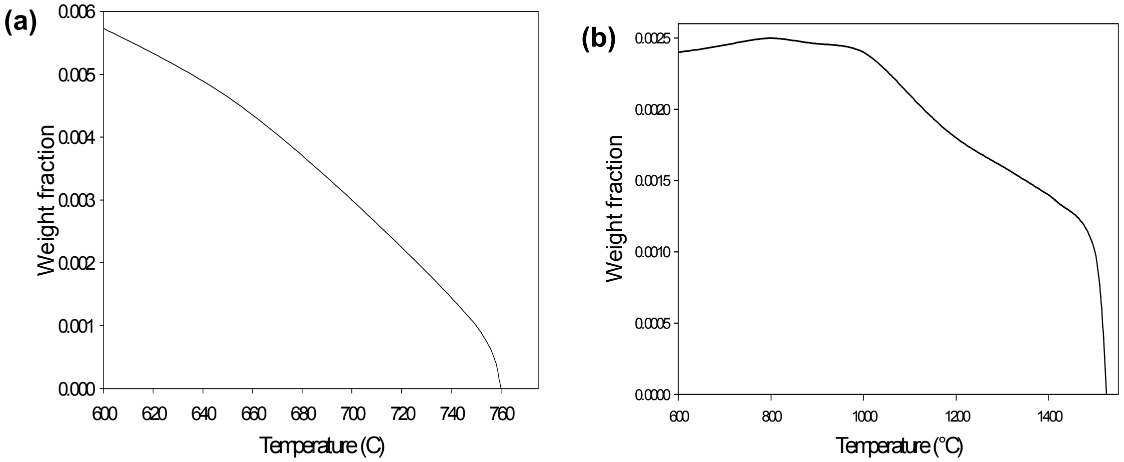

Figure 5.6. Thermo-calc® plots of weight fraction of the stable phases as a function of the temperature in the Steel C with composition 0.36Nb-0.171Ti; (a) Laves phase and (b) (Ti,Nb)(C,N).

Nb-Ti-Mo Alloy: Steel D

Figure 5.7 shows the weight fractions of the equilibrium phases in steel D with composition 0.39Nb-0.171Ti-0.54Mo. Figure 5.7 (a) shows the Laves phase weight fraction, which is estimated to be about 1.11 wt% at 600 °C, and this weight fraction decreases with increasing temperature. The solvus temperature of the Laves phase in this steel is estimated to be about 810 °C. The addition of 0.54%wt molybdenum has a significant impact on the predicted weight fraction of the Laves phase, that is, Mo additions increase the weight fraction of the Laves phase, but do not have a significant impact on the solvus temperature of the Laves phase.

Figure 5.7 (b) shows the weight fraction of the (Ti,Nb)(C,N) phase, which is estimated to reach a maximum of 0.18 wt% at about 800 to 850 °C, and its solvus temperature is about 1520 °C. Also, the increase in both carbon and nitrogen levels has a significant impact on the (T,N)(CN) weight fraction whereas the level of titanium and niobium have no major impact on this value.

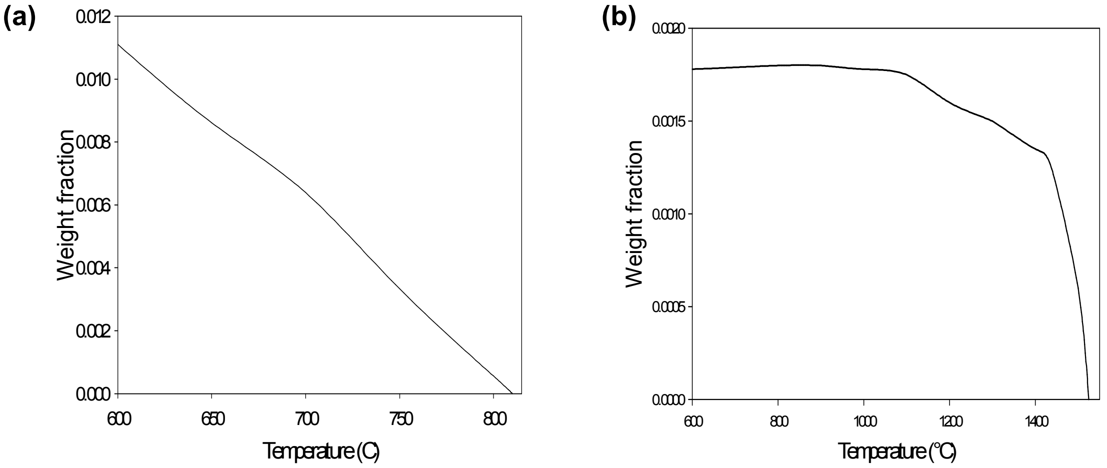

Figure 5.7. Thermo-calc® plots of weight fraction of the stable phases as a function of the temperature in the Steel D with composition 0.36Nb-0.171Ti-0.54Mo; (a) Laves phase and (b) (Ti,Nb)(C,N).

AISI type 444: Steel E

Figure 5.8 shows the weight fraction of the equilibrium phases in steel E with composition 0.251Nb-0.106Ti-1.942Mo and this steel falls under the category of a steel commonly referred to as a high molybdenum, high chromium steel; usually with a composition of 19Cr-2Mo. Figure 5.8 (a) shows the weight fraction of Laves phase expected to be about 1.54 wt% at 600 °C, and this also decreases with increasing temperature. The solvus temperature of the Laves phase in this steel is estimated to be about 780 °C. The addition of 1.942%wt molybdenum is predicted to have a significant impact on the weight fraction of the Laves phase, that is, Mo additions increase the weight fraction of the Laves phase, but at the same time they do not increase its solvus temperature. This shows that only niobium additions have a significant impact on both the weight fraction and the solvus temperature of the Laves phase.

Figure 5.8 (b) shows the weight fraction of the (Ti,Nb)(C,N), which is estimated to be about 0.155 wt% maximum at about 800 °C. The solvus temperature of the TiNb (NC) is about 1500 °C.

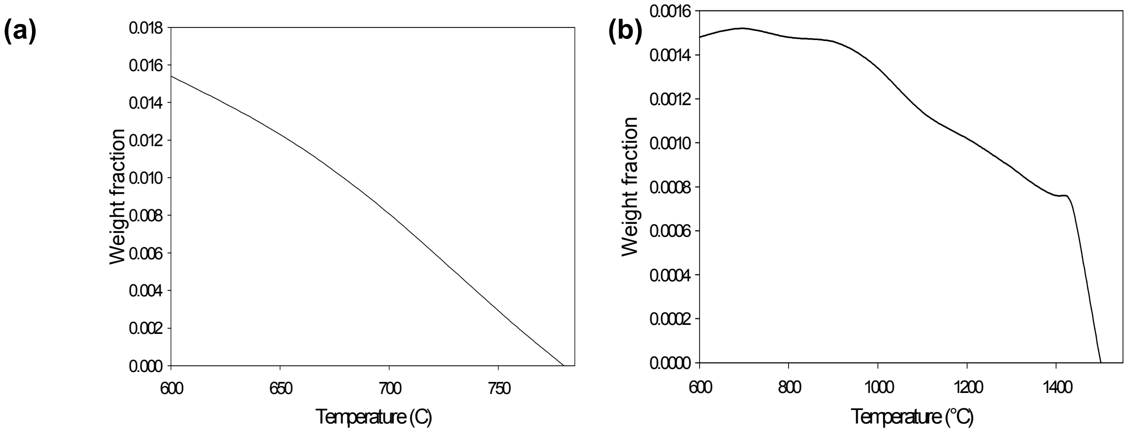

Figure 5.8. Thermo-calc® plots of the weight fraction of the stable phases as a function of the temperature in the Steel E with composition 0.251Nb-0.106Ti-1.942Mo; (a) Laves phase and (b) (Ti,Nb)(C,N).

5.8 EQUILIBRIUM CHEMICAL COMPOSITION OF THE LAVES PHASE

The chemical composition of a precipitate shifts towards the equilibrium composition during growth in which local equilibrium is maintained at the interface. Coarsening may then occur at a slower rate. The chemical compositions of the equilibrium Laves phase as a function of temperature are shown in Figure 5.9 – 5.13. The summary of the normalised weight fractions of the elements that form the Laves phase's composition at their respective temperatures, are shown in Table 5.6.

AISI type 441: Steel A

Figure 5.9 (a) shows the composition of the Laves phase (in mole fractions) which is mainly composed of Fe and Nb in the ratio of about 2:1, with less than 0.1% mole fraction of other alloying elements present within its composition, Ti being the major one at lower temperatures and Cr entering this phase at higher temperatures. Therefore, it can be concluded that the composition of the Laves phase is given by $(Fe,Cr)_2(Nb,Ti)$.

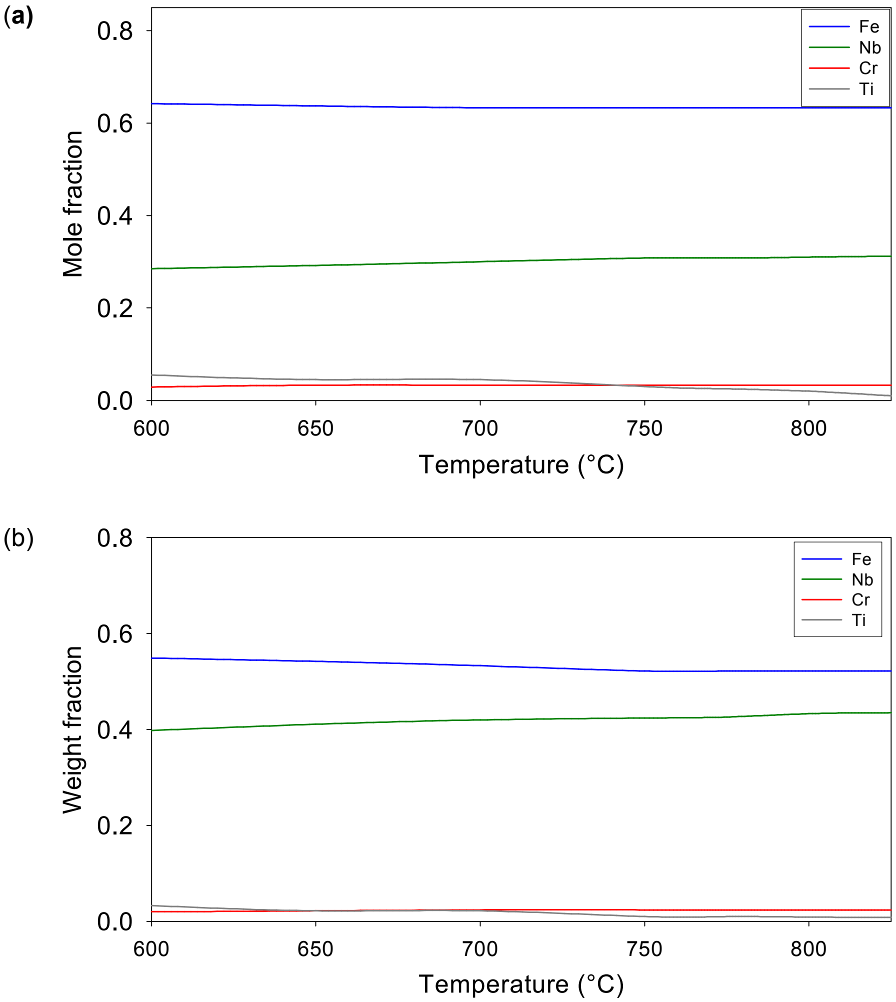

Figure 5.9. The normalised chemical composition of the Laves phase in Steel A: (a) is the mole fraction and (b) is the weight fraction of a component in the phase.

AISI type 441: Steel B

Figure 5.10 shows the composition of the Laves phase which consists mainly of Fe and Nb in the ratio of about 2:1, with less than 0.1% mole fraction of other alloying elements present within its composition, Cr being the major third element in this steel and with the Ti presence that is minimal in this steel as compared to Steel A. Therefore, it can be concluded that the composition of the Laves phase in this steel is also given by $(Fe,Cr)_2(Nb,Ti)$.

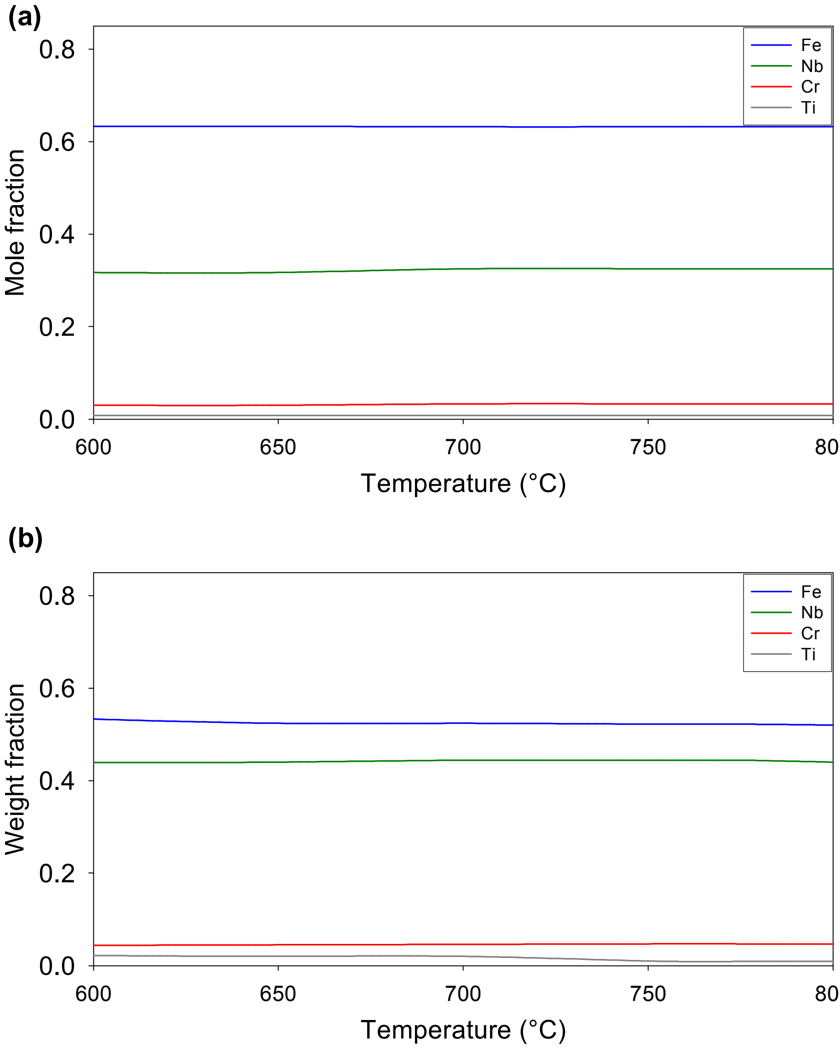

Figure 5.10. The normalised chemical composition of the Laves phase in Steel B: (a) is mole fraction and (b) is a weight fraction of a component in a phase.

Nb – Ti alloy: Steel C

Figure 5.11 (a) shows the composition of the Laves phase in this steel, which mainly consists of Fe and Nb in the ratio of 2:1, with less than 0.05% mole fraction of other alloying elements present within its composition. Ti does not play a significant role in the composition of the Laves phase as was also the case in Steel A, but the Cr does plays a significant role. Therefore, it can be concluded that the composition of the Laves phase is predicted to be $(Fe,Cr)_2Nb$ in this steel.

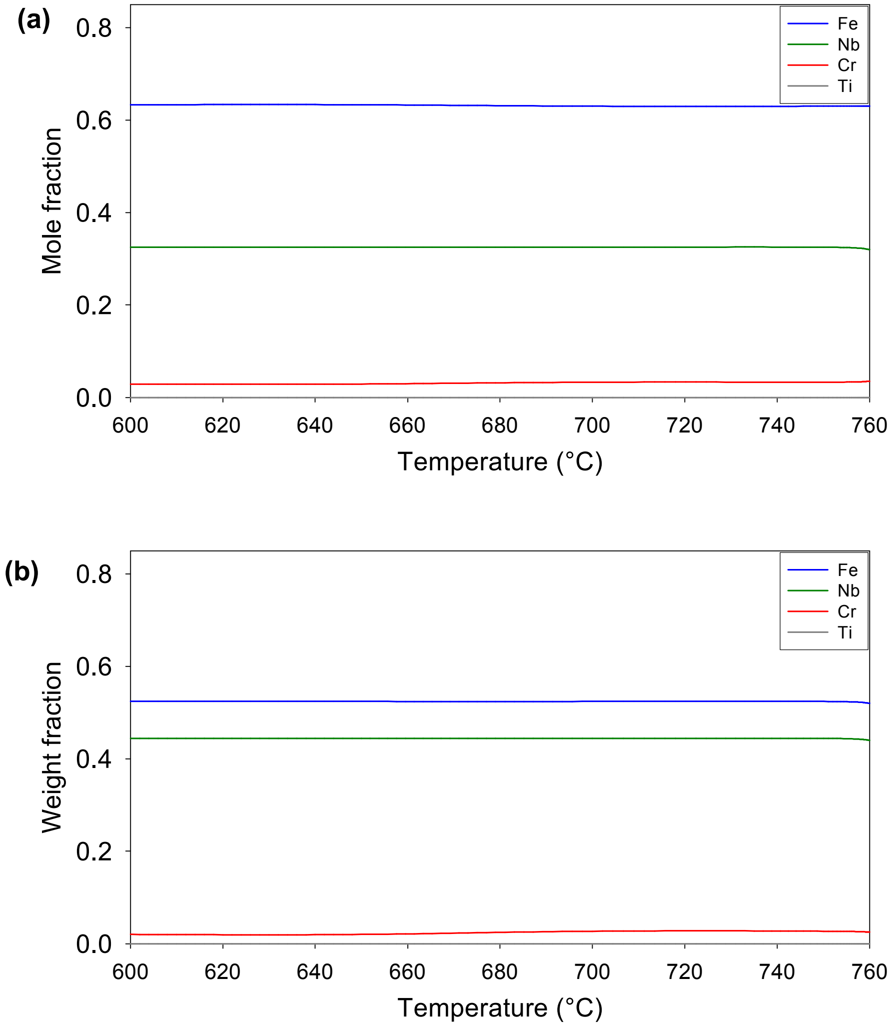

Figure 5.11. The normalised chemical composition of the Laves phase in Steel C: (a) is the mole fraction and (b) is the weight fraction of a component in the phase.

Nb – Ti – Mo alloy: Steel D

Figure 5.12 shows the composition of the Laves phase in steel D which consists mainly of Fe, Mo and Nb. Note that Mo enters the Laves phase composition at lower temperatures, and its content within the Laves phase decreases gradually with increasing temperature whilst the Nb content, on the other hand, increases. This indicates that an addition of about 0.5wt.% Mo to an AISI type 441 stainless steel has a significant impact on both the composition and the volume fraction of the Laves phase. The composition of Laves phase changes from about 600 °C and higher as the Nb starts to replace the Mo to some degree. Also, Cr enters this phase at higher temperatures, therefore, it can be concluded that the composition of the Laves phase is predicted to be $(Fe,Cr)_2(Nb,Mo,Ti)$ in this steel.

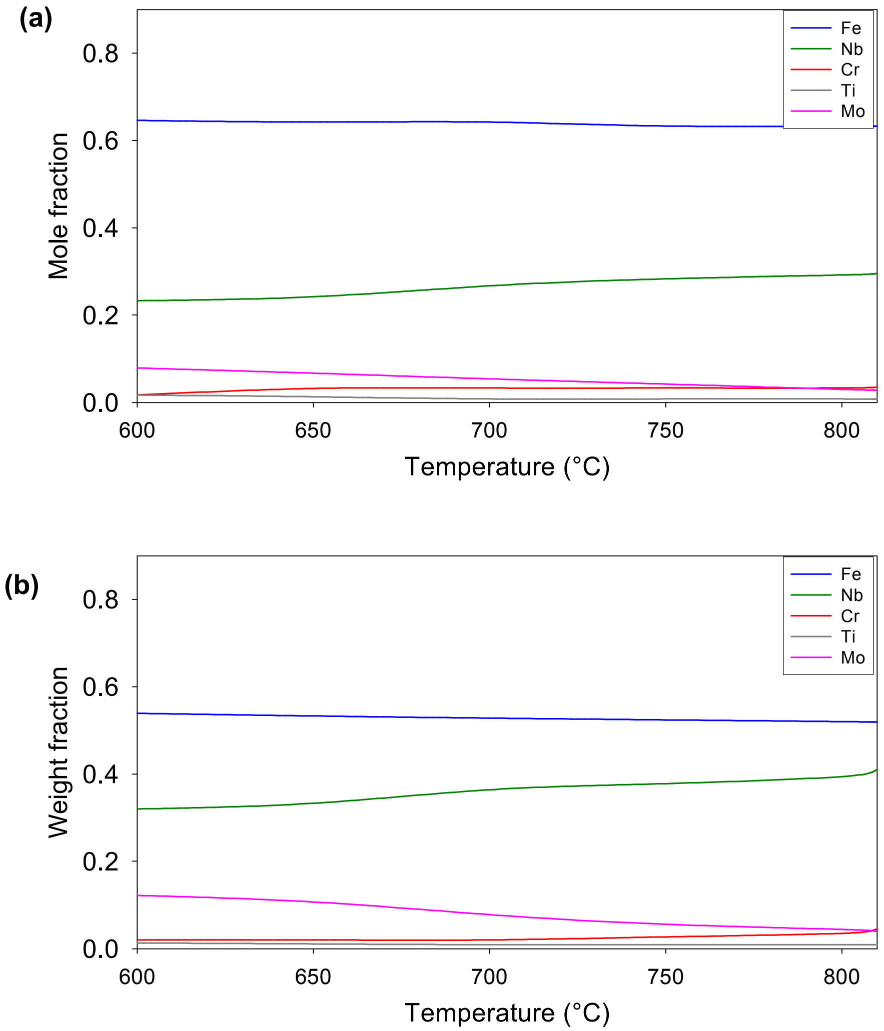

Figure 5.12. The normalised chemical composition of the Laves phase in Steel D: (a) is the mole fraction and (b) is the weight fraction of the component in the Laves phase.

AISI type 444: Steel E

Figure 5.13 shows that the composition of the Laves phase in Steel E consists mainly of Fe and Mo, with Nb entering this phase at higher temperatures. Cr forms a minor content of this phase. Therefore, it can be concluded that the composition of the Laves phase in this steel is predicted to be $(Fe,Cr)_2(Nb,Mo)$ with Nb and Fe being the major elements up to about 700°C and Fe and Mo the major elements above that temperature. Also, from this steel it is observed that although a Mo addition increases the Laves phase's content it also lowers it solvus temperature. Fujita et al. [99] have observed this enhancement of the Laves phase precipitation by a Mo addition, and they have suggested that a Mo addition can slow the precipitation rate of the Laves phase by lowering the diffusivity of Nb.

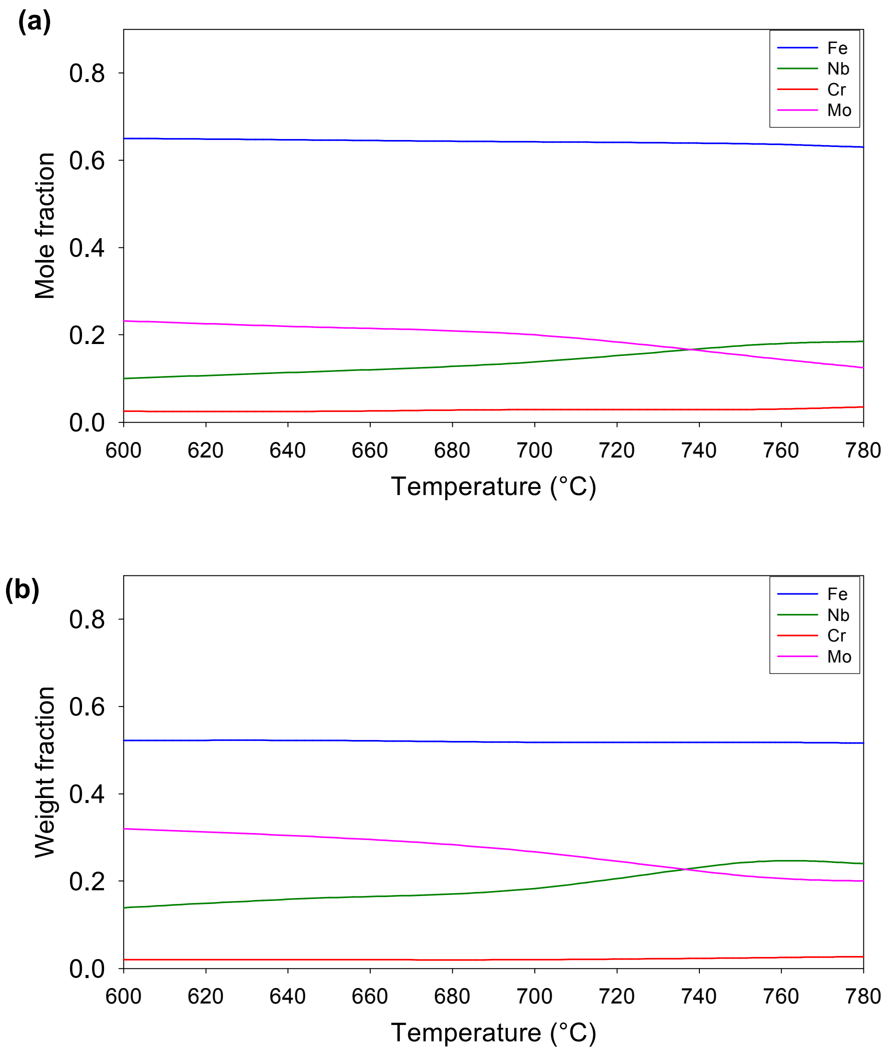

Figure 5.13. The normalised chemical composition of the Laves phase in Steel E: (a) is the mole fraction and (b) is the weight fraction of a component in the Laves phase.

5.9 DRIVING FORCE FOR NUCLEATION

The Gibbs free energy changes for the Laves phase formation in the five steels were also calculated using Thermo-Calc®. Figure 5.14 shows the relationship of the free energy change for the Laves phase reaction in these steels as a function of temperature and for equilibrium states. The free energy change increases (becomes less negative) as the temperature increases from 600°C towards the solvus temperature, and its values are dependent on the composition of the specific alloys.

The calculated values are not the driving force for nucleation ΔG_V but rather the overall Gibbs free energy change ΔG for the reaction. With these results, the driving force for nucleation ΔG_V can be obtained from:

$$\Delta G_V = \frac{\Delta G}{\upsilon V} \qquad \text{Equation 5.1}$$

where V is the equilibrium volume fraction of the Laves phase and υ is the molar volume of the Laves phase.

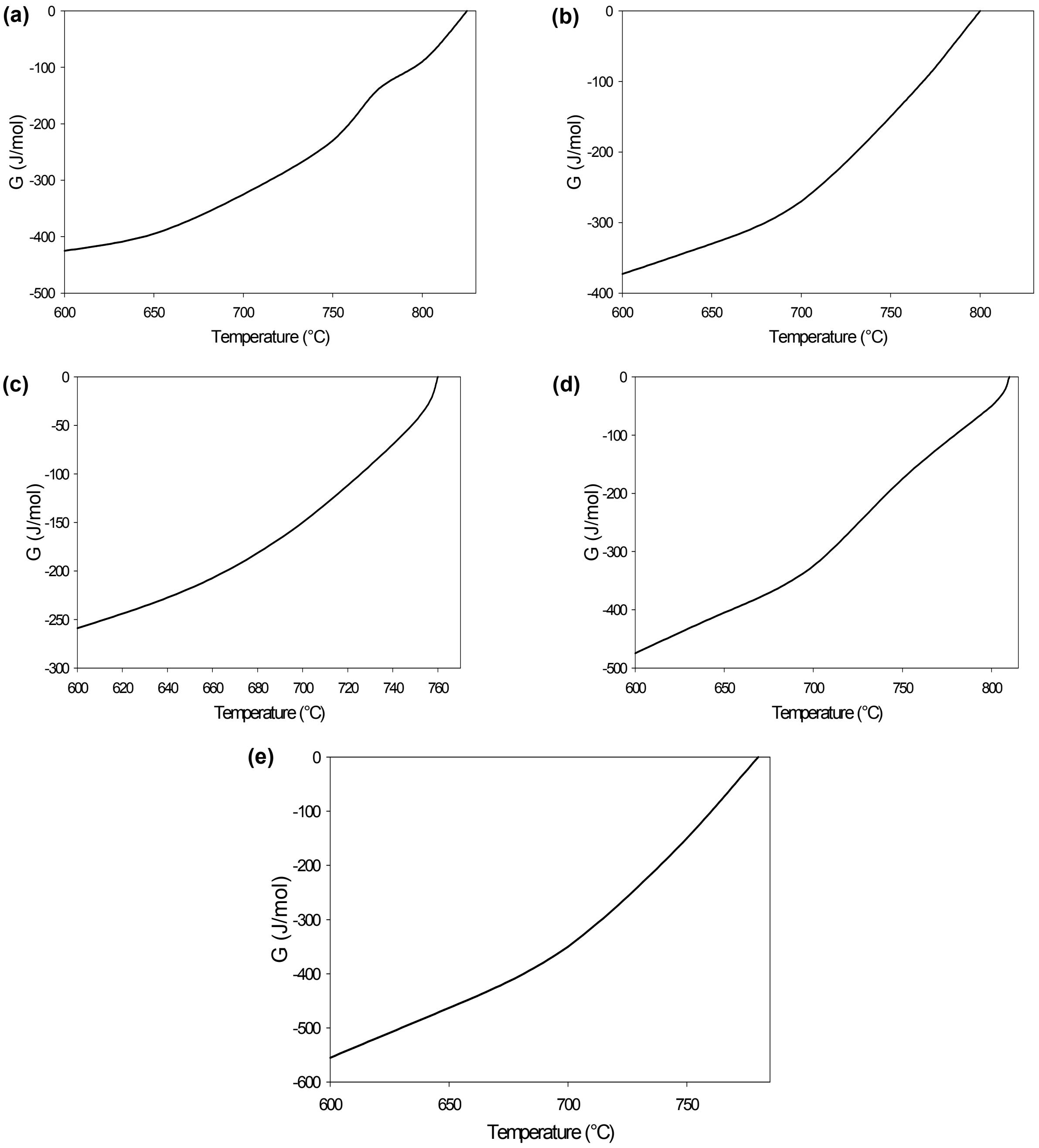

Figure 5.14. The free energy change ΔG for the precipitation reaction of Laves phase in ferrite with temperature for : (a) Steel A; (b) Steel B; (c) Steel C; (d) Steel D and (e) Steel E, calculated using Thermo-Calc®, (G = J/mol).

5.10 SUMMARY

The thermodynamic equilibrium data have been generated for AISI type 441 ferritic stainless through Thermo – Calc® software, see Table 5.5 for a summary table and Table 5.6 for a detailed comparison. These data will be used to determine the nucleation kinetics in the alloys. The results obtained from this model will be compared directly to the experimental results. Hopefully, a better understanding of the Laves phase precipitation will be possible, and the effects of composition on its kinetics will be predicted.

Table 5.5. A summarised results from the Thermo-Calc® predictions.

Steel	Main secondary alloying elements	Composition differences with reference to steel A	Laves phase			(Ti,Nb)(C,N)		Conclusions
			%Wt frac. at 600 °C	Solvus temp °C	Molar composition	%Wt frac at 600 °C	Solvus temp °C	
A	0.012C-0.0085N-0.444Nb-0.153Ti-~0 Mo	Main reference steel	0.920	825	$(Fe,Cr)_2(Nb,Ti)$	0.108	1480	
B	0.015C-0.021N-0.445Nb-0.149Ti-0.008Mo	Increased N content but C, Nb and Ti relatively unchanged	0.840	800	$(Fe,Cr)_2(Nb,Ti)$	0.173	1550	Increased weight fraction of (Ti,Nb)(C,N) from increased N content
C	0.023C-0.024N-0.36Nb-0.171Ti-<0.01Mo	Increased (C+N), lower Nb and higher Ti content	0.573	764	$(Fe,Cr)_2(Nb)$	0.225	1525	Laves phase solvus decreases with lower Nb content
D	0.012C-0.026N-0.39Nb-0.171Ti-0.54Mo	Lower C ad Nb content, N and Ti relatively unchanged, and Mo addition	1.111	815	$(Fe,Cr)_2(Nb,Mo,Ti)$	0.176	1520	Laves phase content increased with the addition of Mo. (Ti,Nb)(C,N) content and solvus temp increased from increased N content
E	0.014C-0.016N-0.251Nb-0.106Ti-1.942Mo	C relatively unchanged, N increased, lower Nb + Ti contents, high Mo content addition	1.542	780	$(Fe,Cr)_2(Nb,Mo)$	0.150	1500	Laves phase content increases with the Mo addition. Its solvus temp decreased with lower Nb content

Table 5.6. Detailed results of thermodynamic calculations (Thermo-Calc®). The normalised weight and mole fractions of the Laves phase composition components are shown.

Steel	Solvus temp (°C)	Temp (°C)	ΔG J/mol	Wt frac. (%)	Concentration in Laves phase ppt (wt)					Concentration in Laves phase ppt (mole)				
					Fe	Nb	Cr	Ti	Mo	Fe	Nb	Cr	Ti	Mo
A	825	600	-425	0.920	0.549	0.398	0.020	0.033		0.642	0.285	0.029	0.050	
		650	-395	0.817	0.542	0.411	0.022	0.022		0.637	0.292	0.033	0.055	
		700	-325	0.617	0.533	0.420	0.024	0.022		0.633	0.300	0.033	0.055	
		750	-230	0.413	0.522	0.424	0.024	0.010		0.633	0.308	0.033	0.055	
		775	-125	0.283	0.522	0.426	0.024	0.010		0.633	0.308	0.033	0.055	
		800	-90	0.142	0.522	0.433	00.24	0.009		0.633	0.310	0.033	0.055	
B	800	600	-373	0.840	0.533	0.439	0.044	0.022		0.633	0.317	0.030	0.008	
		650	-330	0.607	0.524	0.440	0.044	0.044		0.633	0.317	0.030	0.008	
		700	-270	0.520	0.524	0.444	0.044	0.044		0.632	0.325	0.033	0.008	
		750	-150	0.273	0.522	0.444	0.044	0.044		0.632	0.325	0.033	0.008	
		775	-80	0.160	0.522	0.444	0.044	0.044		0.632	0.325	0.033	0.008	
C	760	600	-259	0.573	0.524	0.444	0.020			0.633	0.325	0.029		
		650	-218	0.464	0.524	0.444	0.020			0.633	0.325	0.029		
		700	-150	0.300	0.524	0.444	0.027			0.630	0.325	0.033		
		750	-46	0.100	0.524	0.444	0.027			0.630	0.325	0.033		
D	810	600	-475	1.111	0.539	0.320	0.020	0.013	0.122	0.646	0.233	0.017	0.017	0.079
		650	-405	0.861	0.533	0.333	0.020	0.011	0.107	0.642	0.242	0.032	0.013	0.067
		700	-325	0.639	0.528	0.364	0.020	0.009	0.078	0.642	0.267	0.033	0.008	0.054
		750	-175	0.333	0.524	0.378	0.020	0.009	0.056	0.633	0.283	0.033	0.008	0.042
		800	-50	0.056	0.520	0.394	0.020	0.009	0.044	0.633	0.292	0.033	0.008	0.030
D	780	600	-555	1.542	0.522	0.139			0.320	0.650	0.100	0.025		0.232
		650	-463	1.231	0.522	0.162			0.300	0.646	0.117	0.025		0.217
		700	-350	0.807	0.518	0.183			0.267	0.642	0.138	0.029		0.200
		750	-150	0.292	0.518	0.242			0.213	0.638	0.175	0.029		0.154

CHAPTER SIX

EXPERIMENTAL RESULTS

6.1 INTRODUCTION

This chapter examines collectively the experimental results. The main focus is on the Laves phase formation and its dissolution and how it affects the mechanical properties of the AISI type 441 ferritic stainless steel. To gain a better understanding of the embrittlement effect from the Laves phase, the results are divided into three parts:

1. microstructural analysis from the failure of materials to understand the source of this embrittlement;
2. effect of the annealing treatment on the Laves phase precipitation and, therefore, its embrittling effect; and
3. the kinetics of the Laves phase formation, and the parameters (such as, temperature and composition) that affect its formation.

6.2 MICROSTRUCTURAL ANALYSIS OF AN AISI TYPE 441 FERRITIC STAINLESS STEEL

In order to understand the source of embrittlement in this steel, microstructural analyses were carried out. These analyses range from simple optical microscopy to more complex transmission electron microscopy analysis. The analyses were carried out on the ferritic stainless steel AISI type 441, and particularly on Steel A that had failed during processing. As it has previously been determined by Columbus Stainless, the source of embrittlement was apparently not grain size related, as the grain size was measured to be 24.8 ± 4.2 μm which is still considered to be fine enough not to have embrittled this material, see Figure 6.1(a). The general grain microstructure had a pan cake structure with the grains elongated in the rolling direction. The scanning electron microscopy (SEM) micrographs show the presence of the grain boundary and matrix precipitates, see Figure 6.1(b).

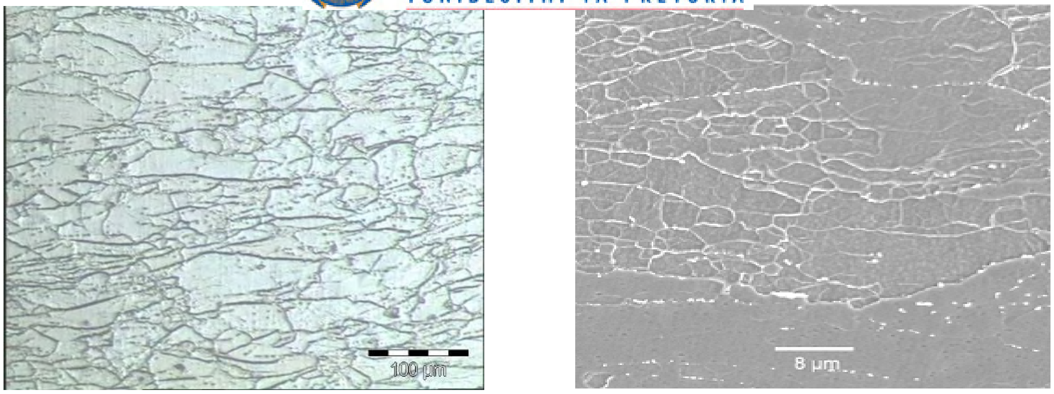

(a) **(b)**

Figure 6.1. Micrographs from Steel A in the as received hot rolled condition, showing the grain structure. (a) optical microscopy image and (b) SEM images. Note the large difference in magnification with figure (a) showing the "particle decorated" grain structure while figure (b) shows primarily the "particle decorated" subgrain structure.

6.2.1 PRECIPITATE'S IDENTIFICATION

The morphology of the various precipitates in this Steel A changes with the choice of annealing treatment, as revealed by the two types of precipitates (that is, by relative size) that was observed from the SEM micrographs in Figure 6.2. Only the large particles could be analysed successfully using the SEM energy dispersive X-ray technique while the small precipitates were too fine for even a representative semi-quantitative analysis. The large precipitates were found to be most likely a titanium carbo–nitride, which had varying degrees of smaller niobium carbo–nitride precipitates clustered around it and the central precipitate's size was in the region of 2 to 10 μm, see Figure 6.3. According to Gordon and van Bennekom [55], they have reported that the colour of the carbo – nitride changes with the ratio of N/C in the steel. A yellow/orange colour indicates a Ti(C,N) as found in this steel that contains about 10 at. % TiC, see Figure 6.2(a).

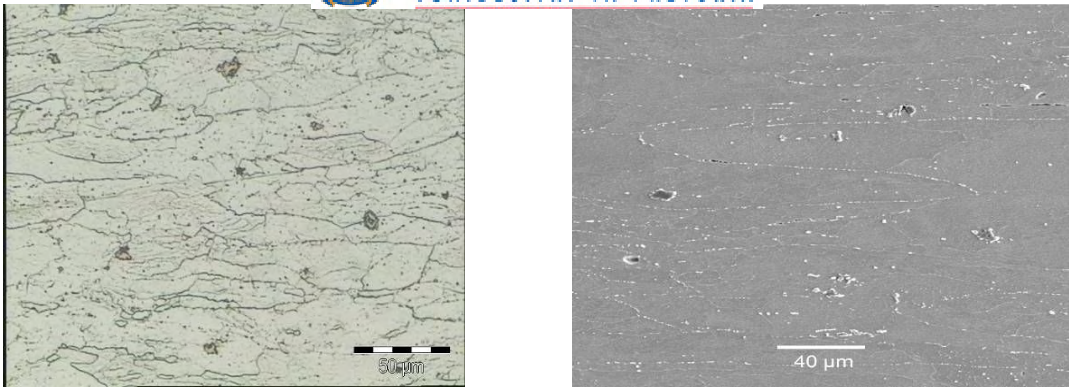

(a) (b)

Figure 6.2. Micrographs of the as received hot rolled Steel A showing its grain structure. (a) An optical microscopy image and (b) a SEM image.

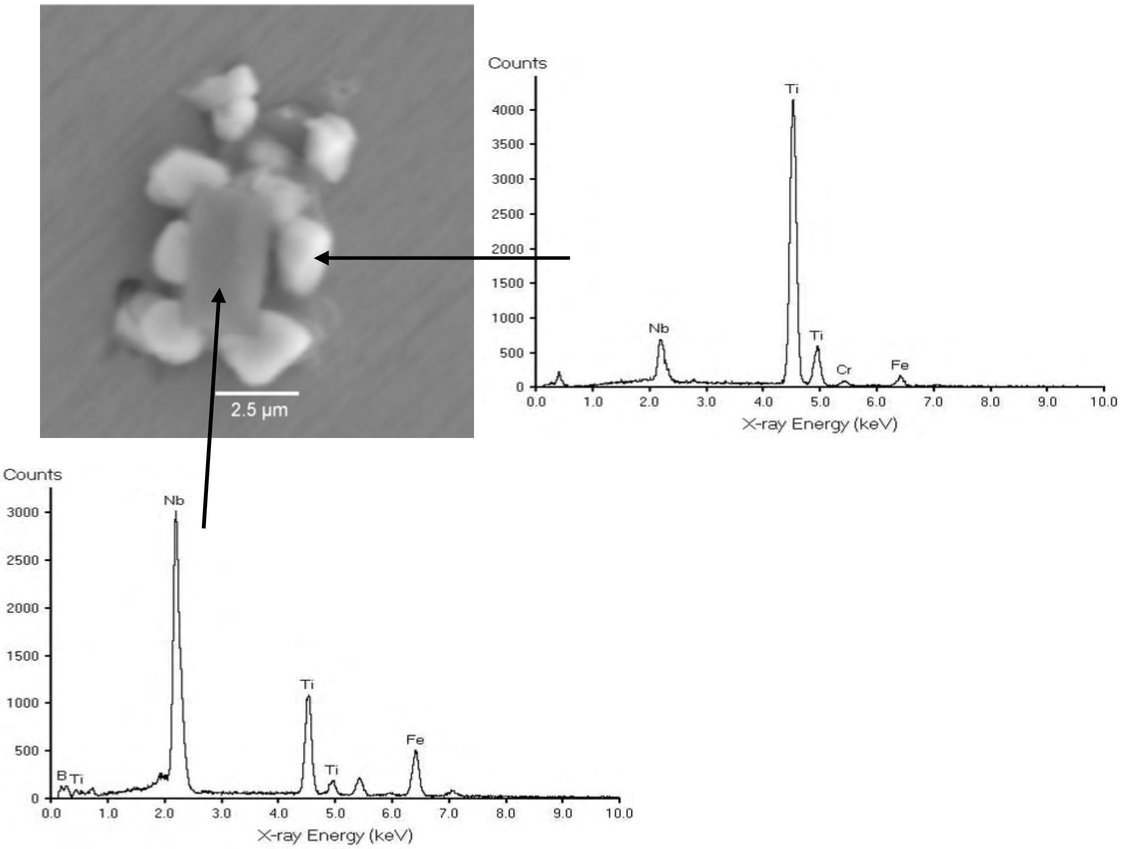

Figure 6.3. SEM – EDS micrograph showing a precipitate consisting of a central cubic core of a mainly titanium containing particle surrounded by a cluster of niobium precipitates.

The SEM results confirm the predictions made by Thermo-Calc®, in that both nitrides and carbides are formed as complex FCC (Ti,Nb)(C,N) precipitates with the Ti(C,N) nucleating first and then the Nb(C,N) nucleating on its surface as a shell or alternatively as a cluster of loose particles around the Ti(C,N). This is not surprising as Ti(C,N) is known to have a lower solubility in these steels than Nb(CN) and will, therefore, form first during cooling from the melt while the Nb(CN) subsequently forms at slightly lower temperatures by heterogeneous nucleation on the existing Ti(CN). Furthermore, in the work done by Craven et al.[130], they also observed that the (Ti,Nb)(C,N) complex has a least soluble core consisting of TiN that precipitates at higher temperatures during cooling from the melt, and the Nb/Ti ratio in the core is markedly affected by the cooling rates during solidification and later thermomechanical processing.

The small precipitates, however, were analysed using transmission electron microscopy (TEM) and XRD techniques. To be able to analyse the types of precipitates present in this steel without any interference from the matrix, carbon extraction replicas of the precipitates were used and TEM energy dispersive X-ray spectrometer (TEM-EDS) and electron diffraction patterns were used in identifying these precipitates. The transmission electron microscopy (TEM) micrographs for the as received hot rolled Steel A are shown in Figure 6.3. Three types of precipitates were analysed from this specimen;

1. large plate–like precipitates (analysis 1);
2. needle – like precipitates (analysis 2); and
3. small plate-like precipitates (analysis 3),

while there were some fine globular precipitates that could not be accurately analysed using both of these techniques because of their small size. In the work done by Fujita et al [6] it was suggested that the intensity ratio of niobium to iron, Nb/Fe in EDS analysis for the M_6C (Fe_3Nb_3C) type carbide is larger than that for Laves phase (Fe_2Nb). This suggests that large plate – like precipitates (analysis 1) are the M_6C carbide and both the needle–like and small plate–like particles (analyses 2 and 3) are the Laves phase Fe_2Nb. Both M_6C type carbide and Laves phase particles include small amounts of titanium and chromium. However, the amounts of titanium and chromium in both precipitates are much less than those of niobium and iron. From these observations it can be concluded that the composition of the M_6C and Laves phase precipitates are most likely to be $(Fe,Cr)_3(Nb,Ti)_3C$ and $(Fe,Cr)_2(Nb,Ti)$, respectively.

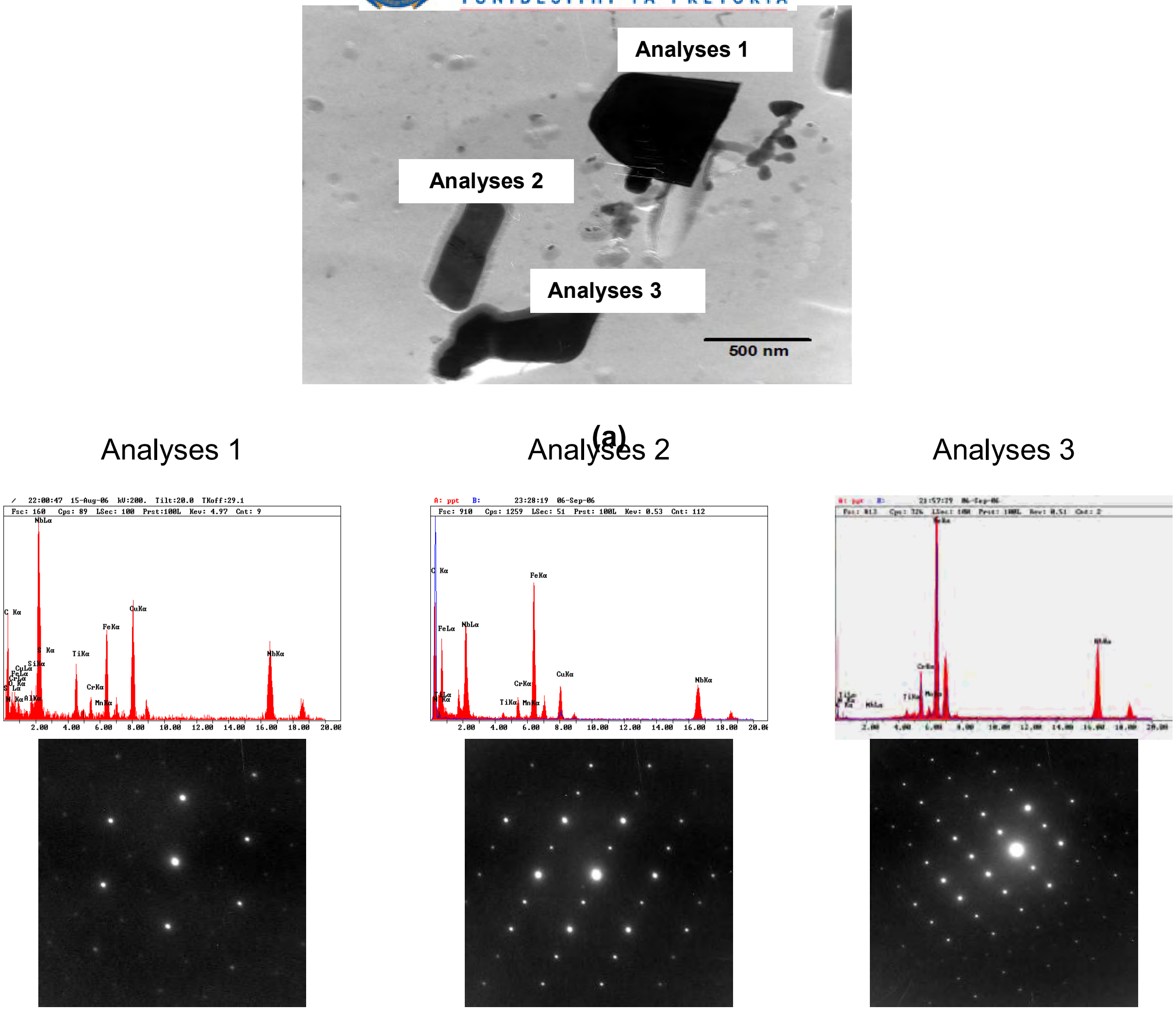

Fe$_3$Nb$_3$C [$\bar{1}$11]   Fe$_2$Nb [$\bar{1}$00]   Fe$_2$Nb [10$\bar{2}$]

(b)

Figure 6.4. Transmission electron micrographs of particles from extraction replicas and their analyses by electron diffraction and EDS of the as-received hot rolled Steel A showing different particle morphologies.

The diffraction patterns of the large globular precipitates (analysis 1) show a cubic crystal structure with a lattice parameter a_o = 1.11 nm. Therefore, these precipitates are identified as most likely to be cubic M_6C carbides. On the other hand, the diffraction patterns of the needle-like or elongated phase (analysis 2) and plate-like precipitates (analysis 3) show the crystal structure to be most likely identified as hexagonal. The lattice parameters were measured to be a_o = 0.48 nm and c_o = 0.79 nm, with c_o / a_o = 1.64, which is close to the $MgZn_2$ C14-type of the Laves phase.

Figure 6.5 shows the results of the XRD analyses of the precipitate residues after electrolytic extraction from the as received material, Steel A. Two main types of precipitates where detected, i.e., the Laves phase and the carbo-nitrides, but there was a small amount of M_6C carbides also present, as was also found in the TEM analysis. From Figure 6.5 , the peaks for the M_6C phase is not clearly visible, but when the Rietveld refinement approach was used to quantify these phases, its presence was detected as a small amount. Note, however, that it is not always possible to get a fully pure precipitate extraction of precipitates without the interference of the matrix material, the α-Fe matrix phase is considered to be also present in this measurement. Table 6.1 shows the weight fractions of the precipitates present in this steel, with the error calculated as a 3 sigma error (meaning three times the standard deviation). The volume was calculated using the densities of each phase and the total mass of precipitates' residue extracted from the steel by weighing. The results indicate that the normalised weight fractions for the Laves phase and (Ti,Nb)(C,N) to be about 1.14% and 0.33%, respectively.

Using the Rietveld refinement approach, the lattice parameters of the Laves phase were determined to be a_o= 0.481 nm and c_o = 0.784 nm and these values are close to the ones determined above from the TEM diffraction patterns.

Table 6.1. The measured weight fractions of the precipitate phases found in the as received hot – rolled material, Steel A.

	XRD analysis		Calculated values			
Phase	Weight fraction (%)	3 σ	Weight phase (g)	Normalised weight frac. (%)	Density (g/cm^3)	Vol. (x 10^{-3}cm^3)
Fe_2Nb	56.36	2.04	0.037	1.143	8.63	1.32
M_6C	2.02	0.66	0.001	0.041	8.44	0.05
α - Fe	16.24	0.84	0.011	0.329	7.87	0.42
(Ti,Nb (C,N)	25.39	2.52	0.017	0.515	7.82	0.80

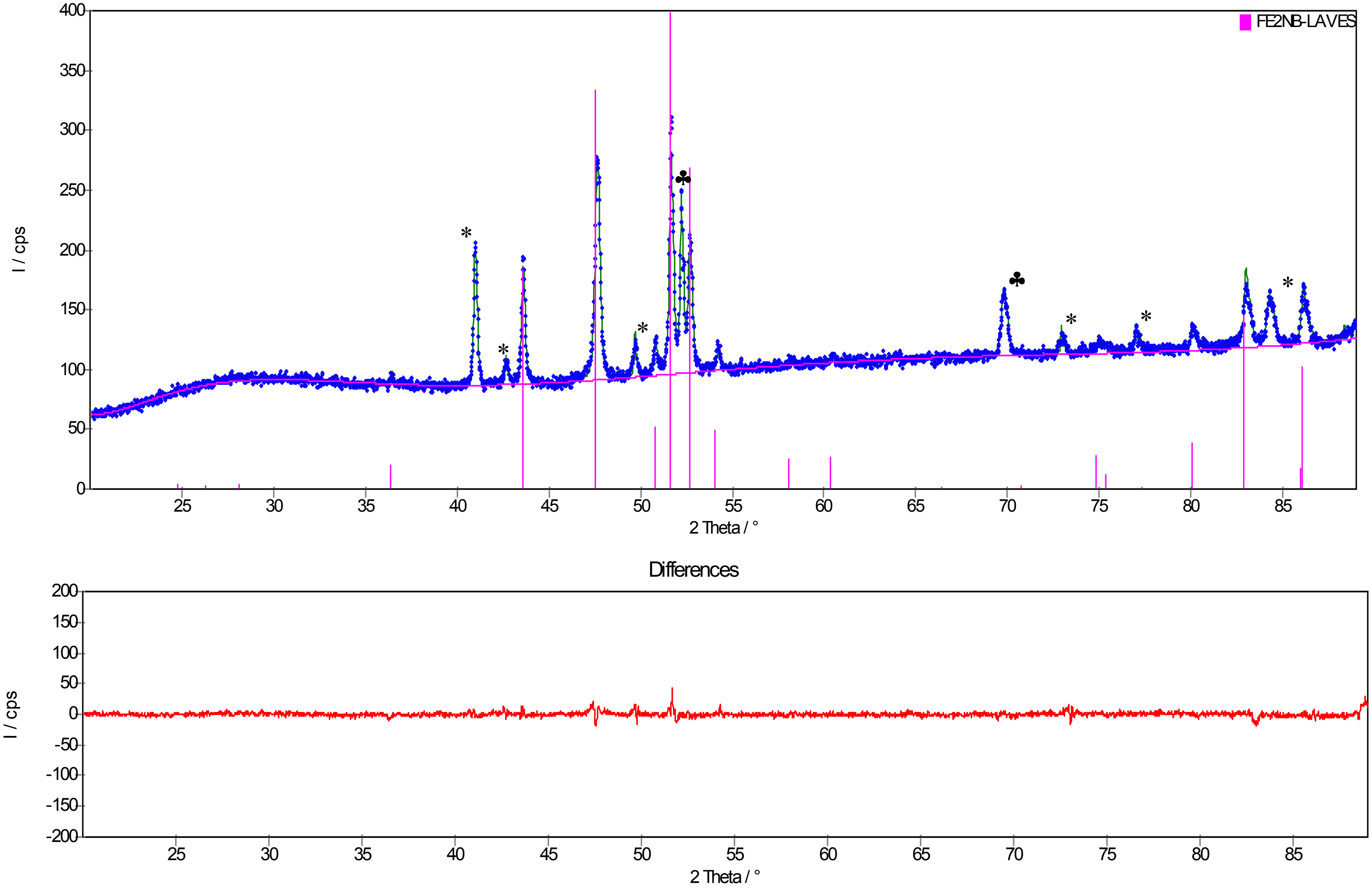

Figure 6.5. A typical XRD scan of the precipitate residue after electrolytic extraction from Steel A, i.e. the as received material, showing the presence of the Laves phase peaks (indicated by the lines in the top figure). The remaining peaks are the carbides and nitrides, indicated by (∗) and the α - Fe matrix, indicated by (♣). Note the good residual difference between the calculated and the measured spectrum as is shown by the spectrum below.

Fujita et al., [101] using the *MTDATA* thermodynamic software, have modelled the precipitation kinetics in the Fe-Nb-C system for a 9Cr-0.8Nb steel at 950 °C. They have observed that the atomic ratio of Fe to Nb in the extracted residue in their steel approaches unity with increasing ageing time, and this indicates that the Laves phase (Fe_2Nb), which contains more iron than required by stoichiometry in Fe_3Nb_3C, dissolves to give way to Fe_3Nb_3C. This meant that the Laves phase was a metastable phase that gave way to the precipitation of Fe_3Nb_3C, and they have suggested that the precipitation sequence towards the equilibrium phases in their high niobium content stabilised ferritic stainless steel to be NbN and Fe_3Nb_3C:

$$\alpha \rightarrow \alpha + Nb(C,N) + Fe_2Nb + Fe_3Nb_3C \rightarrow \alpha + NbN + Fe_3Nb_3C$$

where α represents ferrite. In this study on the embrittled Steel A with a lower niobium content reported here, the Thermo-Calc® prediction did not show this reaction sequence of Fujita et al., [101] because this sequence is a time dependent reaction, and Thermo-Calc® calculations only apply to the phases at full equilibrium. Secondly, the relatively large difference in niobium content between the two steels should also be noted. In order to prevent a great loss in strength during service, it is necessary to control the precipitation sequence during high temperature aging. This can be achieved by reducing the carbon content or by adding some other alloying elements that have a stronger affinity for carbon, and this will impede precipitation of the coarse M_6C carbides.

6.3 EFFECT OF ANNEALING TREATMENT ON THE MICROSTRUCTURAL AND MECHANICAL PROPERTIES

6.3.1 MICROSTRUCTURAL ANALYSIS

Figure 6.6 shows the effect of annealing heat treatment on the grain structure evolution from the as-received hot-rolled material, Steel A. During this process the grain size was measured by the linear intercept method. The microstructural analysis of the as received material shows that full dynamic or static recrystallisation had indeed not occurred during and after hot rolling and, therefore, there was no measurable grain refinement from dynamic recrystallisation during hot rolling. In fact, full recrystallisation was observed to have occurred only at temperatures above 1000 °C. With annealing at temperatures below 1000 °C, the grain size evolution shows that only recovery had taken place and only a minimal level of grain growth was observed.

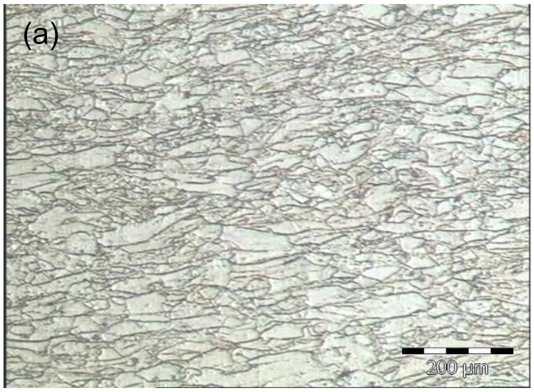

As received

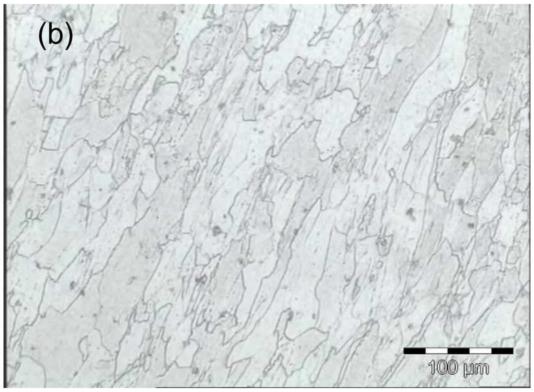

850 °C

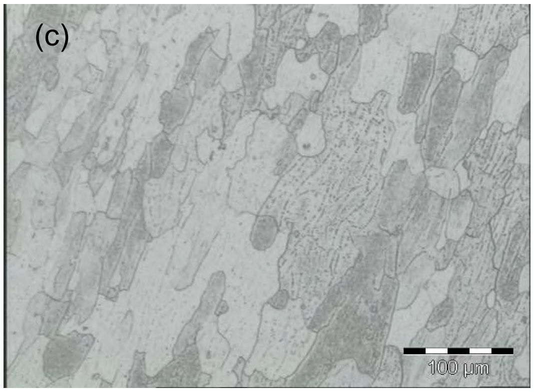

875 °C

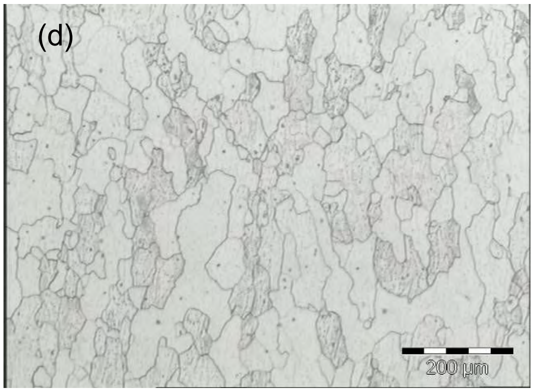

900 °C

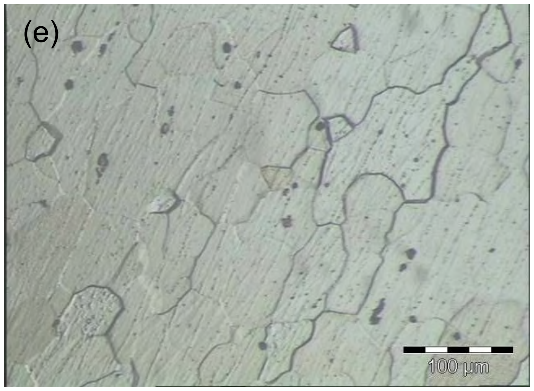

950 °C

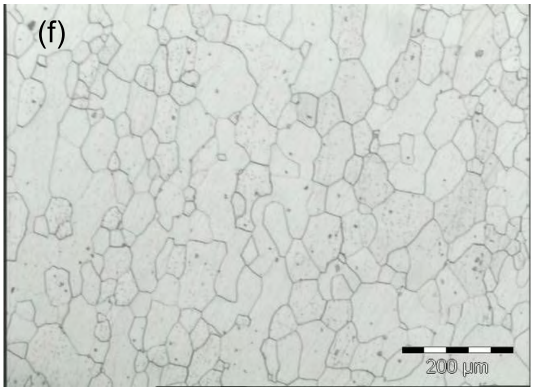

1000 °C

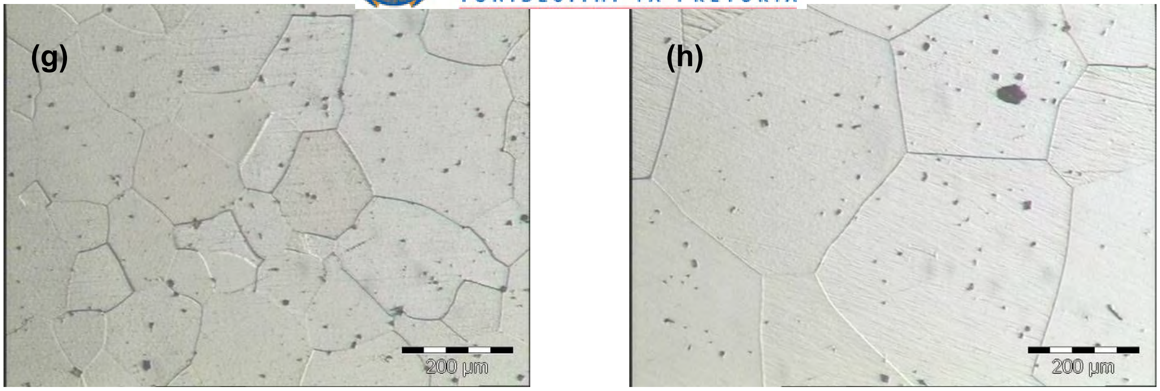

1050 °C **1100 °C**

Figure 6.6. Optical micrographs of the specimens from Steel A after annealing at different temperatures for 30 minutes followed by water quenching (In comparing the microstructures, note the differences in magnifications).

The SEM and TEM results also indicate that the volume fraction of fine Laves phase precipitates tends to decrease as the annealing temperature increases towards the solvus (see Figure 6.7 and 6.9, respectively), as would be expected also from the Thermo-Calc® predictions. Both micrographs show that the Laves phase has precipitated on the sub-grain and grain boundaries and only small amounts are found within the grains. This indicates that the Laves phase possibly nucleates firstly at the sub-grain and grain boundaries and then, only after site saturation, within the grain matrix. With annealing temperatures above 900 °C, complete dissolution of the Laves phase is observed, and the grain's microstructure has fully recrystallised. At annealing temperatures between 700 °C and 850 °C, the TEM micrographs show that there is a higher volume fraction of the grain boundary Laves phase, and these precipitates have coalesced to form stringers. It is these grain boundary precipitates that would later result in embrittlement of this material. In the study done by Sawatani et al [8] the same observation was also made, and they have found that the quantity of the precipitates in their as-hot rolled material, reaches a maximum after being annealed and slowly cooled from about 700 °C but that the volume fraction then decreases with slow cooling from above 900 °C. They have also observed that the Laves phase dissolves into a solid solution at an annealing temperature of over 900 °C, and this finding coincides with the results of the XRD and TEM analyses, where Laves phase was detected only at temperatures up to 850 °C.

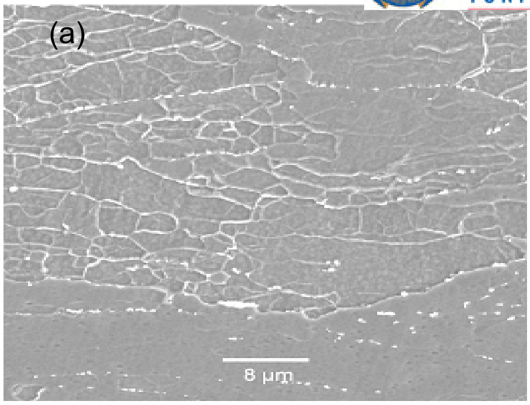

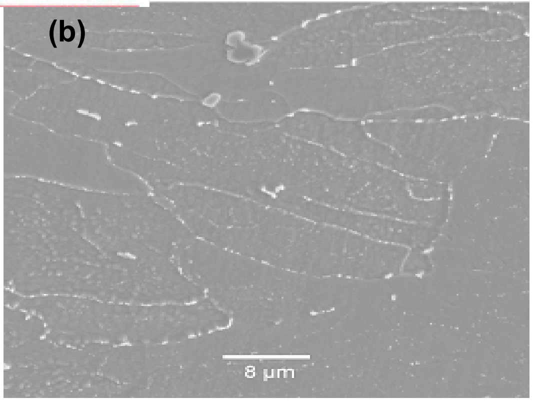

As received

850 °C

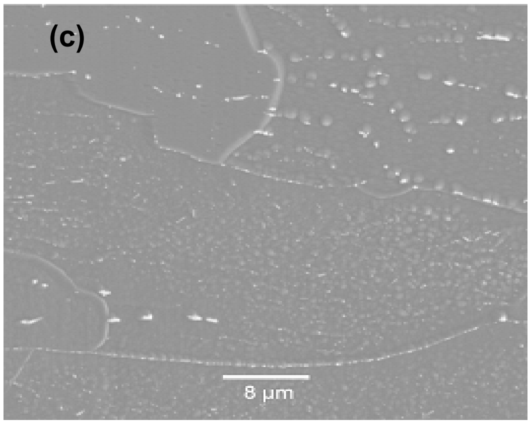

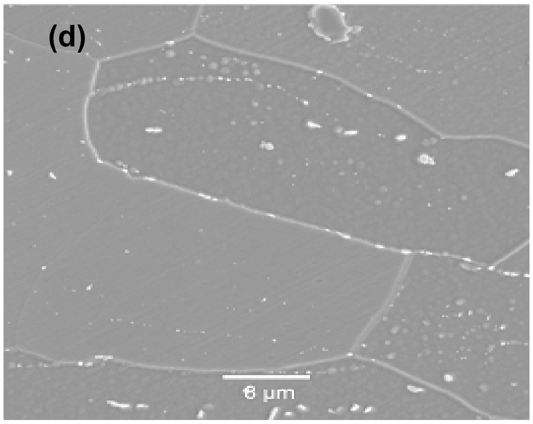

875 °C

900 °C

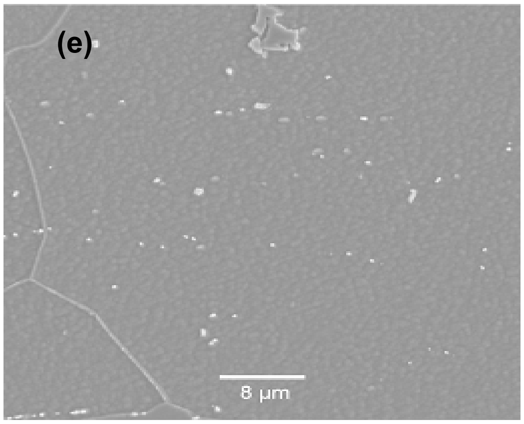

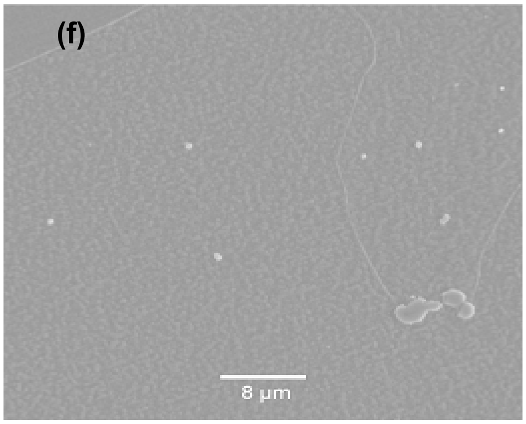

950 °C

1000 °C

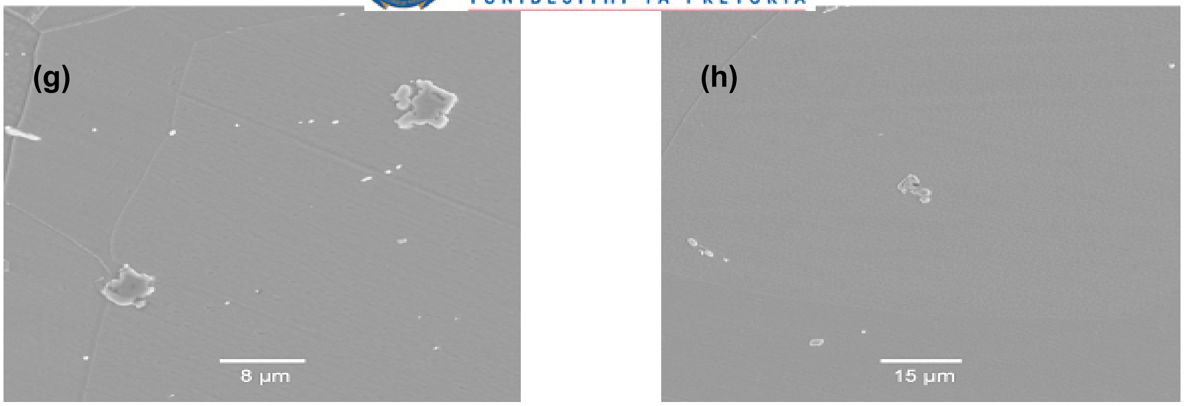

1050 °C 1100 °C

Figure 6.7. SEM micrographs of Steel A showing the effect of annealing temperature on the morphology of the second phase.

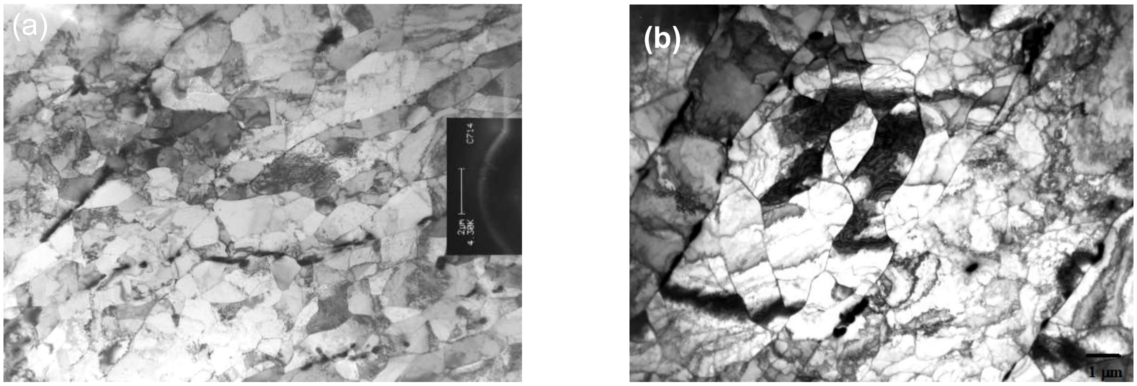

As received 600 °C

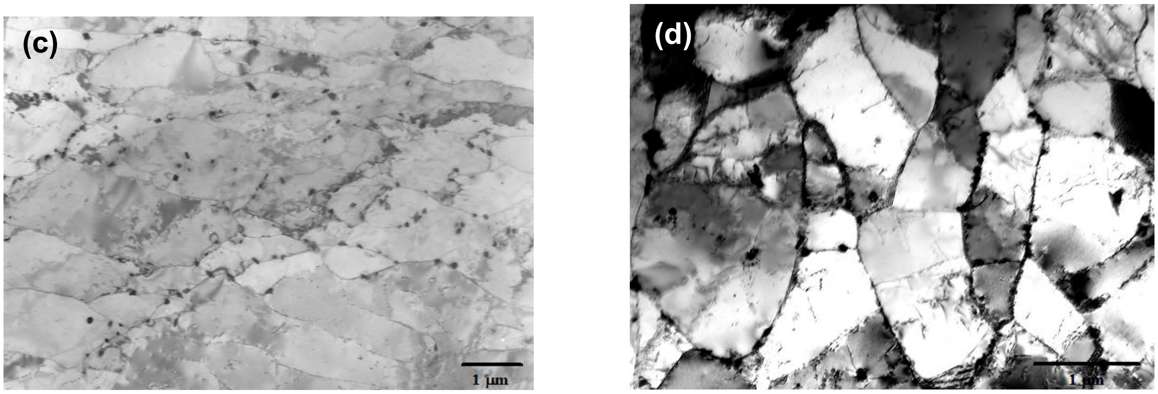

650 °C 700 °C

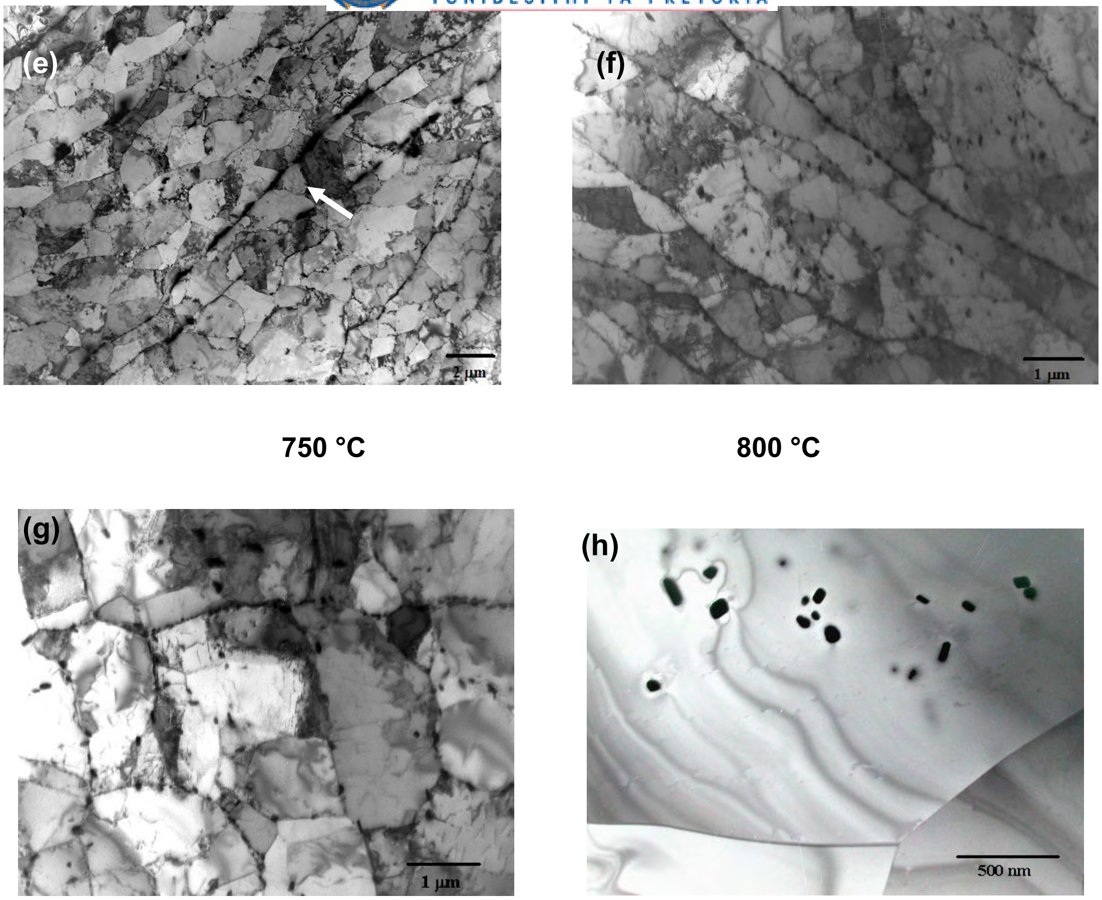

750 °C

800 °C

850 °C

900 °C

Figure 6.8. TEM micrographs from Steel A showing the presence of the fine Laves phase precipitates on the subgrain boundaries of the specimens that were annealed at the shown different temperatures for 1 hour and then water quenched.

6.3.2 PRECIPITATE'S MORPHOLOGY

Transmission electron microscopy micrographs (TEM) of the dislocation structures in the specimen annealed at 700 °C and then water quenched, are shown in Figure 6.9. The precipitation of Fe_2Nb particles on the dislocations and subgrain boundaries are shown in Figure 6.9 (a & b). The halo surrounding these particles within the grains is believed to be associated with the strain fields surrounding these particles [92]. Nucleation of the Fe_2Nb occurs firstly on grain boundaries, then at dislocations, and at a later stage within the matrix. In the work by Li [131] on the precipitation of Fe_2W Laves phase in a 12Cr-2W alloy, the author observed that Laves phase particles on grain boundaries are coherent with one grain but grow into the adjacent grain with which they do not have a rational orientation relationship. This is due to the higher mobility of the incoherent interface if compared to the semi- or coherent one. This may also be clearly seen in this

Steel A on the "horizontal" grain boundary in the middle of Figure 6.9 (a) where all the Laves phase particles appear to be growing only into the top grain.

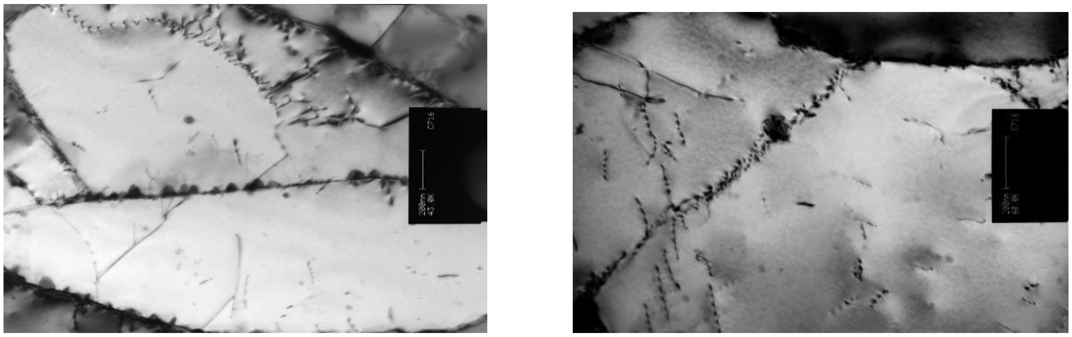

(a) **(b)**

Figure 6.9. Thin foil electron transmission micrographs from steel A, annealed at 700 °C for 1 hour and then water quenched. The micrographs show (a) the nucleation of the Laves phase precipitates on grain boundaries and dislocations and (b) some fine matrix precipitates surrounded by a strain halo as well as dislocation nucleated precipitates.

6.3.3 MECHANICAL PROPERTIES

The results from the V-notch room temperature Charpy impact tests on specimens solution treated at different temperatures and water quenched of the process embrittled Steel A, are shown in Figure 6.10. The Charpy Impact Energy (CIE) shows a maximum of about 60 J for the specimens that had been annealed at 850 °C, which coincides with the predicted Laves phase solvus temperature, but with a decreasing CIE with annealing on both sides of this temperature. In the specimens that had been annealed at 900 °C and above where no Laves phase is present, the impact energy averaged only about 10 J. It can be concluded that above 850 °C, a grain size effect from grain growth plays a major role in lowering the impact energy, but below 850 °C, the precipitation of the intermetallic Laves phase contributes to the lowering of the impact toughness. Comparing these results with the prediction from Thermo-Calc® (Section 5.7), it can be seen that as the volume fraction of the Laves phase decreases in the steel with a rise in the annealing temperature towards 850 °C, the impact toughness also increases to its maximum of 60 J at 850 °C. Beyond 850 °C grain growth plays a major role in embrittling this ferritic steel, a problem that is well known in most ferritic stainless steels.

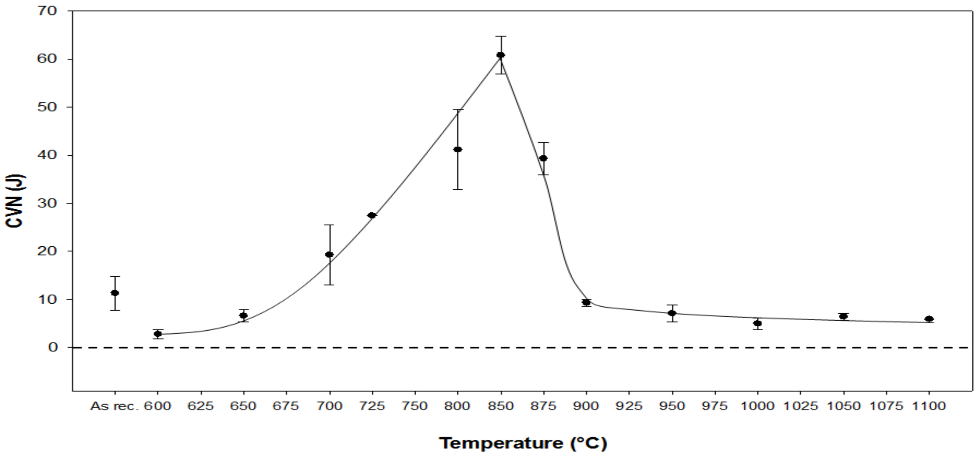

Figure 6.10. Effect of annealing temperature on the room temperature Charpy impact energy of the as hot rolled and annealed AISI 441 stainless Steel A. The samples were annealed for 30 minutes and then water quenched.

Typical fracture surfaces from specimens after annealing at different temperatures are shown in Figure 6.11. In Figure 6.11 (a) the micrograph is shown of the as received and process embrittled Steel A with a CIE of only slightly above 10 J, with the fracture surface showing both macro- and micro-voids in a dimpled surface, which is characteristic of a ductile failure although the CIE was actually relatively low. The (Ti,Nb)(C,N) particles are readily identifiable as “blocky” precipitates, as clearly seen in Figure Figure 6.12 (b). These macro-voids appear to be formed by the presence of these large cuboidal particles which indicates a low cohesive force between these carbo-nitride precipitates and the steel matrix. These precipitates are, therefore, possibly not the direct cause of the brittleness of the alloy. The presence of the Laves phase on the grain boundaries (see Figure 6.7 and Figure 6.8 (as received)) must then have contributed to the brittleness of these materials, but the exact mechanism could not be revealed from the fractured surface analysis.

Figure 6.11 (c & d) show the fractographs of the specimen that had been annealed at 850 °C where the maximum CIE was found, indicating that fracture had occurred in a ductile manner. Noticeable, however, are the large numbers of voids situated on a few of the grain boundaries in Figure 6.11 (d), indicating the presence of particles on some of these grain boundaries, most likely the last remaining Laves phase. There are, however, no further significant or obvious differences in the observed failure mode between the hot rolled as received material with a CIE of only about 10 J and the sample annealed at 850 °C with a CIE of 60 J, except that there are also a few Laves phase precipitates present on the grain boundaries of the as received steel (see Figure 6.7(a)) whereas the steel annealed at 850 °C, according to Thermo-Calc® should have had no Laves phase in its microstructure. Previous studies have shown that the presence of the Laves phase degrades the mechanical properties of this high chromium ferritic steel where ever this phase is formed within the temperature range of 500 – 750 °C [132]. Figure 6.11 (e & f) show the fracture surfaces of the specimen that had been annealed at 900 °C; which shows transgranular cleavage fracture with individual grains identified by changes in the directions of the river markings. Figure 6.11(f) shows the specimen displaying microcracks that are clearly visible on the fracture surface. Evidence suggesting cleavage or grain boundary microcracking was occasionally observed, but little role of microstructure in the crack initiation process could be directly observed.

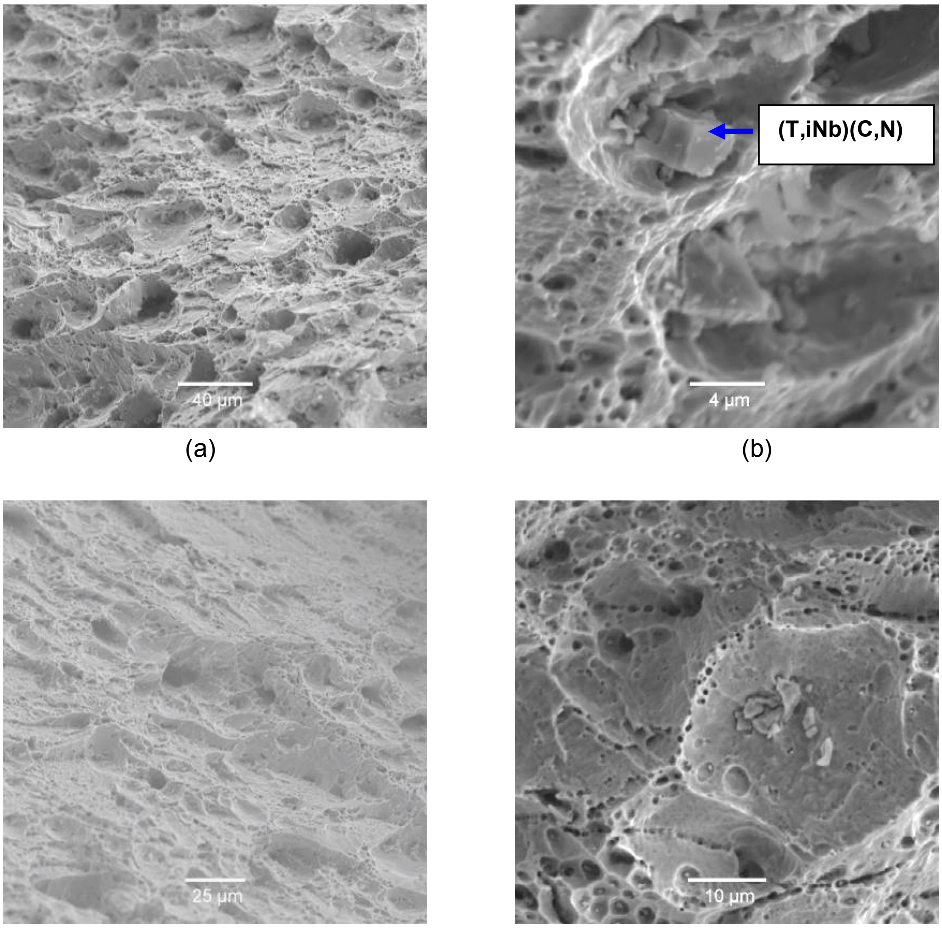

(a) (b)

(c) **(d)**

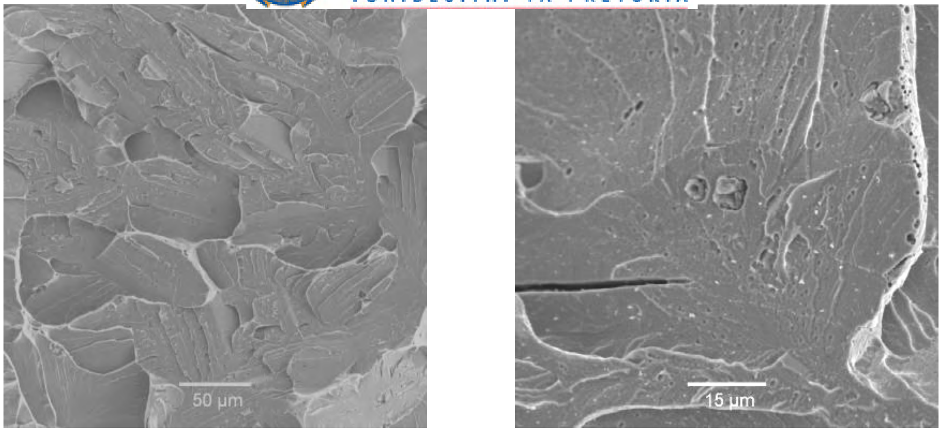

(e) (f)

Figure 6.11. Examples of the Charpy fracture surfaces at different magnifications of steel A (a & b) from the as received specimen; (c & d) after annealing at 850 °C; and (e & f) after annealing at 900°C.

6.3.4 EFFECT OF GRAIN SIZE ON THE MECHANICAL PROPERTIES OF STEEL A

Figure 6.12 shows the variation of the hardness and grain size as a function of the solution annealing temperature above 850 °C, i.e. where there should not be any Laves phase present in the Steel A but where grain growth is expected. The results indicate that there is a steady decrease in the Vickers hardness whereas the as-received and brittle hot-rolled steel shows a much higher hardness than that of the specimens that had been annealed in the grain growth region. This can not be attributed purely to the grain growth effect since there is only a relatively small difference in grain size between the as-received hot rolled material and the specimen that had been laboratory annealed at 850 °C after hot rolling. This difference in hardness may, however, arise from accumulated strains induced during the hot rolling process in the as received steel, particularly if full dynamic recrystallisation had not occurred. The microstructural analysis of the as received material shows that full dynamic recrystallisation had indeed not occurred, and therefore, there was no measurable grain refinement from dynamic recrystallisation, see Figure 6.13. The presence of the fine grain size and the Laves phase could have contributed to a much higher hardness value of the as received material; but as the steel is further annealed, recrystallisation starts to occur and thereby softens the steel.

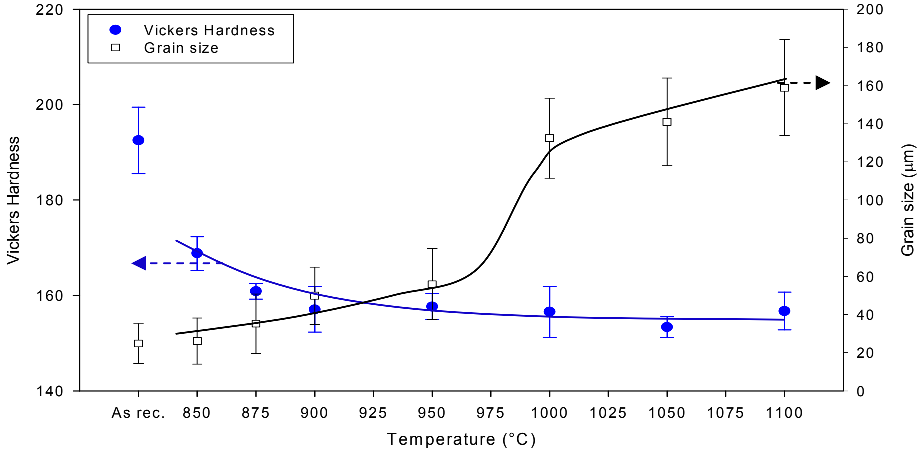

Figure 6.12. **Effect of annealing temperature above 850 °C on the grain size and Vickers hardness for the AISI type 441 ferritic stainless Steel A.**

Figure 6.13. **TEM micrograph showing the presence of a dislocation substructure and some fine Laves precipitates in the as received hot rolled specimen of Steel A, indicating a lack of full dynamic recrystallisation during the last stage of hot rolling.**

The results also show that there is a steady increase in grain size up to about 950 °C, but between 950 °C and 1000 °C there is a sudden and rapid 60 % increase in the grain size. The TEM micrographs of the specimens that were annealed at 850 °C and 900 °C respectively, with the presence of some remnants of Laves phase in the specimen that was annealed at 850 °C, were shown in Figure 6.8. At 900 °C this phase had completely dissolved, see Figure 6.8 for the microstructural evolution during annealing at these temperatures.

Figure 6.14 shows the effect of annealing temperature at and above 850 °C on the tensile properties of the Steel A. Both the 0.2 % offset yield strength and ultimate tensile strength (UTS) decrease whilst the percentage elongation increases with increasing annealing temperature. Significantly, however, the specimen that had been heat treated at 850 °C shows a relatively poor elongation whereas at 900 °C the elongation had already increased significantly, confirming that at 850 °C some last remaining and embrittling Laves phase was still present while at 900 °C it had completely dissolved. The effect of grain growth on the 0.2% yield strength in this steel was tested according to the Hall-Petch relationship, and was found that it only applies in the temperature range of 850 °C to 950 °C but beyond 950 °C, the relationship did not hold.

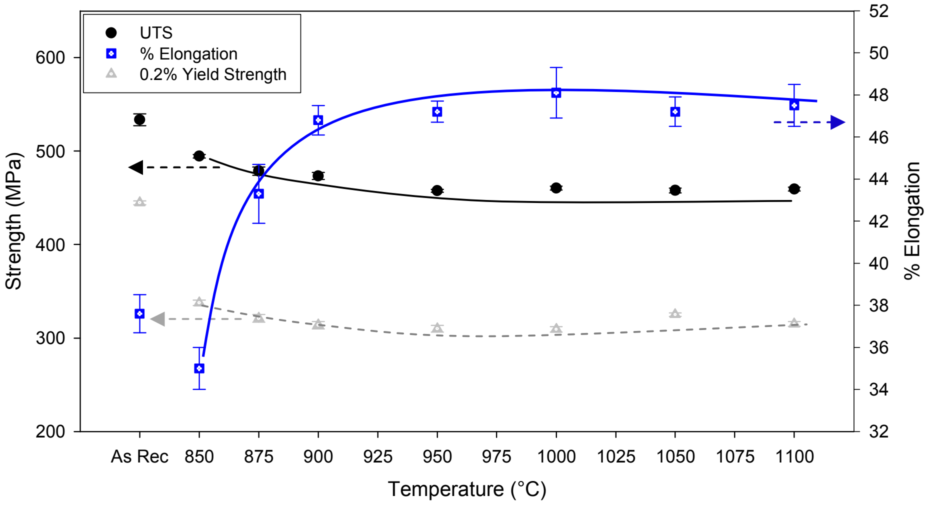

Figure 6.14. Effect of annealing temperature at 850 °C and above on the tensile strength and elongation of the 441 stainless steel A.

6.4 EFFECT OF ANNEALING TREATMENT ON THE CHARPY IMPACT ENERGY AND DBTT

The results of Charpy impact tests at various testing temperatures on the heat treated specimens of this 441 ferritic stainless steel (Steel A) are shown in Figure 6.15. The specimens were initially annealed in the temperature range of 600 to 950 °C for 30 minutes and subsequently quenched in water. The specimen that was quenched from 850 °C exhibits a maximum toughness of about 60 J at 25 °C and a Ductile Brittle Transition Temperature (DBTT) of about 5 °C at about 30 J. Solution treatment at 950 °C resulted in the DBTT to be as high as 40 °C, in comparison with the steel treated at 850 °C while all these specimens fractured in a brittle manner. On the other hand, the upper shelf energy for the specimen solution treated at 950 °C was found to be much higher, averaging about 90 J.

The grain size of the heat treated samples varied from about 22 to 60 μm as the annealing temperature was increased from 850 to 950 °C (see Figure 6.15). The DBTT was observed to rise with increasing grain size from both specimens, but the upper shelf energy seemed to be independent of the grain size. This could be caused by the presence of some Laves phase on the grain boundaries still present in the specimen that was annealed at 850 °C, resulting in lowering the upper shelf energy to about 60 J compared to 90 J in the specimen that was annealed at 950 °C.

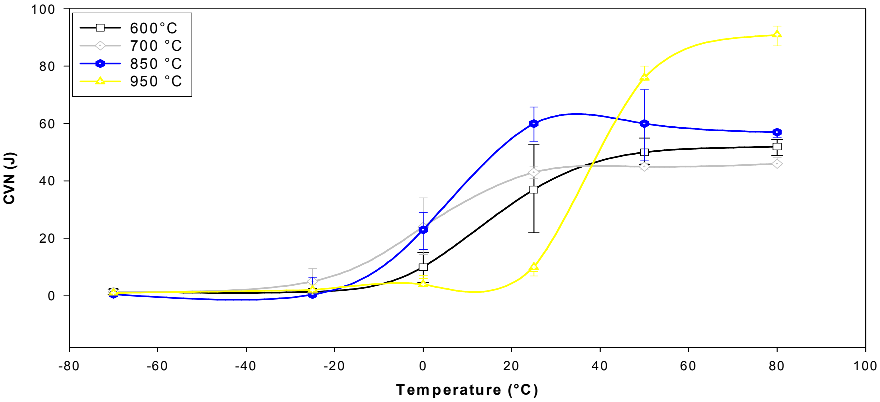

Figure 6.15. Charpy impact energy of the 441 ferritic stainless steel A as a function of the test temperature from specimens that were annealed at four different temperatures, both within and outside the Lave phase formation region.

6.5 Effect of Re –embrittlement treatment on The Room Temperature Charpy Impact Energy

6.5.1 Effect Of Cooling Rate

The effect of cooling rate on the room temperature impact toughness of the steel after annealing at 850 °C and 950 °C respectively for 5 min in the Gleeble simulator followed by forced helium cooling at different linear cooling rates, is shown in Figure 6.16. The aim of this exercise was to simulate the effect of the post-hot rolling cooling rate on the final grain size and on the precipitation of Laves phase and hence their impact on the Charpy impact energy to provide process guidance on the importance of rapid cooling rates after the final stage of hot rolling. As observed before, rapid cooling from 850 °C gives a higher impact energy than after cooling from 950 °C, and this is caused initially by a difference in grain size. This can be observed from the specimens that were subject to cooling rates of about 50 °C/s, where there was a difference of 34 J in the upper shelf energy between the specimens annealed at 850 °C and 950 °C respectively, see Figure 6.16, with results that are comparable to those in Figure 6.10. Note furthermore, that the impact strength after cooling from 950 °C is only marginally affected by differences in cooling rate while this is not so after cooling from 850 °C where faster cooling results in smaller volumes of Laves phase forming during cooling and, hence, in higher impact strengths. This difference is significant as it proves that the embrittling effects of a large grain size introduced by cooling from 950 °C, overrides any further embrittlement by Laves phase caused by slow cooling. Embrittlement in these ferritic stainless steels from a larger grain size, therefore, appears to be even more deleterious than that of Laves phase if both are present together.

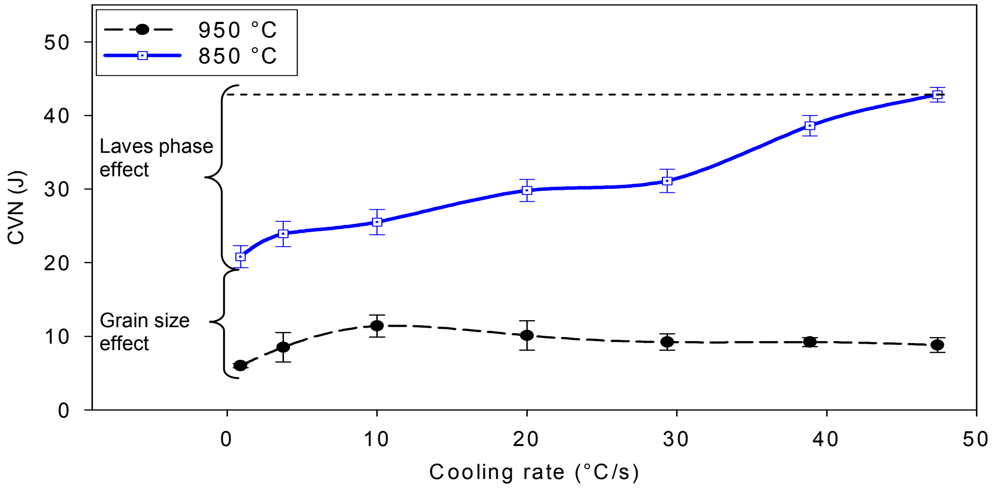

Figure 6.16. Effect of linear cooling rate in °C/s on the room temperature impact toughness of the specimens from Steel A that were cooled at linear cooling rates from 850 °C and 950 °C, respectively.

In relation to the observed toughness behaviour, the Laves phase precipitation behaviour was considered. The metallurgical observation from the two samples that were solution treated at these temperatures and cooled at 60 °C/s, shows two completely different microstructures, see Figure 6.17. After solution treatment at 850 °C, the microstructure has not recrystallised and the electron micrograph shows the presence of a subgrain structure in Figure 6.17 (a & b). Solution treatment at 950 °C, however, shows that the microstructure has now fully recrystallised and is without any subgrain structure in Figure 6.17 (c & d). In both cases, there are few large particles still present that were analysed as niobium carbo-nitride, Nb(C,N) using TEM EDX.

Figure 6.18 shows the effect of the cooling rate on the precipitation of the Fe_2Nb Laves phase after cooling at a rate of 1 °C/s. Figure 6.18 (a & b) show a band of fine precipitates from the samples that were solution treated at 850 °C and 950 °C and then cooled slowly, respectively. Note that these fine precipitates are found on the grain boundaries in the sample that was solution annealed at 850 °C, whereas in the sample that was solution treated at 950 °C, these precipitates where observed within the grains.

This suggests that the Laves phase can precipitate homogeneously in a coarse grain microstructure. The volume fraction of the Laves phase in the steel decreases with increasing cooling rates, as seen in Figure 6.17 and Figure 6.18. From this investigation, the quantitative work on the amount of the Laves phase precipitated from the two solution annealing temperatures was then carried forward.

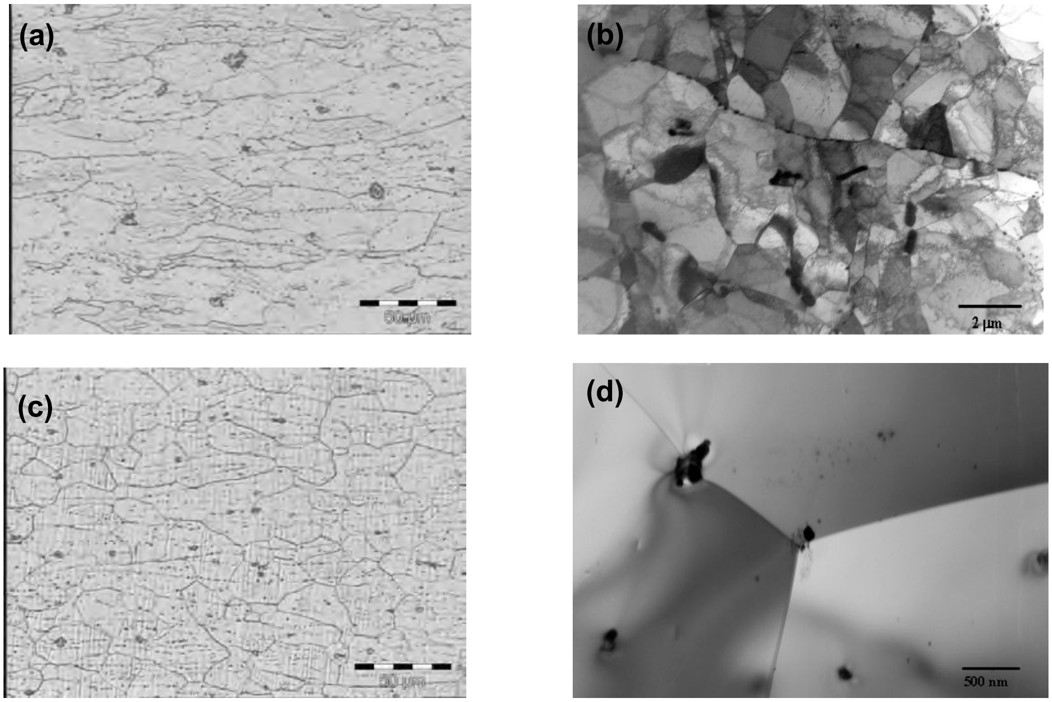

Figure 6.17. TEM micrographs of the samples of Steel A that were solution annealed at 850 °C and 950 °C for 5 min then cooled at 60 °C/sec. (a & b) solution treated at 850 °C; (c & d) solution treated at 950 °C. Note the differences in the microstructures from both samples.

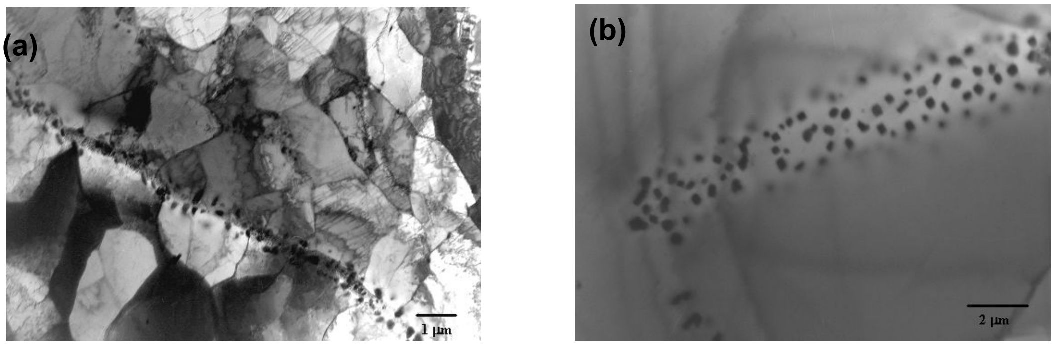

Figure 6.18. TEM micrographs of the samples from Steel A after being cooled at 1 °C/sec from: (a) solution annealed at 850 °C and (b) 950 °C for 5 min before cooling.

The effect of the cooling rate on the amount of Laves phase precipitated from the specimen annealed at 850 °C is shown in Figure 6.19. As the cooling rate increases, the amount of the Laves phase formed decreases and the Charpy impact value increases (see Figure 6.16). This serves as evidence showing that the volume fraction of the Laves phase plays an important role in embrittling this steel. In the work by Sawatani et al.[8], they have also found that a large amount of fine Laves phase nucleates first at the grain boundaries and then within the grains during cooling. As the cooling rate becomes lower, the amount of Laves phase that forms increases, as would be expected. These large amounts of precipitates were found to increase the strength and decrease the elongation [8,69], whilst also decreasing the toughness of the steel. The toughness and ductility can be recovered by heating the material again to above 900 °C to dissolve the Laves phase, followed by rapid cooling.

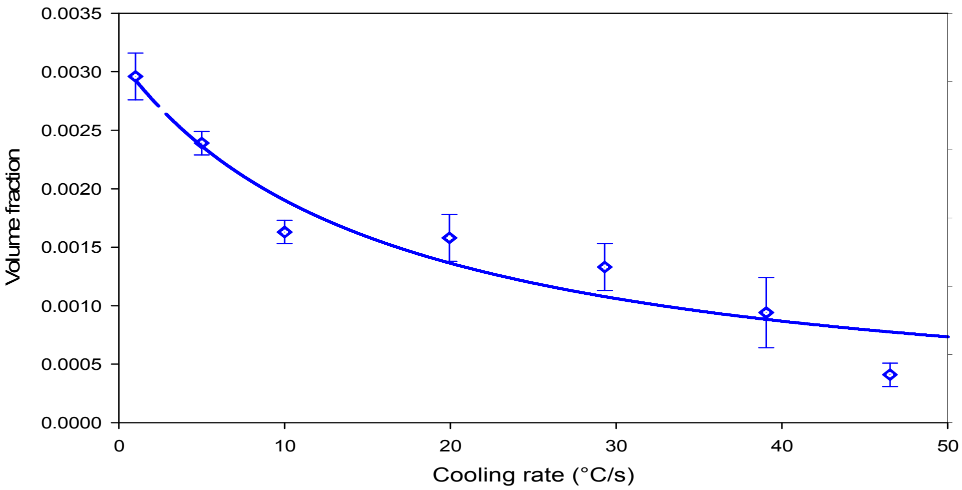

Figure 6.19. Effect of the cooling rate on the volume fraction of the Laves phase in Steel A after cooling at different rates from annealing at 850°C.

6.5.2 EFFECT OF THE REHEATING TREATMENT

The results of the Steel A samples that were reheated at 600 °C to 900 °C for 30 minutes after being solution treated at 950 °C for 1 hour, are shown in Figure 6.20. The aim of these tests was to dissolve the Laves phase completely and then re–precipitate them at the different annealing temperatures. After the reheating treatment, all the samples show a significant decrease in both ductile-to-brittle transition and upper-shelf energy. All the samples that were supposed to be embrittled have a transition temperature of about 15 to 18 °C. Solution treatment at 950 °C resulted in the DBTT to be as high as 40 °C, in comparison with the steel treated at 800 °C while all these specimens fractured in a brittle manner, due to a large grain size that originated from annealing at 950 °C. The upper shelf energy seemed to be independent of the Laves phase precipitation. Figure 6.21 shows the microstructural evolution during the reheating treatment; and from this optical micrograph the grain boundary Laves phase precipitates could be observed. At both 600 and 900 °C, there are few precipitates present as compared to the specimens annealed at 700 and 800 °C. The hardness results in Figure 6.22, show the effect of this Laves phase re-precipitation on the hardness values of the Steel A. The result shows a slight increase in the hardness value at the annealing temperature of 700 °C, then the hardness decreases with annealing at higher temperatures. Comparing these results with those from Figure 6.22, it can be concluded that there is no clear correlation between the Laves phase precipitation and the Charpy upper shelf energy.

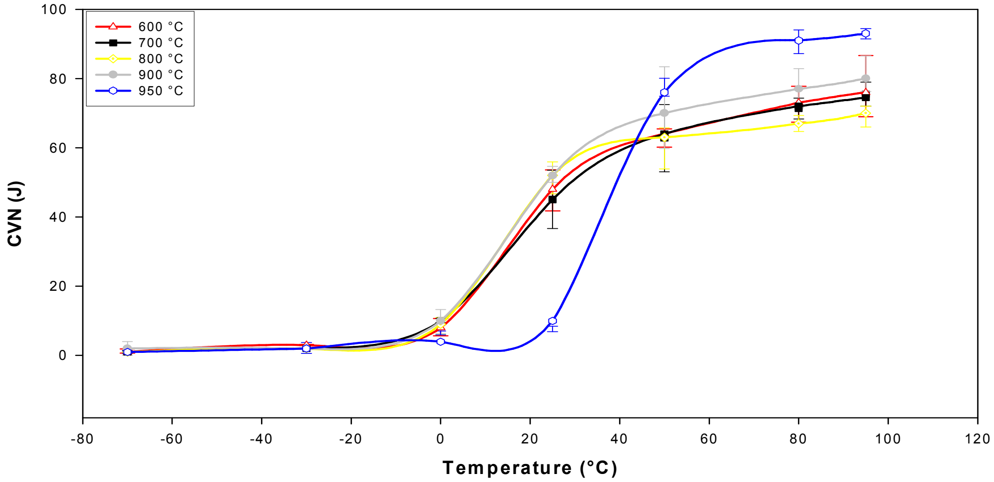

Figure 6.20. Charpy impact energy of Steel A as a function of the test temperature of specimens first solution annealed at 950°C and then re-annealed at different temperatures.

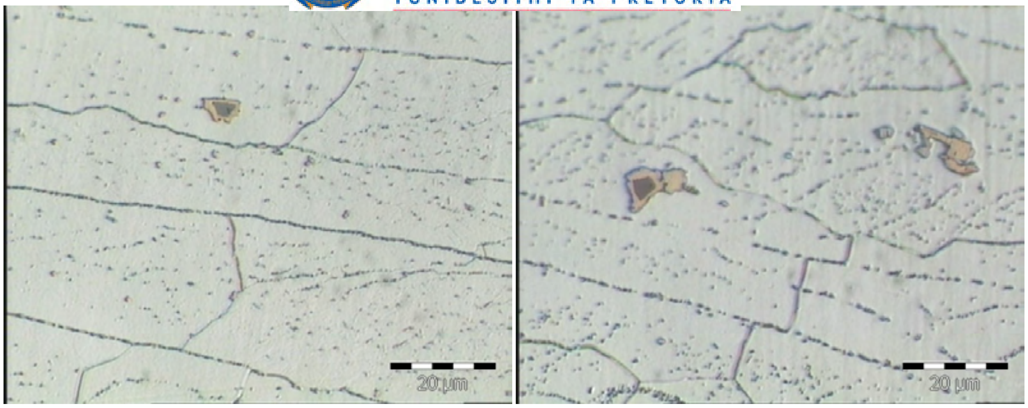

600 °C **700 °C**

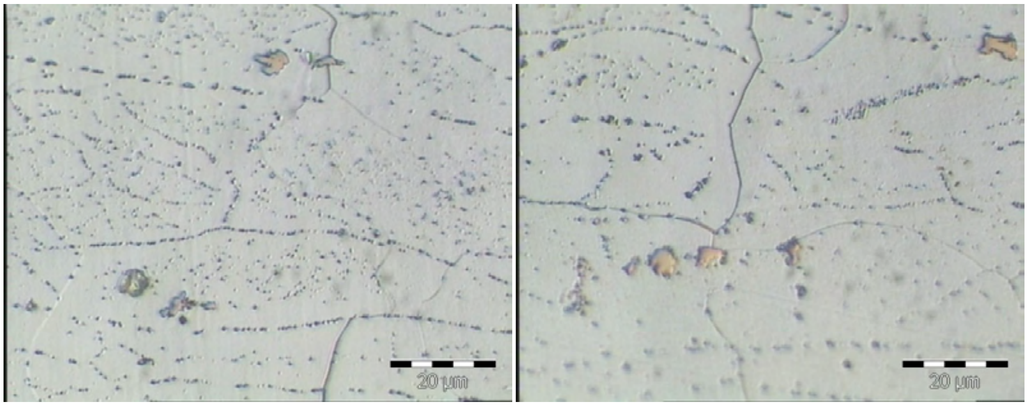

800 °C **900 °C**

Figure 6.21. Optical microscopy micrographs showing microstructural evolution in Steel A during re – heating treatments after an original solution treatment at 950°C.

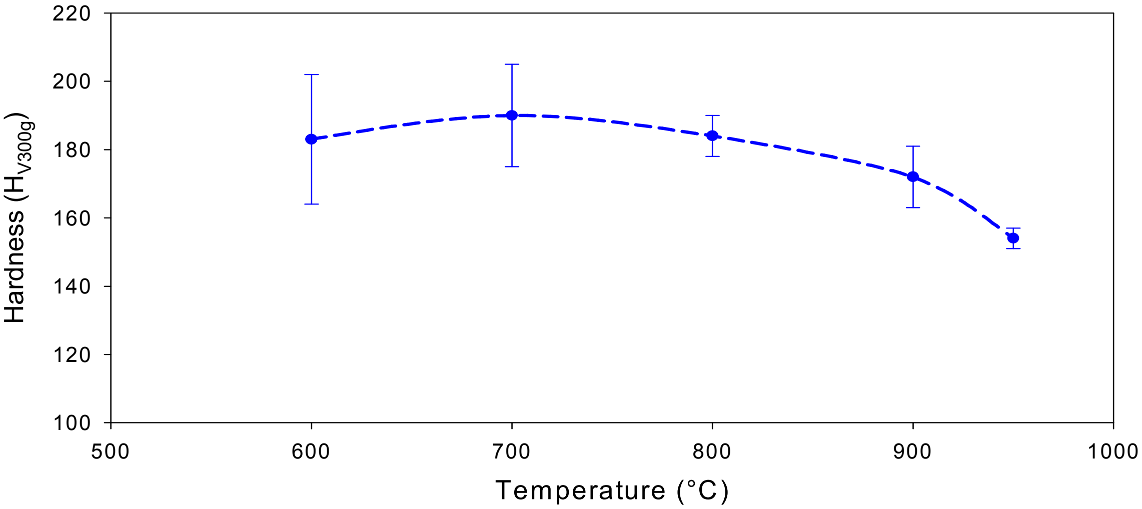

Figure 6.22. Effect of the Laves phase re-precipitation in Steel A on the hardness of the material during embrittlement treatment after an original solution treatment at 950°C.

CHAPTER SEVEN

EXPERIMENTAL RESULTS

EFFECT OF THE STEEL'S COMPOSITION

7.1 EFFECT OF ANNEALING TREATMENT ON STEEL B

In order to understand the precipitation behaviour of the Laves phase more precisely, an AISI type 441 (Steel B (0.149%Ti-0.445Nb-0.008%Mo)) that did not fail during processing was used. The Charpy impact specimens from this steel were annealed at temperatures between 850 °C and 950 °C for 30 minutes followed by quenching into water. The quantity of precipitates in the steel after annealing was then electrolytically extracted and the volume fraction of Laves phase was measured and calculated through powder XRD. The results in Figure 7.1 show that after annealing at 850 °C, the amount of Laves phase has decreased to about 0.13% from the 0.2% in the as received condition, and annealing at 950 °C, a further decrease to about 0.05% occurred. A small remnant of Laves phase of about 0.05% volume fraction was still found in this steel, even after annealing at the temperature of 950 °C. This contrasts with the calculated solvus temperature of about 800 °C as was found by Thermo-Calc® for this particular steel.

The Charpy impact tests, however, reveal that after annealing at 850 °C, the remaining quantity of Laves phase of about 0.15% does not reduce the CIE as significantly as did the larger Laves phase volume fraction of 0.2% on the grain boundaries upon hot rolling in the as received material. In this particular steel it, therefore, appears that a critical maximum volume fraction of Laves phase that may avoid significant impact embrittlement is about 0.15% although this particular value may also depend on the size of the Laves phase particles on the grain boundaries and on the precise alloy composition. With annealing at 950 °C, grain growth starts to affect the CIE value and the very small volume fraction of about 0.05% of remaining Laves phase is probably insignificant.

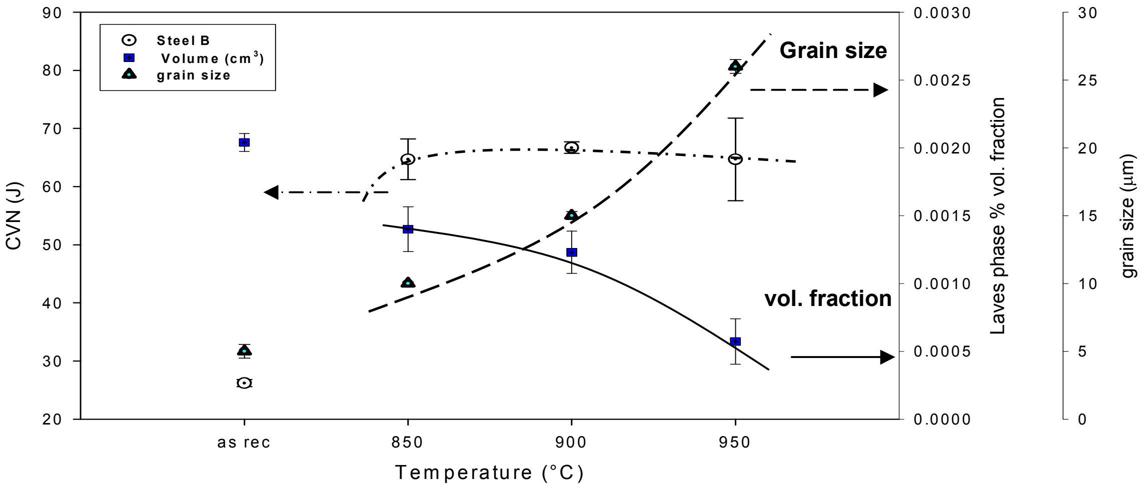

Figure 7.1. Effect of annealing treatment on the Laves phase's % volume fraction, grain size and the Charpy impact toughness of the 441 ferritic stainless steel, Steel B.

7.2 EFFECT OF THE EQUILIBRIUM LAVES PHASE VOLUME FRACTION ON THE ROOM TEMPERATURE CHARPY IMPACT ENERGY

In the above experiment discussed in Section 7.1, a constant annealing time of 30 minutes was used at various temperatures to vary the volume fraction of the Laves phase, i.e. at lower temperatures it may be that equilibrium conditions had not been fully achieved. A second set of Charpy specimens was then used with annealing at a constant temperature of 800 °C but with now varying the time to study any possible effects of achieving or not achieving equilibrium conditions in the Laves phase formation. The Charpy impact specimens were, therefore, heated at 800 °C for a period of between 5 minutes and 300 minutes followed by quenching into water and then the quantity of the Laves phase precipitates was measured. The results are given in Figure 7.2, which show that in the as received hot rolled material which had a relatively high volume fraction of about 0.2% of Laves phase, this had resulted in lowering the CIE to about 25 J, and after annealing at 800 °C for 5 minutes, 33% of the Laves phase had already dissolved in this steel and this resulted in a large improvement in its CIE to above 50 J. Further annealing periods did improve the CIE only marginally to about 60 J. It, therefore, appears that equilibrium conditions are neared relatively quickly in the first few minutes of annealing at 800 °C with only a small time dependence after longer annealing times.

Considering the change in volume fraction in Figure 7.2 it appears that the dissolution of the slightly more than 0.2% Laves phase in the starting or as received material, takes place very rapidly with only about 0.07% left after 5 minutes at 800 °C. A very small degree of "overshoot" then seems to take place in the dissolution rate before equilibrium is established after 30 to 60 minutes at 800 °C. The reasons for such an "overshoot" are not quite clear but it would clearly fall into a non-equilibrium transient process. The very rapid dissolution rate in the first 5 minutes is even more remarkable if one considers that the heating up time within these first few minutes of the 5 mm thick specimens, should really be discounted from these first 5 minutes.

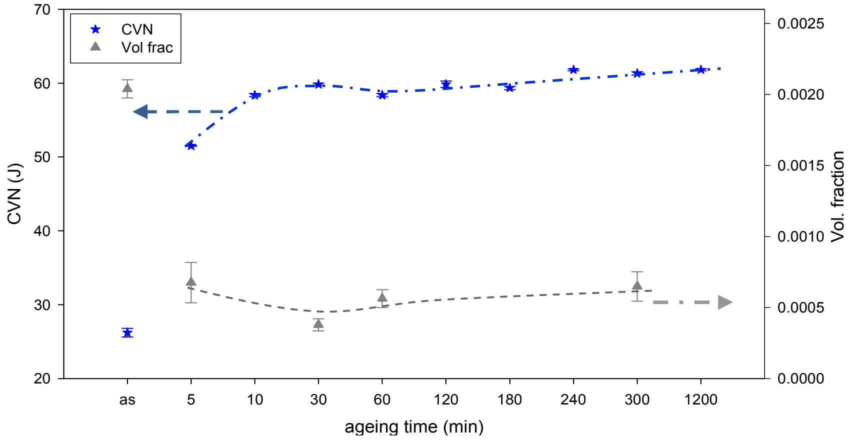

Figure 7.2. Effect of the Laves phase precipitation kinetics on the Charpy impact toughness of Steel B.

Comparing the CIE values in this Steel B with the earlier reported ones for Steel A in Chapter 6, it is surprising that there is only about 14 J difference in the CIE between the two as received hot rolled materials as processed by Columbus with Steel A rejected by Columbus due its CIE of only about 10 to 11 J and Steel B's 25 J which was accepted by Columbus. Microstructural analysis, however, revealed that Steel B had a much finer grain size than Steel A, and this may have resulted in the higher CIE for Steel B.

Figure 7.3 shows the optical microstructural evolution of Steel B in the as received hot rolled condition and after annealing treatments at different temperatures ranging from 850 to 950 °C. The as received microstructure in Figure 7.3(a) appears to be a partly dynamically recrystallised microstructure or alternatively, a post-rolling statically recrystallised microstructure with some recrystallised grains in an overwhelmingly unrecrystallised microstructure. Note furthermore, that recovery appears to have taken place primarily during static annealing at 850 °C with full recrystallisation only occurring at temperatures of 900 to 950 °C.

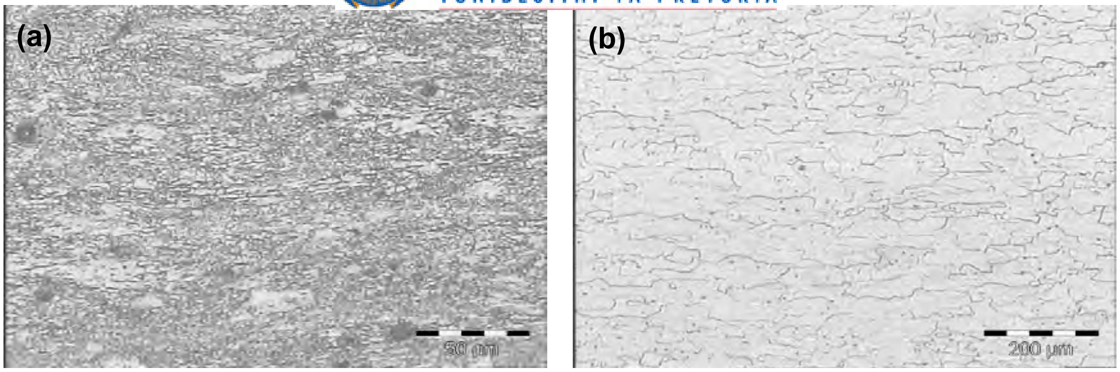

As received 850 °C

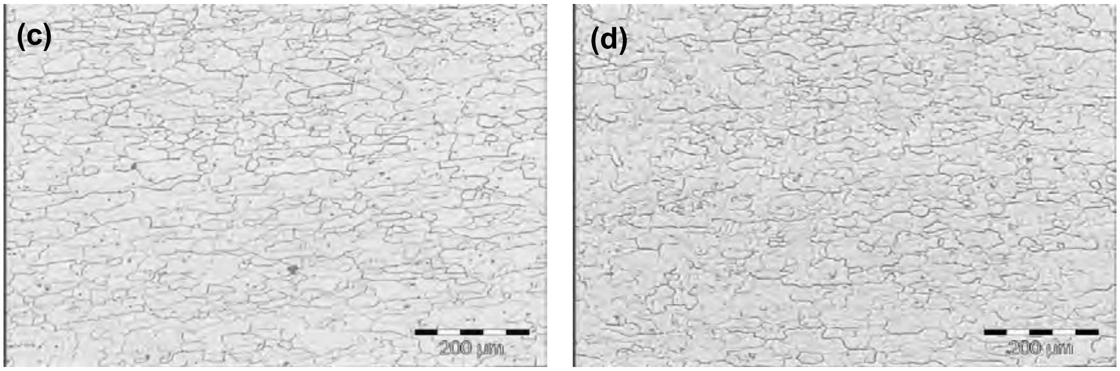

900 °C 950 °C

Figure 7.3. Optical micrographs of the specimens from steel B in the (a) as received plant hot rolled condition and (b) to (d) after being annealed at different temperatures from 850 to 950°C for 30 minutes followed by water quenching.

7.3 EFFECT OF ANNEALING TREATMENT ON THE EMBRITTLEMENT OF THE EXPERIMENTAL STAINLESS STEELS C TO E

Figure 7.4 shows the Charpy impact toughness behaviours of Steels C to E as a function of annealing treatment. These alloys are brittle over a very wide range of temperatures with the toughness's averaging below 5 J. It should be noted that some of these results from Steel C (0.36%Nb – 0.171%Ti - <0.01%Mo alloy, i.e. higher in Ti and lower in Nb than the commercial Steels A and B) are scatted between roughly two extremes; i.e. specimens of this steel are either entirely brittle or entirely ductile. Steels D (0.54%Mo) and E (1.942%Mo) are the molybdenum containing steels and they have shown very similar brittle behaviour. This suggests that any Mo additions to a AISI 441 type stainless steel has a negative impact on the toughness of this alloys, no doubt due to the expected higher volume fractions of Laves phase as predicted earlier in Chapter 5 by Thermo – Calc®. Comparing the CIEs of Steel C (Mo-free) to those of the Mo-containing Steels D and E, it can be seen that Steel C had a much higher CIE at a number of annealing temperatures than the other two steels, although at some temperatures this was not the case where Steel C was equally brittle to Steels D and E. Again, this can be related to the quantity of Laves phase in Steel C, as it was previously shown by Thermo-Calc® predictions (see, Chapter 5.) that the Laves phase volume fraction in this steel should be much lower than in Steels D and E. Any Mo additions to a type 441 ferritic stainless steel should, therefore, be avoided.

Secondly, comparing the somewhat erratic CIE behaviour of Steel C (lower Nb and higher Ti contents) with annealing to the more consistent behaviour of the two commercial Steels A and B, one may conclude that lowering the Nb content and raising the Ti content in the dual stabilisation from the standard dual stabilisation, should be carefully considered in practice as it may have negative consequences. This tentative conclusion is, however, somewhat uncertain as these experimental steels also had a much larger grain size (see below) than the two commercial steels and some further studies could be considered to fully prove or disprove this tentative conclusion. The initial observation of the microstructure of the laboratory hot rolled experimental Steels C, D and E prior to any annealing treatment, showed them to have much larger grain sizes, typically more than 150 μm if compared to the plant hot-rolled materials in Steels A and B, see Figure 7.5. The effect of grain size on the toughness of ferritic stainless steels has been well documented over the years, and it is known that a large grain size decreases the toughness of the steel significantly. Because of the larger grain sizes than expected, no further work was done on the brittle behaviour of these three steels although they were still included in the studies to determine the effect of composition on the nucleation and kinetic precipitation behaviour of the Laves phase in these alloys.

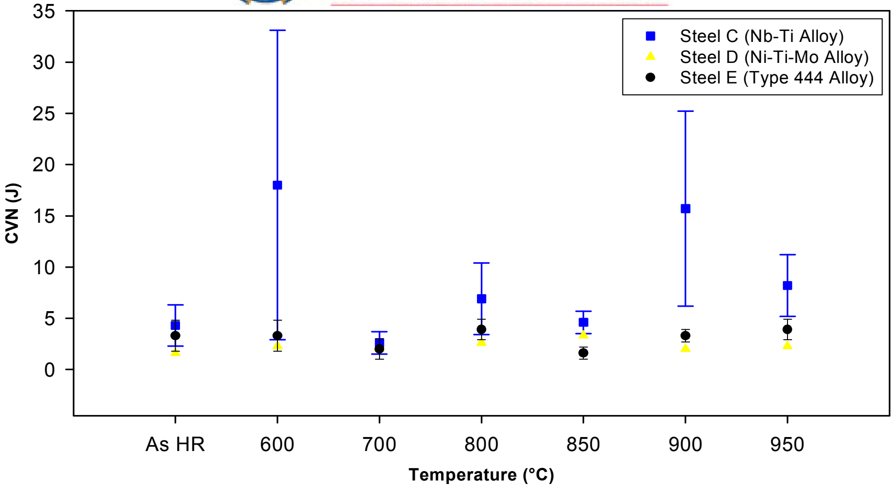

Figure 7.4. Effect of annealing temperature on the room temperature Charpy impact energy of the laboratory hot rolled materials. The samples were annealed for 30 minutes at different temperatures and then water quenched: Steel C (Nb-Ti alloy); Steel D (Nb-Ti-Mo alloy) and Steel E (Type 444 alloy).

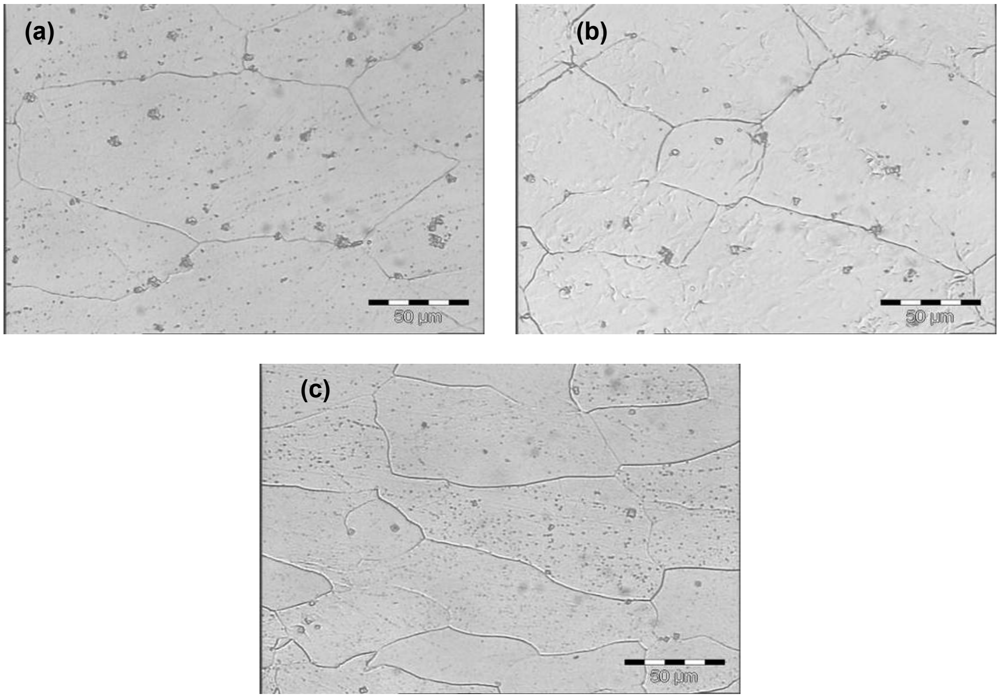

Figure 7.5. The microstructure of the laboratory hot-rolled experimental steels, showing different grain size distributions if compared to those of the commercial Steels A and B: (a) Steel C; (c) Steel D; and (d) Steel E.

CHAPTER EIGHT

EXPERIMENTAL RESULTS

LAVES PHASE KINETICS STUDY

8.1 INTRODUCTION

One of the most important aspects of this research work was to study the transformation kinetics of the Laves phase, in particular its nucleation and the overall volume fraction evolution. The research, therefore, focused on determining the Laves phase volume fraction as a function of time during annealing below 850 °C and this produced a frequently found sigmoidal or S–shaped curve. The transformation kinetics are then described using the well known Johnson–Mehl–Avrami–Kolmogorov (JMAK) type of equations [95]. The following parameters that affect the kinetics of the Laves phase precipitation were considered: annealing temperature and time, the alloy's and Laves phase's composition and the steel's grain size.

8.2 EQUILIBRIUM LAVES PHASE FRACTION

Thermo-Calc® software was first used to estimate the equilibrium Laves phase fraction in Steel A, as a function of temperature, see Chapter 5. All the possible phases, including the carbo-nitrides, were included in the calculations. The equilibrium fraction of the Laves phase as it was formed after long time annealing was then determined experimentally from the Steel A, i.e. the steel which had failed during production. The materials were first annealed at 850 °C for 2 hours in order to dissolve and minimise the Laves phase content and at the same time making sure that there was minimal grain growth, and the material was then quenched into water. The specimens where then annealed at temperatures between 600 and 850 °C for periods ranging from 5 to 1000 minutes and then water quenched. The precipitate residues where electrolytically extracted and analysed from these annealed specimens using XRD techniques. The physical quantity of the precipitates was determined from the relative intensity of XRD lines using a Rietveld technique, which enables the volume fraction – time relationship to be found with fair accuracy. Figure 8.1 shows the typical S-shaped curves plotted from these analyses. Note that the XRD analyses give the fractions in weight fraction, and these values had to be converted to volume fractions using the densities of each phase and using the overall weighed amount of the precipitate residues collected. An example of such a calculation was shown in Section 6.2.1 and the overall results are shown in Figure 8.1.

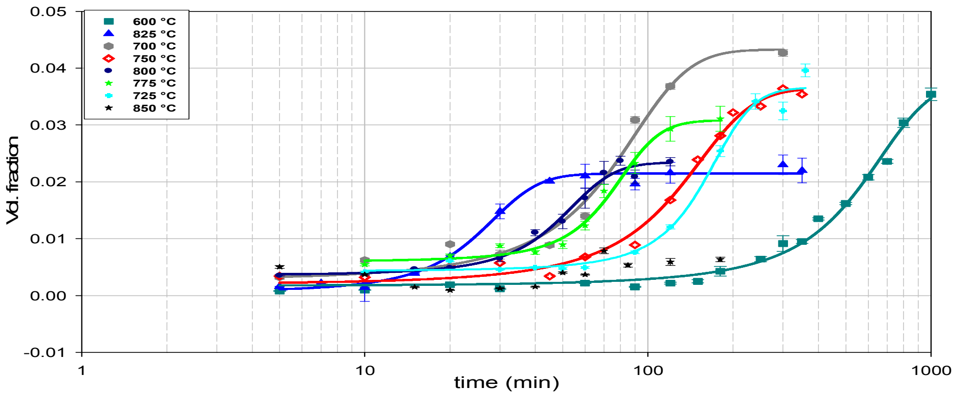

Figure 8.1. The Laves phase volume fraction – temperature/time curves during isothermal annealing in the temperature range 600 °C to 850 °C.

From Figure 8.1, it was observed that for the specimens that were heated at 600 °C, even after annealing for 1000 minutes, the Laves phase transformation had not reached equilibrium and was still continuing. This indicates that although the chemical driving force for Laves phase nucleation should be relatively high at this temperature due to a high undercooling, the lowered diffusivity of Nb atoms at this temperature led to a low overall nucleation rate. Also, it was observed that at 700 °C, the transformation kinetics of the Laves phase are much higher than those of the specimens annealed at higher temperatures of 750 °C and above, i.e. the volume fraction of Laves phase was observed to be much higher at 700 °C than with any other specimen annealed at higher or lower temperatures. This already hints at the possibility of a second lower temperature nose in a TTT diagram for this phase. The same observation was made by Sawatani et al [8], on the Ti and Nb stabilised low C, N – 19%Cr – 2%Mo stainless steel, where they have observed the Laves phase precipitates to be in a far larger quantity after annealing at about 700 °C. At 850 °C in Figure 8.1, the volume fraction of the Laves phase precipitates in Steel A reached a maximum of only 0.005 %, and a proper S-curve could not be established. However, this already shows a discrepancy between the experimental evidence of 0.005% volume fraction remaining at 850 °C versus the Thermo-Calc® prediction that no Laves phase should be present at and above about 825 °C in this Steel A.

8.3 LAVES PHASE TRANSFORMATION KINETICS

The kinetics of an isothermal transformation is usually expressed by the modified *Johnson–Mehl–Avrami–Kolmogorov* (*JMAK*) type of equation:

$$V_v = 1 - \exp\left(-kt^n\right) \qquad \text{Equation 8.1}$$

where V_v is the Laves phase volume fraction, k is the reaction rate constant, and n is the time exponent. From Figure 8.1, the points that fall between 5 and 95 percent on the S- curves (on the specimens annealed in the temperature range of 700 – 825 °C) were used to determined the evolution of the Laves phase by plotting them in the {*lnln [1/(1-V$_v$)]*} vs {*ln t*} relationship, see Figure 8.2. The results produced a linear relationship with the slope n and intercept *ln k*, and the calculated values are shown in Table 8.1. The time exponent values of n were found to range between 1.48 and 1.54, with n at 800 °C the lowest with n = 1.37. The results suggest that Laves phase nucleation takes place on either plane or edge grain boundaries [108].

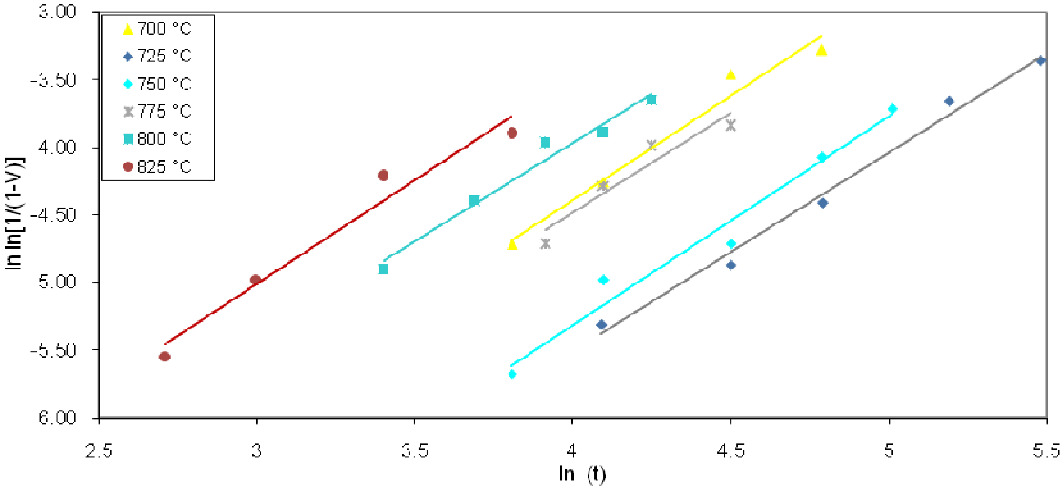

Figure 8.2. The Laves phase transformation curves according to the Johnson–Mehl–Avrami–Kolmogorov (JMAK) type of equation.

Table 8.1. The measure values of the time exponent *n* and the rate constant *k,* obtained from the best fit equation of the plots in Figure 8.2.

Temp (°C)	Best fit eqn	R^2	n	ln k	k
700	y=1.54x – 10.54	0.97	1.54	-10.54	2.65E-05
725	y=1.48x – 11.42	0.99	1.48	-11.42	1.10E-05
750	y=1.48x – 11.23	0.99	1.48	-11.23	1.33E-05
775	y=1.48x – 10.40	0.91	1.48	-10.40	3.04E-05
800	y=1.37x – 9.64	0.98	1.37	-9.64	8.54E-05
825	y=1.54x – 9.61	0.96	1.54	-9.61	6.69E-05

The activation energy for the Laves phase was estimated from the reaction rate constant k which is temperature dependent and can be expressed as :

$$k = A\exp\left(\frac{-Q}{RT}\right) \qquad \text{Equation 8.2}$$

where A is the pre-exponentials factor, Q is the activation energy, R is the gas constant, and T is the temperature. By plotting a linear relationship of *In k vs 1/T,* the activation energy for the Laves phase precipitation was determined as the slope using the following relationship:

$$Q = -R\left(\frac{\partial \ln k}{\partial \frac{1}{T}}\right) \qquad \text{Equation 8.3}$$

and Q was estimated to be 211.3 kJ/mol, a value that is somewhat lower than the activation energy for the diffusion of Nb in a ferrite matrix, which was estimated to be about 240 kJ/mol [103]. It should be noted that this measurement of the activation energy was carried out using only data from the temperature range of 750 to 825 °C as it appears that the precipitation mechanism may be different at lower temperatures than that in this temperature range. If all the data points from all temperatures were used the activation energy was estimated to be much lower, only about 107.5 kJ/mol, possibly suggesting the introduction of enhanced diffusion along grain boundaries into the kinetics.

8.4 TEMPERATURE EFFECT ON ISOTHERMAL TRANSFORMATIONS

The kinetics of the Laves phase transformation were found experimentally at a number of different constant temperatures, and this led to a complete isothermal transformation diagram being drawn. Figure 8.3 is a time – temperature – precipitation (*TTP*) diagram for the Laves phase formation, and it gives the relation between the temperature and the time for the fixed fractions of transformation to be attained. Three of these curves are given in the *TTP* diagram, for the measuring times ($t_{5\%}$ and $t_{95\%}$) for the beginning and end of transformation and for 50% transformation, i.e. $t_{50\%}$. From Figure 8.3, it should be noted that the points on the solid line were determined experimentally and the dash lines are extrapolated estimated lines.

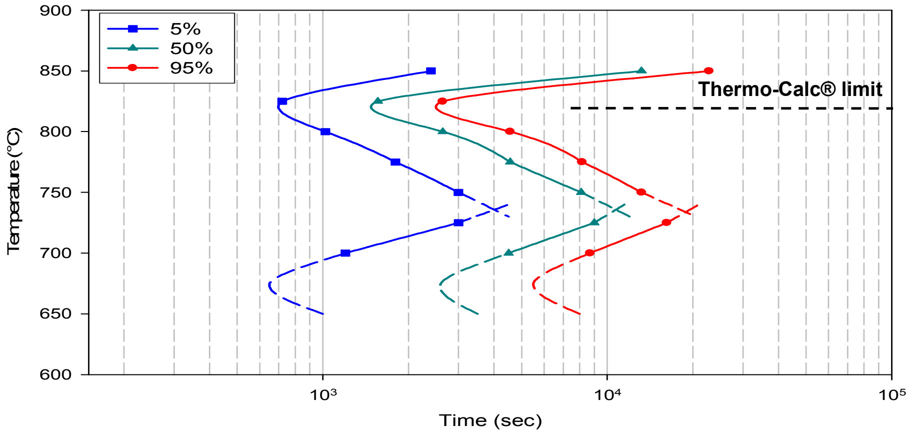

Figure 8.3 A time – temperature – precipitation (TTP) diagram for the Laves phase formation in Steel A.

The results show two classical C noses on the transformation curves, the first one occurring at a higher temperature of about 825 °C and the second one at much lower temperatures, estimated to possibly be in the range of about 650 to 675 °C. Because of extraordinary long annealing times due to the much slower diffusion, it was found to be impractical to find the exact point of this lower temperature nose. The available results, however, are sufficient to show that there are probably two types of the Laves phase transformations controlled by different nucleation mechanisms that are taking place in this steel. In the work done by Silva et al. [133] on the AISI 444 ferritic stainless steel (that is, similar to Steel E from this work, but slightly different in composition), the authors have also estimated the C nose of the transformation curve to be around 800 to 850 °C. Thermo-Calc® predictions on this Steel A have estimated the solvus temperature of the Laves phase to be 825 °C, but the experimental results indicate that the Laves phase still exists up to the temperature of 850 °C or even more.

8.5 EFFECT OF THE GRAIN SIZE ON THE TRANSFORMATION KINETICS OF LAVES PHASE

The transformation kinetics of the Laves phase were compared in two specimens from Steel A with different grain sizes, with the objective to evaluate the effect of grain size on the formation of the Laves phase precipitates in this AISI type 441 ferritic stainless steel. The materials were first annealed at the temperatures of 850 °C and 950 °C for 2 hours and then water quenched. The corresponding linear intercept grain sizes were determined to be 49.9 µm and 152.1 µm, respectively from which the grain boundary surface areas per unit volume S_V were calculated to be $4.008 \mathrm{x} 10^4$ and $1.315 \mathrm{x} 10^4$ m^2/m^3 respectively, i.e. a difference of 67% in the potential nucleation site availability for grain boundary nucleation. Subsequently, the specimens were annealed at 750 °C for different periods in order to determine the Laves phase transformation kinetics. Figure 8.4 show the two typical S – shaped transformation curves obtained from the XRD analyses. The results show that the precipitation kinetics of the Laves phase is retarded by the large grain size, and this is due to a smaller number of nucleation sites. However, it was observed that an equal level of the maximum volume fraction could be achieved from both grain sizes, although at different annealing times. Within the specimen with a larger grain size the same volume fraction of Laves phase precipitates could be achieved but by annealing for approximately an extra 400 minutes. It is revealing to note that the difference in time to achieve the 50% transformation level in Figure 8.4 is reasonably close to the earlier 67% difference in the grain boundary nucleation site availability. These results confirm that grain boundary nucleation of the Laves phase's nuclei is of overriding significance. In a similar study done by Pardal et al. [134] on a superduplex stainless steel UNS S32750, the authors have made similar qualitative observations, but they did not determine the overall effect of the grain size on the volume fraction as was done here.

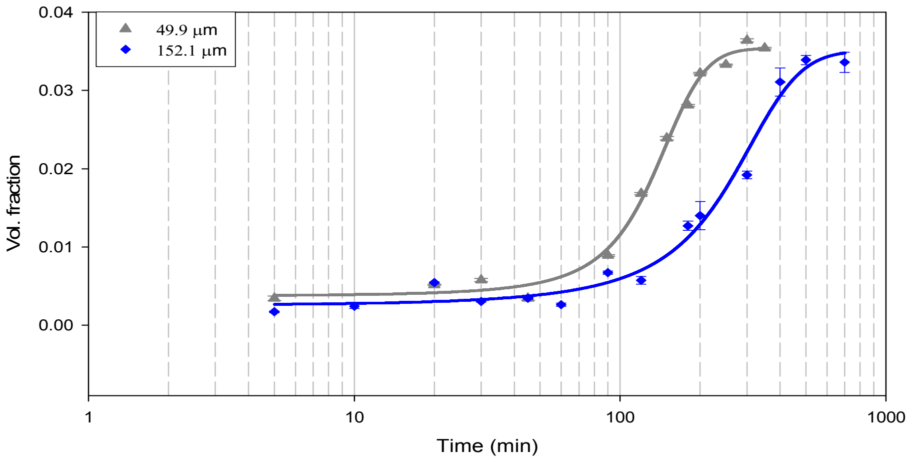

Figure 8.4. Effect of the grain size on the Laves phase kinetics transformation in Steel A. The specimens were annealed first at 850 and 950°C respectively to set different grain sizes and were then annealed both at 750 °C for different annealing periods.

8.6 EFFECT OF THE STEEL'S COMPOSITION ON THE LAVES PHASE'S TRANSFORMATION KINETICS

The effect of the steel's composition on the Laves phase kinetics was investigated comparing Steel A (0.444Nb – 0.153 Ti – ~ 0Mo), with the Steel C (0.36Nb – 0.171Ti –<

0.01Mo) and Steel D (0.251Nb – 0.106Ti – 1.942Mo). The grain size of these materials was kept constant and the transformation kinetics was investigated by annealing the specimens at 750 °C over different periods of time. Figure 8.5 shows the results of the effect of composition on the kinetics of the Laves phase precipitation, which indicates that at 750 °C, Steel A has a much higher volume fraction of Laves phase precipitates than Steels C and E, and this coincides with the Thermo-Calc® predictions. Note that from Figure 8.5, in order to be able to compare the volume fractions of Laves phase of Steels C and E, their smaller values are shown on the secondary axis while that of Steel A is shown on the primary axis.

These results also indicate that by reducing the Nb and Ti contents as with Steel C (in comparison to Steel A), this did not have any significant impact on the kinetics of the Laves phase precipitation but only on the final volume fraction. But the addition of 1.942% Mo has a measurable impact by retarding the precipitation rate of the Laves phase. In the work published by Ahn et al. [135] the authors have observed that the precipitation of Fe_2Nb Laves phase in 0.01C–0.38Nb–1.2Mo steel was slower than in an 0.01C-0.38Nb steel, and this was due to Mo retarding the rate of Nb diffusion**.**

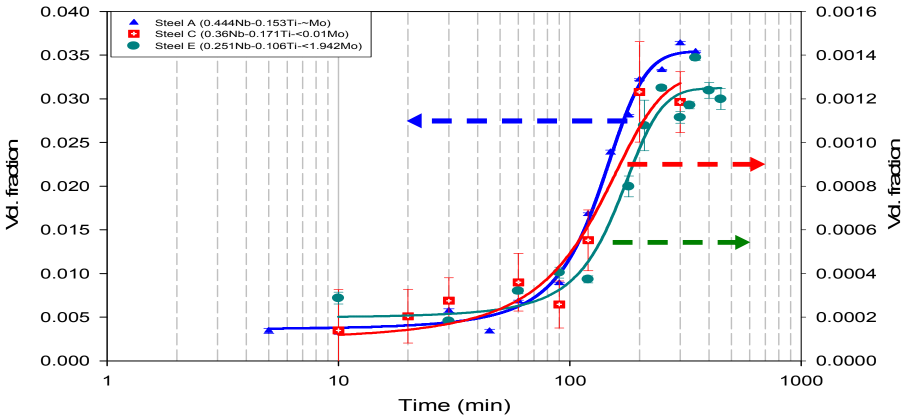

Figure 8.5. Effect of the steel's composition on the Laves phase transformation kinetics. The specimens from these steels were all annealed at 750 °C for different annealing periods.

8.7 MICROSTRUCTURAL ANALYSIS OF THE TRANSFORMATION KINETICS

The nucleation mechanisms of the Laves phase precipitates during transformation was investigated from the specimens that were annealed at 600 °C, 750 °C and 800 °C for 30 minutes, which allowed for a suitable time of precipitate growth, so that they could be analysed using TEM – EDX.

Figure 8.6, shows the microstructure of the specimen annealed at 600 °C. At the lower magnification (Figure 8.6(a)) the remnant of the grain boundary Laves phase precipitates could be found from the solution treatment at 850 °C for 2 hours. At a higher magnification (Figure 8.6(b), the same area analysed from Figure 8.4 (a) is indicated by a circle, and the micrograph indicates that the nucleation site for the Laves precipitation is mainly at dislocations and subgrain boundaries, with only a very few precipitates on grain boundaries and almost none within the grains themselves. Laves phase precipitates that have nucleated on the grain boundaries, are possibly coherent or alternatively have a low mismatch with one grain but grow into the adjacent grain with which they do not have a rational orientation relationship because of that interface's higher mobility. Similar observations were made by Li [131] on 12Cr – 2W steel, where it was found that with the nucleation and growth of the Fe_2W Laves phase precipitates, the coherent or low mismatch interfaces have a low mobility while the incoherent ones have a higher mobility, and therefore, the incoherent interface will grow into the grain with which there is no rational orientation relationship.

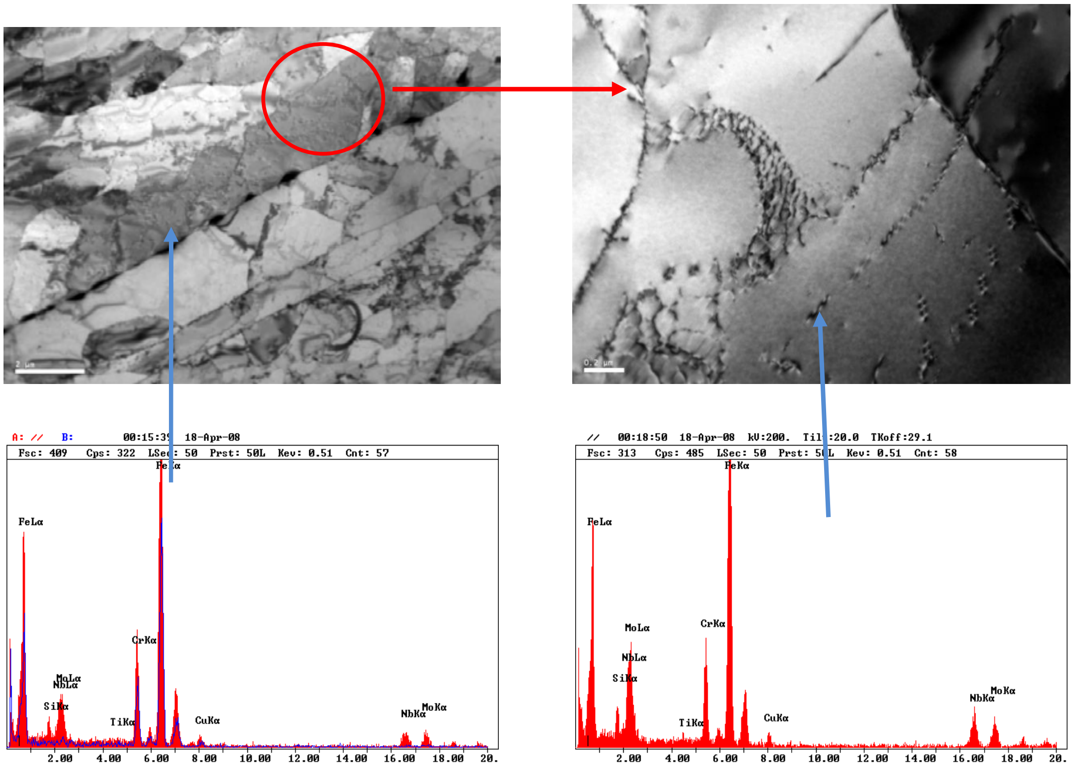

(a) (b)

Figure 8.6. TEM micrographs of the specimen of Steel A annealed at 600 °C; (a) a low magnification micrograph shows coarse grain boundary Laves phase precipitates, and (b) the same area but at a high magnification, showing Laves phase precipitates nucleated on subgrain boundaries and dislocations.

The microstructure of the specimen of Steel A that was annealed at 700 °C is shown in Figure 8.7. Comparing this specimen with the one that was annealed at 600 °C, it can be seen that even after only 30 minutes of annealing, the volume fraction of the Laves phase is higher, also suggesting a high nucleation rate at 700 °C in this specimen. Also, there is more of the grain boundary Laves phase precipitation than the dislocation precipitates, see Figure 8.7 (a). This suggests that the most preferred nucleation site for the Laves phase are the grain and subgrain boundaries, unlike as in the specimen annealed at 600 °C, where more precipitates on dislocations were observed.

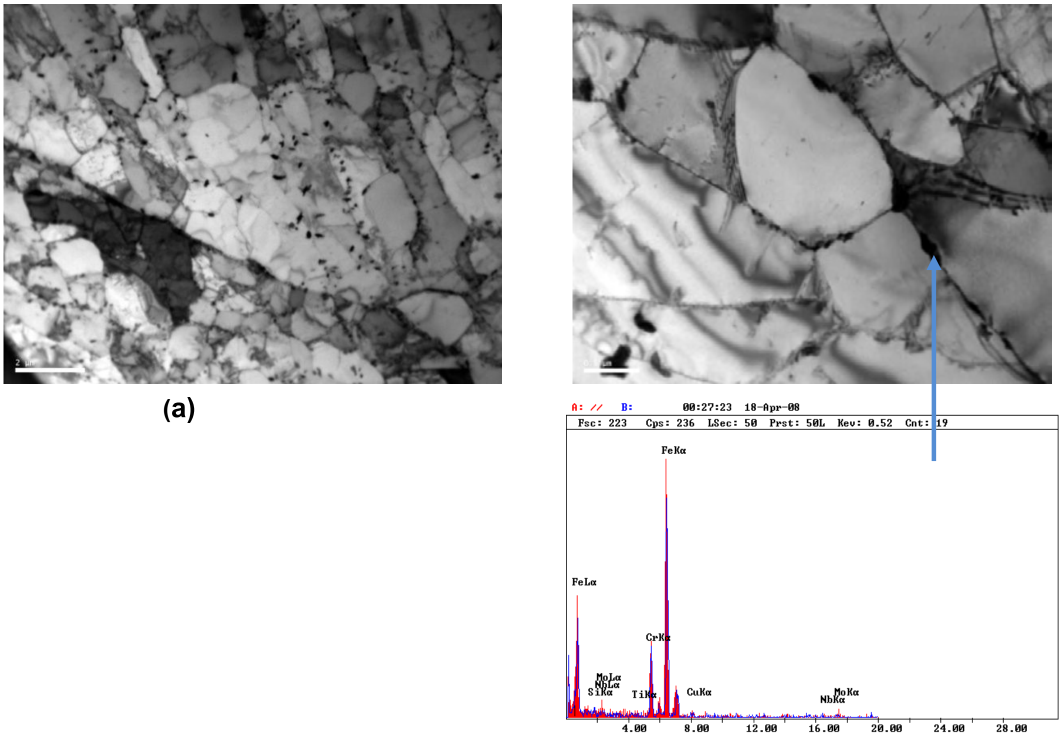

(a)

(b)

Figure 8.7. TEM micrographs of the specimen of Steel A annealed at 750 °C; (a) a low magnification micrograph showing grain and subgrain boundary Laves phase precipitates, and (b) at a high magnification, showing Laves phase precipitates nucleated on the subgrain boundaries.

Figure 8.8 shows the micrographs of the specimen that was annealed at 800 °C, which is heavily "decorated" with the Laves phase precipitates. At the higher magnification, it was observed that the preferred sites for the Laves phase nucleation are grain boundaries, with very few precipitates on dislocations compared to the specimen annealed at 600 °C. Also, it can be observed that the presence of the dislocation density did not assist as much as preferred nucleation sites for the Laves phase precipitation as was the case at lower temperatures.

Comparing all of the microstructures at these three different temperatures, it can be concluded that dislocations, subgrain and grain boundaries act as preferred nucleation sites for Laves phase precipitation. Analyses of the microstructures and also on the basis of the classical heterogeneous nucleation theory, demonstrates that nucleation on the grain boundaries is dominant at the higher testing temperatures of 750 °C and above, see Figure 8.7 and Figure 8.8, where the undercooling and hence the driving forces for nucleation are relatively low and the system then lowers its retarding forces through grain boundary nucleation. As the temperature is decreased and the undercooling and hence the driving forces are higher, however, heterogeneous nucleation on dislocations becomes more significant.

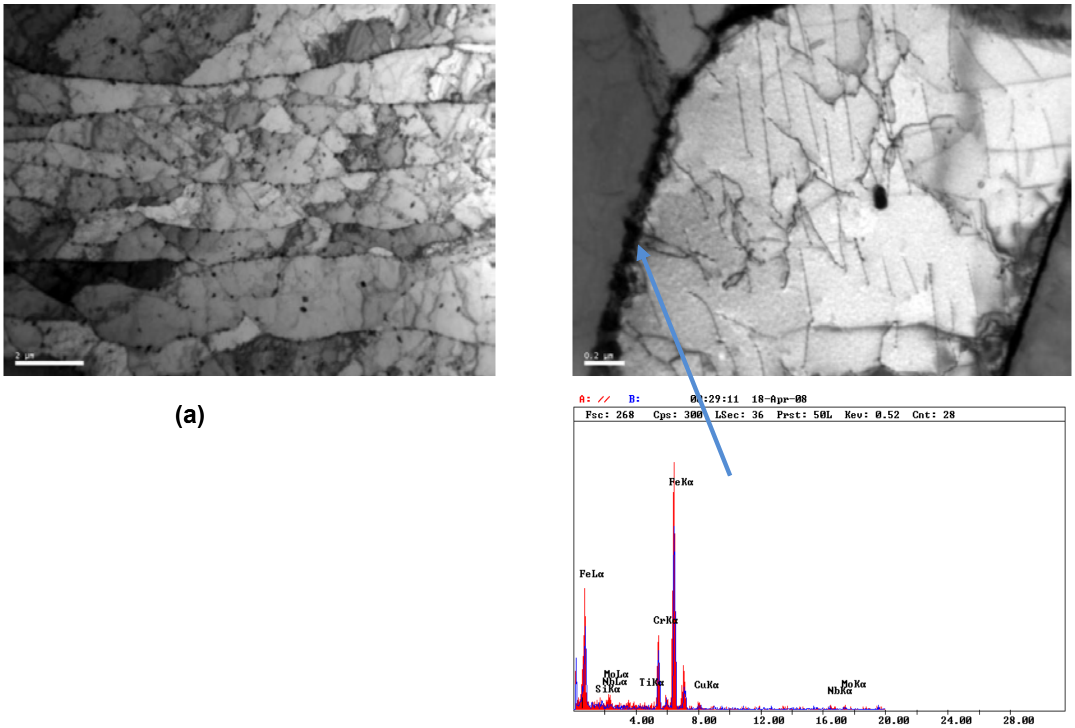

(a)

(b)

Figure 8.8. TEM micrographs of the specimen annealed at 750 °C; (a) at a low magnification, showing grain boundary Laves phase precipitates, and (b) at a higher magnification showing Laves phase precipitates nucleated on the subgrain boundaries.

8.8 ORIENTATION RELATIONSHIP BETWEEN THE LAVES PHASE AND THE FERRITE MATRIX

Figure 8.9 to Figure 8.11 show bright field images and the corresponding selected area diffraction patterns (SADP) from the Steel A specimens annealed at 600 to 800 °C, for 30 minutes. The microstructure consists of a number of differently shaped particles ranging from needle-shape at 600 °C, globular-shaped at 750 °C and plate–like at 800 °C. These precipitates were all identified as Fe_2Nb Laves phase with a C14 crystal structure.

Figure 8.9 shows the specimen of Steel A that was annealed at 600 °C and the crystallographic orientation relationship between the needle-like Laves phase and the matrix was analysed using the SAD pattern as:

$$(21\bar{1})_{\alpha-Fe} // (\bar{1}101)_{Fe2Nb} \text{ and } [011]_{\alpha-Fe} // [1\bar{1}02]_{Fe2Nb} . \qquad (1)$$

According to Cocks and Borland [90], by rotating the above orientation relationship (1) to within ±5° around the habit plane $\{111\}_{\alpha\text{-Fe}}$ and a direction in this plane, the following orientation relationship is found;

$$(1\bar{1}1)_{\alpha-Fe} // (11\bar{2}0)_{Fe2Nb} \text{ and } [121]_{\alpha-Fe} // [0001]_{Fe2Nb} . \qquad (2)$$

The needle-like Laves phase particles found in this specimen are, therefore, elongated in the $\langle 112 \rangle$ matrix directions.

Figure 8.10 shows the specimen that was annealed at 750 °C, in which the crystallographic orientation relationship between the globular-like Laves phase and the ferrite matrix was analysed to be the following orientation relationship:

$$(211)_{\alpha-Fe} // (0001)_{Fe2Nb} \text{ and } [\bar{1}11]_{\alpha-Fe} // [01\bar{1}0]_{Fe2Nb} \qquad (3)$$

According to Yamamoto et al.[91], using the stereographic projection of the orientation relationship (1) between the Laves phase and the ferrite matrix, they have found that this orientation relationship is equivalent to the following expression by the lower mirror indices;

$$(211)_{\alpha-Fe} // (0001)_{Fe2Nb} \text{, and } [0\bar{1}1]_{\alpha-Fe} // [\bar{2}110]_{Fe2Nb} \qquad (4)$$

Figure 8.11 shows the specimen that was annealed at 800 °C, in which the crystallographic orientation between the plate-like Laves phase and the ferrite matrix was analysed to follow the orientation relationship:

$$(110)_{\alpha-Fe} // (0001)_{Fe2Nb} \text{ and } [\bar{2}33]_{\alpha-Fe} // [11\bar{2}0]_{Fe2Nb} \qquad (5)$$

If the orientation relationship (5) is rotated by ±5° from the above mentioned relationship, it will follow:

$$(110)_{\alpha-Fe} // (0001)_{Fe2Nb} \text{ and } [001]_{\alpha-Fe} // [1\bar{2}10]_{Fe2Nb} \qquad (6)$$

The habit plane from this orientation relationship is $\{110\}_{\alpha\text{-}Fe}$, and the preferred growth orientation must be in the $\langle 001 \rangle$ matrix directions.

Comparing all three of these SAD patterns, it can be seen that the orientation relationship between the Laves phase particle and the ferrite matrix may have a significant effect on the shape of the particles. Also, the orientation relationships for the particles analysed are completely different from one another, and the habit planes are also different.

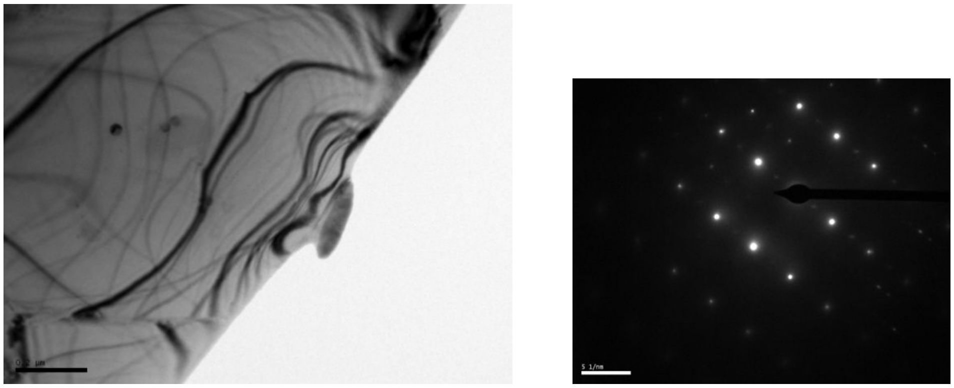

$[011]_{\alpha-Fe} // [1\bar{1}02]_{Fe2Nb}$

Figure 8.9. Transmission electron micrographs and corresponding selected area diffraction (SAD) pattern from Steel A annealed at 600 °C.

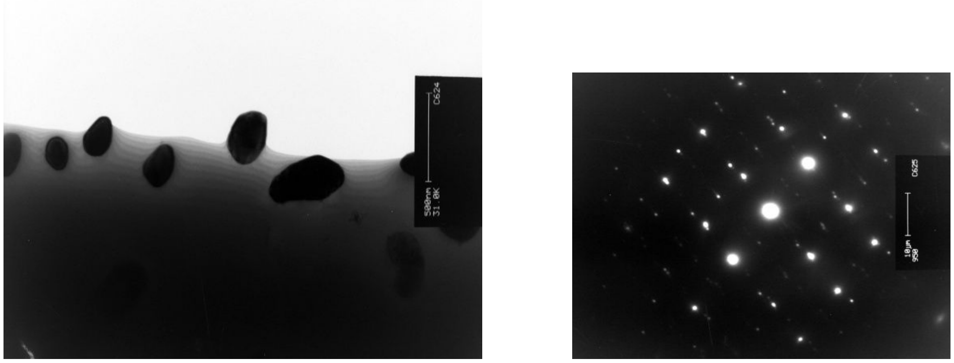

$[\bar{1}11]_{\alpha-Fe} // [01\bar{1}0]_{Fe2Nb}$

Figure 8.10. Transmission electron micrographs and corresponding selected area diffraction (SAD) pattern from Steel A annealed at 750 °C.

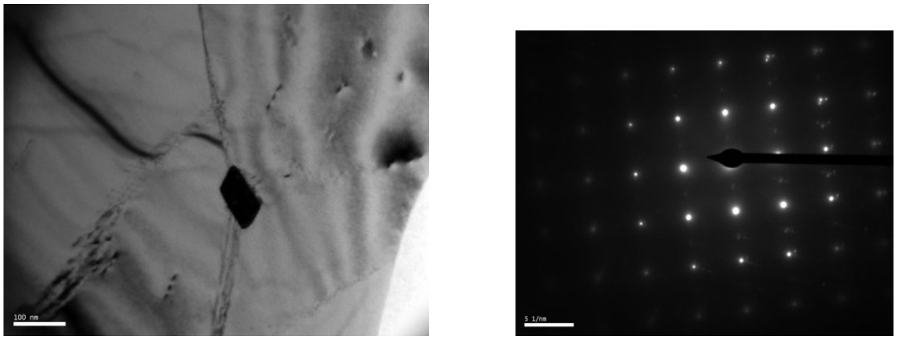

$[\bar{2}33]_{\alpha-Fe} // [11\bar{2}0]_{Fe2Nb}$

Figure 8.11. Transmission electron micrographs and corresponding selected area diffraction (SAD) pattern from Steel A annealed at 800°C.

CHAPTER NINE

DISCUSSIONS

LAVES PHASE EMBRITTLEMENT

9.1 INTRODUCTION

In this chapter the parameters that affect embrittlement of the type 441 ferritic stainless steel are discussed. Parameters such as the grain size, grain boundary Laves phase and the cooling rate were tested against existing fracture theories of Stroh, Cottrell and Smith. Also, the effect of possible niobium solute drag during the recrystallisation and grain growth was considered qualitatively.

9.2 PRECIPITATES FOUND IN AISI 441 FERRITIC STAINLESS STEEL

Thermo-Calc® calculations predict that the phases that are stable over a wide range of temperatures in these steels are the Laves phase, carbo–nitrides and the sigma phase in a structure that remains completely ferritic from its initial solidification. The presence of the M_6C or (Fe_3Nb_3C) type carbides were detected experimentally using XRD and TEM analyses. But this precipitate seems to appear infrequently in these steels and its volume fraction could not be quantified due to its low value. In the TEM image they appear as coarse grain boundary precipitates, see Figure 9.1. Such coarse precipitates are known not to cause any significant strength after high temperature ageing [5]. But the presence of the coarse M_6C type carbides can be prevented by adding elements which have a stronger affinity for carbon than the Nb in these steels, that is Ti. The amount of Nb addition depends on the carbon and nitrogen content, and it was found that an addition of 0.1wt.%Ti is normally enough to stabilise 0.02 wt.%C and N as Ti(C,N) [5].

Angular carbo-nitrides of titanium and niobium that have precipitated from or soon after the melt are randomly dispersed throughout the structure. The presences of these second phases in these steels tend to lower the melting point of the steel [55]. Excess niobium is taken into solid solution during high temperature annealing and is re-precipitated as very fine particles of the Laves phase (Fe_2Nb) upon either slow cooling or upon holding at intermediate temperatures of 600 – 950 °C [136]. Strengthening by this dispersion was found to be responsible for improved elevated temperature strength [8,69]. Although Thermo-Calc® calculations show the presence of the sigma phase as an equilibrium phase, others have indicated that this phase is not supposed to form in this type of alloy and neither was it encountered in this study. It has often been reported that sigma phase precipitates in high chromium ferritic stainless steels but only after very long periods at high service temperatures [25,26,27].

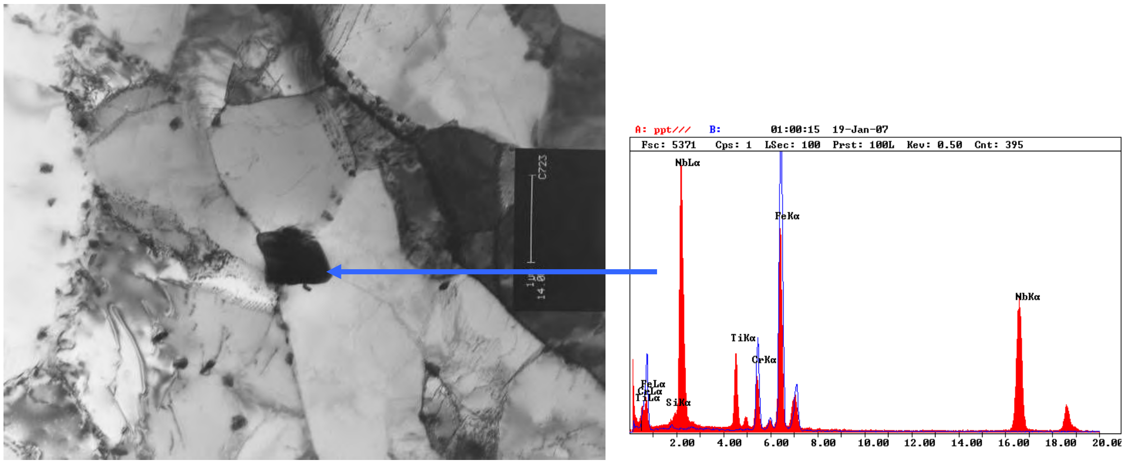

Figure 9.1. TEM micrograph shows the presence of the M_6C or (Fe_3Nb_3C) type carbide in the subgrain structure from Steel A. Note that the specimen was annealed at 700 °C for 30 minutes and other fine particles were determined to be Fe_2Nb Laves phase particles.

9.2.1 EFFECT OF THE STEEL'S COMPOSITION ON THE PRECIPITATE'S SOLVUS TEMPERATURE

The solvus temperature and volume fraction for each phase is alloy composition dependent. From the Figures 5.4 to 5.8 in Chapter 5; the minimum temperature for the dissolution of the Laves phase and the carbonitrides were estimated. These dissolution temperatures for the Laves phase were used as a guide to avoid excessive grain growth during higher annealing temperatures. Using Steel A with a nominal composition of 0.012C-0.0085N-0.444Nb-0.153Ti-~0Mo as this study's reference steel, it was established that the C and N contents have a significant impact on both the solvus temperature and composition of the (Ti,Nb)(C,N), with increasing one or both of them resulting in increments of both solvus temperature and volume fraction.

The Laves phase's formation was found to be more dependent on the Nb content than on the Ti content. Decreasing the Nb content of the steel, decreased both the solvus temperature and volume fraction of the Laves phase. For instance, by reducing the Nb content to 0.36wt % in Steel C (0.023C-0.024N-0.36Nb-0.171Ti-<0.01Mo) as compared to 0.444wt % in Steel A, this resulted in lowering the solvus temperature to 765 °C (as compared to 825 °C in Steel A) and the weight fraction determined at 600 °C was reduced to 0.573 wt% (compared to 0.92 wt% in Steel A). An increase in Ti content in Steel C, to 0.171 wt% (compared to 0.153 wt % Ti in Steel A) did not have any significant impact on the both solvus temperature and weight fraction of the Laves phase. A Mo addition was found to increase the volume fraction of the Laves phase, whilst at the same time lowering its solvus temperature. For instance, it has been observed in this study that a Mo addition from practically zero in Steel A to 1.94 wt % in Steel E enhanced the formation of the Laves phase in the Nb-Ti-Mo steel (see Figure 5.8 and Table 5.6), while at the same time slowing its precipitation kinetics (see Figure 8.5). Some authors have observed that this is due to the Mo retarding the diffusivity of Nb to form Laves phase precipitates [5,6,135]. A more detailed analysis of the kinetics of nucleation of the Laves and other second phases in this and other similar Nb-containing ferritic stainless steels will be reported in Chapter 10.

The Thermo-Calc® results of Steel A where compared with the experimental results of obtained from the XRD analysis, see Figure 9.2. The results from Thermo-Calc® predict that at 825 °C, the weight fraction of the Laves phase should be zero, whereas the experimental results found that there was still about 0.031wt% present and a further remnant still existed even at 850 °C and above. The presence of the Laves phase up to a temperature of 950 °C in a similar ferritic stainless steel to the one studied in this work, was observed by other researchers, where they have observed that the Laves phase improved the high temperature strength of their steel [69,136].

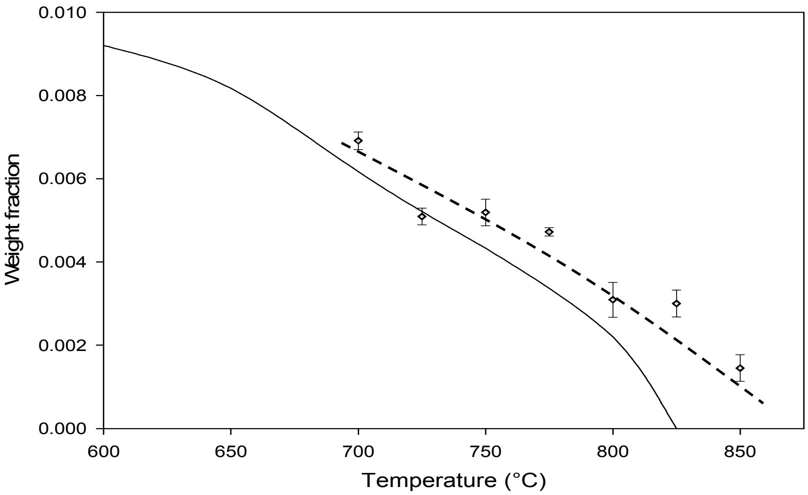

Figure 9.2. Comparison between experimental and Thermo-Calc® calculated weight fractions of Laves phase in Steel A. The points and dotted line represent the experimental results while the full line is as predicted by Thermo-Calc® for this steel.

9.2.2 EFFECT OF THE STEEL'S COMPOSITION ON THE PRECIPITATE'S COMPOSITION

It was established from the Thermo-Calc® predictions that the composition of the titanium and niobium carbonitrides (Ti,Nb)(C,N) is not affected by a change in the steel's composition, but only the stoichiometric composition is affected. On the other hand, the Laves phase's composition is highly affected by the change in the steel's composition. Thermo-Calc® predictions show that the composition of the Laves phase in Steels A and B contains the following elements: Fe, Cr, Ti and Nb, but no C or N, and this led to the conclusion that the Laves phase is in the form of $(Fe,Cr)_2(Nb,Ti)$. The absence of C or N in the Laves phase was also observed by Sawatani et al. [8], using an electron probe microanalysis technique, but in the work of Lundin [137] on a 10.6Cr-1.01W-1.02Mo-0.04Nb ferritic stainless steel and using an atom-probe field-ion microscopy (APFIM) analysis of the Laves phase, the author found carbon to be soluble in the Laves phase. It needs to be noted, however, that the respective carbon contents of the two steels from the work by Sawatani [8] and Lundin [137] were 0.008%wt. and 0.11%wt, respectively. Therefore, the solubility of the carbon in the Laves phase appears to be directly dependent on the carbon content of the steel.

When the Nb content is reduced and the Ti content is increased (as in the Steel C (0.36Nb-0.171Ti)) or only the Ti is decreased (as in Steel E (0.251Nb-0.106Ti)), Thermo-Calc® predictions show that Ti is not taken up into the Laves phase, but resulted in an increase in the Ti-content of the Ti(C,N) in this steel. The discrepancy caused by the Ti solubility in these alloys as compared to other alloys could not be established from this work. Therefore, a further study to gain a better understanding on the solubility of Ti in the Laves phase in these steels is needed.

In the case where Mo additions were made, such as in Steels D and E, it was found that Mo is taken up into the Laves phase as $((Fe,Cr)_2(Nb,Ti,Mo)$ for Steel D and $(Fe,Cr)_2(Nb,Mo)$ for Steel E respectively. It was, therefore, concluded that the nominal composition of the Laves phase should be reported according to the major alloying elements, i.e. for Steels A – D as Fe_2Nb and for Steel E as $Fe_2(Nb,Mo)$ respectively.

9.3 EMBRITTLEMENT OF TYPE 441 FERRITIC STAINLESS STEEL

9.3.1 EFFECT OF GRAIN SIZE ON FLOW STRESS: THE HALL-PETCH RELATIONSHIP

The change in grain size of Steel A was introduced by annealing the as received and plant-embrittled material at temperatures of 850 to 1100 °C, i.e. above the estimated Laves phase solvus temperature. From Section 6.3.4 in Chapter 6, the results show a steady increase in grain size up to about 950 °C, but between 950 °C and 1000 °C there is a sudden and rapid 60 % increase in the mean linear intercept grain size. When the effect of the grain growth on the 0.2% yield strength in this steel was tested according to the Hall-Petch relationship, it was found that it only applies in the temperature range of 850 °C to 950 °C (see Figure 9.3) but beyond 950 °C, the relationship did not hold. The Hall – Petch relationship is given by:

$$\sigma_y = \sigma_0 + k_y^s d^{-\frac{1}{2}} \qquad \text{Equation 9.1}$$

where σ_0 is the friction stress due to dislocation obstacles on the slip plane in the materials, k_y^s is the locking parameter representing the grain boundary as an obstacle to propagation of deformation, and d is the grain size. According this Equation 9.1, plastic deformation leads to a pile-up of dislocations at the head of a slip plane at a grain boundary. This pile-up causes stress concentrations at the boundary and in the adjacent grain. When the stress concentration is high enough and reaches a critical value, a dislocation source in the adjacent grain may be activated and plastic deformation can spread out into this next grain. The values for σ_0 and k_y^s in this material were determined experimentally as 229.03 MPa and 469.8 MPa .μm$^{1/2}$, respectively from Figure 9.2, although the relatively few data points and their scatter (see the relatively low value of the regression coefficient R^2) make these values somewhat approximate. In the work by Miyahara et al. [138], working on two types of ferritic steels with a fine and coarse grain size, the authors have estimated a locking parameter of 260.0 MPa .μm$^{1/2}$ which was in good agreement with the conventional results for a low – carbon steel from Pickering's [47].

Comparing this value with the value obtained from this work, it can be concluded that grain boundary strengthening at temperatures ranging up to 950 °C was sufficient to prevent the embrittlement of this steel and, therefore, the source of embrittlement found in this study is most likely from the presence of the Laves phase precipitates on sub- and grain boundaries.

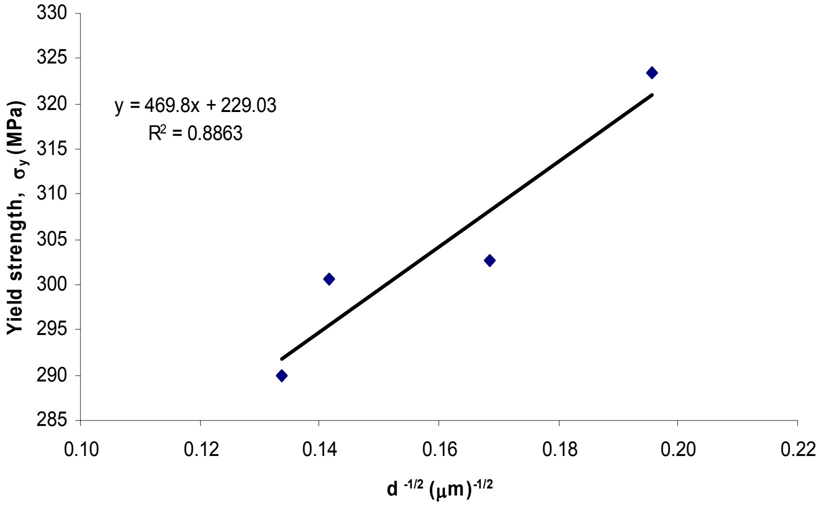

Figure 9.3. The effect of grain size on the yield strength of Steel A.

9.3.2 CRACK NUCLEATION

According to Stroh [36], the value for the shear stress created by a dislocation pile – up of length *d/2* to nucleate a microcrack is as follows:

$$\tau_e \geq \left[\frac{\pi G_m \gamma_f}{2(1-\nu)d}\right]^{\frac{1}{2}} \qquad \text{Equation 9.2}$$

where τ_e is the effective shear stress; γ_f is the effective surface energy of the crack; G_m is the shear modulus; ν is Poisson's ratio; d is the grain size. The shear stresses are comparable for the constant $G_m b/\gamma_f \sim 8$ [36], where b is the Burgers vector of the slip plane. Assuming that $G_m b/\gamma_f \approx 8$, with $G_m = 8.6 \times 10^{10}$ Pa and $b = 2.48 \times 10^{-10}$ m, then $\gamma_f \approx 2.67$ J/m^2. It should be noted that this estimated effective surface energy of the crack is much higher than that of the grain boundary energy in stainless steels which is in the region of 0.5 to 0.7 J/m^2 and that for the free surface about three times higher, i.e. about 1.5 to 2.1 J/m^2 [40,139]. According to Cottrell [38], an effective surface energy of the crack greater than the true one appears to be a common feature of brittle fracture in iron which is thought to be mainly due to irreversible work of tearing grain boundaries. For the specimen annealed at 850 °C which had a grain size of 26.1 μm, and with ν = 0.28 and using Equation 9.2, produces an estimate of the effective shear stress of approximately 438 MPa. This value is significantly higher than the measured yield strength of 323.5 MPa for this steel (see Figure 9.4) after annealing at 850 °C, leading to a conclusion of ductile and not brittle failure at this grain size. From these results, it can furthermore be concluded that if a crack nucleus can form, any increase in its propagating length can lead to a decrease in the total system's energy, provided that there is no change in the surface energy encountered during the crack growth. The critical number of dislocations that is sufficient to nucleate a crack at the end of the slip-band is given by:

$$n = \frac{\pi^2 \gamma_f}{2\tau_e b} \quad \text{Equation 9.3}$$

If the steel does show a tendency to fracture in a brittle manner, either because of a low temperature or from brittle precipitates on the grain boundaries, then a smaller grain size d would be helpful. The shear stress at the head of the dislocation pile up is given by $n\tau_e$, *i.e.* the smaller the grain size, the smaller the number of dislocations in the pile-up when the slip band arrives at the grain boundary.

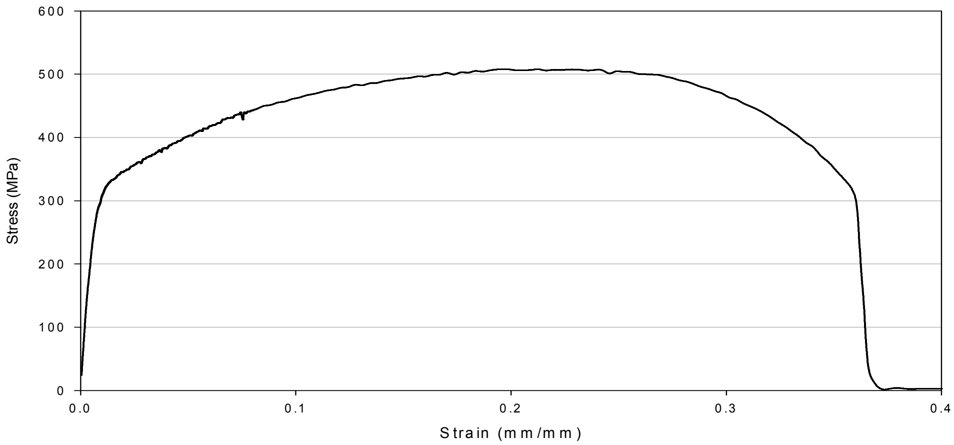

Figure 9.4. A room temperature tensile test of the specimen of Steel A that was annealed at 850 °C for 30 minutes and then water quenched.

When secondary precipitates are inhomogeneously distributed (such as the grain boundary Laves phase precipitates) the value of the surface energy γ_f may be reduced and the amount of work done in nucleating a crack decreases. Thus the crack initiates more easily at grain boundaries, even though the resulting cracks probably propagate transgranularly and not intergranularly. In the present study there is evidence of the (Ti,Nb)(C,N) precipitates that have cracked after Charpy impacting the sample annealed at 850 °C (see Figure 9.5). These carbo-nitride precipitates present on the fracture face were found to be distributed within the grains, and their volume fraction V_v was relatively much lower compared with that of the Laves phase. In this case, for the given volume fraction of the (Ti,Nb)(C,N) precipitates γ_f will be higher for a distribution within the grain's interior.

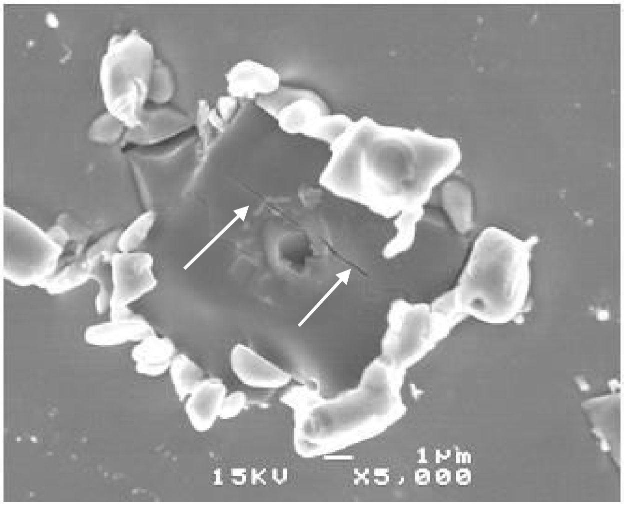

Figure 9.5. High resolution field emission scanning microscope image showing the cracking of (Ti,Nb)(C,N) particles after impact testing the specimen at room temperature. This specimen of Steel A was annealed at 850 °C followed by quenching in water.

The stress causing cleavage fracture is, therefore, predicted to be the effective shear stress:

$$\tau_e = \tau_y - \tau_i = k_y^s d^{-\frac{1}{2}} \qquad \text{Equation 9.4}$$

where τ_y is the shear yield strength and τ_i is the lattice friction stress. If yield occurs at the head of the slip band by nucleation of a crack, it can be assumed that the friction stress for yield is approximately the same as for the dislocations in the piled up slip band [24]. The above Equation 9.4, does not explain why cleavage fracture is predominant in the presence of precipitates (where the yield strength is high, but the $(\tau_y - \tau_i)$ may be little different from its value at room temperature).

9.3.3 EFFECT OF PRECIPITATES IN THE EMBRITTLEMENT OF THIS STEEL

9.3.3.1 EMBRITTLEMENT AND THE COTTRELL'S APPROACH

Based on the results of Steel A as shown in Chapter 6, it was observed from Figure 6.12 that the Charpy impact energy values indicate decreasing embrittlement with increasing annealing temperature up to 850 °C, which correlates with the Thermo – Calc® predictions of a decreasing volume fraction of Laves phase as 825 □C is approached. The same observations where made by Sawatani et al.[8] working on a Ti and Nb stabilised low C, N – 19%Cr – 2%Mo stainless steel whereby they have observed that an increase in the volume fraction of the Laves phase has a significant impact in promoting embrittlement of their steel, but the authors did not make any detailed analysis of why the presence of the Laves phase deteriorates the impact toughness. In the work done by Grubb et al.[140], they have suggested that the embrittling effect arises from the flow stress increase associated with the α' – precipitation (i.e. 475 °C embrittlement) and this can be readily understood using the approach of Cottrell. This approach provided a useful basis for understanding the micromechanics of brittle fracture even though, strictly speaking, the model does not encompass all the practical modes of crack initiation [38]. The conditions for cleavage fracture can be expressed by the Cottrell equation:

$$\sigma_f k_y^s d^{\frac{1}{2}} = C_1 G_M \gamma_f \qquad \text{Equation 9.5}$$

where σ_f is the fracture stress, C_1 is a constant related to the stress (~4/3 for a notched specimen and 4 for a plain specimen [21]), and the rest are as mentioned previously. The ferritic stainless steels generally display a substantial increase in lattice friction stress σ_0, upon rapid cooling. This increase manifests itself in an increase in the ductile to brittle transition temperature (DBTT), in accordance with the Cottrell approach, which predicts that the DBTT or brittle fracture with grain size as a variable, will occur when $\sigma_f = \sigma_y$ which would lead to [18,19]:

$$\sigma_y k_y^s d^{\frac{1}{2}} = k_y^{s^2} + \sigma_i k_y^s d^{\frac{1}{2}} = C_1 G_M \gamma_f \qquad \text{Equation 9.6}$$

Therefore, if $\sigma_y k_y^s d^{\frac{1}{2}} > C_1 G_M \gamma_f$, then brittle fracture occurs, and if $\sigma_y k_y^s d^{\frac{1}{2}} < C_1 G_M \gamma_f$, then ductile fracture will take place. The yield strength σ_y is related to the grain size through the Hall – Petch equation, that is Equation 9.1. At 850 °C, assuming that the yield strength σ_y = 323.5 MPa, k_y^s is approximately 469.8 MPa .µm$^{1/2}$ and with a grain size of 26.1 µm, it can be seen qualitatively that according to Equation 9.6, this steel will be brittle at the temperatures *above* 850 °C where the grain size increases due to grain growth. However, there is not much of a difference in grain size between the as received steel and the specimen of Steel A annealed at 850 °C or at lower temperatures. Therefore, it cannot be confidently assumed that at temperatures *below* 850 °C, that the grain size plays a significant role in embrittling this steel.

The presence of large pre-existing cracks is, therefore, not a necessary prerequisite to cause a brittle fracture [43]. It is obvious from Equation 9.6 that grain size has a direct effect on the ductile – to – brittle transition temperature (DBTT). A reasonable relationship expressing the DBTT at which the fracture stress (σ_f) and yield strength (σ_y) are equal for a given grain size d^* has been proposed, i.e. for a given material, there is a theoretical and experimental justification of a relationship between the grain size and transition temperature :

$$DBTT = D + 1/\beta \ln d^{*\frac{1}{2}}$$ Equation 9.7

where D is a constant and the slope ($1/\beta$) should also be constant. These variations of the DBTT with the grain size that turn out to be consistent with Equation 9.7 have been noted previously by different authors [19,43,141]. The same relationship was tested in the current work, and it was observed that there is a tendency for the DBTT to increase linearly with $\ln d^{*\frac{1}{2}}$ (see Figure 9.6). For AISI type 441 stainless steel studied here, it was observed that over the range of grain sizes from 25.2 to 55.9 µm, there is a shift of 35 °C in the transition temperature. In the work of Plumtree and Gullberg [43] on Fe-25Cr ferritic stainless steels with 0.005 wt%C and 0.15 wt%N, the authors noted a positive shift of 26 °C in a grain size increase of 33 to 95 μm. These authors have also observed that by increasing the interstitial element contents of the steel, this will reduce the sensitivity of the transition temperature to the grain size. This indicates that by changing the composition of the steel and making it less impure (such as with Steel C – E), the dependence of the DBTT to the grain size becomes less sensitive. According to some authors [43,19], they have observed that from a qualitative viewpoint, the effect of grain size on the ferritic stainless steel's transition temperature may be somewhat less than projected by Equation 9.7. But from the current work it was observed that a shift of even 10 °C is significant to be considered when using Equation 9.7.

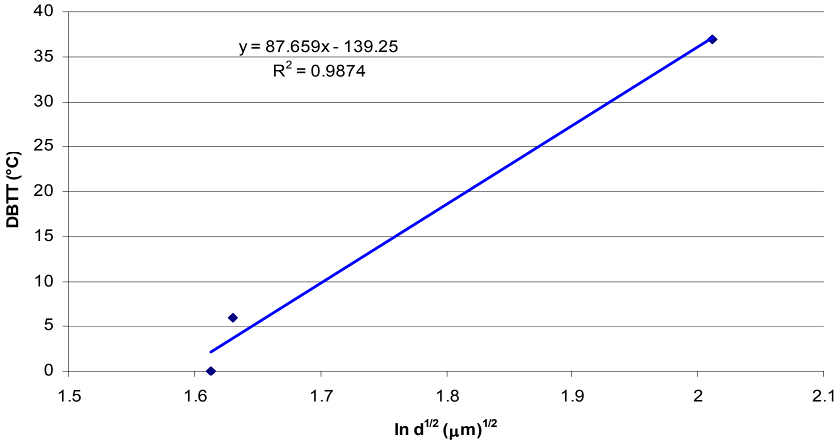

Figure 9.6. The plot of transition temperature versus {ln $d^{1/2}$} of 441 ferritic stainless steel, Steel A.

Generally, the toughness of ferritic stainless steel can be assessed in terms of the DBTT, or a temperature below which Equation 9.6 appears to be satisfied for a given material by the flow stress also being the fracture stress, i.e. brittle fracture without any significant plastic yielding. The satisfaction of Equation 9.6 with decreasing temperature is generally associated with the tendency for the flow stress to increase with decreasing temperature. High strain rates and constraints to plastic flow at the root of a notch have the effect of raising the flow stress and lowering the value of C_1 and thus, promoting satisfaction for Equation 9.6. According to the Cottrell model this phenomenon may be explained by the fact that the locking of dislocations by interstitials in bcc materials causes the flow stress to increase. However, the solubility level of the interstitials carbon and nitrogen in ferritic stainless steel is sufficiently low that it is rarely possible to distinguish between solute embrittling effects and the effect of second-phase precipitates.

9.3.3.2 EMBRITTLEMENT BY GRAIN BOUNDARY PRECIPITATES (THE SMITH'S MODEL)

The precipitates, in fact, become more important than the solute when the amount of interstitial elements significantly exceeds the solubility limit. The presences of interstitials in an amount in excess of the solubility limit, serves to increase the DBTT still further. This embrittling effect is closely linked to the number and size of precipitates formed on the grain boundaries. Thick precipitate films act as strong barriers to slip propagation across the grain boundaries and raise k_y^s . In this case, the Smith approach [39] can be used for a growth controlled cleavage fracture that incorporates a brittle precipitate on grain boundaries. Here a Laves phase particle of thickness C_o at the grain boundary dividing adjacent grains, is cracked by the dislocation pile – up of length d *(which may be related to the grain size itself).* The important stress in causing fracture is predicted to be the effective shear stress, and it may be analysed in a manner similar to that for the Cottrell model to obtain a failure criterion in the absence of plastic flow by dislocations:

$$\sigma_f > \left[\frac{4E\gamma_f}{\pi\left(1-\nu^2\right)C_o}\right]^{\frac{1}{2}} \qquad \text{Equation 9.8}$$

where E is Young's Modulus, σ_f is the fracture stress; γ_f is the effective surface energy of the interface between the ferrite grain and the Laves particle, and ν is Poisson's ratio. Assuming, the earlier estimated effective surface energy of $\gamma_f \approx 2.67$ J/m^2, with $G_m = 8.6 \times 10^{10}$ Pa and $E = 8/3\ G_m = 2.29 \times 10^{11}$ Pa. For the specimen annealed at 850 °C, the largest Laves phase precipitates measured were about 513 nm in thickness. With $\nu = 0.28$ and using Equation 9.8, this gives a fracture stress of approximately 787 MPa. This value is much higher than the experimentally determined yield strength value of 323.5 MPa, once more not predicting brittle fracture to occur. Although not agreeing quantitatively with Smith's model, the above relationship clearly indicates qualitatively that coarser Laves particles with a higher value of C_0 give rise to lower fracture stresses, and also predict that σ_f is independent (directly) of the grain size. However, in practice a fine grain size is often associated with thinner particles due to a higher nucleation rate upon forming the particles, and the value of σ_f is then expected to be higher. Grain boundary Laves phase precipitation can be suppressed by quenching from above the solution temperature when the interstitial content is low. However, the resulting fine intergranular precipitation may increase the DBTT by increasing the lattice friction stress (σ_o). This model appears to explain at least qualitatively the cause of the embrittling effect associated with the Laves phase precipitation in the fracture of AISI type 441 ferritic stainless steel.

In work done by Sim et al.[3] on a Nb stabilised ferritic stainless steel, they have shown that the high temperature strength decreases with increasing ageing time at temperatures between 600 °C and 950 °C, and this was mainly due to the loss of the solid solution hardening effect as the Nb is transferred from the matrix into the Laves phase. They have also observed that the rate of reduction in yield strength as a function of the Nb content at an ageing temperature of 700 °C, showed a linear relationship with the Nb content in solid solution. In their conclusion, they observed that during ageing at 700 °C, Nb(C,N) and Fe_3Nb_3C precipitate out and decrease the high temperature strength slowly while the precipitation of the Fe_2Nb Laves phase at 700 °C decreases the high temperature strength more abruptly. This is reasoned to be because of the *Lifshitz-Slyosov-Wagner* (LSW) quasi-equilibrium coarsening rate of the Laves phase that appears to be much faster compared to that of Nb(C,N). This was believed to be due to the incoherent high energy interface between the Fe_2Nb and the matrix, with the Fe_2Nb having a higher surface energy than that of Nb(C,N). Thus, it can be concluded that coarse Fe_2Nb precipitates are very detrimental to the high temperature strength of type 441 stainless steels.

In work done by other researchers on ferritic stainless steels it was shown that the tensile strength increases with annealing temperature above 1000 °C whilst the percentage elongation decreases [8]. Therefore, from such an observation it can be postulated that as the annealing temperature increases the amount of niobium in solution also increases due to dissolution of precipitates and this should, therefore, increase the yield strength due to solid solution hardening. But in the present work the same effect was not observed since the yield strength decreased with increasing solution treatment temperature (see Figure 6.16), which is indicative of a grain coarsening effect. Yamamoto et al.[69] have observed in a ferritic steel with composition Fe – 10at.% Cr – Nb with 0.5 – 5 at.%Nb, that it is possible to design a steel strengthened by Fe_2Nb Laves phase to give an excellent high temperature strength. They have suggested that the strength is insensitive to Nb content, but an optimum concentration of about 1 – 1.5 at.% Nb would provide a proper volume fraction of the Laves phase to ensure good room temperature ductility. None of these authors, however, had attempted to make any correlation between the Laves phase volume fraction present and high strain rate testing such as the Charpy impact test. It is of course well known that one may find good strength and even good ductility values at slow strain rate testing without any sign of brittleness and the practicality of strengthening these alloys by Laves phase needs to be approached with caution.

It should be noted that both the fracture and the yield strength depend on the grain size, and refining the grain size will result in an increase of these strengths. According to the above Cottrell model on the DBTT, the effective temperatures for the DBTT from an increased grain size exists when the flow stress practically equals the fracture stress with very little measurable plastic strain. In this case, that will be at 950 °C where there is no grain boundary Laves phase. From Figure 9.7, the grain size increase between 850 and 950 °C is about 1.6 times or a 60% increase. According to Equation 9.1, it can be concluded that by increasing the grain size, both the fracture stress and the flow stresses will be decreased, and this will certainly shift the DBTT upwards. In work by Kinoshita [42] on 18Cr-2Mo steel and 26Cr–4Mo steel, the author however, found no significant grain size dependence of the DBTT where the grain size was varied through strain annealing. However, many other authors have reported such a relationship as was also found here. In cases where there are grain boundary precipitates present, such as with the specimens annealed below 850 °C, the Laves phase will tend to lower the cleavage fracture stress. In this case a crack nucleus is formed by the separation of the particle–matrix and this interfacial crack initiates transgranular fracture, but that has not been observed to cause grain separation.

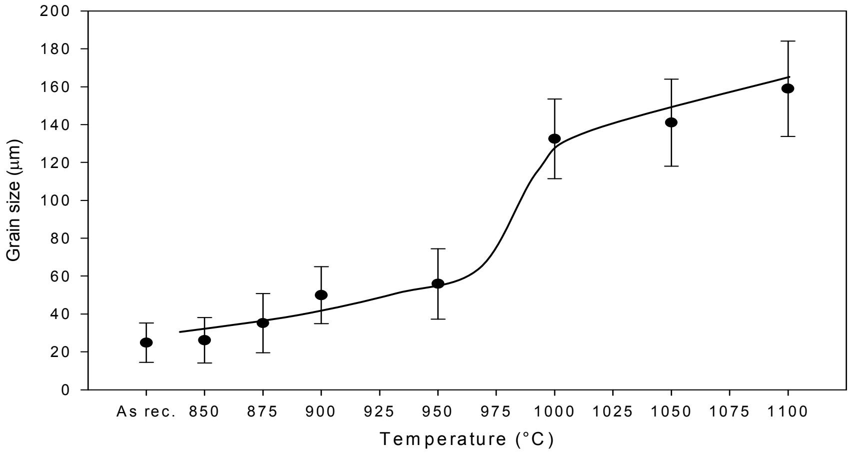

Figure 9.7. Effect of annealing temperature above 850 °C on the grain size for the AISI type 441 stainless steel, Steel A.

9.3.3.3 EFFECT OF COOLING RATE

When the specimens were slowly cooled from the solution treating temperature above the Laves phase solvus temperature, precipitation of the Laves phase occurred afterwards during slow cooling. Steels embrittled from such a treatment behave very similarly to those treated below the solvus temperature [7]. This points to the usefulness of constructing a time – temperature – precipitation (*TTP*) curve for Laves phase formation and such a *TTP* curve was determined experimentally for Steel A and was reported in Chapter 8. Heat treatments that accelerate the precipitation of the Laves phase (that is, below 850 °C) decrease the resistance to crack initiation significantly during dynamic loading. It can be assumed that the volume fraction of the Laves phase, particularly on the sub- and grain boundaries, plays a significant role in affecting both the transition temperature and the upper-shelf energy and that the degree of embrittlement should increase as the volume fraction increases at lower annealing temperatures (see

Figure 5.4), as also predicted by the Smith model of embrittlement by grain boundary phases in ferritic steels. The width C_o (according to Equation 9.8) of the embrittling second phase is related firstly, to the volume fraction V_v of the Laves phase but also secondly, to the grain size, the latter through the grain boundary nucleation site concentration with a larger sub- and grain size leading to a thicker C_0 through less available Laves phase nucleation sites. Therefore, both a higher volume fraction as well as a larger sub- and grain size will then indirectly decrease the effective fracture stress of the steel through a higher value of C_0. This was indeed found in Figure 6.12 with annealing temperatures decreasing from 850 to 600°C, raising the volume fraction of the Laves phase. Other authors have shown that there is an optimum annealing temperature at which the quantity of the Laves phase Fe_2Nb reaches a maximum, and this temperature depends critically on the Nb content in the steel [7,4,99], no doubt through non-equilibrium volume fractions according to a relevant CCT type phase transformation diagram. In the current work reported here, therefore, some remaining Laves phase on grain boundaries at 850°C could have contributed to a lower upper shelf energy if compared to the specimen annealed at 950 °C where dissolution should have been complete.

Further analyses on the specimens that were annealed at 600, 700 and 850 °C, showed from the Thermo-Calc® results (see Figure 5.4), that the predicted weight fraction of the Laves phase at 600 °C is about 0.92 %wt, at 700 °C is about 0.67 %wt and at 800 °C is about 0.14 %wt and that there should be no Laves phase present at 850 °C. Note, however, that Thermo-Calc® only gives an estimated weight fraction at *full equilibrium conditions* and it does not reveal anything about the nucleation rate and the kinetics of the Laves phase formation before equilibrium has been achieved. In the current study as reported in Chapter 8 on the kinetics of the formation of the Laves phase, it was observed that the precipitation kinetics of the Laves phase are much higher at 700 °C than at either 850 °C or 600 °C, and this resulted in a double nose *TTP* curve. From this it follows that at 700 °C after equal times at temperature, the volume fraction of the Laves phase would be much higher than either at 850 or at 600°C and this will result in the specimen having a lower upper shelf energy at 700°C than the specimen annealed at 600 °C.

From the measurement of the DBTT at room temperature and shown in Figure 6.17, which falls within the ductile to brittle transitions but not at the same points for the two temperatures, the specimen annealed at 950 °C is at the very bottom of the transition while at 850 °C it is in the middle. A direct comparison of the absolute values on the two curves is, therefore, not feasible as they fall within different parts of the transition curve. At 950 °C the grain size effect is overwhelming (even more significant than the effect from the Laves phase) and that the addition of Laves phase to an already brittle steel at slow cooling rates, brings in no measurable further embrittlement. Therefore, the full effect of the Laves phase precipitation on the Charpy impact toughness could be seen only in the specimen annealed at 850 °C where the grain size effect was minimal. Therefore, samples that were solution treated at 850°C show a significant decrease in the impact toughness with decreasing cooling rates that allow Laves phase to form during slow cooling. Specimens that were solution treated at 950 °C, however, show only a slight increase in impact toughness after slow cooling of 10 °C/sec, and then the toughness levels off with a further increase in cooling rate (see Figure 6.18). Again, as the cooling rates decrease the amount of the Laves phase that precipitates increases, resulting in deterioration in the impact strength. Therefore, comparing the curves for 850 and 950 °C annealing in Figure 6.18, it can be concluded that grain size plays a measurable role in the nucleation of the Laves phase, as already stated above. The results of this study on the effect of cooling rate on the Charpy impact toughness of ferritic stainless steels, therefore, largely agree with the work of other researchers [7,8,99], i.e. with the cooling rate having a pronounced influence on the impact energy transition of low interstitial ferritic stainless steels, with the lower cooling rates showing a higher transition temperature.

9.4 RECRYSTALLISATION AND GRAIN GROWTH

Although grain growth experienced in this alloy at annealing temperatures above 850°C is generally expected, the “sudden” significant increase in grain size by about 60% within the temperature region 950 to 1000 °C cannot be readily explained by normal grain growth theories and needs some discussion. The most obvious explanation of “grain boundary particle unpinning by dissolution” in this temperature range is the immediate and obvious candidate. Particles that had nucleated on the recrystallisation front may impede the motion of the grain boundary due to Zener drag [142,143]. The resulting retarding force Δp_{ppt} exercised by these particles on the grain boundary is given by:

$$\Delta p_{ppt} = \left(\frac{3}{4}\gamma\right)\left(\frac{V_v}{r}\right) \qquad \text{Equation 9.9}$$

where γ = grain boundary free energy, V_v = volume fraction of the precipitates and r = radius of the precipitate. Note that a significant retarding force is only achieved with a large volume fraction and small particles. At 850 °C the retarding force may have a relatively small estimated value of ~2 x 10^4 J/m^3 (i.e. small volume fraction and large radius of the Laves phase) and a condition will not easily be reached where it effectively blocks firstly, full recrystallisation and subsequently grain growth to a large degree. A number of authors [143,144,] however, have proposed and observed an alternative process of “continuous recrystallisation” in aluminium alloys in which particles occupy mainly subgrain boundaries and these only become “released” after some coarsening of the particles, where after “full recrystallisation” appears to have occurred in a gradual process. That such a “continuous recrystallisation” process may have occurred also here is quite possible if the TEM microstructures after annealing at 850 and 900°C are compared with each other in Figure 9.8 (a) and (b). After annealing at 850°C subgrains are still very much present and are heavily decorated by the last remnants of the Laves phase while at 900°C, the subgrain boundaries have completely disappeared and the grain boundaries are clean of any Laves or other phases. The effective rate of continuous recrystallisation is, therefore, determined by the rate of coarsening (which is accompanied by the rate of disappearance of the smaller particles), of the Laves phase particles. At 850 °C, recovery has taken place but no recrystallisation while at 900 °C where full recrystallisation has taken place. This shows that at 850 °C, the last remnants of the Laves phase particles are still effective in locking subgrain boundaries but not at 900 °C. Therefore, it cannot be concluded that the sudden increase in grain size at the higher temperature of between 950 °C and 1000 °C was due to an unpinning effect of the grain boundaries by the Laves phase, which had already taken place earlier between 850 and 900 °C.

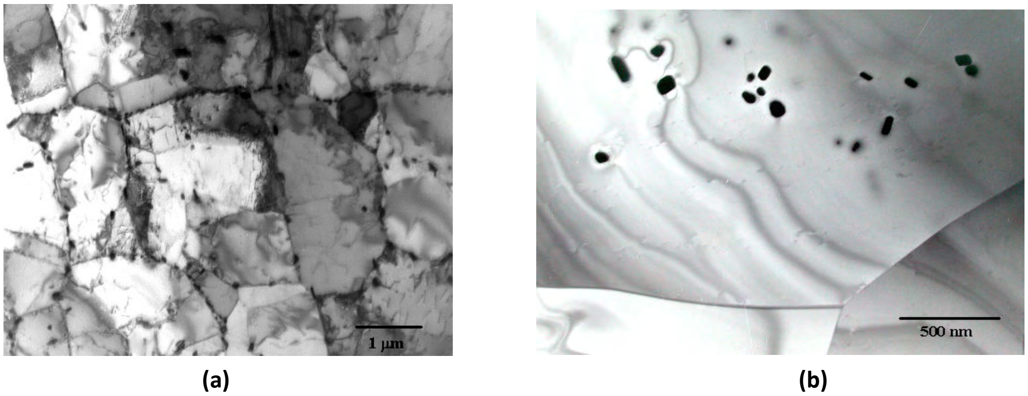

(a) (b)

Figure 9.8. TEM micrographs of the microstructures of the specimens from Steel A that were annealed at (a) 850 °C and (b) 900 °C. Note that with the specimen that was annealed at 900 °C, there were no grain boundary Laves phase precipitates.

An alternative reasoning of “Nb solute drag of sub- and grain boundaries” may be considered in explaining this “sudden” 60% increase in grain size at annealing temperatures between 950 and 1000 °C.

The rate of movement v_b of a recrystallisation boundary in austenite is given by $v_b = p_d M_b$, where p_d is the driving force for recrystallisation and M_b is the boundary’s mobility [145]. An increase in recrystallisation rate and subsequent grain growth may, therefore, result either from an increase in the driving force p_d or the mobility M_b of the moving sub- or grain boundary. The quantitative theory of the solute drag effect on a moving grain boundary during recrystallisation was originally formulated by Lücke and Detert [59]. It was later modified by Cahn [60] and then by Lücke and Stüwe [61]. Since then, this theory has been further refined by several authors [57,58,62]. The equation proposed by Cahn on the rate of grain boundary movement as it is affected by solute drag is [63,64]:

$$\frac{p_d}{v_b} = \frac{1}{M_T} = \frac{1}{M_0} + \frac{\alpha X_s}{(1+\beta^2 v_b^2)} \qquad \text{Equation 9.10}$$

where p_d and v_b are defined as above, M_T is the overall mobility due to *intrinsic plus solute drag*, M_0 is the intrinsic grain boundary mobility in pure material, X_s is the atom concentration of solute in the bulk metal, α is a term related to the binding energy of solute to the grain boundary and β is a term related to the diffusion rate of the solute near the grain boundary. The product (αX_s) primarily governs the overall mobility M_T because $(1+\beta^2 v_b^2) > 1$, while if $(1+\beta^2 v_b^2) >> 1$, then $M_T \approx M_0$ and no solute drag occurs. The apparent mobility factor M_T is critically dependent on the binding energy factor α of solute to the boundary and the solute concentration X_s in the bulk metal. The possibility needs to be considered that a fundamental change from “*solute plus intrinsic drag by Nb atoms*” (i.e. controlled by the overall mobility parameter M_T) to one of only “*intrinsic drag*” and now controlled only by the mobility parameter M_0, may occur within the temperature range 950 to 1000°C in this alloy. The question, however, immediately then arises whether such a transition from “solute plus intrinsic drag” at lower temperatures to one of only “intrinsic drag” at about 950 to 1000 °C would not rather be a gradual one than a “sudden” one? That such a “sudden” departure from solute plus intrinsic drag to only intrinsic drag occurs “suddenly” at critical concentrations of the solute or at critical temperatures, has indeed been found by some authors [58].

Firstly, that such a sharp “break” in the effect of low level concentrations of solute in solute drag on grain boundaries (such as the Nb in solution in this alloy) is to be expected, was shown by Suehiro [57]. The author had investigated the effect of temperature on solute drag during recrystallisation in an Fe-Nb alloy. The theoretical analysis predicted that small Nb-additions to iron would reveal a two orders of magnitude sudden decrease in the grain boundary velocity v_b at 700ºC at a critical Nb concentration of 0.15 %wt and this depends on the temperature and total driving force. This retardation was found to be caused by the solute drag effect of Nb on grain boundaries. In further work by Suehiro et al. [58], the author studied the effect of Nb on the austenite to ferrite transformation in an ultra low carbon steel. Their results indicate that there is a critical temperature where the rate of transformation changes drastically. The transformation that occurs above and below the critical temperature are both partitionless massive transformations. The critical temperature was found to be composition dependent, and for the 0.25% Nb alloy it was found to be 760 °C and for 0.75%Nb alloy it was 720 °C. This is in line with the earlier conclusion that the overall mobility parameter M_T is critically dependent on the binding energy α of the solute to the grain boundary. This segregation energy of solute to a grain boundary actually determines the critical concentration of solute at which the mode of recrystallisation may change from interfacial mobility control (or M_0) to one of solute drag (or M_B).

Secondly, the analysis by Le Gall and Jonas [63] of solute drag by sulphur atoms in pure nickel also showed that this transition from solute plus intrinsic drag to purely intrinsic mobility of a grain boundary is not a gradual one but occurs at a critical temperature that provides a “break” in the mobility versus inverse temperature relationship. Furthermore, this critical transition temperature was found to be highly dependent on the concentration of the “dragging” sulphur atoms in solution [64] and may, therefore, vary with different Nb concentrations in solution which, in turn, will be determined by the alloy content and/or by the heat treatments that have led to the Nb in solution.

Although the likelihood that solute drag by Nb atoms was responsible for the sudden increase in grain size between 950 and 1000 °C, could of course, not be fully proven in this study, it remains currently as the only plausible mechanism. The possibility of Nb solute drag affecting the full recrystallisation and later grain growth of type 441 stainless steels may, therefore, be a useful avenue of further study to confirm the above possibility of solute drag being responsible for the “sudden” 60% increase in grain size at about 950 to 1000 °C in this alloy.

CHAPTER TEN

DISCUSSIONS

TRANSFORMATION KINETICS MODELLING

10.1 INTRODUCTION

The purpose of this chapter is to model the transformation kinetics of the Laves phase in AISI type 441 ferritic stainless steel during the isothermal annealing as a typical case. This model takes into account the diffusion of Nb, and is based on the assumption that the precipitation of the Laves phase is the only one taking place. This has been done within the framework of nucleation and growth theory which leads naturally to the coarsening process.

10.2 MODELLING IN KINETICS OF LAVES PHASE PRECIPITATION

10.2.1 NUCLEATION

Classical nucleation theory is used to estimate the nucleation rate for the Laves phase precipitation. There are several formulae for the nucleation rate, for simplicity the general equation for calculating the rate of isothermal heterogeneous nucleation is given by [108]:

$$\dot{N} = \bar{c} N_o \frac{kT}{h} \exp\left(- \frac{\Delta G^* + Q}{RT} \right) \qquad \text{Equation 10.1}$$

$$\Delta G^* = \frac{4\pi\gamma^3 \{2 - 3\cos\theta + \cos^3\theta\}}{3(\Delta G_v + \Delta G_\varepsilon)^2} \qquad \text{Equation 10.2}$$

where $\bar{c}$ is the amount of Nb additions in the steel, N_o is the number of available nucleation sites, k and h *are* the Boltzmann's and Planck's constants respectively, T is the absolute temperature, ΔG^* is the activation energy for nucleation and γ is the surface energy per unit area of the precipitate – matrix interface. θ is the contact angle between the Laves phase particle and the grain boundary. The critical embryo size r^* for forming a nucleus is given by:

$$r^* = \frac{-4\gamma}{(\Delta G_v + \Delta G_\varepsilon)\{2 - \cos\theta - \cos^2\theta\}} \qquad \text{Equation 10.3}$$

where ΔG_V is the chemical free energy change per unit volume and ΔG_ε is the misfit strain energy around the particle, which is often relatively small compared to the driving force ΔG_V and, hence, was neglected in the calculations for ΔG^* and r^*.

10.2.2 GROWTH

To simplify this model, it is assumed that all the Laves phase precipitation occurs along the grain boundaries and the growth and nucleation of the precipitates takes place simultaneously as it has often been observed that nucleation is superseded by growth very early within the precipitation process. The growth of the precipitates is assumed to be controlled by the diffusion of the Nb in the ferrite matrix. Assuming that the particle size is large enough for the interface between the precipitate and the matrix to be considered, the position of the interface under one dimensional parabolic growth, which corresponds to the radius of large spherical particles, is given by [5,99,146,147]:

$$r = \Omega\sqrt{D_{Nb}t} \quad \text{with} \quad \Omega \approx \sqrt{2\frac{\bar{c}-c^{\alpha\beta}}{c^{\beta\alpha}-\bar{c}}} \qquad \text{Equation 10.4}$$

where D_{Nb} is the Nb diffusion coefficient in the ferrite matrix, t is the reaction time, Ω is the supersaturation, $\bar{c}$ is the alloying concentration, $c^{\alpha\beta}$ and $c^{\beta\alpha}$ are the equilibrium concentrations in the ferrite matrix α and in the precipitate β (i.e. the Laves phase, Fe_2Nb), respectively. Assuming that $c^{\alpha\beta}$ is approximated to be the solute concentration after ageing for a long period of time and is obtained from the Thermo – Calc® calculations (Table 5.6), the supersaturation of Nb for each steel can be calculated and is shown in Table 10.1.

Table 10.1. Calculated equilibrium mole fractions at the interface Fe_2Nb / ferrite for Nb between 600 and 800 °C in AISI type 441 ferritic stainless steel.

Temperature (°C)	Nb addition (Mole fract.)	Nb in precipitates (Mole fract.)	Nb in solid solution (Mole fract.)	Supersaturation Ω
600	2.83×10^{-3}	2.25×10^{-3}	5.80×10^{-4}	1.410
650		2.00×10^{-3}	8.30×10^{-4}	1.411
700		1.50×10^{-3}	1.33×10^{-3}	1.414
750		1.00×10^{-3}	1.83×10^{-3}	1.416
800		4.20×10^{-4}	2.41×10^{-3}	1.420

From this model, it is further assumed that the nucleation rate $\dot{N}$ for the Laves phase is a constant during precipitation in the ferrite matrix, and that soft – impingement does not occur. At time t the radius of the particle nucleated at time t_1 $(0< t_1 <t)$ is expressed

by Equation 10.6. Assuming a spherical particle, the growth rate G_r at time t_1 is given by:

$$G_r = 4\pi r^2 \frac{dr}{d(t-t_1)} \qquad \text{Equation 10.5}$$

Therefore, the number of nuclei precipitated between t_1 and $t_1 + dt_1$ is $\dot{N}\,dt_1$. The rate of the increase in volume of all the particles formed at t_1 is then given by:

$$\frac{dV}{dt} = \frac{8\sqrt{2}}{3}\pi D_{Nb}^{3/2}\left[\frac{\bar{c}-c^{\alpha\beta}}{c^{\beta\alpha}-\bar{c}}\right]^{\frac{3}{2}}\dot{N}(t-t_1)^{\frac{3}{2}} \qquad \text{Equation 10.6}$$

To convert Equation 10.6 to the volume fraction of the precipitates V_v, this equation is multiplied by $\left(\bar{c}-c^{\alpha\beta}\right)/\left(c^{\beta\alpha}-\bar{c}\right)$. By considering the composition factor and integrating Equation 10.8, the following equation can be obtained [146,147]:

$$V_v = 1-\exp\left\{-\frac{16\sqrt{2}}{15}\pi D_{Nb}^{3/2}\left[\frac{\bar{c}-c^{\alpha\beta}}{c^{\alpha\beta}-\bar{c}}\right]^{\frac{1}{2}}\dot{N}t^{\frac{5}{2}}\right\} \qquad \text{Equation 10.7}$$

Equation 10.9 above, is the typical Johnson-Mehl-Avrami-Kolmogorov (*JMAK*) equation applied to describe the kinetics of the single precipitating Laves phase in an AISI type 441 ferritic stainless less and utilising Thermo – Calc® software to predict the driving forces.

10.2.3 COARSENING

The coarsening rate of precipitates can be calculated using the classical theory of the Ostwald ripening equation that is due to Lifshitz and Slyozov [113] and Wagner [114] and is often called LSW coarsening. The LSW coarsening rate equation for diffusion controlled coarsening on a grain boundary is given by:

$$r^4 - r_o^4 = \frac{K_1\gamma\upsilon^{\beta}D_{gb}c^{\alpha\beta}\delta_{gb}}{kT}t \qquad \text{Equation 10.8}$$

where r is the average particle radius, r_0 the initial average particle radius, γ is the interfacial energy, K_1 is a constant, D_{gb} is the diffusion coefficient down the grain boundary, δ_{gb} is the width of the grain boundary, υ^{β} is the molar volume, T is the absolute temperature and t is the holding time at the isothermal heat treatment temperature. The above coarsening Equation 10.10 is also only fully valid if all of the precipitates were situated on grain boundaries and this is, of course, quite difficult to achieve. One factor that strongly affects the coarsening stage is the interfacial energy, even though the equilibrium concentration $c^{\alpha\beta}$ is of a primary concern as this may vary by many orders of magnitude from system to system. The coarsening rate is also influenced by the distribution of the particles before the coarsening stage, which is also determined by the nucleation and growth stages. However, in this work there are not enough experimental data to describe quantitatively all of the details of the coarsening process. The specific data that are needed for the further discussion are the changes in the particle size distribution during high temperature ageing.

10.2.4 DIFFUSION COEFFICIENTS

The knowledge of the appropriate diffusion coefficients is required for all the diffusion controlled transformation equations. The overall diffusion coefficient is given by:

$$D = D_o \exp\left(\frac{-Q}{RT}\right) \qquad \text{Equation 10.9}$$

where D_o is the pre-exponent factor, Q is the activation energy for diffusion, R is the gas constant and T is the absolute temperature. Fridberg et al. [148] reported the intrinsic chemical coefficient D_0 for the diffusion of several solutes in a ferritic matrix and that were used in this work, see Table 10.2 below.

Table 10.2 Chemical diffusion coefficients and activation energies of elements in ferrite [after Fridberg et al. 148].

Elements	D_o (m^2s^{-1})	Q ($Jmol^{-1}$)
Cr	1.5×10^{-4}	240×10^{3}
Mo	1.5×10^{-4}	240×10^{3}
Nb	1.5×10^{-4}	240×10^{3}

10.3 PARAMETERS REQUIRED FOR CALCULATIONS

The term ΔG_v, the chemical free energy change per unit volume of precipitate, is given by:

$$\Delta G_V = \frac{\Delta G}{\upsilon V_v} \qquad \text{Equation 10.10}$$

where V_v is the equilibrium volume fraction of the Laves phase and υ is the molar volume of the Laves phase, and ΔG is the molar free energy change of the precipitation reaction. ΔG can be obtained with from the thermodynamic calculations using the

Thermo-Calc ® software, see Figure 5.14 and Table 5.6. However, it can also be estimated from the precipitation reaction:

$$[Nb] + 2[Fe] \rightleftharpoons Fe_2Nb \qquad \text{Equation 10.11}$$

where [Nb] and [Fe] are the concentrations in solution in the ferrite. The activity of pure solid Fe_2Nb can be taken to be unity, assuming that the activities of the other elements are equivalent to the concentrations. The solubility product is expressed as the solubility of Nb with the following equation:

$$\ln x_{Nb}^{\alpha\beta} = \frac{A}{T} + B \qquad \text{Equation 10.12}$$

with $A = \frac{\Delta G_o}{R}$ and $B = -\ln[Fe]^2$

and for the driving force ΔG:

$$\Delta G = \Delta G_o - RT \ln x_{Nb}^{\alpha\beta} \qquad \text{Equation 10.13}$$

ΔG can be estimated if the values of A and B are available. $x_{Nb}^{\alpha\beta}$ is the equilibrium mole fraction of Nb in solution in ferrite. Assuming that all of the carbon and nitrogen precipitated as (Ti,Nb)(C,N) and the Fe concentration [Fe] is constant, it is possible to calculate the volume fraction and concentrations in the ferrite at the interface of Nb. Table 10.1 shows the calculated concentrations obtained from the Thermo-Calc® predictions. By plotting the relationship between $\ln x_{Nb}^{\alpha\beta}$ and $1/T$, the constants A, B and ΔG_o in the Equation 10.14 were obtained, as illustrated in Figure 10.1 and the results are given in Table 10.3.

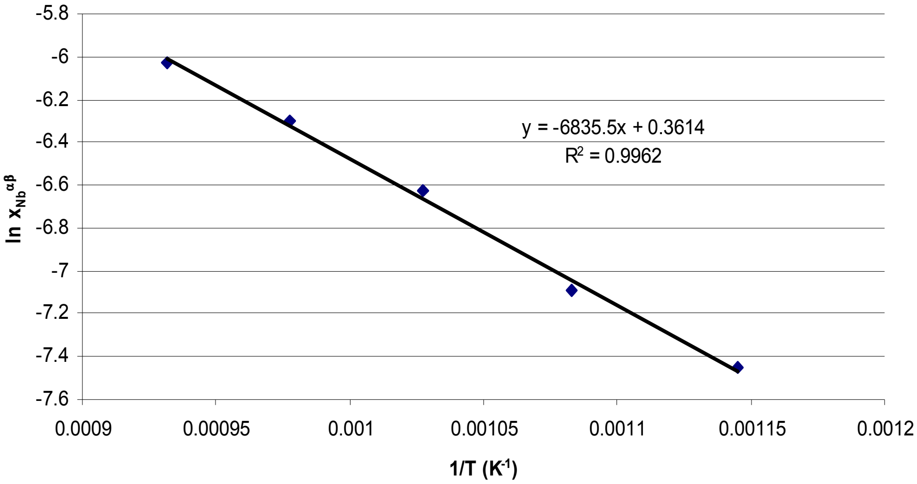

Figure 10.1. The relationship between $\ln x_{Nb}^{\alpha\beta}$ and T^{-1} for AISI type 441 ferritic stainless steel.

Table 10.3. Calculated values of *A, B* and ΔG_o for Fe_2Nb in AISI type 441 ferritic stainless steel.

	A (K^{-1})	B	ΔG_o ($Jmol^{-1}$)
Values for mole fraction and natural logarithm	-6835.5	0.3614	-56830.35
Values for wt fraction and natural logarithm	-2968.6	0.1569	

The solubility product for the Laves phase Fe_2Nb in the Steel A that was studied here was obtained from Thermo-Calc® calculated data and the experimental data. This expression of the solubility product with weight fraction is given as:

$$\log [Nb] = -2968.6/T + 0.1569 \qquad \text{Equation 10.14}$$

This expression is different from the one obtained by Fujita and co-workers [6] in their recent work. These authors were also working on niobium alloyed ferritic stainless steels, and their expression is as follows:

$$\log [Nb] = -3780.3/T + 2.4646 \qquad \text{Equation 10.15}$$

The thermodynamic expressions for the free energy change ΔG for the precipitation reaction of Laves phase in type 441 ferritic steels were also calculated. This expression with the mole fractions in the ferrite matrix, is given by:

$$\Delta G = -56830.35 - RT\{0.3614 + \ln x_{Nb}^{\alpha\beta}\} \qquad \text{Equation 10.16}$$

From Equation 10.16, it was established that the calculated values for ΔG are about ten times higher than the one obtained by Thermo-Calc® predictions. Therefore, it will be reasonable to rather use the values from the Thermo-Calc® predictions, since they are closer to the values from the literature [117].

10.4 CALCULATIONS

Before the calculations for the Laves phase transformation kinetics can be made, it needs to be noted that the following assumptions were used; (i) no treatment of soft impingement was introduced during the nucleation and growth stage, (ii) the particle – size distribution at different nucleation times and growth rates remained constant and (iii) that the precipitation proceeds in an Fe –Nb –C alloy system. Also, it was assumed that Nb(C,N) does not form, and if it does, its volume fraction will be negligible and, therefore, only the nucleation and growth of Laves phase is taking place. There are two unknown parameters, the number density of nucleation sites N_o and the interfacial energy γ. These parameters are treated as fitting parameters. The calculations were carried out at the two temperatures of 700 and 800 °C. The diffusion coefficient and the activation energy for the diffusion of Nb listed in Table 10.3 were used. The parameters that were used for the Laves phase transformations are shown in Table 10.1.

Table 10.4. Parameters used in the calculations for Laves phase transformation.

Parameters	Values
Boltzmann's constant, h (J/K)	1.38×10^{-23}
Planck's constant, k (Js)	6.626×10^{-34}
Gas constant, R (J/K/mol)	8.314
Avogadro constant, N_A (mol^{-1})	6.022×10^{23}
Unit cell volume, V_{cell} (m^3)	1.57×10^{-28}
Molar volume υ_m for Fe_2Nb (m^3/mol)	2.36×10^{-23}
Density ρ of Fe_2Nb (kg/cm^3)	8.58
Lattice parameter of bcc a_{Fe} (nm)	0.28
Contact angle, θ (°)	24

The activation energy for nucleation ΔG^* and the critical particle size r^* for the Laves phase's nucleation assuming the of the surface energy of the Laves phase γ to be 0.331 Jm^{-2} [5], are shown in Table 10.5 below. It should be noted that both the values of ΔG^* and r^* are dependent on γ, and the values obtained at both temperatures are realistic enough for the particle's nucleation and growth.

Table 10.5. The calculated values of the activation energy for the nucleation ΔG^*, and the critical particle size r^* for the Laves phase's nucleation at the two temperatures of 700 and 800 °C.

Temp. (°C)	ΔG (J/mol)	ΔG_v (J/mol)	ΔG^* (J)	r^* (nm)
700	-325	-1.92×10^{8}	8.28×10^{-18}	29.8
800	-90	-2.30×10^{8}	5.72×10^{-18}	24.7

10.4.1 Volume Fraction and Particle Size

Calculated volume fractions for the Laves phase during isothermal annealing at 700 and 800 °C are shown in Figure 10.2 and Figure 10.3 respectively, and compared with the respective experimental observations. The results also show the calculated mean particle's radius with time, but there are no experimental values for comparison. One of the draw backs of this approach is that it does not show an actual estimate of the volume fraction within the steel, i.e the calculations show only the accumulated volume fraction of the Laves phase during the transformation kinetics. Therefore, for comparison purposes the experimental values had to be normalised with respect to their equilibrium volume fraction.

Figure 10.2 shows a similar comparison of the experimental and calculated values for the change of volume fraction and the mean particle radius with time at 700 °C, using reasonable values of $N_o = 4.3 \times 10^{14}$ m^{-3} and $\gamma = 0.331$ Jm^{-2}. However, at 800 °C the calculated results estimated that there are now ten time lower initial nucleation sites for Laves phase than at 700 °C, that is $N_o = 2.9 \times 10^{13}$ m^{-3} and $\gamma = 0.331$ Jm^{-2}. This resulted in lowering the transformation kinetics of the Laves phase nucleation at 800 °C, while the particle's growth rate at 800 °C is much higher than at 700 °C, and this is related to a higher diffusivity of the Nb. Accordingly, a large particle, which has nucleated within the early stages of precipitation, grows continuously even while the volume fraction approaches equilibrium. Because of the capillarity effect, the small particles which nucleated late begin to dissolve from coarsening even though the large one continues to coarsen. It has been demonstrated in the past that the mean particle radius at first increases approximately parabolically with time as all the particles grow from solid solution [105]. The mean radius changes at a rate of about $t^{\frac{1}{3}}$ at longer times as the number density of the particles decreases, and this is consistent with expectations from coarsening theory.

When the experimentally determined activation energy (that is, Q = 211 kJ/mol within the temperature range of 750 to 825 °C) for the Laves phase transformation kinetics is employed in the model, this gives the initial nucleation site density N_o approximately 4.95×10^9 m^{-3} at 800 °C.

The sensitivity of the number density of the nucleation sites N_o and the interfacial energy γ has been established in the niobium – alloyed ferritic stainless steel also for M_6C carbides by Fujita et al [5] and it was observed that the results are affected more by the interfacial energy than by the number density. As an example, it was found that an order of magnitude increase in N_o will lead to about a 20% decrease in mean particle size and a corresponding increase in γ will lead to about a three fold increase in mean particle size [5]. The parameters in this work were chosen as fitting parameters to obtain a reasonable agreement with the experimental results.

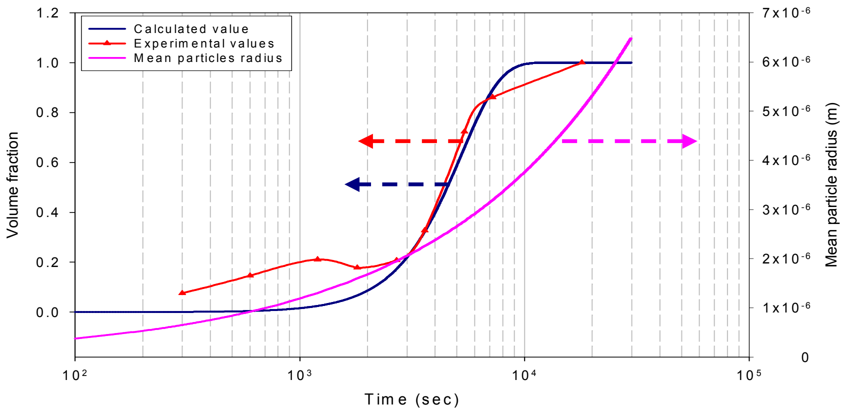

Figure 10.2. Comparison between the experimental data and calculated isothermal transformation curves for the Laves phase's precipitation at 700 °C in the AISI type 441 ferritic stainless, with $N_o = 4.3 \times 10^{14}$ m^{-3} and $\gamma = 0.331$ Jm^{-2}.

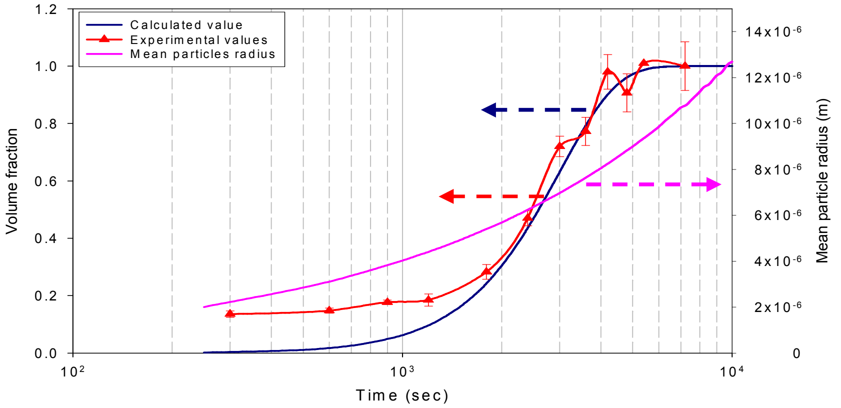

Figure 10.3. Comparison between the experimental data and calculated isothermal transformation curves for the Laves phase precipitation at 800 °C in the AISI type 441 ferritic stainless, with N_o = 2.9 x 10^{13} m^{-3} and γ = 0.331 Jm^{-2}.

10.5 SUMMARY

This model agrees reasonably well with the experimental results and analyses of the microstructures and also qualitatively with the basis of the classical heterogeneous nucleation theory. For instance, it demonstrates that nucleation of the Laves phase on grain boundaries (where the initial nucleation site density N_0 is relatively much lower than for homogeneous nucleation), is dominant at the higher annealing temperatures of 800 °C and above, where the undercooling ΔT and hence the driving forces ΔG_v for nucleation are relatively low and the system then lowers its retarding forces through grain boundary nucleation. As the temperature is decreased and the undercooling ΔT and hence the driving forces are higher, however, heterogeneous nucleation on dislocations becomes more significant, and hence, the initial number of the nucleation sites N_0 becomes higher. The initial number of nucleation sites N_o has a significant impact on the transformation kinetics of the Laves phase, any increase in it results in a decrease in the transformation kinetics, i.e. note the lower value in Figure 10.2 and 10.3 for $t_{50\%}$ at 800°C with N_0 = 2.9x10^{13} m^{-3} if compared to the higher value for $t_{50\%}$ at 700°C with N_0 = 4.3x$10^{14}$$m^{-3}$.

CHAPTER ELEVEN

CONCLUSIONS AND SUGGESTIONS FOR FURTHER WORK

11.1 CONCLUSIONS

The effects of some metallurgical and mechanical factors on the Charpy impact toughness of AISI type 441 have been investigated. The following may be concluded:

- The steel has an acceptable impact toughness of approximately 60 J after being solution annealed at 850°C while below or above this heat treatment the impact toughness decreases significantly, falling to values as low as only 10 J. At temperatures above 850 °C grain growth plays a dominant role in lowering the impact toughness, but at temperatures below 850 °C, the low impact toughness is associated with the precipitation of the intermetallic Laves phase on grain boundaries. The results of the effect of annealing temperature on the Laves phase precipitation agrees with the prediction made by Thermo – Calc®, whereby an increase in Laves phase volume fraction resulted in lowering of the room temperature impact toughness of this AISI type 441 ferritic stainless steel.

- When comparing the results for Steel A from the Thermo-Calc® predictions and the experimental values, Thermo-Calc® predicts that at 825 °C, the weight fraction of the Laves phase should be zero, whereas the experimental results prove that there is still about 0.031wt% of Laves phase present and this remnant still exists even up at 850 °C and above.

- Also, the Thermo-Calc® predictions and the experimental results show that the volume fraction, the solvus temperature and the composition of the precipitates are dependent on the composition of the steel. The stoichiometric composition, also changes with the annealing temperatures.

- The ductile – to – brittle transition temperature (DBTT) is dependent on both the grain size and the presence of Laves phase precipitates on grain boundaries, but the upper shelf energy appears to be only dependent on the presence of the Laves phase precipitates. When a Cottrell approach was used to model the effect of grain size on the embrittllement of the Steel A, it was observed that according to the model, that at temperatures above and below 850 °C the steel will still be brittle. Therefore, it cannot be confidentially assumed that at temperatures below 850 °C, the grain size plays a significant role in embrittling this steel. It was also observed that over the range of grain size from 25.2 to 55.9 µm in Steel A, there is a positive shift of 35 °C in the transition temperature. It was found that this sensitivity of the DBTT on grain size can be lowered by increasing the alloy content of the steel, making it less pure (such as in Steels C to E).

- When applying the Smith model of brittle grain boundary carbides on the embrittlement of Steel A, the predicted outcome and the experimental results do not agree quantitatively although qualitatively some resemblance between what is predicted and what was found was observed. For instance, the width C_o of the embrittling second phase is related, firstly, to the volume fraction V_v of the Laves phase but also secondly, to the grain size, the latter through the grain boundary nucleation site concentration with a larger sub- and grain size leading to a thicker C_o through less available Laves phase nucleation sites. Therefore, both a higher volume fraction as well as a larger sub- and grain size will then decrease the effective fracture stress of the steel though a higher value of C_o. Due to the low volume fractions of the (Ti,Nb)(C,N) and M_6C type Fe_3Nb_3C carbides, it was concluded that they don't have any significance in the embrittllement in these steels. In this case, for any given volume fraction of the (Ti,Nb)(C,N) precipitates, the effective surface energy of the crack γ_f will be higher for a distribution within the grain's interior. Therefore, the possibilities of transgranular or cleavage fracture occurring are minimised.

- The cooling rate has a pronounced influence on the severity of the Laves phase embrittlement of these steels after annealing at 850 °C. After cooling from 950 °C with an already embrittled structure from grain growth, the introduction of Laves phase during slow cooling does not introduce a significant and measurable additional embrittlement. In steels of this type, the embrittlement caused by excessive grain growth is, therefore, overriding.

- Annealing at temperatures above 850 °C in this alloy, generally expected grain growth was experienced, but, there was a "sudden" significant increase in grain size of about 60% within the temperature region 950 to 1000 °C. As no grain boundary pinning was evident at these temperatures, it was postulated that Nb solute drag may be responsible for this "sudden release" of the grain boundaries, affecting the full recrystallisation and later grain growth of type 441 stainless steels at lower temperatures.

On the transformation kinetics of the Laves phase precipitates, the following could be concluded:

- A time – temperature – precipitation (*TTP*) diagram for the Laves phase that was determined from the transformation kinetic curves appears to show two classical C noses on the transformation curves, i.e. the first one occurring at higher temperatures of about 750 to 825 °C and the second one at much lower temperatures, estimated to possibly be in the range of about 650 to 675 °C. The transmission electron microscopy (TEM) analyses show that there are two independent nucleation mechanisms that are occurring at these temperatures. At the lower temperatures of about 600 °C, the pertaining nucleation mechanism is principally on dislocations and as the temperature is increased to above 750 °C, grain boundary nucleation becomes more dominant.
- The effects of grain size and Mo additions on the transformation kinetics of the Laves phase, showed that, by increasing the grain size or adding the alloying element Mo, that these lower the rate of formation of the Laves phase.
- By assuming an interfacial energy of 0.331 Jm^{-2} for the Laves phase, the kinetic model predicts that at 700 °C and 800 °C the initial number of nucleation sites N_o is 4.3×10^{14} m^{-3} and 2.9×10^{13} m^{-3} , respectively. These parameters fit well with the experimental results. When the experimentally determined activation energy of Q = 211 kJ/mol for the Laves phase transformation kinetics is employed in the model, this gives the initial nucleation site density N_o approximately as 4.95×10^{9} m^{-3} at 800 °C, indicating that there might be fewer nucleation sites than expected. This would agree well with heterogeneous nucleation on grain boundaries with a much lower nucleation site density instead of homogeneous nucleation.
- The solubility products of the Laves phase Fe_2Nb in the AISI type 441 ferritic stainless steel obtained from Thermo-Calc® calculated data and the experimental data, is given as:

$$\log [Nb] = -2968.6/T + 0.1569$$

11.2 SUGGESTIONS FOR THE FURTHER WORK

The effect of the steel's composition on the toughness of AISI type 441 ferritic stainless steel still needs to explored further, especially the optimum Mo content that is required to lower both the solvus temperature and the volume fraction of the Laves phase precipitation. Also, the minimum Nb content that will be optimum to stabilise the type 441 ferritic stainless steels, whilst at the same time providing the desired heat resistant properties, and lowering the Laves phase content, also needs to be investigated further.

The possibility of Nb solute drag affecting the full recrystallisation and later grain growth of type 441 stainless steels will be a useful avenue of further study to confirm possibility of the disappearance of Nb solute drag being responsible for the "sudden" 60% increase in grain size at about 950 to 1000 °C in this alloy.

Validation of the modelling of the transformation kinetics for the Laves phase that will improve the precision of any predictions in future:

1. specific characteristics of the nucleation sites;
2. measurement of the interfacial energy; and
3. modelling of precipitation on grain boundaries.

APPENDIX A

SYMMETRY (TRANSLATIONAL AND SPACE GROUP), UNIT CELL DATA AND ATOMIC POSITION PARAMETERS

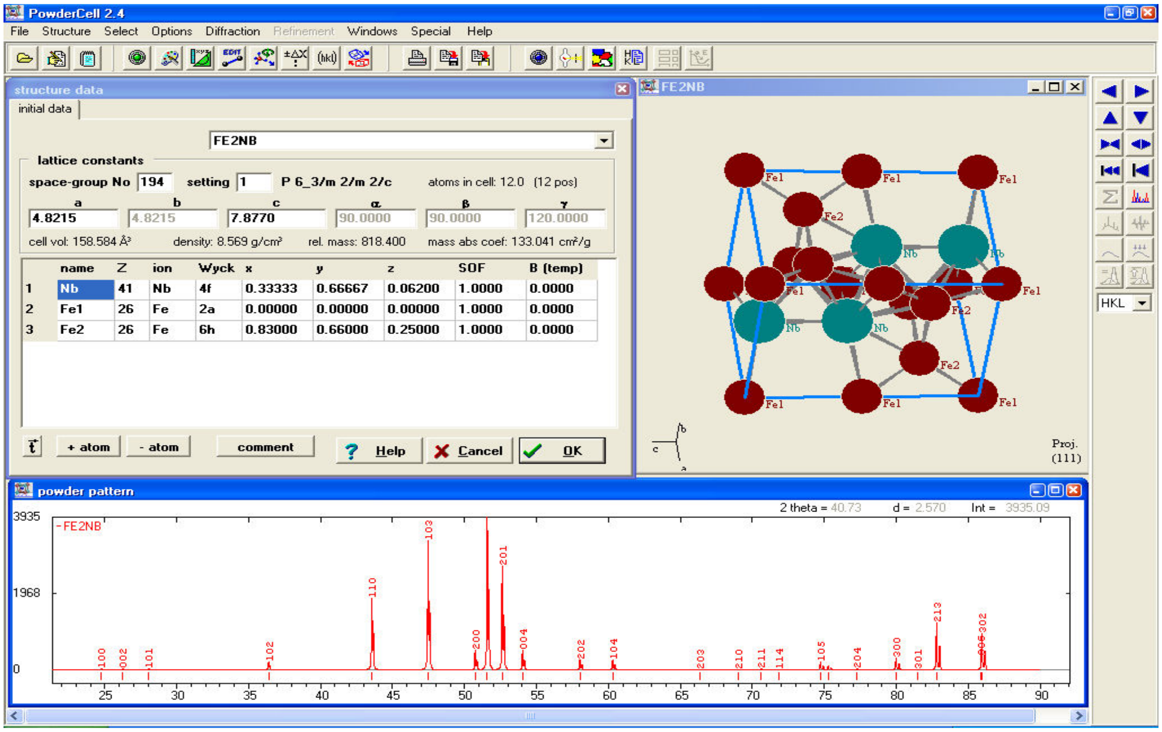

FE2NB

lattice constants

space-group No 194 setting 1 P 6_3/m 2/m 2/c atoms in cell: 12.0 (12 pos)

a	b	c	α	β	γ
4.8215	4.8215	7.8770	90.0000	90.0000	120.0000

cell vol: 158.584 Å³ density: 8.569 g/cm³ rel. mass: 818.400 mass abs coef: 133.041 cm²/g

	name	Z	ion	Wyck	x	y	z	SOF	B (temp)
1	Nb	41	Nb	4f	0.33333	0.66667	0.06200	1.0000	0.0000
2	Fe1	26	Fe	2a	0.00000	0.00000	0.00000	1.0000	0.0000
3	Fe2	26	Fe	6h	0.83000	0.66000	0.25000	1.0000	0.0000

2 theta = 40.73 d = 2.570 Int = 3935.09

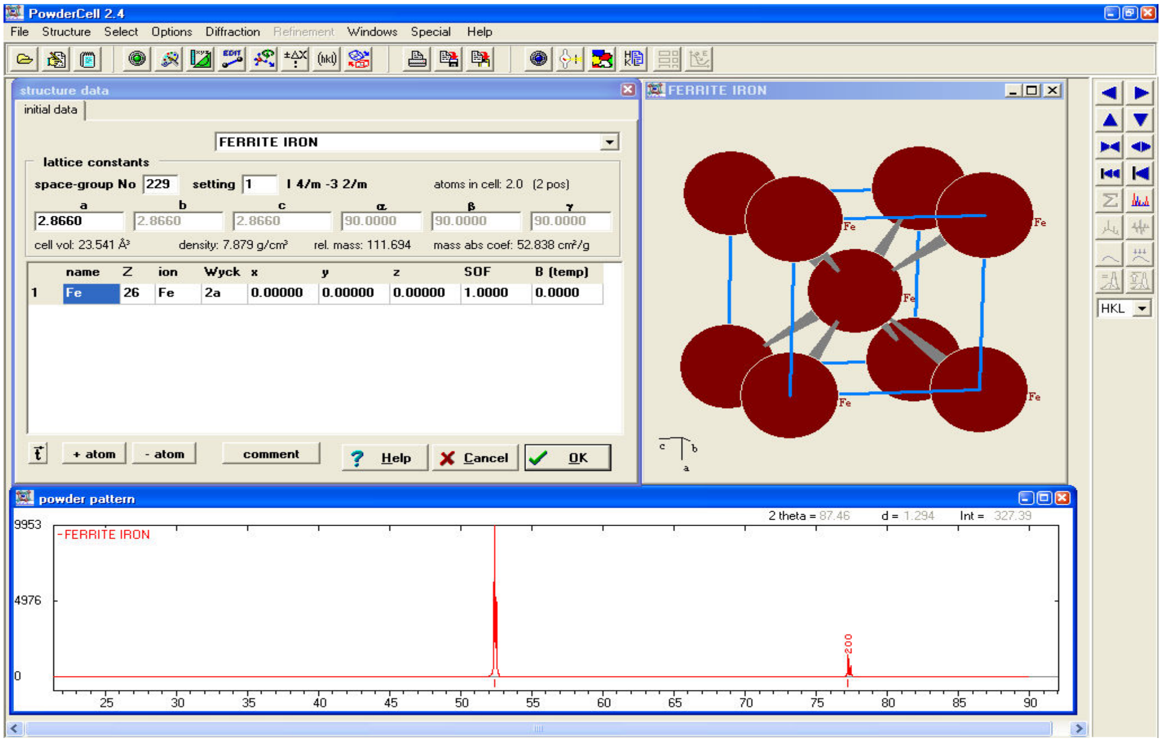

FERRITE IRON

lattice constants

space-group No 229 setting 1 I 4/m -3 2/m atoms in cell: 2.0 (2 pos)

a	b	c	α	β	γ
2.8660	2.8660	2.8660	90.0000	90.0000	90.0000

cell vol: 23.541 Å³ density: 7.879 g/cm³ rel. mass: 111.694 mass abs coef: 52.838 cm²/g

	name	Z	ion	Wyck	x	y	z	SOF	B (temp)
1	Fe	26	Fe	2a	0.00000	0.00000	0.00000	1.0000	0.0000

2 theta = 87.46 d = 1.294 Int = 327.39

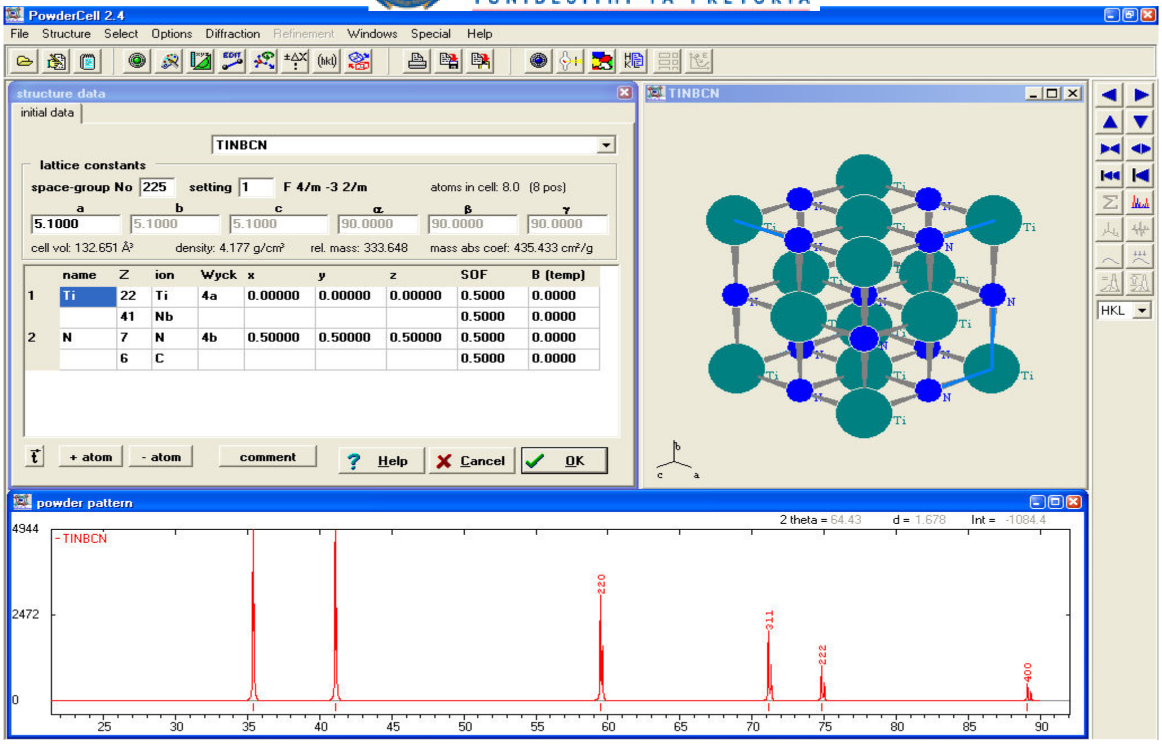

TINBCN

lattice constants

space-group No 225 setting 1 F 4/m -3 2/m atoms in cell: 8.0 (8 pos)

a	b	c	α	β	γ
5.1000	5.1000	5.1000	90.0000	90.0000	90.0000

cell vol: 132.651 Å³ density: 4.177 g/cm³ rel. mass: 333.648 mass abs coef: 435.433 cm²/g

	name	Z	ion	Wyck	x	y	z	SOF	B (temp)
1	Ti	22	Ti	4a	0.00000	0.00000	0.00000	0.5000	0.0000
		41	Nb					0.5000	0.0000
2	N	7	N	4b	0.50000	0.50000	0.50000	0.5000	0.0000
		6	C					0.5000	0.0000

2 theta = 64.43 d = 1.678 Int = -1084.4

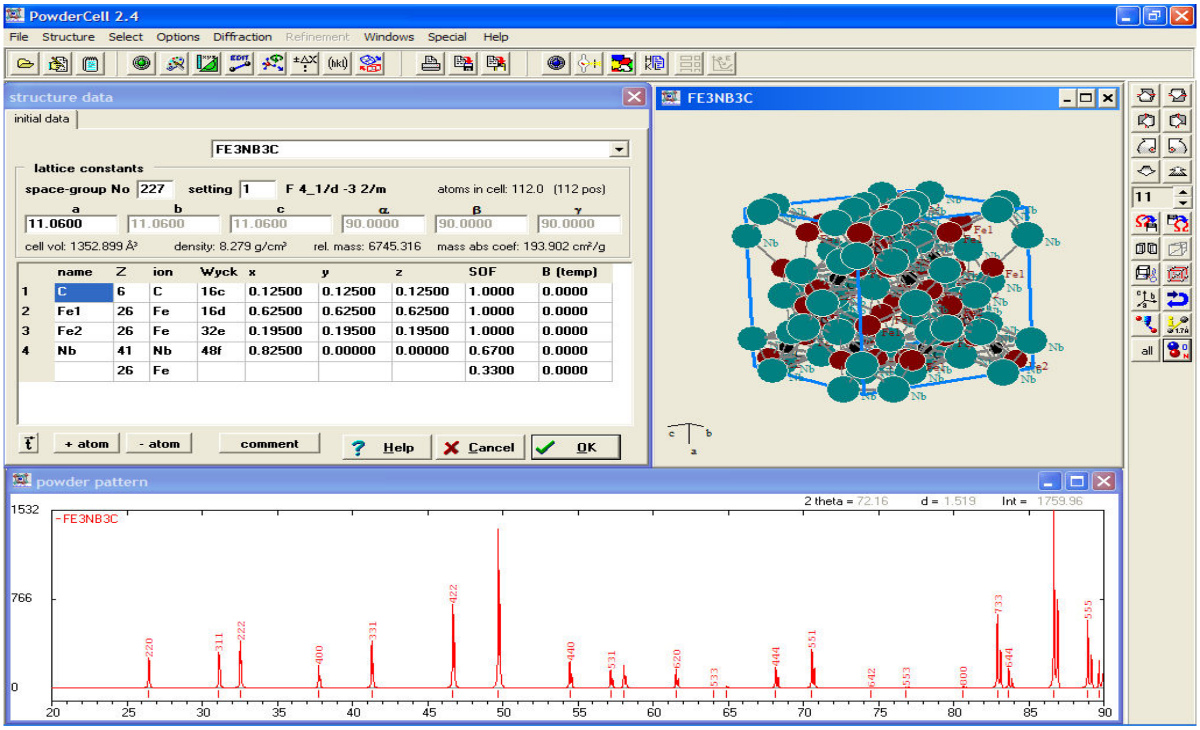

FE3NB3C

lattice constants

space-group No 227 setting 1 F 4_1/d -3 2/m atoms in cell: 112.0 (112 pos)

a	b	c	α	β	γ
11.0600	11.0600	11.0600	90.0000	90.0000	90.0000

cell vol: 1352.899 Å³ density: 8.279 g/cm³ rel. mass: 6745.316 mass abs coef: 193.902 cm²/g

	name	Z	ion	Wyck	x	y	z	SOF	B (temp)
1	C	6	C	16c	0.12500	0.12500	0.12500	1.0000	0.0000
2	Fe1	26	Fe	16d	0.62500	0.62500	0.62500	1.0000	0.0000
3	Fe2	26	Fe	32e	0.19500	0.19500	0.19500	1.0000	0.0000
4	Nb	41	Nb	48f	0.82500	0.00000	0.00000	0.6700	0.0000
		26	Fe					0.3300	0.0000

2 theta = 72.16 d = 1.519 Int = 1759.96

APPENDIX B

THERMODYNAMIC MODELLING USING THERMO-CALC® SOFTWARE

Definitions of the Abbreviated Parameters Used In the Calculations

go data – go to thermodynamic database module
sw-dat – switch database
tcfe3 – Thermo-Calc® Steels/Fe-alloys database
def-sys – define system
l-s – list system
get – get data from the database
go p-3 – go to module Poly 3
s-c – set conditions
l-c – list condition
c-e – compute equilibrium
s-a-v – set axis variable
t – temperature
s-d-a – set diagram axis
set – lab – set label
def-mat – define materials

TEMPLATE USED TO CALCULATE EQUILIBRIUM THERMODYNAMIC PARAMETER OF TYPE 441

```
go data
sw-dat
tcfe3
def-sys
fe c mn co cr b v s si ti ni n al p cu nb o
l-s
CONSTITUENT
reject phase*
restore phase liquid, fcc, bcc, hcp, laves_phase, m6c, m23c6

get
go p-3
s-c n=1, p=101325, t=1773
s-c w(c)=0.00012
s-c w(mn)=0.0051
s-c w(co)=0.0003
s-c w(cr)=0.1789
s-c w(b)=0.000004
s-c w(v)=0.0012
s-c w(s)=0.00001
s-c w(si)=0.005
s-c w(ti)=0.00153
s-c w(ni)=0.0019
s-c w(n)=0.000085
s-c w(al)=0.00009
s-c w(p)=0.00025
s-c w(cu)=0.0008
```

```
s-c w(nb)=0.00444
s-c w(o)=0.000076
l-c
@&
c-e
s-a-v
1
t
473
2000
3
save MPO_3533603
step
normal
post
s-d-a x t-c
s-d-a y np(*)
*
plot SCREEN
set-tit
Intermetallic phases
set-lab
d
s-t-m-s
x
s-s x n 450 1800
plot
SCREEN


set-inter
```

TEMPLATE USED TO CALCULATE THE ISOPLETHS OF TYPE 441

```
go p-3
def-mat
tcfe3
fe
Y
c
.012
mn .51
co .03
cr 17.89
v .12
si .5
ti .153
n .0085
nb .444
ni .19
mo .5
s .001
b .0004
al .009
p .0025
cu .08
o .0076

1000
*
liquid, bcc_a2, fcc_a1, laves_phase_c14, m23c6, m3c2, m6c, sigma,
NONE
Y
N
l-e
SCREEN
VWCS
s-a-v 1 w(c)
0
.03
2.5e-4
s-a-v 2 t
200
1800
40
save
map
post
s-p-f
1
plot
SCREEN
s-d-a w-p c
s-d-a x w-p c
s-d-a y t-c
plot
```

```
SCREEN
s-s x n 0 1
s-s y n 200 1600
plot
SCREEN
s-lab n
plot
SCREEN
s-lab b
plot
SCREEN
PLOT,,,,,;
```

REFERENCE

---

1. http://www.sassda.co.za/sectors/catcon.html/ visited on 19 June 2006

2. http://www.aksteel.com; Aksteel Product Data Bulletin 441 Stainless Steel

3. G-M. Sim, J. C. Ahn, S. C. Hong, K. J. Lee & K. S. Lee; *Effect of Nb Precipitate on the High Temperature Strength in Nb Containing Ferritic Stainless Steels*; Materials Science and Engineering, A396 (2005) pp. 159-165

4. N. Fujita, K. Ohmura, M. Kikuchi & T. Suzuki; *Effect of Nb on High Temperature Properties for Ferritic Stainless Steels*; Scripta Materialia, vol. 35, No. 6, (1996) pp. 705-710

5. N. Fujita, K. Ohmura & A. Yamamoto; *Changes of Microstructure and High Temperature Properties During High Temperature Service of Niobium Added Ferritic Stainless Steels*; Materials Science and Engineering, A351 (2003) pp. 271-281

6. N. Fujita, K. Ohmura & M. Kikuchi; *Expressions for Solubility Products of* Fe_3Nb_3C *carbide and* Fe_2Nb *Laves Phase in Niobium Alloyed Ferritic Stainless Steels*; ISIJ International, vol. 43, No. 12, (2003) pp. 1999-2006

7. A. Miyazaki, K. Takao & O. Furukimi; *Effect of Nb on the Proof Strength of Ferritic Stainless Steels at Elevated Temperature*, ISIJ International 42 (2002) pp. 916 – 920

8 .T. Sawatani, S. Minamino & H. Morikawa; *Effect of Laves Phase on the Properties of Ti and Nb Stabilised Low C, N-19%Cr-2%Mo Stainless Steel Sheets*; Transaction ISIJ, Vol. 22 (1982) pp.172-180

9. A. Bjärbo; *Computer Simulation of Growth and Coarsening of Laves Phase in a Modified 12% Chromium Steel;* Scandinavian Journal Of Metallurgy; 32 (2003) pp. 94-99

10. D.G Morris, M. A. Muñoz-Morris & C. Baudin; *The High-Temperature Strength of Some* Fe_3Al *Alloys*; Acta Materialia, 52 (2004) pp. 2827 - 2836

11. T. Sawatani, S. Minamino & H. Morikawa; *Effect of Laves Phase on the Properties of Ti and Nb Stabilised Low C, N-19%Cr-2%Mo Stainless Steel Sheets*; Tetsu-to-Hagane Vol. 65, No 8 (1979) pp. 1194-1203

12 G. Dimmler, P. Weinert, E. Kozeschnik & H. Cerjak; *Quantification of the laves phase in advanced 9–12% Cr steels using a standard SEM*, Materials Characterization 51 (2003) pp. 341– 352

13 R. P. Reed; *Nitrogen in austenitic stainless steels*, Journal of Metals (1989) pp.16 – 21

14 J. W. Simmons; *Overview: High nitrogen alloying of stainless steels*, Materials Science & Engineering. A207 2 (1996) pp.159 – 169

15 W. E. Stumpf; *: "Course materials for NFM 700, Chpt 4- Precipitation of intermetallics compounds in higher alloyed steels",* Phase transformation in metals and their alloys, University of Pretoria

16 A. L. Schaeffler; Constitution diagrams for stainless steel weld metal -3a: Welding and Joining, *Metal Progr. Databook*, 6 (1973) pp. 207

17 Computational Thermodynamics; Calculation of Phase Diagrams using the CALPHAD method. *Iron-Chromium (Fe-Cr) Phase Diagram*. http://www.calphad.com/iron-chromium.html, visited on 4 July 2007

18 A. C. T. M. Van Zwieten & J. H Bulloch; *Some considerations on the toughness properties of ferritic stainless steels – A brief review*, International Journal of Pressure Vessel & Piping 56 (1993) pp. 1 - 31

19 R. N. Wright; **"***Toughness of Ferritic Stainless Steels"*, **Toughness of ferritic stainless steels,** ASTM STP 706, R. A. Lula, Ed., American Society for Testing and Materials, (1980) pp. 2 – 33

20 N. Ohashi, Y. Ono, N. Kinoshita & K. Yoshioka; "*Effect of metallurgical and mechanical factors on Charpy impact toughness of extra-low interstitial ferritic stainless steels*," **Toughness of Ferritic Stainless Steels**, ASTM STP 706, R. A. Lula, Ed., American Society for Testing and Materials, (1980) pp. 202 – 220

21 A. Plumtree & R. Gullberg; "*Influence of interstitial and some substitutional alloying elements*," **Toughness of Ferritic Stainless Steels**, ASTM STP 706, R. A. Lula, Ed., American Society for Testing And Materials, (1980) pp. 34 – 55

22 J. R. Wood; "*Effect of residual elements and molybdenum addition on annealed and welded mechanical properties of 18Cr ferritic stainless steels*," **Toughness of Ferritic Stainless Steels**, ASTM STP 706, R. A. Lula, Ed., American Society for Testing And Materials, (1980) pp. 145 – 160

23 R.D Campbell; *Ferritic stainless steel welding metallurgy*, Key Engineering Materials, 69 &70 (1992) , pp. 167 – 216

24 T. J. Marrow; *The fracture mechanism in 475 °C embrittled ferritic stainless steels*, Fatigue & Fracture of Engineering Materials & Structure, Vol.19 no. 7 (1996) pp. 919 – 933

25 G. Restrepo Garcé, J. Le Coze, J. L. Garin, & R. L. Mannheim; *σ-Phase precipitation in two heat-resistant steel- Influence of carbides and microstructure*, Scripta Materialia, 50 (2004) pp. 651–654

26 T-H. Lee, C-S. Oh, C. G. Lee, S-J Kim & S. Takaki; *Precipitation of σ-phase in high-nitrogen austenitic 18Cr-18Mn-2Mo-0.9N stainless steel during isothermal aging*, Scripta Materialia, 50 (2004) pp. 1325 – 1328

27 V. Kuzucu, M. Aksoy & M. H. Korkut; *The Effect of strong carbide-forming elements such as Mo, Ti, V And Nb on the microstructure of ferritic stainless steel*, Journal of Materials Processing Technology, 82 (1998) pp. 165 – 171

28 K. Kimura, M. Abe, M. Tendo & T. Senuma; *Influences of heating and coiling temperatures on recrystallisation during hot-rolling process in Ti added high-purity ferritic stainless steel*, International congress Stainless Steel '99: Science and Market, 3rd European congress Proceedings – Vol 2: Innovation in Processes and Products, Italy 6 -9 June 1999, pp 77 - 84

29 Y. Hosoi, N. Wade, S. Kunimitsu & T. Urita; *Precipitation behavior of Laves phase and its effect on toughness of 9Cr – 2Mo Ferritic – Martensitic Steel*, Journal of Nuclear Materials, 141 – 143 (1986) pp. 461 – 467

30 V.V Satyanarayana, G. Madhusudhan Reddy & T. Mohandas; *Dissimilar metal friction welding of austenitic – ferritic stainless steels*, Journal of Materials Processing Technology, 160 (2005) pp. 128 – 137

31 M. Hua, C. I. Garcia, G. Thither & A. J. DeArdo; *Dual–stabilized ferritic stainless steels for demanding applications such as automobile exhaust systems*, 38th Mechanical Work and Steel Processing Conference; Procedings, Vol. XXXIV, Cleveland, Ohio, October 13 – 16,(1996) pp. 453 – 457

32 A.J. De Ardo, *Influence of Niobium and Tantalum on Stainless Steel*, International Symposium on Tantalum and Niobium, Orland, Florida; USA; 7 – 9 Nov 1998, pp. 435 - 465

33 S.R Keown; *Niobium in Stainless Steels*, 1946, Niobium Technical Report, NbTR – 09/86, ISSN 0101 – 5936

34 J. D. Redmond; ***"Toughness of 18C-2Mo ferritic stainless steels,"*** *Toughness of Ferritic Stainless Steels,* ASTM STP 706, R. A. Lula, Ed., **American Society for Testing And Materials**, (1980) pp. 123 – 144

35 A. Valiente, J. Ruiz & M. Elices; *A probabilistic model for pearlite – induced cleavage of plain carbon structural steel*, Engineering Fracture Mechanics, 72 (2005) pp. 709 – 728

36 A. N. Stroh; *The formation of cracks as a results of plastic flow*, Proceeding of Royal Society A, 223 (1954) pp. 404 – 414

37 A. N. Stroh; *A theory of the fracture of metals*, Advanced in Physics, 6(24) (1957) pp. 418 – 465

38 A. H. Cottrell, *Theory of brittle fracture in a steel and similar metals,* Transactions of the Metallurgical Society of AIME, (1958) pp. 192 -

39 E. Smith; *The nucleation and growth of cleavage microcracks in mild steel.* In: Proceedings of the conference on physical basis of fracture. London: Institute of Physics and Physics Society, (1966) pp. 34 – 46

40 G. G. Chell, Developments if fracture mechanics – 2: the mechanics and mechanisms of fracture in metals, Applied Science publishers, London 1981, pp 104

41 J. F. Knott, Fundamentals of Fracture mechanics, Butterworth, London, 1973

42 N. Kinoshita; *Brittle cracking in extra low interstitial ferritic stainless steels*, Stainless Steel '84, Chalmers University of Technology, Goteborg; Sweden, 1984 September 3 – 4 , pp. 43–49

43 A. Plumtree & R. Gullberg; *"Embrittlement of a continuously cooled Fe – 25Cr alloy"*, Metallurgical Transactions A, 7A (1976) pp. 1451 – 1458

44 H. Liebowitz; Fracture: An Advanced Treatise, Volume VI: Fracture for metal, Academic Press , New York 1969

45 R. T. J. Whillock, R. A. Buckley & C. M. Sellar; *The influence of thermomechanical processing on recrystallisation and precipitation in austenitic alloys with particular reference to the effects of deformation and ageing conditions*, Materials Science and Engineering A276 (2000) pp. 124 – 132

46 L. Columbier & J. Hochmann; *Stainless and Heat resisting steel,* Paraguay : AsunciBon, 1968

47 F. B. Pickering; *Physical metallurgy and the design of steels*, Materials Science Series, Applied Science Publishers Ltd, 1978, pp 78

48 J. E. G. Gonzalez; *Study of the effect of hot rolling processing parameters on the variability of HSLA steels*, MSc Dissertation, University of Pittsburgh, 2002

49 H. F. G. de Abreu, A. D. S. Bruno, S. S. M. Tavares, R. P Santos & S. S. Carvalho*; Effect of high temperature annealing on texture and microstructure on an AISI – 444 ferritic stainless steel*, Materials Characterization, 57 (2006) pp. 342 – 347

50 Y. Koyama, A. Takahashi, T. Shimada, N. Fujita & S. Maeda; *Ferritic stainless steel for exhaust equipment of vehicle*, United States Patent, Patent number: 5,843,370 1 December (1998)

51 Y. Uematsu, N. Hiramatsu & S. Nakamura; *Heat resisting ferritic steel excellent in low temperature toughness, weldability and heat resistance*, United State Patent, Patent number: 5,302,214, 12 April 1994

52 D. C. Oliver & M. Sephton; *External corrosion resistance of steel and ferritic stainless steel exhaust systems*, The Journal of the South African Institute of Mining And Metallurgy, March (2003) pp. 93 - 100

53 Y. Inoue & M. Kikuchi; *Present and future of stainless steel for automotive exhaust system*, Nippon Steel Technical Report, No. 88 July (2003) pp. 62 – 69

54 A. Miyazaki, T. Yokota & F. Togashi; *Hot – rolled ferritic steel for motor vehicle exhaust members*, United States Patent, Patent number: 5,792,285, 11 August 1998

55 W. Gordon & A. van Bennekom; *Review of stabilisation of ferritic stainless steels*, Materials Science & Engineering, A351 (2003) pp. 126 – 131

56 C. Jian-chun, L. Qing-you, Y. Qi-long & S. Xin-jun; *Effect of niobium on isothermal transformation of austenite to ferrite in HSLA low – carbon steel*, Journal of Iron and Steel Research, International, 14(3) (2007) pp. 51 – 55

57 M. Suehiro; *An analysis of the solute drag effect of Nb on recrystallisation of ultra low carbon steel*, ISIJ International, 38 (6) (1998) pp. 547 – 552

58 M. Suehiro, Z.-K. Lui & J. Ågren; *Effect of niobium of massive transformation in ultra low carbon steels: A solute drag treatment,* Acta Materialia, 44 (1996) pp. 4241 – 4251

59 K. Lücke & K. Detert, *A quantitative theory of grain boundary motion and recrystallisation in metals in the presence of impurities,* Acta Metallurgica, 5 (1957) pp. 628 – 637

60 J. W. Cahn; *The impurity-drag effect in grain boundary motion*, Acta Metallurgica, 10 (1962) pp. 178 – 798

61 K. Lücke & H. P. Stüwe; *Theory of impurity controlled grain boundary motion*, Acta Metallurgica, 19 (1971) pp. 1087 – 1099

62 M. Hillert; *Solute drag in grain boundary migration and phase transformations*, Acta Materialia, 52 (2004) pp. 5289 – 5293

63 R. Le Gall & J. J. Jonas; *Solute drag effect during the dynamic recrystallisation of Nickel*, Acta Materialia, 47 (1999) pp. 4365 – 4374

64 W. Stumpf & K. Banks; *The hot working characteristics of boron bearing and a conventional low carbon steel*, Materials Science and Engineering A 418 (2006) pp. 26 - 94

65 M. Hillert & B. Sundman; *A treatment of the solute drag on moving grain boundaries and phase interfaces in binary alloys*, Acta Metallurgica, 24 (1976) pp. 731 – 743

66 M. Hillert & B. Sundman; *A solute drag of the transition from diffusion controlled to diffusionless solidification*, Acta Metallurgica, 25 (1977) pp. 11 – 18

67 J-H. Schmitt; *Some examples of stainless steel use in the automotive industry*, Key Engineering Materials, 230 – 232 (2002) pp. 17 – 22

68 Technical Data Blue Sheet-Stainless Steel Type 441, AL 441HP Alloys. Allengheny Ludlum Corporation

69 K. Yamamoto, Y. Kimura, F-G. Wei & Y. Mishima; *Design of Laves phase strengthened ferritic heat resisting steel in Fe-Cr-Nb(-Ni) system*, Materials Science and Engineering A329 – 331 (2002) pp. 249 – 254

70 Columbus Stainless, *Personal Communications*

71 Y.A. Chang, S. Chen, F.Zhang, X. Yan, F. Xei, R. Schmid-Fetzer & W. A. Oates; *Phase diagram calculation: past, present and future*; Progress in Materials Science; 49 (2004) pp. 313 - 345

72 C. Wolverton, X-Y. Yan, R. Vijayaraghavan & V. Ozoliņš; *Incorporating first-principles energetics in computational thermodynamics approaches*, Acta Materialia, 50 (2002) pp. 2187 – 2197

73 A. Schneider & G. Inden; *Simulation of the kinetics of precipitation reactions in ferritic steels*, Acta Materialia 53 (2005) pp. 519 – 531

74 J–O. Anderson, T. Helander, L. Höglund, P. Shi & B. Sundman; *THEMO-CALC & DICTRA, Computational Tools for materials science*, Chalphad Vol. 26, no.2 (2002) pp. 273 – 312

75 Jyrki Miettinen; *Thermodynamic description of solution phases of systems Fe-Cr-Si and Fe-Ni-Si with low silicon contents and with application to stainless steels*, Calphad, Vol 23, No2 (1999) pp. 249 – 262

76 Jyrki Miettinen; *Approximate Thermodynamic solution phases data for steels*, Calphad, Vol 22, No 2 (1998) pp 275 – 300

77 J. D. Robson & H. K. D. H. Bhadeshia; *Kinetics of precipitation in power plant steels*, Calphad, Vol 20, No4 (1996) pp. 447 – 460

78 C.T. Liu, J. Stringer, J. N. Mundy, L. L. Horton & P. Angelini; *Ordered intermetallic alloys: an assessment,* Intermetallics 5 (1997) pp. 579 - 596

79 J. H. Zhu, L. M. Pike, C. T. Liu & P. K. Liaw; *Point defects in binary Laves phase alloys*, Acta Materialia Vol. 47 No. 7 (1999) pp. 2003 - 2018

80 K. S. Kumar & P. M. Hazzledine; *Polytypic transformations in Laves phase*, Intermetallics 12 (2004) pp. 763 – 770

81 J.H Westbrook & R.L Fleischer; Intermetallic compounds: principles and practice, V*olume 1 – principles*, John Wiley & Sons, England, 1995, pp. 107 – 109

82 C. T. Liu, J. H. Zhu, M. P. Brady, C. G. McKamey & L. M. Pike; *Physical metallurgy and mechanical properties of transition-metal Laves phase alloys*, Intermetallics 8 (2000) pp. 1119 – 1129

83 Pearson's Handbook Of Crystallographic Data For Intermetallic Phases Edited by P. Villars & L.D Calvert: vol. 1. American Society for Metals, 1985, pp. 568, 605, 760

84 W.B. Pearson: A Handbook of Lattice Spacing and Structure of Metals and Alloys, Chapter III: *Structure determination and lattice spacing in the theory of alloy formation,* Pergamon Press Ltd, London,1958, , p30

85 F. Stein, M. Palm, G. Sauthoff; *Structure and stability of laves phases. Part I. Critical assessment of factors controlling laves phase stability*, Intermetallics 12 (2004) pp. 713–720

86 S. Hong & C. L. Fu; *Phase stability and elastic moduli of* Cr_2Nb *by first-principles calculations*, Intermetallics 7 (1999) pp. 5 – 9

87 T. F. de Andrade, A. M. Kliauga, R. L. Plaut & A. F. Padilha; *Precipitation of Laves phase in a 28%Cr-4%Ni-2%Mo-Nb superferritic stainless steel*, Materials Characterization *59* (2008) pp. *503-50*

88 F. Gauzzi & B. Verdini; *Analysis of precipitates in low-interstitial 18Cr-2Mo ferritic stainless steels*; Metallurgical Science and Technology 2 (1984) pp. 48 – 53

89 Y. Murata, M. Kamiya, T. Kuneida, A. M. Abdel-Daiem, T. Koyama, M. Morinaga & R. Hashizume; *Dependence of solvus temperature of the Laves Phase on (Mo + W + Re) contents in high Cr ferritic steels*, ISIJ International, 45 (2005) pp. 101 - 106

90 G. J. Cocks & D. W. Borland; *The orientation relationship and morphology of* Fe_2Nb *precipitates in ferrite*, Metal Science 9 (1975) pp. 384 – 389

91 K. Yamamoto, Y. Kimura & Y. Mishima; *Effect of matrix substructures on precipitation of the Laves phase in Fe – Cr – Nb – Ni system*, ISIJ International 43 (2003) pp. 1253 – 1259

92 G. R. Speich; *Precipitation of Laves phase from iron-niobium (columbium) and iron-titanium solid solutions*, Transaction of the Metallurgical Society of AIME 224 (1962) pp. 850 - 858

93 K. Miyahara, J-H. Hwang & Y. Shimoide, *Ageing phenomena before the precipitation of the bulky Laves phase in Fe-10%Cr ferritic alloys*, Scripta Metallurgica et Materialia, Vol. 32 No. 12 (1995) pp. 1917 – 1921

94 Y. Murata, T. Koyama, M. Morinaga & T. Miyazaki; *Prediction of the Laves phase Morphology in Fe-Cr-W-C quaternary steel with the aid of system free energy concept,* ISIJ International, 42 (12) (2002) pp. 1423 – 1429

95 W.E Stumpf, Phase Transformation in Metals and their Alloys, Course materials for NFM 700., *Chapter 1: Nucleation and growth of Precipitates in a Supersaturated Solid Solution*, 2006, University of Pretoria

96 F. R. N. Nabarro, *The strain produced by the precipitation in alloys,* Proceedings of the Royal Society of London. Series A, Mathematical and Physical Science**,** Vol. 175, No. 963 (Jul.18, 1940), pp.519 - 538

97 H.-J. Rajek; "*Computer simulation of precipitation kinetics in solid materials and application to the complex power plant steel CB8"* PhD Thesis, Graz University of Technology, Austria, 2005

98 D. A. Porter & K. E. Easterling, *Phase transformations in metals and alloys, 2nd edition,* London: Chapman and Hall (1992), p. 147.

99 N. Fujita, H. K. D. H. Bhadeshia & M. Kikuchi, *Precipitation Sequence in Niobium-Alloyed Ferritic Stainless Steel.* Modeling and Simulation in Materials Science and Engineering 12 (2004) pp. 273 – 284

100 N. Fujita, *Modeling Carbide Precipitation in Alloy Steels*, PhD Thesis in Materials Science and Engineering, University of Cambridge, 2000

101 N. Fujita & H. K. D. H. Bhadeshia, *Modelling Simultaneous Alloy Carbide Sequence in Power Plant Steels***,** ISIJ International 42 (2002) pp. 760 - 769

102 T. Sourmail & H. K. D. H. Bhadeshia, *Modelling Simultaneous Precipitation Reactions in Austenitic Stainless Steels,* Computer Coupling of Phase Diagrams and Thermochemistry 27 (2003) pp.169 – 175

103 N. Fujita, H. K. D. H. Bhadeshia & M. Kikuchi, *Modeling M_6C Precipitation in Niobium-Alloyed Ferritic Stainless Steel,* Metallurgical and Materials Transactions A 33A (2002) pp. 3339 – 3347

104 N. Fujita & H. K. D. H. Bhadeshia., *Modelling Precipitation of Niobium Carbide in Austenite: Multicomponent Diffusion, Capillarity, and Coarsening.* Materials Science & Technology 17 (2001) pp. 403 – 408

105 H. K. D. H. Bhadeshia, *Advances in the Kinetics Theory of Carbides Precipitation*, Materials Science Forum 426 – 432 (2003) pp. 35 – 42

106 R.G. Nooning, Jr., *Effect of Stabilizing Elements of the Precipitation Behavior and Phase Stability of Type 409 Ferritic Stainless Steels*, MSc in Materials Science and Engineering Thesis, University of Pittsburgh, 2002

107 H. B. Aaron & G. R. Kotler; *Second phase dissolution*, Metallurgical Transaction 2 (1971) pp. 393 – 408

108 J. W. Christian; *The theory of transformations in metals and alloys: an advanced textbook in physical metallurgy. Part 1: Equilibrium and general kinetic theory*, 2nd Ed. New York: Pergamon Press, 1975

109 J.D. Robson; *"Modelling of precipitation in power plant steels":* PhD Thesis in Materials Science and Engineering, University of Cambridge, (1996)

110 N. Fujita & H. K. D. H. Bhadeshia; *Precipitation of Molybdenum Carbide in Steel: Multicomponent Diffusion and Multicomponent Capillarity Effects,* Materials Science & Technology 15 (1999) pp. 627 – 634

111 W.E Stumpf, Phase Transformation in Metals and their Alloys, Course materials for NFM 700., *Chapter 2: Coarsening of Precipitates*, 2006, University of Pretoria

112 P. E. J. Rivera-Díaz-del-Castillo & H. K. D. H. Bhadeshia; *Theory for Growth of Spherical Precipitates with Capillary Effects,* Materials Science & Technology 17 (2001) .30 – 32

113 I. M. Lifshitz & V. V. Slyozov; *The Kinetics of Precipitation from Supersaturated Solid Solutions*, Journal of Physical Chemistry Solids 19 (1961) pp.35 – 50

114 C. Wagner; *Theory of precipitate change by redissolution,* Z Electrochem 35 (1961), pp. 581 – 591

115 A. Kostka, K. –G. Tak, R.J. Hellmig, Y. Estrin & G. Eggeler; *On the contribution of carbides and micrograin boundaries to the creep strength of tempered martensite ferritic steels*, Acta Materialia 55 (2007) pp. 539 – 550

116 T. Mukherjee, W. E. Stumpf, C. M. Sellar & W. J. McG. Tegart; *Kinetics of coarsening of carbides in Chromium steels at 700 °C*, Journal of Iron and Steel Institute 207 (1969) pp. 621 – 631

117 J.D. Robson & H. K. D. H. Bhadeshia, *Modeling Precipitation Sequences in Power Plant Steels. Part 1 – Kinetic Theory,* Materials Science & Technology 13 (1997) pp. 631 – 639

118 J.D. Robson & H. K. D. H. Bhadeshia, *Modeling Precipitation Sequences in Power Plant Steels. Part 2 – Application of Kinetic Theory*, Materials Science & Technology 13 (1997) pp. 640 – 644

119 TCFE3– Thermo–Calc Database (Version 3.0), Royal Institute of Technology, Foundation of Computational Thermo – dynamics, Stockholms/Sweden, 2002

120 L.B McCuster, R.B. Von Dreele, D. E. Cox, D. Louër & P. Scardi; *Rietveld refinement guidelines*, Journal of Applied Crystallography 32 (1999) pp. 36 – 50

121 Course in *Advanced X-ray powder diffraction and Rietveld Refinement*, University of Johannesburg, 29 Oct. – 02 Nov 2007

122 *International Centre for Diffraction Data* (ICDD) reference database

123 K. W. Andrews, D. J. Dyson, and S. R. Keown; (1971). *Interpretation of electron diffraction patterns,* Hilger, London

124 J. W Edington (1975), *Practical electron microscopy in materials science; monograph two: electron diffraction in the electron microscope,* The Macmillan Press Ltd, London

125 TCFE3– Thermo–Calc Database (Version 3.0), Royal Institute of Technology, Foundation of Computational Thermo – dynamics, Stockholms/Sweden, 2002

126 J–O. Anderson, T. Helander, L. Höglund, P. Shi & B. Sundman; THEMO-CALC & DICTRA, Computational Tools for materials science, Calphad Vol. 26, no.2 (2002) pp. 273 – 312

127 B. Jansson, B. Jönsson, B. Sundman & J. Ågren; The Thermo Calc Project, Thermochimica Acta, 214 (1993) pp. 93 – 96

128 http://www.calphad.com

129 TCC ^{TM} Thermo-Calc® Software Users' Guide Version Q

130 A. J. Craven, K. He, L. A. J. Gravie & T. N. Baker; *Complex heterogeneous precipitation in titanium–niobium microalloyed Al-killed HSLA steels—I. (Ti,Nb)(C,N) particles*, Acta Materialia 48 (2000) 3857

131 Q. Li; *Precipitation of Fe_2W Laves phase and modelling of its direct influence on the strength of the a 12Cr-2W stee*l, Metallurgical and Materials Transaction A 37A (2006) pp. 89 – 97

132 B.A. Senior; *Materials Science and Engineering* A119 (1989) L5 (letter)

133 C. C. Silva, J. P. Farias,H. C. Miranda, R. F. Guimares, J. W. A. Menezes & M. A. M. Neto; *Microstructural characterization of the HAZ in AISI 444 ferritic stainless steel welds,* Materials Characterization 59 (2008) pp. 528 – 533

134 J. M. Pardal, S. S. M. Tavares, M. Cindra Fonseca & J. A. de Souza; *Influence of the grain size on deleterious phase precipitation in superduplex stainless steel UNS S32750*, Materials Characterization 60 (2009) pp. 165 – 175

135 J. C. Ahn, G. M. Sim & K. S. Lee; *Effect of ageing treatment on high temperature strength of Nb added ferritic stainless steels*, Materials Science Forum, 475 – 479 (2005) pp. 191 – 194

136 Technical Data Blue Sheet - Stainless Steel Type 441, AL 441HP Alloys, Allengheny Ludlum Corporation

137 L. M. Lundin; *Direct measurement of carbon solubility in the intermetallic $(Fe,Cr)_2(Mo,W)$ Laves phase using atomic-probe field-ion microscopy,* Scripta Materialia 34 (1996) pp. 741 – 747

138 K. Miyahara, S. Matsuoka & T. Hayashi; *Nanoindentation as a strength probe – a study on the hardness dependence of indent size for fine – grained and coarse – grained ferritic steel,* Metallurgical and Materials Transaction A 32A (2001) pp. 761 – 768

139 Fracture: An Advanced Treatise*,* ed. H. Liebowitz; *Volume III: Engineering Fundamentals and Environmental Effects*, Academic Press , New York 1971

140 J. F. Grubb, R.N. Wright & P. Farrar, Jr.; *Toughness of ferritic stainless steel,* ASTM STP 706, R.A Lula, Ed., American Society for Testing and Materials (1980) pp. 56

141 M. Semchyshen, A. P. Bond & H.J. Dundas; In: *Proceedings, symposium towards improved ductility and toughness*, Kyoto, Japan (1971) pp. 239 – 53

142 C. S. Smith, *Grains; Phases and Interfaces: An Interpretation of Microstructure*, Transactions of the Metallurgical Society of AIME 175 (1948) pp. 15 – 51

143 R. Higginson & P. Bate; *Substructure drag effects and recrystallisation textures in aluminium*, Acta Materialia. 47(1999), pp. 1079 – 1090

144 M.J. Jones & F.J. Humphreys; *Interaction of recrystallization and precipitation: The effect of Al_3Sc on the recrystallization behaviour of deformed Aluminium* Acta Materialia 51 (2003) 2149–2159

145 J.E. Bailey & P. B. Hirsch; *The recrystallisation process in some polycrystalline metals*, Proceeding of the Royal Society A 267 (1962) pp. 11 – 30

146 H. Yu, Y. Kang, Z. Zhao & H. Sun; *Morphology and precipitation kinetics of MnS in low – carbon steel during thin slab continuous casting process*, Journal of Iron and Steel Research, International, 13 (2006) pp. 30 – 36

147 Y. Kang, H. Yu, J. Fu, K. Wang & Z. Wang; *Morphology and precipitation kinetics of AlN in hot strip of low carbon steel produced by compact strip production,* Materials Science & Engineering A351 (2003) pp. 265 – 271

148 J. Fridberg, L. Torndal & M. Hillert; *Diffusion in iron,* Jern-kontorets Annaler 153 (1969) pp. 263 -279